,

Ultraluminous X–ray Sources

Andrew King[a,b,c], Jean-Pierre Lasota[d,e], Matthew Middleton[f]

[a]*Astrophysics Division, School of Physics & Astronomy, University of Leicester, Leicester LE1 7RH, UK*
[b]*Astronomical Institute Anton Pannekoek, University of Amsterdam, Science Park 904, 1098 XH Amsterdam, Netherlands*
[c]*Leiden Observatory, Leiden University, Niels Bohrweg 2, NL-2333 CA Leiden, Netherlands*
[d]*Institut d'Astrophysique de Paris, CNRS et Sorbonne Université, UMR 7095, 98bis Bd Arago, 75014 Paris, France*
[e]*Nicolaus Copernicus Astronomical Center, Polish Academy of Sciences, ul. Bartycka 18, 00-716 Warsaw, Poland*
[f]*Department of Physics and Astronomy, University of Southampton, Highfield, Southampton SO17 1BJ, UK*

Abstract

The study of ultraluminous X-ray sources (ULXs) has changed dramatically over the last decade. In this review we first describe the most important observations of ULXs in various wavebands, and across multiple scales in space and time. We discuss recent progress and current unanswered questions. We consider the range of current theories of ULX properties in the light of this observational progress. Applying these models to neutron-star ULXs offers particularly stringent tests, as this is the unique case where the mass of the accretor is effectively fixed.

1. Introduction

Ultraluminous X–ray sources (ULXs) are usually defined by fluxes which, if assumed isotropic, give luminosities

$$L_X > 10^{39}\,\mathrm{erg\,s^{-1}}. \tag{1}$$

The implication is that ULXs appear to be above the Eddington critical luminosity

$$L_{\rm Edd} = 1.3\times 10^{38}\left(\frac{M}{\rm M_\odot}\right)\mathrm{erg\,s^{-1}}, \tag{2}$$

for accretor masses $M \lesssim 10\,\mathrm{M_\odot}$ (see Eq. 20 for the exact definition of the luminosity $L_{\rm Edd}$). Early systematic X–ray surveys found significant numbers of these objects: Fabbiano (1989) reported 16 sources with $L_X > 10^{39}\,\mathrm{erg\,s^{-1}}$. By now, more than about 1800 ULXs (Walton et al., 2022) are known, including several with $L_X > 10^{41} - 10^{42}\,\mathrm{erg\,s^{-1}}$. ULXs are (almost) all in external galaxies, but not located in their nuclei, making them distinct from accreting super-massive black holes

From the beginning it was clear that the brightest ULXs required a significant shift in the standard paradigm for the then known accretion–powered sources, and this provoked a wide variety of speculations. An obvious possibility was that the accreting mass M was unusually large. Colbert and Mushotzky (1999) used a sample of ~ 20 ULXs with apparent X–ray luminosities in the range $10^{40} - 10^{42}\,\mathrm{erg\,s^{-1}}$ to argue that the typical accretors were black holes with masses in the range $10^2\,\mathrm{M_\odot} \lesssim \mathrm{M} \lesssim 10^4\,\mathrm{M_\odot}$. The suggested objects soon acquired the name 'intermediate–mass black holes', or IMBH (Taniguchi et al., 2000). Models for IMBH[1] formation include rapid merging of stellar–mass black holes in globular clusters (Miller and Hamilton, 2002), or of stars in dense clusters (Portegies Zwart and McMillan,

[1]Some dwarf galaxies have active nuclei powered by accretion on to black holes of masses $\sim 10^5\,\mathrm{M_\odot}$, and so with similar luminosities to some ULXs. These black holes appear to obey the same $M-\sigma$ relation between black hole mass and host spheroid velocity dispersion as universally holds for higher mass nuclear black holes and their host galaxies (see Baldassare et al. 2020; King and Nealon 2019 for a discussion). Unlike these objects, ULXs are not unique systems at the dynamical centres of their hosts. Accordingly, in this review we confine use of the term 'IMBH' to objects *not* in the nuclei of dwarf galaxies (see Section 2.7).

Preprint submitted to New Astronomy Reviews. Published: 2023, Volume 96. DOI:10.1016/j.newar.2022.101672 *February 22, 2023*

2002). A problem for all these models was to ensure that the IMBH would find a companion star and then form a binary able to sustain mass transfer at the required rate (up to $\sim 10^{-5} - 10^{-4}\,\mathrm{M_\odot\,yr^{-1}}$).

A quite different idea was that ULXs were fairly standard X–ray binaries with $M \lesssim 10\,\mathrm{M_\odot}$ in unusual states. Begelman (2002) suggested that the accretion discs in standard black hole X–ray binaries might be unstable to the photon–bubble instability, and simply radiate at super–Eddington luminosities. This is limited to luminosities $L_{\rm sph} \lesssim 3 \times 10^{40}\,\mathrm{erg\,s^{-1}}$, and requires that mass loss from the disc surface is small. Körding et al. (2002) suggested that the high luminosities of ULXs could result from relativistic beaming in jets from microquasars oriented towards the observer. This is again limited, to $L_{\rm sph} \lesssim 10^{40}\,\mathrm{erg\,s^{-1}}$. Similarly, it was known that magnetic fields with the strength $\sim 10^{12} - 10^{13}\,\mathrm{G}$ found in accreting neutron stars reduced the electron scattering opacity for X–rays propagating perpendicular to the field (Canuto et al., 1971)[2], but this works only for $L_{\rm sph} \lesssim 3 \times 10^{40}\,\mathrm{erg\,s^{-1}}$, and even then requires a magnetar–strength field $B \sim 10^{14}\,\mathrm{G}$ (Mushtukov et al., 2015b), although these do not seem to appear in binary systems (see Section 3.9). The limits for all three of these stellar–mass models are incompatible with the luminosities $L_X > 10^{41} - 10^{42}\,\mathrm{erg\,s^{-1}}$ observed in some ULXs. Narayan et al. (2017) suggested that radiatively inefficient accretion on to black holes could explain ULXs as the radiative output was tightly beamed. Here much of the accreting gas is swallowed by the hole without radiating.

King et al. (2001) noted that the non–magnetic neutron star in the low–mass X–ray binary Cyg X–2 (not a ULX) was known from evolutionary arguments (King and Ritter, 1999; Podsiadlowski and Rappaport, 2000, see Section 3.11 below) to have survived a previous phase where it was subject to mass transfer at rates $\sim 10^2 - 10^3$ times its Eddington accretion rate of $\sim 10^{-8}\,\mathrm{M_\odot\,yr^{-1}}$. The neutron star had evidently ejected the vast bulk ($\sim 2 - 3\,\mathrm{M_\odot}$) of the transferred mass, retaining no more than a few $\times\, 0.1\,\mathrm{M_\odot}$. Ejection like this is expected in the simple picture of Shakura and Sunyaev (1973) of mass expulsion by radiation pressure from thin accretion discs fed at super–Eddington rates[3] (see Section 3.3 below), so a plausible deduction was that the intense accretion disc wind might block the emitted X–rays from many lines of sight, perhaps leaving only narrow escape routes near the disc's rotational poles. If these had total solid angle $4\pi b$, with $b \ll 1$, an observer viewing the source along these directions but assuming that the emission was isotropic would ascribe a luminosity

$$L_{\rm sph} = \frac{1}{b} L \gg L \tag{3}$$

to the source, where L is its true luminosity[4].

Early discussion of this model was hampered by the lack of a clear relation between the beaming factor b and other physical variables, which left a spurious degree of freedom. This gap was later closed (see Section 3.6), but even before this the model made interesting and testable predictions. Simple estimates showed that the characteristic velocity of the accretion disc wind was $\sim 0.1c$ (King and Pounds, 2003, compare Section 3.14). If $b \lesssim 10^{-2}$, the X–ray fluxes of the early observed ULXs gave $L = bL_{\rm sph} \lesssim 10^{39}\,\mathrm{erg\,s^{-1}}$, below the Eddington value for a $10\,\mathrm{M_\odot}$ black hole. King et al. (2001) also noted that for $b \lesssim 10^{-3}$, the deduced L would be compatible with a neutron star accretor, as expected if Cyg X-2 is a survivor of a ULX phase, and with a white dwarf accretor in cases where the observed X–ray flux was soft (photon energies $\lesssim 0.1\,\mathrm{keV}$). The brightest ULXs would correspond to the same value $b = 10^{-3}$ of the beaming factor, but with a $10\,\mathrm{M_\odot}$ black hole accretor.

This idea gave sensible answers for the likely populations and lifetimes of ULXs (King et al., 2001). It suggested that ULXs were an extremely common stage of high–mass X–ray binary evolution characterised by very large mass transfer rates.

From the analysis of Cyg X-2's evolution, the best candidate for this stage was the preceding phase of super–Eddington mass transfer. This inevitably follows the standard wind–fed high–mass X–ray binary stage once the donor star fills its Roche lobe, as this is always more massive than the accretor. Then mass transfer shrinks the binary to conserve orbital angular momentum, maintaining very high mass rates limited only by the companion's ability to expand rapidly, usually on its thermal timescale (see Section 3.11). Begelman et al. (2006) noted that the extreme

[2] The possibility of this effect is probably the reason why the occasional $L_X \simeq 10^{39}\,\mathrm{erg\,s^{-1}}$ outbursts of the Be–star – magnetic neutron star system A0538-66 (White and Carpenter, 1978) did not attract more attention.

[3] Note that advection, neglected by Shakura and Sunyaev (1973), cannot change the accretion luminosity for a neutron star accretor.

[4] Although this is almost always called 'beaming', as in this review, it is important to note that it is simply collimation, rather than more complex processes such as relativistic beaming.

binary SS433 was probably a system of this type, but not viewed along the accretion disc axis, so was probably a ULX 'viewed from the side'.

The current value of the mass transfer rate $\dot{M}_{\rm tr}$ in any system like this is (as usual) hard to determine from direct observations. In particular measuring the rate $\dot{P}$ of change of the orbital period P gives at best a wide upper limit $\dot{M}_{\rm tr} \lesssim |\dot{P}/P| M_2$ to the mass transfer rate (where M_2 is the mass of the donor star). This is clearly seen for high–mass X–ray binaries: Falanga et al. (2015) measure $\dot{P}/P \sim -10^{-6}\,{\rm yr}^{-1}$ for LMC X-4, Cen X-3, 4U1538-522 and SMC X-1, which would give maximum mass transfer rates $\sim 10^{-6}\,{\rm M}_{\odot}\,{\rm yr}^{-1}$ and make all of these systems ULXs, but their observed luminosities are all sub–Eddington ($\dot{M}_{\rm tr} \lesssim 10^{-8}\,{\rm M}_{\odot}\,{\rm yr}^{-1}$).

We now know that a small group of high–mass X–ray binaries with Be–star companions can occasionally produce very high mass transfer rates for short intervals because of dynamical effects on the Be–star disc – see Section 3.15. These systems are unique in repeatedly making transitions from a 'normal' X–ray binary to a ULX and back. This property distinguishes very sharply between models for ULXs.

The short lifetimes of both types of high–mass X–ray binary (pre–ULX, or Be–star) showed that the disc–wind beaming model required an association of ULXs with star formation. This was already suspected, in particular following the discovery of 7 ULXs in *Chandra* observations of the Antennae, where the merger of two galaxies has provoked vigorous star formation (Fabbiano et al., 2001). *Chandra* observations of the Cartwheel galaxy (Gao et al., 2003) soon strongly confirmed it. They revealed more than 20 ULXs with $L_{\rm sph} > 3 \times 10^{39}\,{\rm erg\,s^{-1}}$, four of them in the range $1 - 5.5 \times 10^{41}\,{\rm erg\,s^{-1}}$, in a spreading ring of star formation triggered some 3×10^{8} yr ago when a smaller intruder galaxy crossed the plane of the Cartwheel disc close to its nucleus. None of these features were easily compatible with the IMBH hypothesis for ULXs (King, 2004). The proof that at least some ULXs had stellar masses, and indeed

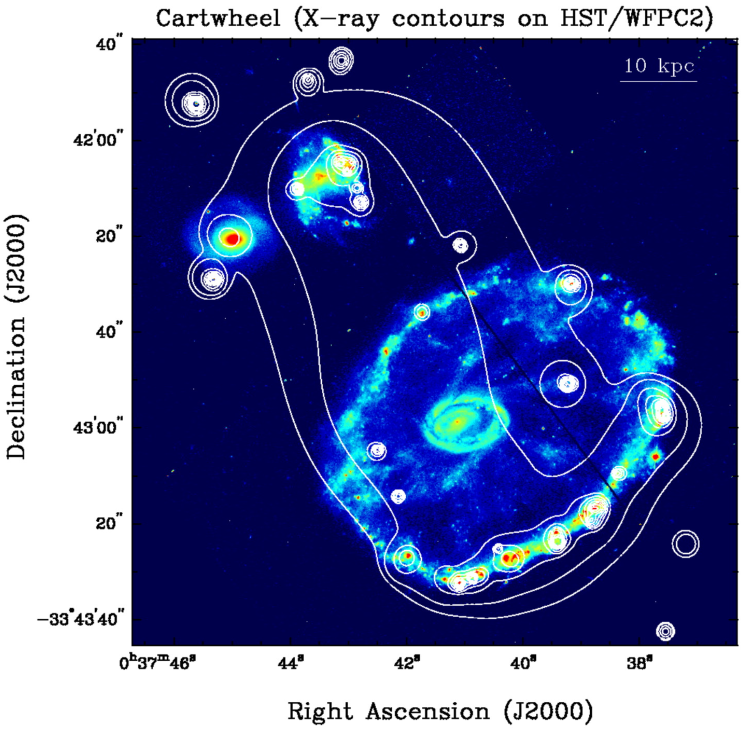


Figure 1 Broadband X-ray contours overlaid on the HST/WFPC2 optical image. The lowest contours are 0.0345, 0.0431 counts pixel^{-1} (pixel=$\sim$ 0".5) and then increase successively by a factor of 2.(Gao et al., 2003).

neutron star accretors, as suggested by King et al. (2001) (see the discussion after Eq. 3), finally arrived when Bachetti et al. (2014) found a coherent periodicity $P = 1.37$ s in the ULX M82 X–2, with $L_{\rm sph} \simeq 1.8 \times 10^{40}\,{\rm erg\,s^{-1}}$. The only plausible interpretation, as the spin of a magnetic neutron star, required $M \sim 1\,{\rm M}_{\odot}$, and showed that this object had

an apparent X–ray luminosity $L_{\rm sph}$ more than 100 times its Eddington luminosity. Note that this observation did not identify the *cause* of the neutron star's super–Eddington luminosity – this is still disputed, essentially between geometrical beaming as suggested by King et al. (2001) and the effects of very strong magnetic fields – see the later part of the present review, and the reviews by Fabrika et al. (2021) and Mushtukov and Tsygankov (2022). Models of this type suggest that a significant, if not dominant, fraction of ULXs are accreting NSs (see abstract in Mushtukov et al. 2015a). It is interesting that only 6 out of the ∼ 1800 non–Be ULXs have so far been observed to show pulsing, unlike what we might expect if this dominance holds. (We thank a referee for provoking this insight). A further problem here is that these very strong fields do not seem to be present in binaries which do not have high accretion rates. This picture then requires us to believe that strong–field neutron stars in binaries are unobservable unless the binary companion supplies them with mass, at a super–Eddington rate.

The observation by Bachetti et al. (2014) removed the main argument motivating IMBH models, and discussion of ULXs is now tightly focussed. The finding of ULXs with $L_X > 10^{41} - 10^{42}\,{\rm erg\,s^{-1}}$, at least one of which contains a neutron–star accretor is a stringent test of theoretical models. It is compatible with disc–wind beaming, and this is also the only model naturally allowing standard Be – X–ray binaries to become ULXs during bright outbursts.

The main question in discussions of ULXs is whether they are all generically similar, or divide into subgroups with different physical models for each. We discuss this question in detail at the end of this review (Sect. 4), but note here that in the absence of observations dividing ULXs into clearly distinct groups, Occam's razor[5] leaves disc–wind beaming as the only model open to test against *all* observations of ULXs. For reviews taking differing points of view, see Fabrika et al. (2021), and Mushtukov and Tsygankov (2022), the latter for pulsed ULXs containing very strongly magnetic neutron star accretors.

2. Observations

Following the launch of NASA's *Chandra* (Weisskopf et al. 2000) and ESA's *XMM-Newton* (Jansen et al. 2001) satellites in 1999, the field of studying X-ray binaries in external galaxies was revolutionised. Both satellites carry X-ray CCD instruments sensitive in the 0.3-10 keV range, and have spectral, timing and imaging capabilities (with on-axis resolutions of < 5"), the latter being vital for successfully disentangling an X-ray bright object from the centre of its host galaxy.

2.1. Catalogues & X-ray Surveys

After more than two decades of pointed observations, the number of individual sources now totals over 300,000 from *Chandra* (CSC 2.0: Evans et al. 2010) and over 500,000 from *XMM-Newton* (4XMM-DR9: Webb et al. 2020) respectively. These extensive catalogues (and their previous iterations) have led to the formation of valuable ULX catalogues, most recently by Kovlakas et al. (2020) utilising *Chandra*, Earnshaw et al. (2019) utilising *XMM-Newton* and (Walton et al., 2022) using the combination of *Chandra*, *XMM-Newton* and *Swift* (with previous catalogues by Swartz et al. 2004, 2011; Walton et al. 2011; Wang et al. 2016).

In these catalogues, ULXs (numbering ∼ 1800 in the most recent: Walton et al. 2022) are located by cross-matching against local galaxy catalogues (e.g. HECATE: Kovlakas et al. 2021), with checks that sources lie within the host's optical D_{25} isophote but are not coincident with the central region, and estimates applied for foreground and background (AGN) contamination. These catalogues enable quantification and searches for variability (e.g. propellor states), targeted follow-up observations, and the study of correlations with host type, including star formation rate and metallicity, thereby testing the predictions of binary population synthesis models (e.g. Wiktorowicz et al. 2019; Kuranov et al. 2020).

Both of the most recent ULX catalogues find that spirals are the most common host galaxies – consistent with ULXs being associated with regions of high star formation. An excess of ULXs is found in lower metallicity galaxies (see also Soria et al. 2005; Mapelli et al. 2010; Prestwich et al. 2013; Brorby et al. 2014; Tzanavaris et al. 2016), the numbers scaling with star formation rate as (Kovlakas et al. 2020):

[5] 'Do not multiply hypotheses beyond necessity', or more simply, 'don't invent two theories for the same thing.'

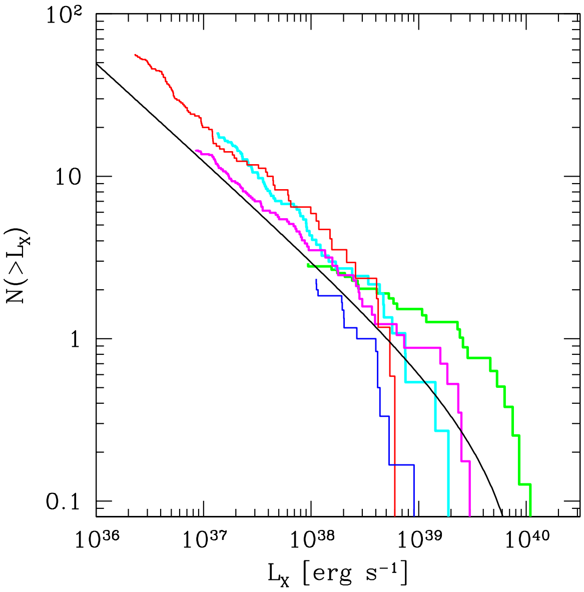


Figure 2 From Mineo et al. (2012) showing the point source X–ray luminosity functions (XLFs) (normalised by star formation rate) created from *Chandra* observations of M101 (blue), NGC 3079 (red), M51 (cyan), Antennae (magenta), NGC 3310 (green).

$$N_{\rm ULX} = 0.45^{+0.06}_{-0.09} \times {\rm SFR}_{M_\odot/{\rm year}} + 3.3^{+3.8}_{-3.2} \times \frac{M_\star}{10^{12} M_\odot}. \tag{4}$$

It is important to note that, regardless of spatial coverage, the long timescale (months or longer) variability of ULXs (as discussed below) demands repeat observing to obtain a reliable census of the population. The all–sky survey by *eROSITA* (eRASS - Cappelluti et al. 2011) will provide precisely these repeat scans, eight being taken over the space of four years (2020-2024) with a far greater sensitivity than the ROSAT all–sky survey (Voges et al. 1999) and coverage from 0.3-10 keV (matching the nominal range of *Chandra* and *XMM-Newton*).

The production of such extensive catalogues provides unique statistical insights, notably the X-ray luminosity function (XLF, such as that shown in Figure 2) giving the combined numbers of low– and high–mass X–ray binary populations and how these depend on metallicty (Lehmer et al. 2021). In turn these XLFs allow estimates for the impact of accreting binary populations on reionisation and galaxy evolution (Fragos et al. 2013; Kovlakas et al. 2022). XLFs can also be directly compared with population synthesis calculations which include the evolution of systems through their various phases (including mass transfer, common envelope, SNe and gravitational inspiral). Recent attempts include those by Wiktorowicz et al. (2019) where the effect of geometrical beaming (following equation 55) is included, Khan et al. (2021), where the observational impact of precession is considered (see below), and Kuranov et al. (2020) who obtain the XLF for magnetised neutron stars in the absence of beaming and precession of the wind-cone (see section 2.3.3).

2.2. Spectroscopy

Chandra and *XMM-Newton* have made it possible to study ULXs with (relatively) high signal-to-noise and energy resolution, and have provided a 'canonical' picture of ULX X-ray spectra. The improved data quality from these satellites allowed single component spectral models to be excluded, instead indicating the presence of a soft excess and signs of a break to a steeper spectral index at the highest energies, where instrumental effective area typically diminishes (e.g. Kaaret et al. 2003; Miller et al. 2004b; Roberts et al. 2005; Stobbart et al. 2006).

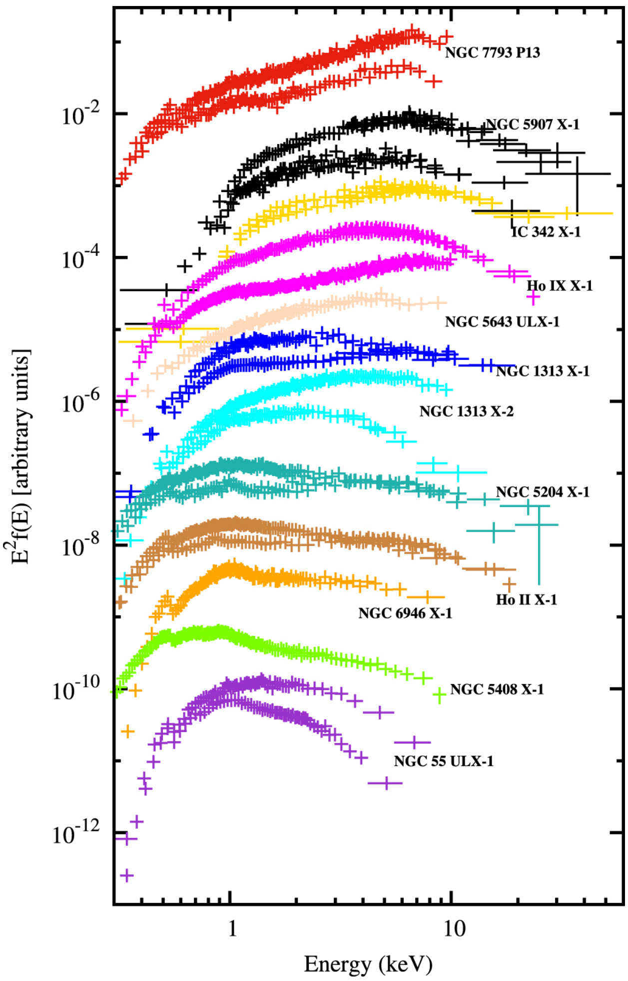


Figure 3 From Pinto et al. (2017), illustrating the variety of observed spectra of ULXs. Each dataset has been unfolded through the instrumental response only (*XMM-Newton* and/or *NuSTAR*) and show two spectral states for each ULX (one hard and one soft). The fluxes on the y-axis are arbitrary.

If the soft excess is modelled as a thin disc (set to truncate at the ISCO), the characteristic temperatures are sufficiently low (0.1-0.2 keV) that IMBHs accreting at significantly sub-Eddington rates were proposed (Miller et al. 2004a,c). But these accretion rates imply an upscattered power-law component extending unbroken to very high energies (around the electron's thermal energy, see e.g. Done et al. 2007). The presence of a break below 10 keV conflicts with this (as too do theoretical arguments - see King 2004), supporting the alternative hypothesis of super–critical accretion (Shakura and Sunyaev 1973). The first large–scale spectral analysis based on a picture of super-Eddington mass supply was performed by Gladstone et al. (2009). Here the harder emission was created by inverse Compton scattering of seed photons (presumed in this case to originate from the soft excess). Since then the field has benefited from data from newer X-ray satellites, notably *NuSTAR*, whose ability to image in the 3-70 keV bandpass (Harrison et al. 2013) confirmed the < 10 keV break with high signal-to-noise ratio (e.g. Bachetti et al. 2013; Mukherjee et al. 2015), and allowed for the most complete picture of the X-ray SEDs of ULXs (Figure 3). This wide band-pass has led to important advances in the field, including the discovery of the first ULX pulsar (Bachetti et al. 2014).

Current modelling of the X-ray spectra of ULXs remains to some degree phenomenological (although more physically motivated models have been developed: e.g. Vinokurov et al. 2013). Models used to describe the soft component variously include an advection dominated disc (typically DISKPBB – with a radial temperature profile $T \propto r^{-p}$ with $p < 0.75$, e.g. Mineshige et al. 1994), or a standard disk blackbody (typically DISKBB – Mitsuda et al. 1984). Each of these has been used to describe the wind, inclination and advection-modified emission from the super-critical disc or from an accretion curtain (depending on field strength and accretion rate – Mushtukov et al. 2017). The harder X-ray emission (typically > 1 keV) is variously modelled with Compton components (with empirical assumptions), broken power-laws and – more recently – the addition of emission from a neutron star accretion column (Walton et al. 2018c). Such two- or three-component spectral fits are motivated by spectral timing methods (e.g. the covariance spectrum - Middleton et al. 2015a) and pulse-resolved modelling (Brightman et al. 2016; Walton et al. 2018b). Although multiple components are often used, simple modelling has encouraged the wide adoption of three simple, empirical categories: soft ultraluminous, hard ultraluminous, and broadened disclike (Sutton et al. 2013 - Figure 4). It is important to note that these definitions are merely descriptive, they do not imply precise statements about the relative contributions of the underlying physical components but provide a useful shorthand for the shape of the spectrum and its evolution with time.

The simple phenomenological modelling described above can be connected to the theoretical picture of super–Eddington mass supply. The characteristic temperatures obtained from modelling the spectra can approximate the colour-corrected temperatures $T_{\rm c,ph}$, $T_{\rm c,sp}$ and $T_{\rm c,max}$, of the quasi-blackbody emission from the disc at characteristic radii (Poutanen et al. 2007): the outer photosphere of the wind ($R_{\rm ph}$), spherization radius ($R_{\rm sph}$ – noting that the assumed position of this radius in Poutanen et al. 2007 slightly differs from Eq. 14), and innermost edge of the disc ($R_{\rm max}$):

$$T_{\rm c,ph} = 0.8 f_{\rm col} \left(\frac{\zeta\beta}{\epsilon_{\rm w}}\right)^{1/2} m^{-1/4} \dot{m}^{-3/4} \ \ {\rm keV} \tag{5}$$

$$T_{\rm c,sp} = 1.5 f_{\rm col} m^{-1/4} \dot{m}^{-1/2} \ \ {\rm keV} \tag{6}$$

$$T_{\rm c,max} = 1.6 f_{\rm col} m^{-1/4} \ \ {\rm keV} \tag{7}$$

Associated values for the accretion rate then follow under the assumption of a fixed fraction of accretion energy deposited in the wind ($\epsilon_{\rm w}$), colour temperature correction ($f_{\rm col}$) as well as dynamical values associated with the wind (i.e. the wind velocity relative to the Keplerian velocity at $r_{\rm sph}$, β, and the cotangent of the wind opening angle, ξ – Poutanen et al. 2007). As an example, typical values of the soft X-ray component's temperature lie between 0.1 and 0.4 keV (Middleton et al. 2015a); for values of $f_{\rm col} \sim 2$ this indicates Eddington-scaled mass supply rates in the range $\sim$ 20-300 for a 10 $M_{\odot}$ black hole and 50-800 for a 1.4 $M_{\odot}$ neutron star.

One must be cautious when modelling ULX spectra, as descriptions are often degenerate (see Section 2.3.4), and the presence of a neutron star can have a major impact on the interpretation of characteristic temperatures (see Section 2.2 for more detail). As an example, strong dipole fields could truncate the *thin* disc (i.e. before the local Eddington limit is reached) which comes with the natural corollary that such a disc emits below the Eddington limit for a neutron star mass (see Middleton et al. 2019a). Additional uncertainty in the spectral fitting (regardless of the nature of the

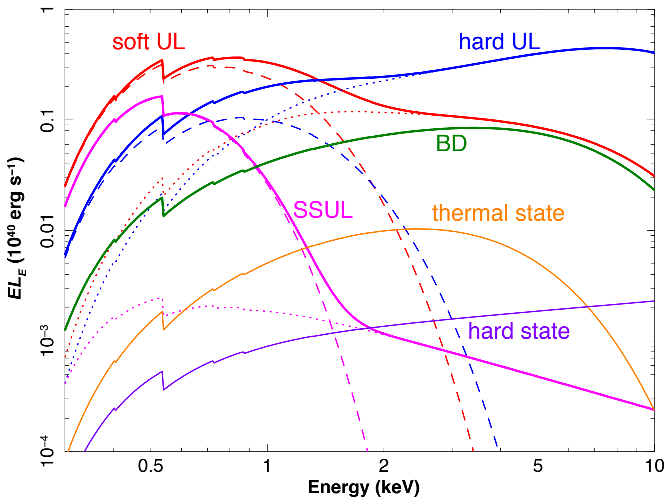


Figure 4 From Kaaret et al. (2017), showing the variety of phenomenological states of ULXs (SSUL: supersoft ultra-luminous; BD: broadened disc; H/SUL hard and soft ultraluminous) as defined by Sutton et al. 2013) as compared to the standard canonical soft (thermal) and hard state spectra of XRBs.

compact object) arises as Compton down-scattering within the wind itself can distort the temperature of the photons produced at various radii. It remains likely that the soft component is inclination-dependent, so that a more edge–on system appears increasingly softer until the temperature from the face of the wind dominates (and from which we expect a luminosity $\sim L_{\rm Edd}$ to be emitted: Poutanen et al. 2007; Zhou et al. 2019; Qiu and Feng 2021). Together with changes in accretion rate, the inclination dependence provides a natural explanation for soft and super-soft (e.g. Feng et al. 2016) ULXs which fit well into the simplified unified model of ULX spectra (Poutanen et al. 2007; Middleton et al. 2015a; Soria and Kong 2016; Urquhart and Soria 2016a; Pinto et al. 2017).

A notable absence from ULX spectra (with the exception of Swift J0243.6+6124: Bykov et al. 2022, see also the claim of a feature in NGC 7456 ULX-1: Mondal et al. 2021) is that of Fe K_α emission, with Walton et al. (2012) placing strong constraints on its presence in Ho IX X-1. This absence is remarkable, given the strong fluorescent yield of Fe and its typically high abundance. Importantly this may point towards an extremely highly ionized gas environment, consistent with an irradiated conical outflow (see also Medvedev and Fabrika 2010; Pinto et al. 2021). It is quite likely that weak Fe K in reflection would be produced far out in the wind cone where the material is not fully ionized, in the disc beyond $R_{\rm sph}$ provided that this radius is small enough that the outer disc is irradiated by X-rays with energies > 7 keV, and beyond the magnetospheric radius (so long as this is > $R_{\rm sph}$).

More elaborate models of emission from slim discs already exist (e.g. Straub et al. 2013), and models for fitting to data may now be obtained directly from 3D radiative MHD simulations for super–Eddington mass supply on to black holes (e.g. Narayan et al. 2017) and magnetised neutron stars (Kawashima and Ohsuga 2020). Still more elaborate spectral modelling may include self–consistent photoionization. Looking forwards, it is hoped that such models may bridge the gap between theory and observation.

2.2.1. High energy-resolution X-ray spectroscopy

Phenomenological models can reasonably describe ULX spectra as observed by current instrumentation, although clear residuals to these models are found between 0.5 and 2 keV (Stobbart et al. 2006) in multiple ULXs (Middleton et al. 2015c), and seen in both *XMM-Newton* and *Chandra* spectra (ruling them out as instrumental artefacts - Roberts et al. 2006; Pintore et al. 2015). Initially thought to originate in diffuse star-forming plasma (Strohmayer et al. 2007; Strohmayer and Mushotzky 2009; Miller et al. 2013), the luminosities are too high for such an interpretation, and an association with mass-loaded outflows was instead made (Middleton et al. 2014). Both via high angular resolution studies with *Chandra* (Sutton et al. 2015), and by studying the correlated variability of the features with spectral

hardness (Middleton et al. 2015c; Pinto et al. 2020b), it was determined that they must be associated with the ULX and not with the surrounding nebula (e.g. Sathyaprakash et al. 2019a).

Instruments with higher energy resolution (e.g. *XMM-Newton*'s Reflection Grating Spectrometer, RGS) have shown that the CCD-quality features are indeed composed of blueshifted absorption lines and rest–frame emission lines (Pinto et al. 2016, 2017 – but see Kosec et al. 2018a for apparently blueshifted emission lines in NGC 5204 X-1), confirming the suggestion by Middleton et al. (2014). In NGC 1313 X-1, counterpart Fe absorption lines have also been found in *NuSTAR* CCD-quality data with a blueshift consistent with that inferred from the lower energy resolved lines (Walton et al. 2016b). The limit implied on the outflow velocity is > 0.2 c, considerably faster than observations of thermal (or magneto-centrifugal) winds from sub–Eddington XRBs (e.g. Ponti et al. 2012), but consistent with radiatively driven winds from a super-critical inflow (e.g. King and Pounds 2003; Jiang et al. 2014; Kitaki et al. 2021).

Ultrafast outflows have now been located in several ULXs via individual searches of RGS spectra (NGC 1313 X-1 and NGC 5408 X-1: Pinto et al. 2016, NGC 55 ULX: Pinto et al. 2017, NGC 247 ULX-1: Pinto et al. 2021) and notably in the transient NS ULXs, NGC 300 ULX-1 (Kosec et al. 2018b) and Swift J0243.6+6124 (van den Eijnden et al. 2019). Intriguingly this latter source simultaneously launches both a wind and a jet (see Section 2.4.1). In addition to these studies, a larger scale search within the data of 19 ULXs, using a faster algorithm by (Kosec et al., 2021), indicates that rest-frame emission lines and blue-shifted absorption lines are indeed a ubiquitous feature.

The velocity of the wind, $v_{\rm wind}$, a measure of the ionisation state, ξ (both obtained by using consistent models for photoionised plasma - Pinto et al. 2016), and an assumption for the ionising luminosity, allows the kinetic luminosity of the wind to be estimated from:

$$P_{\rm wind} = \frac{1}{2}\dot{m}v_{\rm wind}^2 = 2\pi L_{\rm ion}\frac{\Omega}{\xi}v_{\rm wind}^3 m_{\rm p} \tag{8}$$

The filling and covering factor of the wind (Ω) in the above formula remain unknown, but the high projected velocities (which are therefore lower limits on the true velocity) imply the kinetic luminosities for these winds are substantial, and may even dominate over the observed radiated power from the source (Pinto et al. 2016). It is worth noting that such observations are potentially in conflict with MHD models which predict lower fractions of the radiative power spent in launching the wind (Jiang et al. 2014). Questions remain over the nature of the rest-frame emission lines - conceivably these may be due to collisional ionization as a result of interaction with the wind of the companion star (e.g. Oskinova 2005; Mauerhan et al. 2010) or may be associated with lower velocity winds driven from the outer, irradiated disc (Middleton et al. 2021a).

Studies have recently shifted to determining how the wind appears to change as a function of spectral hardness. As first reported in Middleton et al. (2015c), the strength of the CCD residuals in NGC 1313 X-1 appears to anti-correlate with increasing spectral hardness (i.e. the features are weaker when the source appears spectrally harder). One interpretation has been that the wind or system is precessing, or the mass accretion rate changing (the optical depth along our line-of-sight through the wind changing with either/both: Poutanen et al. 2007). A more recent in-depth study of NGC 1313 X-1 based on a series of long *XMM-Newton* observations, has resolved the atomic features in emission and absorption (using the RGS) and made a direct comparison to changes in the X-ray spectrum (Pinto et al. 2020b). These data have allowed for important progress to be made, including the discovery of a slower, more neutral component of the wind (moving with a projected velocity of $\sim 0.08c$ rather than the fast wind of $\sim 0.2c$), pointing towards a complex outflow (as one might expect from simulations - e.g. Takeuchi et al. 2013). These high energy-resolution results broadly confirm the picture from the CCD-quality residuals (as does the larger sample result of Kosec et al. 2021), with the observation of an anti-correlation between spectral hardness and line strength, possibly driven by changes in accretion rate and/or inclination angle via precession (Middleton et al. 2015b,d). Importantly the correlated changes further confirm that the winds are associated with the ULX rather than some surrounding, more distant material (which would not respond on such timescales). The high quality data made available via long RGS exposures has allowed, for the first time, photoionization modelling of a ULX wind (Pinto et al. 2020a, see also Pinto et al. 2021 for a comparison to other ULXs), indicating that material in the innermost regions is potentially thermally unstable. In future, the launch of *XRISM* and *Athena* (with its X-ray Integral Field Unit) will allow for far deeper studies of ULX winds.

2.2.2. Spectral studies of neutron star ULXs

The discovery of several pulsating neutron star ULXs (Bachetti et al. 2014; Israel et al. 2017a,b; Fürst et al. 2016; Tsygankov et al. 2017; Carpano et al. 2018; Sathyaprakash et al. 2019b; Doroshenko et al. 2018 – see Table 2) has led to scrutiny of the X-ray spectrum in light of the expected differences from the standard super-critical model, as a consequence of the presence of the magnetosphere – accretion curtain and column – and surface. The truncation of the disc at the magnetospheric radius and free-fall of material onto the magnetic poles, leads to two likely configurations depending on the accretion rate. At very high accretion rates or low dipole field strengths, the spherization radius is reached at radii greater than the magnetospheric radius – if the wind is optically thick (see Vasilopoulos et al. 2019; Middleton et al. 2019b) it will act to collimate some of the radiation within. Regardless, we expect thermal emission from R_{sph} down to R_{mag}, which tends increasingly towards a blackbody as R_{sph} tends towards R_{mag}. At radii larger than R_{sph}, the emission is from an unmodified, approximately thin disc (thin below ~ 30% Eddington, e.g. McClintock et al. 2006), although this emission is probably modified and scattered by the wind covering those regions between R_{sph} and R_{ph}. For strong magnetic fields or relatively low accretion rates, $R_{sph} < R_{mag}$ and the disc emission beyond R_{mag} originates from an Eddington–limited thin disc. In either accretion-rate regime, within R_{mag}, the material falls freely along magnetic field lines until meeting the standing shock front in the accretion column. The key characteristic of the magnetospheric curtain is the optical depth τ which depends on the accretion rate (and therefore dipole field strength) and angle from the accretion disc plane. According to (Mushtukov et al. 2017) the optical depth is given by:

$$\tau \approx \frac{70 L_{39}^{6/7} B_{12}^{2/7}}{\beta(\theta)} \left(\frac{\cos\theta_0}{\cos\theta} \right)^3 \tag{9}$$

where $\theta_0 \approx \pi - (R/R_{\rm M})^{1/2}$ is the angle to the accretion column base and $\beta(\theta) = v(\theta)/c$ is the local dimensionless velocity along the magnetic field lines. This optical depth determines the shape of the thermal spectrum from the curtain (becoming optically thick for $L_{39} > B_{12}^{1/4}$) with a range of emergent photon temperatures due to inclination dependence, as well as potentially diluting variability Mushtukov et al. 2019) and the presence of cyclotron resonance scattering features (see the following section). A rough estimate for the temperature of the curtain is provided by Mushtukov et al. (2017) as $T_{\rm out} \sim 0.5 L_{39}^{11/28} B_{12}^{-2/7} m^{-1/14} R_6^{-5/7}$ keV (where $R_6 = R/10^6$ cm and $m = M/M_\odot$) which can be $\gtrsim 1$ keV for typical ULX luminosities, and could therefore explain one of the hard components in the spectra of ULXs.

The final set of likely spectral components is then: at high accretion rates/low dipole field strength – thin disc, thick disc and wind, curtain and column, and for low accretion rates/high dipole field strength – thin disc, curtain and column. Using the latter description of the inflow, Koliopanos et al. (2017) explored the possible range of dipole magnetic field strengths for 18 ULXs (containing both pulsing ULXs and those without) under the assumption that $R_{sph} < R_{mag}$, finding values ranging from $\sim 10^{11} - 10^{13}$ G (although there is a tension between the assumption of a thin disc and observed super-Eddington luminosity from the soft component).

The spectrum of the pulsed emission can also be extracted via selecting 'off' versus 'on' pulse times and obtaining the difference spectrum. The latter has been performed by Brightman et al. (2016) in the case of M82 X-2, and Walton et al.

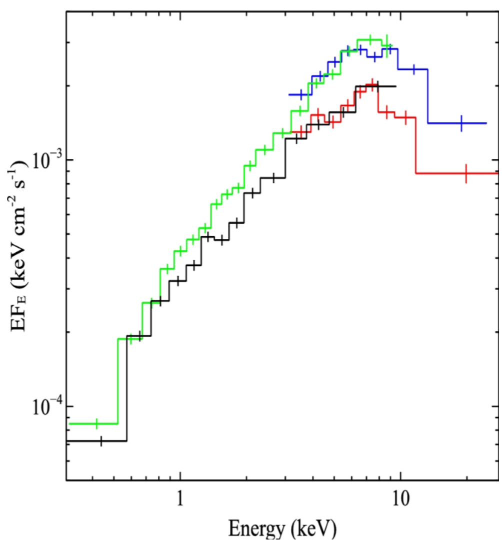


Figure 5 Pulse-on versus pulse-off spectra for NGC 7793 P13 from Walton et al. (2018b), using data from *NuSTAR*.

(2018b) in the case of NGC 7793 P13
(Figure 5), who found the accretion column to be well-modelled by a power-law with an exponential cutoff (see also Pottschmidt et al. 2016 for a similar finding for SMC X-3). The unambiguously spectrally hard nature of the pulsed emission has naturally led to suggestions that other, similarly hard ULXs (e.g. Ho IX X-1: Walton et al. 2017 and IC 342 X-1:Middleton et al. 2015a) may also harbour neutron stars (Pintore et al. 2017; Koliopanos et al. 2017; Walton et al. 2018c; Gúrpide et al. 2021). Showing whether the 'hard excess' is indeed due to the presence of an accretion column will be valuable for identifying neutron star ULXs without the need for deep pulsation searches; this in turn will help reveal ULX demographics and test our grasp of binary evolution.

2.2.3. Cyclotron resonance scattering features

In the presence of strong magnetic fields, electron and proton orbits are quantised into Landau levels; such particles can resonantly scatter incident photons of sufficient energy depending on the quantum mechanical cross section (see Schwarm et al. 2017) and leave cyclotron resonance scattering features (CRSFs) imprinted on the spectrum (although any subsequent scattering, for instance in an accretion curtain, can reduce their detectability - see Mushtukov et al. 2017). The transition energy of such lines is related to the magnetic field strength and particle type according to:

$$\Delta E_{\mathrm{e}^-} = \frac{11.6}{(1+z)}\left(\frac{B}{10^{12}G}\right) \;\; \mathrm{keV} \tag{10}$$

$$\Delta E_{\mathrm{p}^+} = \frac{6.3}{(1+z)}\left(\frac{B}{10^{15}G}\right) \;\; \mathrm{keV} \tag{11}$$

where z is the gravitational redshift, given by:

$$z = \left(1 - \frac{2GM}{r_{\mathrm{cyc}}c^2}\right)^{-1/2} - 1 \tag{12}$$

where r_{cyc} is the distance from the surface of the neutron star to where the line is formed. Studies of CRSFs in Galactic systems (e.g. Tsygankov et al. 2006; Jaisawal and Naik 2016) have been useful for studying the regions in which these lines are formed (see the review of Staubert et al. 2019).

Brightman et al. (2018) reported the first CRSF in a ULX, at an energy of $\approx$ 4.5 keV in a *Chandra* observation of M51 ULX-8 (see Figure 6); as this energy does not correspond to known instrumental features and cannot be readily explained as a highly blueshifted absorption line, a CRSF is a possible explanation. Given the line energy, the implications are either electrons orbiting in a field with a strength of $\sim 5 \times 10^{11}$ G (for z = 0.25) or protons orbiting in a field around $9{\times}10^{14}$ G. Given the narrow width of the line, it was concluded by Brightman et al. (2018) that the feature is a proton CRSF. Combined with constraints from spectral fitting, it was concluded by Middleton et al. (2019a) that the dipole field is likely to be weak with the feature the result of a stronger, higher order multipolar (e.g. quadrupole) component closer to the neutron star (e.g. Israel et al. 2017a,b; Brice et al. 2021), a situation now confirmed in the case of Swift J0243.6+6124 (Kong et al. 2022).

At the time of writing, there is only a single other claim of a CRSF in a ULX, in the transient system, NGC 300 ULX-1, which was identified as a neutron star from its 31.6 second period (Carpano et al. 2018), with the presence of a CRSF inferred from spectral modelling of the pulsed component (Walton et al. 2018a). Although the line energy ($\approx$ 13 keV) appears consistent with the estimate of the dipole field strength from spin-up, doubts have been raised by Koliopanos et al. (2019) as to the presence of the line, as applying a spectral model based on emission from the accretion curtain and additional hard power-law tail, do not argue for its inclusion.

2.2.4. Spectral evolution

ULXs are well known to change in both brightness and in spectral shape over timescales of months or less. Most ULXs tend to follow a roughly predictable track with a given source becoming brighter as the hard and soft spectral components both increase in brightness, with the harder component tending to increase more than the soft (see e.g. Middleton et al. 2015a) although this depends on how the spectrum is modelled (as this delineates the hard and soft components). As a result, for some of the brightest ULXs, there tends to be a clear correlation between the source becoming spectrally harder (with more flux emerging above $\sim$ 1 keV compared to that below) and brighter (Weng and Feng 2018) although this is not universal (see Gúrpide et al. 2021).

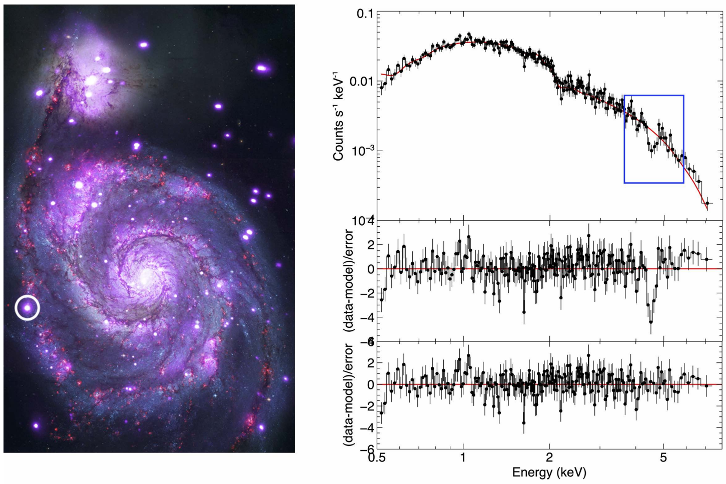


Figure 6 Figure adapted from Brightman et al. (2018) showing the location of ULX-8 in M51 (left), and the CRSF identified at ~4.5 keV in a *Chandra* observation (right).

The coupled changes in X-ray spectrum and observed luminosity can be explained by a given ULX undergoing a change in accretion rate (at large radii), inclination angle (due to precession) or a combination of the two (Middleton et al. 2015a). Under the condition that the neutron star dipole field is weak, so that $R_{\rm sph} < R_{\rm M}$, or the compact object is a black hole, increasing the accretion rate increases the spherization radius and the optical depth of the wind (as it is an integrated quantity – see Poutanen et al. 2007) and decreases the temperature at both the spherization radius and outer photospheric radius (see equations 5 & 6). Accordingly, we should expect to see an anticorrelation between the soft component's luminosity (which may be driven by radii interior to $R_{\rm sph}$) and the temperature at the spherization radius. Identifying and interpreting a correlation (or lack of one) is not necessarily straightforward, as increasing $R_{\rm sph}$, or moving to a more face-on orientation, leads to steadily increased beaming of the radiation interior to $R_{\rm sph}$ (Walton et al. 2017, 2020) which can make unambiguous spectral modelling challenging. Conversely, the hard X-ray emission is not expected to be particularly sensitive to accretion rate (see Eq. 5) but is the region deepest within the wind cone and therefore experiences the largest amount of collimation and beaming (this is an important point when considering the effects on the local environment - see Section 2.6). An increase in accretion rate is only likely to affect the luminosity of the hard component if the wind opening angle is sensitive to accretion rate (c.f. Jiang et al. 2014, 2019a). For a fixed inclination where sight-lines graze or intercept the wind, this picture is further complicated by obscuration and reprocessing (Middleton et al. 2015a, although the effect of absolute collimation at any angle can be inferred numerically – Dauser et al. 2017).

Given the observed precession of SS433 (known to be highly super-critical and established to be a ULX seen edge-on - see Section 2.8.3), it is reasonable to expect precession to occur in other ULXs as well (for a variety of reasons, and with some support from observation e.g. Pasham and Strohmayer 2013; Middleton et al. 2015c; Weng and Feng 2018). It is therefore important to consider the effect such a changing effective inclination of the super-critical flow might have (see Middleton et al. 2015a for details). Also, whilst changes in accretion rate and/or inclination lead to relatively predictable coupled evolution in spectrum and brightness, we also expect an impact on the timing signatures (see Middleton et al. 2015a), and detected strength and speed of winds (see Pinto et al. 2020a, 2021). Such additional considerations are vital as they are independent of the spectral model used to describe the emission which can often be degenerate (see Section 2.3.4).

The *majority* of the spectral evolution observed in ULXs can be fitted into the above picture. Notably the model can broadly explain observations of super soft ULXs, which have extremely low temperature soft components ($kT_{\rm bb} \approx 50 - 150eV$) and very little emission above 1 keV (e.g. Kong and Di Stefano 2003; Urquhart and Soria 2016a; Soria and Kong 2016) and which can be explained by an edge-on orientation and/or very high accretion rates (where the

wind is highly obscuring). Conversely, the brightest and spectrally hardest ULXs, tend to become slightly softer as they brighten, consistent with increased beaming of emission within $R_{\rm sph}$ (Walton et al. 2017, 2020) and where the ULX is viewed at lower inclinations. In spite of the success of this simple model, a number of important open questions remain.

One of the most obvious questions facing the unified inclination/accretion rate model of ULXs is how the presence of a strong dipole field affects the flow. For the most part, and as long as $R_M \ll R_{\rm sph}$, the expectation is that the spectrum will evolve along similar paths, as the position of the magnetospheric radius is expected to be independent of the mass-transfer rate for classical supercritical flows (see Chashkina et al. 2019 for a discussion of how the location of R_M can be affected by advection). Rather more drastic deviations from the model above occur for those NS ULXs (note not necessarily ULX pulsars, as there are many reasons why a pulsation may be absent – e.g. Mushtukov et al. 2020) which are close to spin equilibrium, as the onset of a propeller state can switch off the accretion curtain and column, leading to a quenching of the hardest spectral component (while the other components remain 'on'). There are already hints of propeller states occurring in one ULX pulsar (Tsygankov et al. 2016b) and such states might account for some of the more highly variable ULXs (e.g. Earnshaw et al. 2018, 2020; Song et al. 2020, although a propeller state is ruled out for recent, large-scale changes in X-ray flux observed in NGC 300 ULX: Vasilopoulos et al. 2019, and NGC 7793 P13: Fuerst et al. 2021).

One of the most intriguing observations is that the shape and normalisation of the emission above 10 keV tends to stay remarkably constant in a number of bright ULXs as their spectra evolve (see Walton et al. 2020). This can be explained so long as the innermost regions are maximally beamed and any changes in accretion rate do not change the opening angle of the wind cone appreciably (although see Jiang et al. 2019a for indications that the cone's opening angle may well respond to larger changes in accretion rate). An alternative possibility is that the emission at these energies originates from a stable accretion column, and applying a phenomenological model for the column can indeed provide a good description of the hard emission (Pintore et al. 2017; Walton et al. 2018c).

There are important questions remaining over how the individual spectral components fit into the above picture, typically explored through use of the temperature-luminosity plane. Such analyses have a long history in the study of ULXs, with indications of a strong negative L-T correlation ($L \propto T^{-3.5}$) reported across a *sample* of ULXs (e.g. Kajava and Poutanen 2008, 2009). Given the expectation that the ULX population is heterogeneous, it is important to also study sources individually; this is becoming increasingly feasible with intense observing campaigns.

Walton et al. (2020) examined nine observations of NGC 1313 X-1 (combining *XMM-Newton* with *NuSTAR* data) and fitted the spectra with a two-component thermal model of a disc black-body at low energies and an advection dominated disc at high energies (and an additional component to account for the hard excess). From this they found a positive (and relatively steep) correlation between the temperature and luminosity of the hotter, advection dominated disc (the soft component has a flatter, possibly negative correlation). This correlation is further subdivided into high and low luminosity branches and may provide an intriguing test of what processes drive the changing appearance of ULXs. A similar analysis has been performed by Robba et al. (2021) for the ULX pulsar NGC 1313 X-2, although a second luminosity-temperature branch is not as evident as for NGC 1313 X-1. As shown in several works (Luangtip et al. 2016; Gúrpide et al. 2021), the presence and nature of any correlation (at low or high temperatures) can be affected by the choice of spectral model, reinforcing the important role other methods can play in understanding the nature of the flow and the components in the X-ray spectrum (see Section 2.3.4).

2.2.5. Open questions and future directions

Important questions remain regarding the modelling of ULX spectra, including:

- the apparent stability and similarity at energies above the spectral break (Walton et al. 2020)
- the presence of fainter spectral components which may correspond to bremsstrahlung emission, as seen from SS433's jets (e.g. Walton et al. 2015)
- the trends of luminosity versus temperature for the individually modelled components (Kajava and Poutanen 2009; Walton et al. 2020).
- the impact of spin and advection on the hard spectral emission
- the prevalence (or lack-thereof) of CRSFs

Many of these issues may be resolved as self–consistent spectral models derived directly from 3D simulations of black hole and neutron star ULXs become available, (e.g. Ohsuga and Mineshige 2011; Jiang et al. 2014; Sądowski et al. 2015; Sądowski and Narayan 2016; Narayan et al. 2017; Takahashi et al. 2018; Kawashima and Ohsuga 2020).

2.3. Timing analysis

X-ray spectroscopy has allowed for a broad categorisation of ULXs, but as with other accreting systems, the timing properties (over short and long timescales) are just as important for testing models and for revealing new behaviours.

2.3.1. Short timescales

Because of its large effective area, *XMM-Newton* has been the favoured instrument for studying the short (intra–observation) timescale variability of ULXs. The simplest analysis uses the Fast Fourier Transform (FFT) of the lightcurve to obtain the periodogram (or, if averaged, the power spectral density – PSD). As this is typically normalised to be in $(\text{rms/mean})^2$/Hz units, the integral of the PSD gives the fractional root mean square (rms), which, when Poisson noise corrected and plotted against energy, yields the rms spectrum (see Uttley et al. 2014 for a comprehensive review).

The PSDs extracted from single observations of ULXs are generally described by either a red–noise power law (power scaling as $\nu^{-1} \rightarrow \nu^{-2}$) or a broken power–law (e.g. Strohmayer and Mushotzky 2003; Dewangan et al. 2006; Strohmayer et al. 2007; Heil et al. 2009; Atapin et al. 2019), sometimes designated as the broadband noise. Binning the rms reveals a tentative linear relationship with X-ray flux (Heil et al. 2009; Heil and Vaughan 2010; Hernández-García et al. 2015) as expected from multiplicative propagation of fluctuations in accretion rate (Lyubarskii 1997; Churazov et al. 2001; Arévalo and Uttley 2006). Heil et al. (2009) observed that the variability of some ULXs appeared very low, while conversely others appeared extremely high (up to 30% fractional rms - Middleton et al. 2015a). This can be explained via either the dilution of intrinsic variability from a neutron–star accretion column as photons scatter inside the accretion curtain before eventually escaping (Mushtukov et al. 2019) or by mass loss in the wind, which may remove variability from the inflow (Middleton et al. 2015a). The substantial amounts of short timescale (< 10 ks) variability in those spectrally softer sources – in which there is strong evidence for mass-loaded winds (e.g. NGC 5408 X-1 and NGC 6946 X-1) – could arise from stochastic obscuration by clumps in the wind (Middleton et al. 2011; Sutton et al. 2013), produced via radiative hydrodynamic (e.g. Takeuchi et al. 2013) or Kelvin Helmholtz instabilities.

In addition to the broadband noise, there have been several claims of quasi-periodic oscillations (QPOs – with power concentrated over a small frequency range) at 10s of mHz (NGC 5408 X-1: Strohmayer and Mushotzky 2009; Pasham and Strohmayer 2012, NGC 6946 X-1: Rao et al. 2010, NGC 1313 X-1: Pasham et al. 2015, M82 X-1: Strohmayer and Mushotzky 2003, IC 342 X-1: Agrawal and Nandi 2015) as well as at higher (~Hz) frequencies in M82 X-1 (Pasham et al. 2014). There have been various attempts to use QPOs to obtain the accretor mass, based upon a simple frequency scaling (e.g. Strohmayer and Mushotzky 2009; Pasham et al. 2015), which tend to give masses typical of IMBHs. However, while QPOs are detected from super-critically accreting systems such as TDEs (e.g. Pasham et al. 2019) and in GRS 1915+105 (the well known 67-68 Hz QPO: Belloni and Altamirano 2013), it is not clear that there are well-studied objects with well-understood signals available for direct comparison. At present, the origin of ULX QPOs remains unclear, although models invoking modulations of accretion rate (Okuda et al. 2009) or precession of the radiation-pressure supported disc – which can also explain the lag seen around the QPO frequency (De Marco et al. 2013 – see Section 2.3.4) have both been put forward (Middleton et al. 2019b). With the high throughput of forthcoming instruments (namely ESA's *Athena*), studies of ULX QPOs will become considerably more revealing.

2.3.2. Pulsations

Following the discovery of an X-ray pulsation from M82 X-2 (Bachetti et al. 2014), one of the most important tools now regularly applied to ULX data is the accelerated pulsation search (see e.g. Ransom 2001; Ransom et al. 2002; Andersen and Ransom 2018). This can account for the orbit of the neutron star about the system barycenter, which acts to smear the power in the pulsations over neighbouring Fourier frequency bins. Accelerated searches within both new and archival data have led to the discovery of several more pulsating ULXs (NGC 5907 ULX-1: Israel et al. 2017a; NGC 7793 P13: Fürst et al. 2016; Israel et al. 2017b; SMC X-3: Tsygankov et al. 2017; NGC300

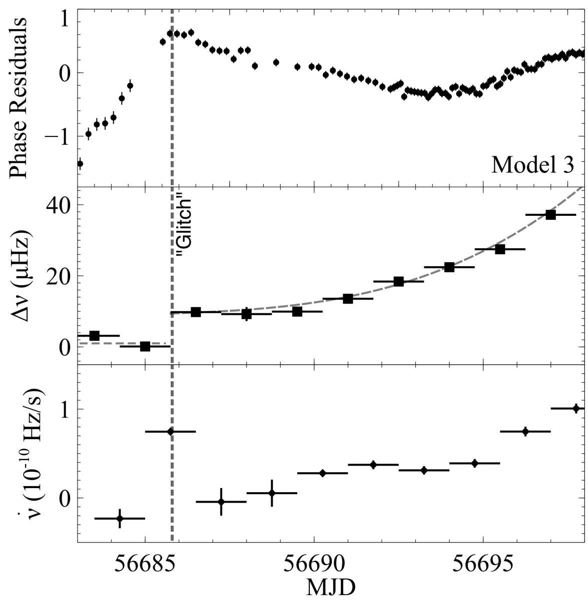


Figure 7 From Bachetti et al. (2020) showing the positive glitch (with a change in frequency $\Delta\nu \sim 8{\times}10^{-11}$Hz/s) in M82 X-2, revealed by extensive monitoring with *NuSTAR*.

ULX-1: Carpano et al. 2018 – first identified as a supernova by Monard 2010; NGC 1313 X-2: Sathyaprakash et al. 2019b; M51 ULX-7: Rodríguez Castillo et al. 2020; RX J0209.6-7427: Vasilopoulos et al. 2020b; Chandra et al. 2020) and Swift J0243.6+6124: Kennea et al. 2017).

The observed pulsing ULXs typically have periods ranging from ~ 1 - 30s (see Table 2). As is apparent from Tables 2, the secular $\dot{P}$ in these systems (i.e. $\Delta P/\Delta T$ where ΔT is typically months or longer – except in the case of NGC 300 ULX-1) reveals a collection of objects which tend to spin up at extremely high rates (notably NGC 300 ULX: Carpano et al. 2018) when compared to Galactic X-ray pulsars (although M82 X-2 is observed to spin *down* between 2014 and 2016: Bachetti et al. 2020). The secular spin up/down rates may differ greatly from the 'instantaneous' $\dot{P}$ obtained over the course of an observation due to the influence of orbital dynamics and changes in accretion rate between observations (Israel et al. 2017a; Bachetti et al. 2020). In addition to these long timescale trends, glitches (perhaps associated with the coupling of differentially rotating inner crust – and possibly core – to outer crust: Anderson and Itoh 1975) have now been observed in M82 X-2 (Bachetti et al. 2020 – Figure 7). These imply a change in spin frequency $\delta\nu/\nu \approx 10^{-5}$, similar in magnitude to glitches seen in magnetars and a small number of accreting neutron stars (Galloway et al. 2004; Dib et al. 2009; Dib and Kaspi 2014; Archibald et al. 2016; Serim et al. 2017). Interestingly, there are two (or possibly three) anti-glitches in NGC 300 ULX-1 (Figure 8, Ray et al. 2019), where the neutron star undergoes a dramatic spin-*down* $\delta\nu/\nu > -10^{-4}$. This may be the result of the enormous spin-up rate creating a sizeable lag between the rotation of the crust and superfluid interior (Ray et al. 2019) and is supported by the lack of corresponding radiative changes during the glitch. Only spin-up glitches have been observed in non-accreting pulsars, but accreting pulsars (Klochkov et al. 2009) and magnetars show both spin-up and spin-down glitches (e.g. Dib and Kaspi 2014). The anti-glitches seen in NGC 300 ULX-1 are the largest yet-observed in any kind of pulsar system.

The known ULX pulsars have pulse fractions (defined as [Pulse max - Pulse min]/[Pulse max + Pulse min]) which increase with photon energy (as seen in Galactic X-ray pulsars: Lutovinov and Tsygankov 2009), and take values from <5-100 % depending on the observation, source and energy band (see Table 2 for more details). Notably, Figure 9 shows that several of the ULX pulsars have an a highly sinusoidal pulse profile (although both NGC 300 ULX-1 and SMC X-3 are notable exceptions), unlike that expected from a pencil beam geometry. This suggests a large emitting region, either a fan-beam geometry (Basko and Sunyaev 1976) or accretion curtain, the latter reprocessing

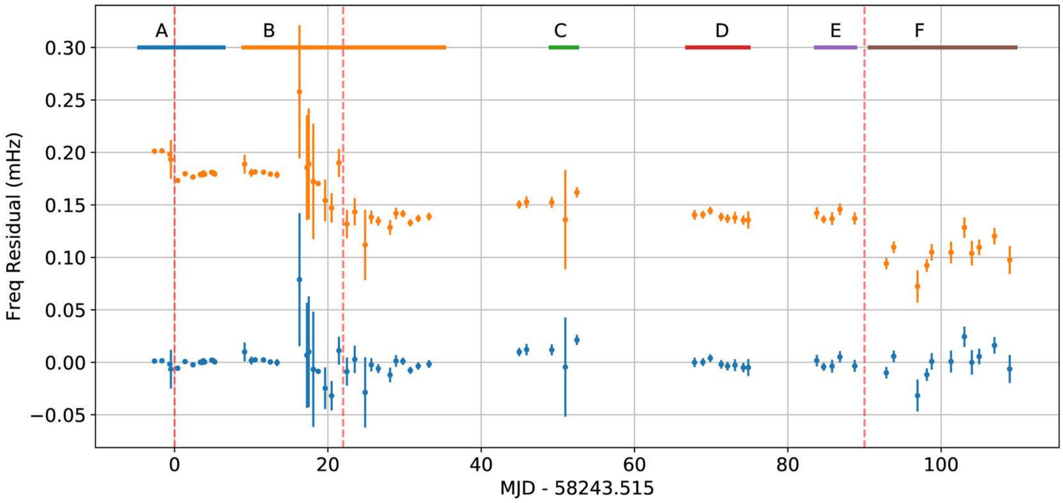


Figure 8 Data from Ray et al. (2019), highlighting the glitches in the ULX pulsar NGC 300 ULX-1. The upper (orange) points show offset residuals from the best-fitting model of the frequency evolution without glitches. These anti-glitches (with $\delta\nu/\nu > -10^{-4}$) are the largest yet observed in any pulsar system, and may be a result of the lag between the rotation of the crust and superfluid interior, driven by the enormous spin-up rate (Table 2).

(and therefore potentially diluting) the pulsed emission (Mushtukov et al. 2017, 2019).

We can obtain a rough indication of the statistical significance of a given pulsed signal (with a width Δnu, fractional rms, r – related to the pulse fraction – in an observation of length T, from a source of count rate I, with background count rate B) from $n_\sigma = 1/2\ [I^2/(I+B)]r^2\sqrt{T/\Delta\nu}$ (Lewin et al. 1997, noting that a true measure of the significance relies on considering both the noise and the number of independent free trials). Of the $\sim$ 1800 known ULXs (e.g. Walton et al. 2022), the vast majority do not have have sufficient data quality for deep pulse searches (down to small r). In those with sufficient data quality and not already identified as PULXs, pulsations appear to be absent down to the detection threshold (e.g. Doroshenko et al. 2015; Israel et al. 2017b).

There are several reasons why pulsations may be absent in a given ULX or in a given observation. Pulsations are observed to be transient in the known ULX pulsars (and indeed in Galactic accreting X-ray pulsars as well, e.g. Kretschmar et al. 2000) for reasons not yet well understood (see Bachetti et al. 2014; Israel et al. 2017a; Sathyaprakash et al. 2019b; Rodríguez Castillo et al. 2020; Bachetti et al. 2020), and conditions during a given observation may not be favourable for detecting the pulsed emission from the column (and/or curtain). As an example, we may be prevented from observing the pulsations by dilution by a stronger stable component in the spectrum (Walton et al. 2018b, e.g. if the disc/wind has precessed or accretion rate has changed Pasham and Strohmayer 2013; Middleton et al. 2015a,c, 2018, 2019b). This can also happen if the neutron star has free-body precessed (Fürst et al. 2017) so that the pulses are considerably weaker or beamed away from us. It may also be that we will *never* observe pulsations in some neutron star ULXs as we may never observe at suitable angles to view the accretion column. Alternatively the field may have been suppressed by accretion (e.g. Urpin and Geppert 1995), the neutron star and inner disc may be aligned (King and Lasota 2020), scattering in the wind cone may have suppressed pulsations on timescales shorter than the light-crossing time (Mushtukov et al. 2020), or some ULXs may simply harbour black holes (see Middleton and King 2017. Binary evolution would seem to make the latter inevitable to some degree – (Wiktorowicz et al., 2019).

2.3.3. Long timescales

It is well-accepted that LMXBs undergoing recurrent outbursts (see Hameury and Lasota 2020) may appear as ULXs for relatively short periods of time (e.g. Middleton et al. 2013; Carpano et al. 2018; van den Eijnden et al.

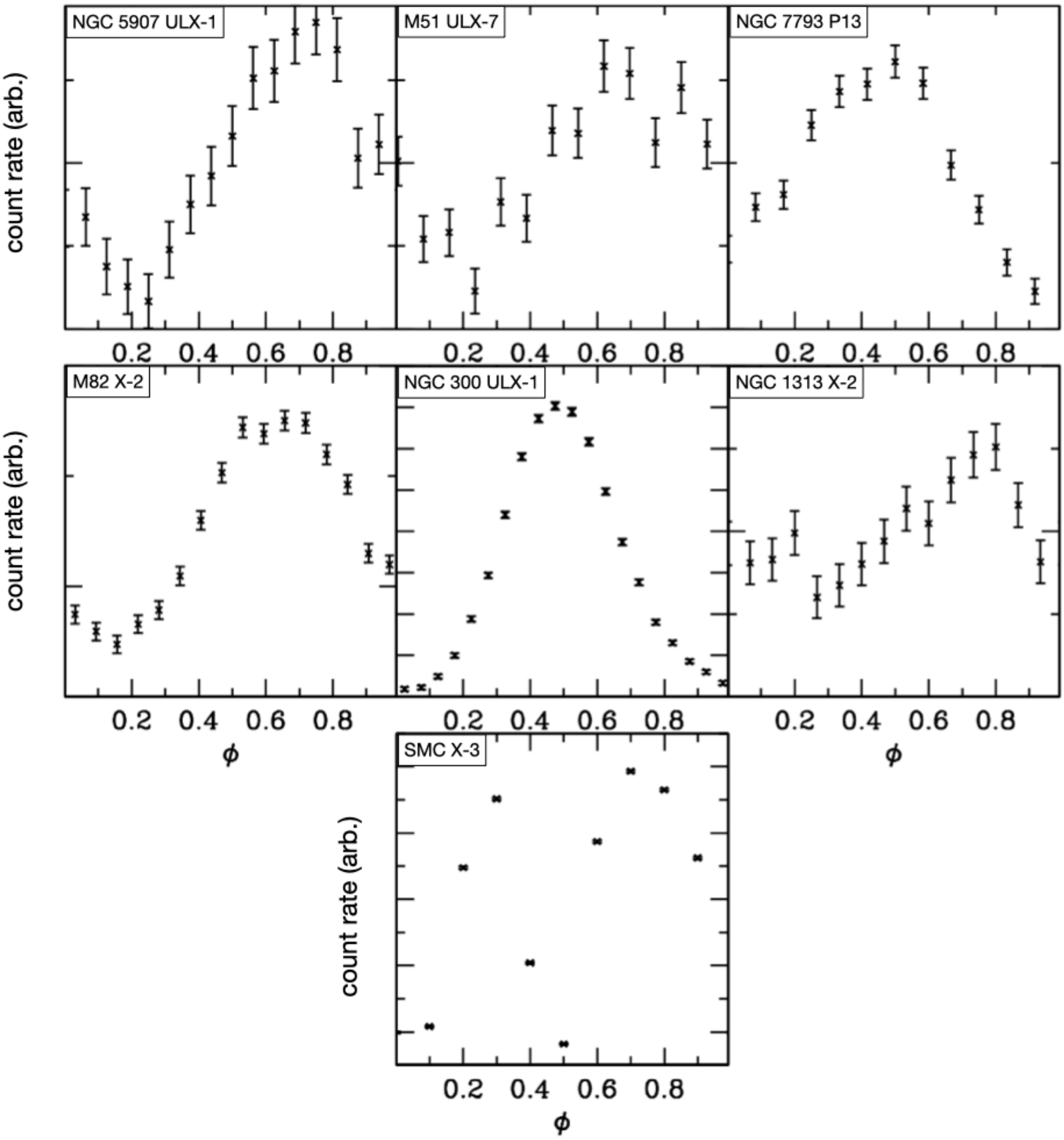


Figure 9 Pulse profiles for the PULXs shown in Table 2, extracted from data taken by *XMM-Newton* (NGC 5907 ULX-1, M51 ULX-7, NGC 7793 P13, NGC 300 ULX-1, NGC 1313 X-1) and *NuSTAR* (M82 X-2 and SMC X-3). Values for the count rates are not provided due to bandpass and detector differences, however, errors are provided for the purposes of comparing the level of constraints within each phase bin.

2018). Many bright ULXs are persistent (although we note the discovery of a new transient ULX in M51 reaching 10^{40} erg/s: Brightman et al. 2020a), but their luminosities can fluctuate by orders of magnitude, periodically/quasi-periodically (on timescales of 10s of days: Kaaret et al. 2006; Kong et al. 2016; Walton et al. 2016a) or seemingly at random. There are several possible explanations for such variations: changes in accretion rate, driven by effects in the outer disc (see Fig. 19, Sec. 3.16 and Hameury and Lasota 2020; Middleton et al. 2021a), an accreting neutron star entering a propeller phase, orbital variability as a neutron star passes through the decretion disc of a Be star, and precession of the disc/wind under external torques. In a number of the pulsating ULXs, the orbital period can be deduced from the Doppler modulation of the pulsations; this gives periods of a few days (see Table 2), with NGC 7793 P13 having a proposed period of 64 days (Motch et al. 2014 although see Fuerst et al. 2021 for details regarding the periodicities in this ULX). Other than NGC 7793 P13, the ~ day orbital periods are considerably shorter than the 'super-orbital' periods typically revealed by *Swift* monitoring but in some cases observed in the optical/UV (e.g. NGC 7793 P13: Fuerst et al. 2021). Both sets of periods are reported in Table 2.

Precession has been proposed as one means by which to explain the ~ 10s of days super-orbital variability of ULXs by a number of authors. Pasham and Strohmayer (2013) suggested that the changes in the spectrum of M82 X-1 associated with a 62 day period (Kaaret et al. 2006; Kaaret and Feng 2007) could result from changes in the projected area of the inner disc (perhaps driven by a radiative warp: Pringle 1996). Middleton et al. (2015c) suggested that changes in the strength of atomic features, now known to be associated with the wind (Pinto et al. 2016, 2020b), could result from precession of the disc and wind in NGC 1313 X-1, and Luangtip et al. (2016) appeal to a combination of precession and changes in accretion rate in order to explain the changing appearance of Ho IX X-1.

There are a number of possible mechanisms for driving a changing view of the inner regions of ULXs, including precession of a neutron star's magnetic dipole field (Lipunov and Shakura 1980):

$$t_{\rm mag,prec} \approx 1.5 \times 10^4 \frac{\mu_{30}^{-2} I_{45} R_{\rm M,8}^3 P^{-1}}{\cos\phi(3\cos\zeta - 1)} \text{ years} \tag{13}$$

where $\mu_{30} = B_{12}R_6^3$, I_{45} is the neutron star moment-of-inertia, ϕ is the angle between the normal to the disc plane and the spin axis, and ζ is the angle between the magnetic axis and the spin axis. To match observations of ULX superorbital periods of months or less, field strengths $> 10^{14}G$ are required (Mushtukov et al. 2017; Vasilopoulos et al. 2020a).

Should the accretion flow be misaligned with the neutron star or black hole spin axis (which seems quite plausible: King and Lasota 2020) then frame-dragging of the fluid induces a torque. Similar to the hot inner flow of X-ray binaries, a thick super-critical disc/wind is expected to have an effective viscosity parameter $\alpha < H/R$. The frame-dragging induced torque is then expected to be communicated as a bending wave from the inner edge of the flow out to the photospheric radius (Middleton et al. 2018, 2019b) which may then induce solid body precession (Fragile et al. 2007) on a estimated timescale of:

$$t_{\rm LT,prec} \sim \frac{GM\pi}{3c^3 a_*} r_{\rm sph}^3 \left[\frac{1 - \left(\frac{r_{\rm in}}{r_{\rm sph}}\right)^3}{\ln\left(\frac{r_{\rm sph}}{r_{\rm in}}\right)}\right] \text{ s} \tag{14}$$

for the disc and

$$t_{\rm LT,prec} \sim \frac{GM\pi}{3c^3 a_*} r_{\rm ph}^3 \left[\frac{1 - \left(\frac{r_{\rm in}}{r_{\rm ph}}\right)^3}{\ln\left(\frac{r_{\rm ph}}{r_{\rm in}}\right)}\right] \text{ s} \tag{15}$$

for the wind (here r is in units of gravitational radius – GM/c^2 – and a_* is the dimensionless spin parameter). Both periods are sensitive to the mass accretion rate. This can be related to properties of the X-ray spectrum and may tell us the nature of the accretor (neutron star or black hole, Middleton et al. 2019b) without the requirement for pulsations which are themselves transient or may be diluted beyond detection (Bachetti et al. 2014; Mushtukov et al. 2020).

If the neutron star is asymmetric about its rotation axis, free-body precession may also occur on a timescale of (Jones and Andersson 2001):

$$t_{\rm free,prec} \approx \frac{2.32\times10^{-5}}{\epsilon}\frac{P_{\rm NS}}{1s}\frac{0.5}{\cos\chi}\ {\rm days} \tag{16}$$

where χ is the angle of the misaligned distortion of the neutron star relative to its rotation axis, and ϵ is the measure of distortion, related to the surface magnetic field strength through (Lander and Jones 2009):

$$\epsilon = 2\times10^{-11}\left(\frac{B_{\rm surf}}{10^{12}G}\right)^2 \tag{17}$$

which, notably, Vasilopoulos et al. (2020a) used to estimate the dipole field strength in M51 ULX-7.

Besides the above torques, other effects may warp and precess the disc, e.g tidal torques from the secondary star (although these are unlikely to be strong in cases with known ~ day orbital periods, e.g. Bachetti et al. 2014), magnetic warping (Lai 2003; Pfeiffer and Lai 2004), and radiative warping (Pringle 1996). In the latter case, where super-critical flows – specifically a large-scale height disc and optically thick wind – are present, it is not clear how efficiently the outer disc is irradiated (see also Middleton et al. 2021a). But if the dipole field is strong and/or the accretion rate low, irradiation may well be possible, and similar warps and precession to that seen in Her X-1 are then quite plausible (see Petterson 1977; Kotze and Charles 2012). Regardless of the mechanism driving the precession, it is possible to build a simplified model of the motion of the cone and then numerically extract the X-ray lightcurve. Dauser et al. (2017) developed a model which can produce a variety of lightcurve profiles (available within XSPEC: Arnaud et al. 1999 as ULXLC), under the assumption that the X-ray source lies at the apex of a cone of outflowing, totally opaque, achromatically scattering plasma. Applying this model to the lightcurve of NGC 5907 ULX-1 implies a small total opening angle (~ 10 – 15 deg) and substantial beaming (amplification by a factor 60-90) although it is as yet unclear whether this is in conflict with scattering reducing the observed pulse fraction (Mushtukov et al. 2020).

It is interesting to consider how the different physical origins for superorbital periods can be distinguished. A natural method would be to consider how the timescales respond to the accretion rate and spin-up/down of the neutron star. Equations 14 & 15 are highly sensitive to the accretion rate (far more so than the spin) and so, where the accretion rate is variable (on long timescales), we would expect variability in the superorbital period (with correlated changes in the X-ray spectrum). Conversely, magnetic and free-body precession is more sensitive to the spin than accretion rate, and the superorbital period should therefore track changes in the neutron star's spin over time.

It is also worth noting that plotting the superorbital period versus the orbital period for Galactic systems and those ULXs with known periods (see Table 2, implies a potential correlation (see Townsend and Charles 2020), although care must be taken in interpreting any correlation between logarithmically scaled values which include systems known to be of very different types. It is plausible that the superorbital periods are in some cases responding to tidal interactions, while the mass supply to the compact object may correlate with the binary period, leading to a positive correlation through e.g. equation 15. This currently remains an open question but we can expect progress as the detected number of constrained superorbital periods increases.

In addition to the smooth, periodic/quasi-periodic variations seen in the X-ray and optical bands, there are a variety of changes in the lightcurves of ULXs which can help reveal the nature of the system. Dips are found in NGC 55 ULX-1 (Stobbart et al. 2004); NGC 5408 X-1 (Grisé et al. 2013), NGC 247 ULX-1 (Alston et al. 2021), M51 ULX-7 (a known ULX pulsar, Vasilopoulos et al. 2021), and J125048.6+410743 (Lin et al. 2013). Significantly, these ULXs tend to have relatively soft spectra (M51 ULX-7 is somewhat harder), possibly implying a correlation with sight-lines intercepting regions in the wind subject to instabilities and clumping (e.g. Middleton et al. 2011, 2015a; Takeuchi et al. 2013).

Whilst dips are seen in the lightcurves of a small number of ULXs, eclipses seem to be mostly absent from the currently known ULX population (Middleton and King 2016). This would make sense if edge-on ULXs emit around the Eddington limit (Poutanen et al. 2007) implying sub-ULX luminosities in many cases (Zhou et al. 2019). However, there have been reports of eclipses in two ULXs in M51 (Urquhart and Soria 2016b; Wang et al. 2018). These give constraints on the angle between the companion star's orbit and the X-ray bright inner regions (noting that these do not have to be aligned in a single plane). If there is an estimate of the mass of the donor star this then constrains the compact object mass (Wang et al. 2018).

Neutron stars probably account for the majority of observed ULXs (King and Lasota 2016; Middleton and King 2017; King et al. 2017; Walton et al. 2018c; Wiktorowicz et al. 2019). Such systems are likely to approach spin

equilibrium between gravity and centrifugal forces during their lifetimes, where the co-rotation radius approaches the magnetospheric radius. Whilst the effective torque vanishes when the two are close (Dai and Li, 2006), should some process push the magnetospheric radius outside the corotation radius, a propeller state ensues where the emission from the accretion column and curtain – but importantly not from radii down to the magnetospheric radius – is switched off. In systems where the magnetospheric radius is large, the result would be a severe drop in flux (although centrifugally driven winds from around the magnetospheric radius would remain). Such propeller states, widely observed in Galactic systems (e.g. Cui 1997; Campana et al. 2008; Tsygankov et al. 2016a) have been invoked to explain the large changes in luminosity seen in M82 X-2 (Tsygankov et al. 2016b). However, in NGC 7793 P13 (Fuerst et al. 2021) and NGC 300 ULX-1 (Vasilopoulos et al. 2019), the spin has continued increasing at the same rate when the source is considerably fainter in the X-rays, implying that some other mechanism – possibly obscuration – drives the change, rather than a propeller state. (In M51 ULX-7 it is at yet unclear whether a similar X-ray off state implies a propeller state or is associated with precession: Vasilopoulos et al. 2021). The predicted large-scale changes in X-ray flux in the propeller state have motivated searches for pulsar candidates among known ULXs. Earnshaw et al. (2018) searched within those ULXs in the 3XMM DR4 catalogue (Rosen et al. 2016) finding five objects which underwent a factor of 10 or more change in flux (with one propeller candidate: M51 ULX-4). Song et al. (2020) compiled *XMM-Newton*, *Swift* and *Chandra* flux lightcurves of 296 ULXs from the Earnshaw et al. (2019) catalogue, and found that 25 out of 296 ULXs changed flux by more than a factor 10 (based on the available sampling), 17 of which show a bi-modal flux distribution, potentially consistent with sources at spin equilibrium.

2.3.4. Spectral-Timing studies

As well as standalone studies focussing on either the spectral evolution or timing characteristics of ULXs, there are an increasing number which bring the two together. Such a spectral-timing analysis can be performed in the time or Fourier domain in a given energy band (e.g. the fractional rms or rms spectrum: Revnivtsev et al. 1999; Gilfanov et al. 2000, and the covariance spectrum: Wilkinson and Uttley 2009), or via lags between bands (via the CCF or Fourier lag spectrum) as a function of energy or frequency (see Uttley et al. 2014 for a comprehensive review). Spectral-timing studies require high signal-to-noise or large amounts of variability (such that the Poisson noise is not dominant), making such analyses challenging for ULXs. However, there have been a number of successful attempts which have provided otherwise inaccessible insights.

Covariance spectra (Wilkinson and Uttley 2009) have an advantage over rms spectra; as the Poisson noise between bands is uncorrelated, when the variability is weighted by the linear coherence between bands (see Vaughan and Nowak 1997; Uttley et al. 2014), the constraints on the variability in each energy bin are improved. Middleton et al. (2015a) presented the covariance spectra for a sample of variable ULXs with relatively high data quality and showed that the variability on relatively short ($\lesssim$ 1 ks) timescales matched well to the shape of the hard component (seen also the studies of the covariance spectra of NGC 55 ULX-1: Pinto et al. 2017 and NGC 1313 X-1: Kara et al. 2020). This can be readily explained if the variability emerges from only this component on the timescales being studied. However, it is less clear why spectrally-harder ULXs (where this component is dominant) appear to be less variable on similar timescales (e.g. Heil et al. 2009). One possible explanation is that the variability is extrinsic and being driven by obscuration by optically thick clumps of wind (Middleton et al. 2011), probably created due to fluid instabilities (Takeuchi et al. 2013). Clumps may also then be responsible for dips seen in the softer ULXs (e.g. NGC 55 ULX-1: Stobbart et al. 2004 and NGC 247: Alston et al. 2021) which in the standard paradigm are viewed at higher inclinations (Poutanen et al. 2007; Middleton et al. 2015a).

The covariance spectrum can also be used to isolate the *non-variable* component in ULXs. This can be modelled and better compared to theories for emission at soft energies (typically either a thin disc beyond the magnetospheric radius or emission from close to the spherisation radius). This can be complex, depending on the role of variable absorption, but it is at least possible to compare luminosities, and rule out the presence of a thin disc. This was demonstrated in Middleton et al. (2019a) (Figure 10), and allowed for independent constraints to be placed on the dipole field strength in M51 ULX-7 (see also discussions in Brightman et al. 2018, and Christodoulou et al. 2019).

Time (or phase) lags between bands may be extracted in the time domain via the CCF (as shown to great effect when studying a variety of features in XRBs, e.g. lags corresponding to propagation in jets: Gandhi et al. 2010) or via the Fourier cross-spectrum (see Uttley et al. 2014 for a detailed step-by-step guide). The lags are related to the nature and geometry of the accretion flow via the transfer function and are imprinted by propagation, and the light-travel time through reverberation or transmission (the latter affected by the amount and state of intervening gas). Lags in ULXs

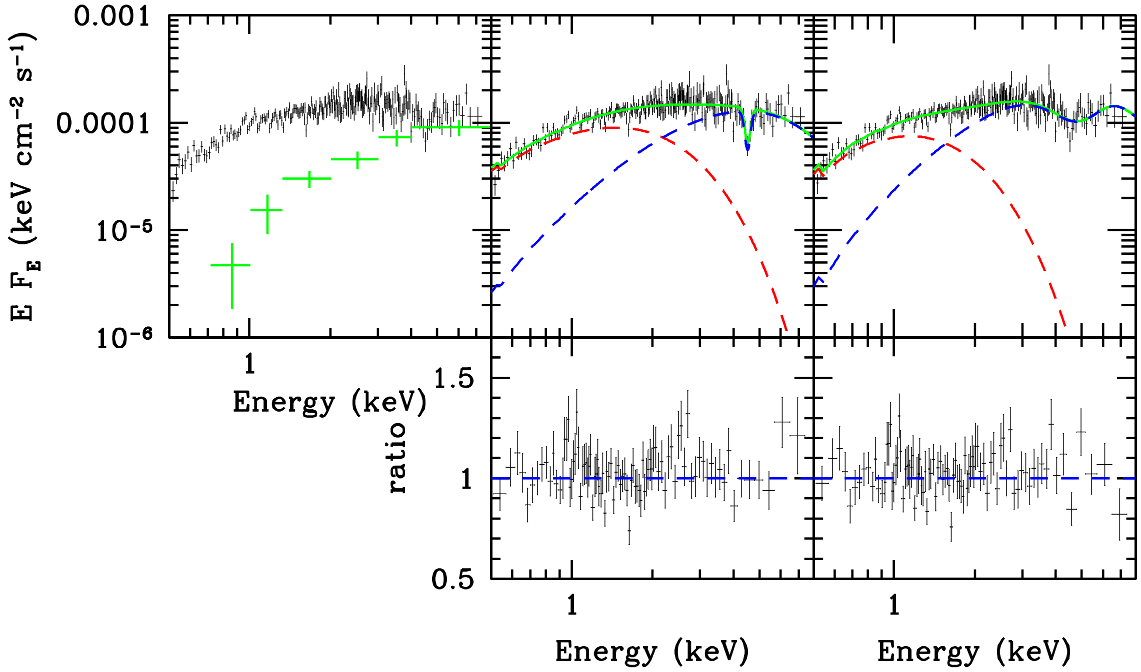


Figure 10 From Middleton et al. (2019a) showing (left-hand panel) the covariance spectrum of M51 ULX-8 (in green) with the time–averaged *Chandra* data (in black). The covariance picks out the linearly correlated variability (see Wilkinson and Uttley 2009) and allows the spectrum to be decomposed. In this case, the additional soft component (shown in red in the middle and right-hand panels) is above the Eddington limit for a neutron star and so inconsistent with a thin disc. This allowed Middleton et al. (2019a) to place indirect constraints on the dipole magnetic field strength (a higher-order multipole field is not excluded).

were first identified in a 2006 observation of NGC 5408 X-1 (Heil and Vaughan 2010) between a soft (0.3 - 1 keV) and hard (1 - 10 keV) band. This 'soft lag' is ~ a few seconds in NGC 5408 X-1 (De Marco et al. 2013) at frequencies of ~ 10 mHz, is ≈ 150s at 0.1 mHz in NGC 1313 X-1 (Kara et al. 2020), and is a few hundred seconds at around the same frequency in NGC 55 ULX-1 (Pinto et al. 2017). Soft lags have been interpreted as reprocessing in distant material (presumably the wind) and intriguingly appear around the QPO frequencies seen in NGC 5408 X-1 (De Marco et al. 2013). Should the lag be imprinted as a consequence of resonant line scattering or Compton down-scattering, the magnitude can provide an estimate of the optical depth and thickness of the wind. An alternative explanation is that hard photons created in the accretion column are Comptonised by a surrounding envelope (Mushtukov et al. 2017) and a lag is imprinted due to the light travel time across the curtain and the time taken to Compton scatter (Mushtukov et al. 2019). This picture would imply very large or dense curtains in the case of ULXs such as NGC 55 ULX-1.

2.4. Multi-wavelength studies

ULXs are defined (albeit empirically) by their X-ray luminosity, although much of the gravitational energy dissipated in the accretion flow may emerge in other wavebands through reprocessing or as kinetic luminosity in the wind and/or jet. It is therefore crucial to obtain as broad an SED as possible, and below we discuss insights obtained in several key bands (note that we discuss observations of bubble nebulae surrounding ULXs separately in Section 2.6.1).

2.4.1. Radio

Radio monitoring campaigns (Körding et al. 2005) and cross-matching of X-ray catalogues with radio surveys (Pérez-Ramírez et al. 2011) have returned limited numbers of ULX radio counterparts, perhaps suggesting that any jets are inherently weak or transient in nature. Targeted observations have tended to focus on the brightest ULXs (HLXs at $\sim 10^{41}$ erg/s) as these remain the most promising candidates for hosting IMBHs other than AGN in dwarf galaxies (Farrell et al. 2009). Their suggested sub-Eddington accretion rates would naturally lead to the expectation of flat spectrum radio emission associated with a compact jet (if in an analogous hard X-ray state as seen in X-ray binaries and AGN). Placing such HLXs on the radio–X-ray fundamental plane (Merloni et al. 2003; Falcke et al. 2004; Gültekin et al. 2009) opens up the possibility of constraining the compact object mass, and this approach has been adopted for a number of ULXs (NGC 4088-X1: Mezcua and Lobanov 2011, NGC2276-3c: Mezcua et al. 2015; N5457-X9: Mezcua et al. 2013a, IC 342 X-1: Cseh et al. 2012).

Confirming the presence of a jet in ULXs can be more difficult given the presence of a radio bright nebula in some cases. These can be up to 100s of pc across: Mezcua et al. 2013b), potentially analogous to the W50 nebula surrounding SS433 (e.g. Pakull et al. 2006; Pakull and Grisé 2008; Russell et al. 2011; Cseh et al. 2012), and energised by termination shocks between the surrounding gas and outflows. In only a single bright ULX – Ho II X-1 – has the nebula emission been resolved by using VLBI into discrete core and lobe emission (Cseh et al. 2014, 2015, although there are also twin lobes either side of a bright radio core in the IMBH candidate NGC 2276-3c, see Mezcua et al. 2015). The fading of Ho II X-1's lobes over a period of around 2 years indicates that the jets are sporadic and may have more in common with the discrete ejections in near-Eddington LMXBs, placing a limit on the mass of the compact object in Ho II X-1 of > 25 $M_\odot$ (Cseh et al. 2015).

Jet-inflated nebulae may provide one of the few ways to locate edge-on ULXs. A key example is the radio-optical nebula in M83 (30 times more luminous than W50 at 5 GHz) and collimated jets in NGC 7793 (S26: Pakull et al. 2010; Soria et al. 2010). In both cases, the estimated jet power lies above 10^{40} erg/s, but the observed X-ray luminosity to-date is 3-4 orders of magnitude lower, and the sources would therefore not qualify as ULXs. These systems are in many ways similar to SS433 (albeit with even higher jet kinetic luminosities) and provide ample evidence for similar edge-on ULXs being located in nearby galaxies.

As well as jets associated with highly super-Eddington rates of mass transfer, transient jet ejections have been observed in some Galactic XRBs moving to less extreme, near-Eddington accretion rates (Fender et al. 2009). These have been successfully detected in nearby galaxies and can be associated with the appearance of a low luminosity ULX (e.g. M31: Middleton et al. 2013). It is plausible that the transient jets detected from HLX-1 (Webb et al. 2012) suggest the source was moving to near-Eddington rates, which, at a luminosity of $> 10^{42}$ erg/s would imply a BH mass of $\sim$10,000 $M_\odot$, consistent with the mass estimate from modelling the X-ray spectrum with relativistic disc models (Davis et al. 2011). In future, with the advent of sensitive all-sky radio monitoring (SKA), the detection of such radio events should become commonplace.

Finally, it is intriguing to note that a jet event has also been detected from the transient X-ray pulsar, Swift J0243.6+6124 – which contains a neutron star with $B > 10^{12}$ G (Doroshenko et al. 2018) – when accreting above its Eddington limit (van den Eijnden et al. 2018). At peak radio brightness, the flux density from the jet was $< 100\mu$Jy at 6 GHz (at an assumed distance ≈ 7 kpc – van den Eijnden et al. 2018). Similar jets are therefore unlikely to be discovered in nearby galaxies (although there is the theoretical potential to drive more powerful jets through tapping the neutron star's angular momentum: Parfrey et al. 2016).

2.5. Infra-red to ultraviolet

Generally speaking, observations of accreting systems at energies intermediate to those of X-rays and radio allow us to study the impact of reprocessing, the highest energy populations of electrons in jets and the nature of the companion star. In ULXs, such studies are of vital importance for constraining the true energy budget and age of the system, for understanding the impact on the surroundings and how such high rates of mass transfer actually occur.

2.5.1. Infrared

Campaigns studying ULXs in the IR have focused mostly on the nature of the donor star, using a combination of imaging and spectroscopy from ground-based instruments. Initial imaging studies by Heida et al. (2014) identified a number of possible red supergiant (RSG) companion stars (11/62 ULXs in 37 galaxies within 10 Mpc) from a

combination of data from WHT/LIRIS, MMT/SWIRC and VLT/ISAAC. Heida et al. (2016) later performed NIR spectroscopy using Keck/MOSFIRE (Multi-Object Spectrometer for Infra-Red Exploration), identifying candidate counterparts for two ULXs (one in NGC 925 and one in NGC 4136) with RSGs. Building on the work of Heida et al. (2016), a large study by López et al. 2017, 2020 made a systematic search for NIR counterparts to 113 ULXs, through use of a combination of instruments (imaging via LIRIS/WHT, SOFI/NTT and WIRC on the Palomar Hale 5-m telescope, and spectroscopy with Keck/MOSFIRE). This study yielded candidate counterparts for 38 ULXs, 5 of which are identified as RSGs. The numbers obtained from ground-based studies match well to mid-IR studies performed using *Spitzer*, where Lau et al. (2019) located 12 candidate RSGs in a sample of 96 ULXs within 10 Mpc. These results point towards a highly probable association of RSGs with some ULXs, and an additional – somewhat less considered – form of mass transfer, i.e. that of wind-fed Roche-lobe overflow (e.g. Copperwheat et al. 2007; El Mellah et al. 2019) which has now been incorporated into models for binary population synthesis (Wiktorowicz et al. 2021).

There have been a number of focused campaigns to explore the brightest ULXs, and specifically the PULXs (determining the companion star in the latter being of obvious value when considering the evolution of these systems). Unfortunately for most PULXs the IR fields are extremely crowded, precluding the identification of a unique counterpart (Heida et al. 2019a). However the companion of the SN imposter, NGC 300 ULX-1 has been identified as an RSG (Heida et al. 2019b).

As well as emission from the companion star, it is quite possible that synchrotron emission from jets and from circumbinary dust could both contribute to observed flux in the IR band. Lau et al. (2019) identify a mid-IR excess and a probable circumbinary disc in several ULXs (including Ho II X-1), and associate variable mid-IR emission from the X-ray spectrally hard ULX, Ho IX X-1, with a jet (as previously suggested by Dudik et al. 2016 and Sathyaprakash et al. 2022 in the case of the pulsating ULX, NGC 1313 X-2).

Indirect constraints on the SED which photoionizes gas surrounding the ULX (see Section 2.6) can be extracted through modelling IR lines. Berghea et al. (2010a) identified Ho II X-1's nebula (thought to be inflated via jets) in *Spitzer* observations and, in Berghea et al. (2010b) later performed photoionization modelling to suggest that the lines are consistent with irradiation by the observed soft X-ray and UV emission, requiring little to no beaming (of these components). This is completely consistent with the picture where the soft emission is less beamed than the hard X-rays. The MF16 nebula surrounding NGC 6946 X-1 has also been detected by *Spitzer*, with photo-ionisation modelling by Berghea and Dudik (2012) indicating the possible presence of an O-type supergiant donor star.

Roche lobe, this mass transfer mechanism known as ”wind Roche lobe overflow” can remain stable even for large donor-star-to-accretor mass ratios

2.5.2. Optical

Identifying a unique optical counterpart to a ULX potentially gives a powerful probe of the system age via binary evolution arguments. If atomic lines can be isolated and associated with the companion, then subsequent studies may allow the mass of the compact object itself to be constrained by standard radial velocity techniques. There are a number of issues which make such investigations challenging. Given the distance to many ULXs, there may be several optical counterparts associated with the X-ray astrometric position (e.g. Gladstone et al. 2013). The distance can make lower mass companion stars undetectable, perhaps misleadingly favouring an association with any high mass star within the neighbourhood of the ULX. Further, the photometric signal of the star may be contaminated by direct emission from the wind photosphere depending on the accretion rate (Poutanen et al. 2007), and emission from the uncovered thin disc which may be increased by irradiation (should the geometry, advection and wind optical depth permit this – Sutton et al. 2014; Yao and Feng 2019). Finally the spectroscopic signatures (e.g. He II emission lines) may also be contaminated or dominated by the wind (Fabrika et al. 2015).

Despite these challenges, there have been a number of attempts to find and study the optical counterparts of ULXs (besides the results discussed in the IR band above). Many studies (too many to recount in this review) over the last 20 years have targeted individual ULXs (see e.g. Roberts et al. 2001), whilst others have aimed at describing the larger population. As important examples of the latter, the sensitivity and angular resolution of HST allowed Roberts et al. (2008) to locate counterparts to four out of six ULXs, whilst Tao et al. (2011) studied the optical counterparts of 13 ULXs, finding the optical flux and colour to vary on the timescale of days to years, ruling out changes in extinction as the origin. Gladstone et al. (2013) utilised HST photometry to study 33 ULXs with *Chandra* positions, locating 13 ± 5 counterparts and finding O–star companions to be rare.

Where unique counterparts have been identified, there have been attempts to constrain the mass and species of compact object via dynamical arguments (most using the broadened He II λ4686 emission line):

- Using *Gemini* observations, Roberts et al. (2011) attempted to constrain the mass of the compact object powering NGC 1313 X-2 (which is now known to be a neutron star: Sathyaprakash et al. 2019b) but were unable to do so due to the absence of sinusoidal motion in the line velocities
- Cseh et al. (2013) were unable to locate an orbital period, but placed a limit on the mass ($< 510 M_{\odot}$) of the compact object in NGC 5408 X-1 from a limit on the semi-amplitude in the absence of periodic modulations, and under the assumption that the He II line is produced in the irradiated outer accretion disc.
- Liu et al. (2013) used the He II λ4686 line to place a lower limit on the mass of the compact object in M101 ULX-1 of 5$M_{\odot}$.
- Motch et al. (2014) placed an upper limit on the mass of NGC 7793 P13 ($<$ 15 $M_{\odot}$) by modelling the $\sim$ 64 d period in the V and U band lightcurves as irradiation of the well-identified B9Ia companion star; this result is of course consistent with the discovery that a neutron star powers this ULX (Fürst et al. 2016; Israel et al. 2017b).

Use of the He II λ4686 emission line to determine the compact object mass via dynamical means is problematic, as Fabrika et al. (2015) show that this line in ULXs probably originates in the outer regions of an outflowing wind, as in SS433. There remains a question about the width of the He II lines in NGC 7793 P13 – these cannot originate from the companion star (Fabrika et al. 2015) but also appear to be modulated on the same 64 d timescale as the optical flux (Motch et al. 2014); this may point towards the wind precessing as it does in SS433 (see Section 2.3.3 for a discussion of super-orbital periods).

2.5.3. UV

Models which consider the temperature dependence of the super-critical inflow (Poutanen et al. 2007) already imply that, for high mass accretion rates, the outer photosphere of the wind should emit in the UV around the Eddington limit for the compact object. Compton down-scattering of photons from the innermost regions could also produce extreme luminosities in the optical/UV band. This may explain the inference that SS433 emits at over 10^{40} erg/s in the UV (Dolan et al. 1997; Waisberg et al. 2019).

UV observations of ULXs are limited by the difficulties inherent in observing in much of this band, but a particularly notable result is that of Kaaret et al. (2010) who observed NGC 6946 X-1 with HST, finding a spectrally soft ULX showing strong variability and QPOs, surrounded by a photoionized and shock-heated optical nebula (MF16 – see below). Spectral fitting carried out by these authors implied a UV luminosity in excess of 10^{39} erg/s, consistent with the luminosity needed to produce the observed HeII λ4686 emission-line luminosity (Abolmasov et al. 2008).

More recently, monitoring of ULXs with *Swift* has started to provide hints of how the X-rays (via the XRT) and UV (via UVOT) may be correlated (or anti-correlated). As shown in Fuerst et al. (2021), the $\sim$ 64 d optical period observed in NGC 7793 P13 (Motch et al. 2014), is also seen in the X-rays (with a precise value of 65.21±0.15, see also Hu et al. 2017), in the UV (with a period of $63.75^{+0.17}_{-0.12}$ d), and in the fits to the changing pulse period, yielding an orbital period of 64.86±0.19 d. It is clear from Figure 11 that the UV brightness is not in phase with the X-rays (and indeed, the UV modulation is considerably stronger when the X-rays are dim).

2.6. The environment of ULXs

ULXs are a product of their host environment, and interact with it through kinetic and radiative feedback. In this section we discuss the small and larger scale environments of ULXs and the insights these provide.

2.6.1. ULX nebulae

As first reported by Pakull and Mirioni (2002), a substantial number of ULXs are observed to be surrounded by a bubble of warm gas (although the phenomenology is in reality somewhat varied), visible in the optical via emission lines (and in some cases detected in the radio as well). As indicated in Table 1, these 'ULX nebulae' are typically $\sim$10 - 100s pc across (the largest presently known being $\sim$500 pc in diameter) and tend to be considerably larger than typical SNRs (e.g. Asvarov 2014) although there is sometimes disagreement on the actual size (e.g. Moon et al. 2011

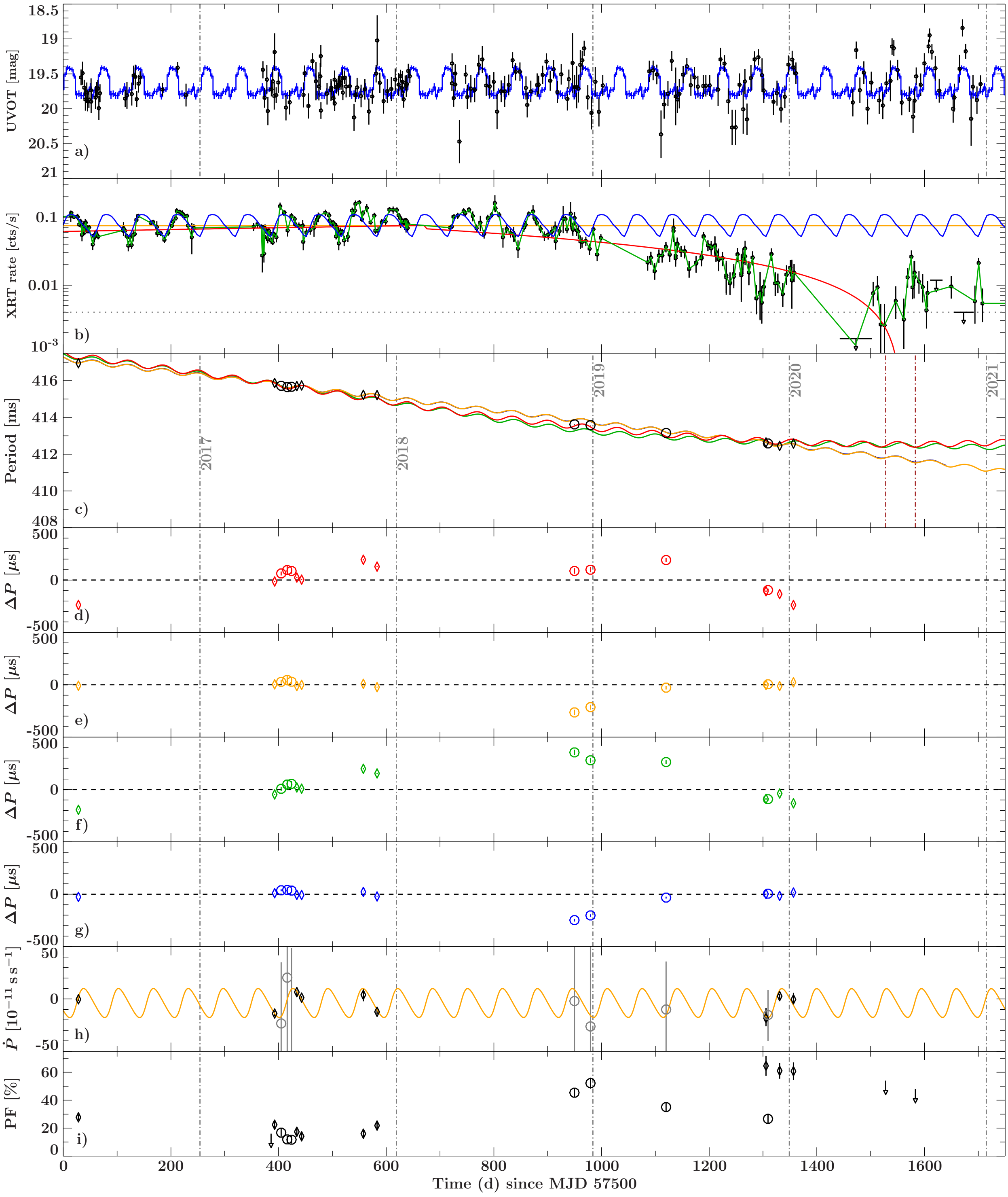


Figure 11 from Fuerst et al. (2021) showing the long term *Swift* X-ray (XRT) and UV (UVOT, U band) lightcurve of the ULX pulsar, NGC 7793 P13, with modulations around a ~65 d period. The drop in X-ray flux in 2019 does not appear to result in a substantial decrease in the spin-up rate as indicated by the lower panels (see Fuerst et al. 2021 for details). It is also intriguing that the UV and X-ray modulations appear to be – to some extent – anti-correlated.

versus Kaaret et al. 2004). Bearing this point in mind, the dimensions provided in Table 1 do not necessarily account for the entire region influenced by the ULX (e.g. there is a reported 800 pc zone of weakly ionised gas surrounding NGC 1313 X-1: Pakull and Mirioni 2002).

Analogous to the W50 nebula of SS433, we expect gas from the original SNR to be inflated by jets and winds from the inner accretion flow (e.g. Feng and Kaaret 2008; Pakull and Grisé 2008) and be photoionized by the UV–X-ray radiation field (which we broadly expect to be anisotropic). Indeed, ULX nebulae show a mixture of photoionized (notably He II 4686λ) and shock ionized lines ([OI] 6300λ and [OIII] 5007λ) – some nebulae appearing to be dominated by one process over the other (although both probably occur in any given source e.g. Abolmasov et al. 2007a). ULX nebulae have conclusively been shown to not be inflated by O star associations (i.e. a superbubble) and are unlikely to be due to a hypernova explosion (Pakull and Grisé 2008).

Applying a model where the ULX nebula is inflated via the mechanical action of outflows (i.e. a shock dominated rather than photo-ionised dominated nebula) gives interesting estimates for the age of the system. This in turn provides clues as to how the binary may have evolved, and for how long super-critical accretion can be maintained. From Weaver et al. (1977) the radius of the bubble is (compare Eq. (117))

$$R = \left(\frac{125}{154\pi}\right)^{1/5} \left(\frac{L_{\rm tot}}{\rho_0}\right)^{1/5} t^{3/5} \tag{18}$$

where R is the radius of the bubble at time t, $L_{\rm tot}$ is the mechanical luminosity of the wind and/or jet, and the ISM density (assumed to be uniform) is $\rho_0 = \mu m_{\rm p} n$, where μ is the mean atomic weight of the gas, $m_{\rm p}$ is the proton mass and n is the hydrogen number density. The characteristic age of the bubble is then given by $\tau = 3R/5v_{\rm exp}$.

These equations allowed Cseh et al. (2012) to determine the energy content and age of several ULX nebulae, the results of which are shown in Table 1. Assuming $L_{\rm k} = 1/2\dot{m}_{\rm wind}v_{\rm wind}^2$, and that the wind provides the entire energy reservoir of the bubble (i.e. provides $L_{\rm tot}$), then equation 18 may alternatively be written in terms of the wind properties (e.g. Pinto et al. 2020a):

$$R = 0.76\left(\frac{\dot{m}_{\rm wind}v_{\rm wind}^2}{2\rho_0}\right)^{1/5} t^{3/5} \tag{19}$$

where $\dot{m}_{\rm wind}$ is the mass loss rate in the wind and $v_{\rm wind}$ is the wind velocity. For measured wind velocities in ULXs (e.g. Pinto et al. 2016; Kosec et al. 2018b), a kinetic luminosity of a few $\times\ 10^{39}$ erg/s is plausible which gives bubble radii $\sim$100 pc, consistent with observation (Table 1). We note however that the radius depends on the driving luminosity (radiative and mechanical) to the power 1/5, so that even a difference of a factor 100 in luminosity alters the radius by only a factor 2.5.

The He II 4686λ recombination line is more easily created via photoionization than by shock-excitation (e.g. Berghea et al. 2010b), so using this line allows us to treat the nebula as a UV–X-ray bolometer, and infer the irradiating luminosity by using photoionization codes such as CLOUDY (Ferland et al. 1998). This has been performed for a number of ULXs, notably Ho II X-1 (Pakull and Mirioni 2002 and Berghea et al. 2010b who used the OIV line in the IR band) and NGC 5408 X-1 (Kaaret and Corbel 2009), with the finding that the required luminosities are a good match to the X-ray luminosities observed from the source.

Such consistency is used as an argument against strong geometrical beaming in these ULXs as the nebula should see the isotropic emission (Pakull and Mirioni 2002). However, the ULX wind photosphere emits a luminosity $\sim L_{\rm Edd}$ which – depending on the mass transfer rate – can have a temperature $\sim 10^6$ K, implying strong near-isotropic soft X-rays and EUV (see the discussion of Eqs. (110, 111 below).

In agreement with this, both Ho II X-1 and NGC 5408 X-1 are spectrally *soft* and potentially viewed at larger inclinations than some of the spectrally harder ULXs. Should this be true then it is not surprising that the irradiating luminosity inferred from photoionisation modeling is consistent with the observed luminosity, as we would naturally expect the more obscured (at such angles) hard X-ray emission to be the most geometrically beamed (rather than the more isotropic soft emission).

In principle, the *number* of ULX bubble nebulae can also be used to explore the role collimation/beaming plays in the wider population based on the reasoning that, for every ULX observed with a given beaming factor, there should be many more which are unbeamed and may not even be detectable as a ULX. As the nebula's photoionisation responds mostly to relatively unbeamed soft X-rays and EUV photons, such a premise would hold only if the nebula

ULX	Dimension(s)	Inferred age (years)	Radio/IR (jet) counterpart?	L_{kin} (10^{39} erg/s)
NGC 1313 X-1	240 pc			
NGC 1313 X-2	350x500 pc[a]	~1×10^6 (b)		~10
IC 342 X-1	110 pc[c]	~6×10^5	Y	~0.7
Ho II X-1	45 pc[d]		Y	
Ho IX X-1	250 pc[e]	~1×10^6	Y	~10
M81 X-6	115 x 42 pc[f]			
IC 2574 X-1				
NGC 2403 X-1	300 pc[g]			
NGC 4559 X-7				
NGC 4631 H7				
NGC 4861 X-1				
NGC 4861 X-2				
NGC 5204 X-1	360 pc			
NGC 5408 X-1	60 pc[h]	~1×10^5 (i)	Y	0.7 (i)
NGC 5885 ULX	200 x 300 pc[g]	6×10^5 (j)	Y	~20 (j)
NGC 6946 X-1	20×34 pc[k]		Y	
NGC 7793 S26	185 × 350 pc (l)	4×10^5 (l)	Y	~10-100 (l,m)
SS433 (W50)	50-70 pc[n]	~2×10^5 (b)	Y	> 0.1
M83 MQ1	13 pc[o]	1.3-2.0×10^4 (o)	Y	~ 30 (n)

Table 1 The properties of ULX nebulae, with non-ULX (i.e. hidden ULX) systems included at the bottom in a detached table. Objects and values from Pakull and Mirioni (2002) unless indicated otherwise. Dimension is diameter unless additional dimension is given. Corresponding references are: a: Ramsey et al. (2006); b: Cseh et al. (2012), c: Roberts et al. (2003); d: Kaaret et al. (2004); e: Miller (1995); f: Moon et al. (2011); g: Pakull and Grisé (2008); h: Grisé et al. (2012); i: Soria et al. (2006); j: Soria et al. (2021); k: Abolmasov et al. (2007a); l: Dopita et al. (2012) m: Pakull et al. (2010); n: Fabrika (2004); o: Soria et al. (2014).

was energised through shocks (which would indeed seem to be the case: Abolmasov et al. 2007a; Gúrpide et al. 2022) or if the accretion rate was high enough such that the photosphere emitted in the UV (with any substantial X-ray emission obscured or reprocessed). This then implies we should detect bubble nebulae with X-ray faint (non-ULX) counterparts; indeed there is already support for such observations both in other galaxies (e.g. Soria et al. 2014) and within our own (SS433: see Section 2.8.3). Searches for X-ray quiet bubble nebulae are made somewhat harder as ULX nebulae with strong photoionisation signatures (NGC 5408 X-1 and Ho II X-1) appear to be smaller (10s of pc rather than 100s of pc: Table 1), precluding detection of such relatively small structures in the absence of high angular resolution, narrow filter instruments (Russell et al. 2011). However, Pakull and Grisé (2008) searched VLT images of NGC 1313 for additional bubble nebulae *without* ULX counterparts and found only one possible candidate. As shown by Wiktorowicz et al. (2019), should geometric beaming be strongly related to accretion rate (King 2009), then binary population synthesis would imply that (in the absence of precession) the difference between the observed and underlying ULX population should be a factor of 5-15 unless black holes are the dominant population (in which case the observed is very similar to the underlying population). This would imply ∼10-30 ULXs should be present in NGC 1313 (assuming neutron stars dominate the underlying population), around 1/3 of which would have large bubble nebulae (Pakull and Grisé 2008). This is not significantly inconsistent with observation and any tension is relaxed if the population demographic is not 100% neutron stars or if the beaming is not as extreme a function of accretion rate as assumed

A number of ULXs have radio nebulae (see Table 1) of a similar size to their optical counterparts (Lang et al. 2007; Cseh et al. 2012). In Ho II X-1 (which shows a clear photo-ionisation dominated optical nebula), the radio nebula has been resolved into a discrete lobe-core-lobe structure (Cseh et al. 2014). The presence and variability of the radio structure in Ho II X-1 implies that repeat ejections also energise the surrounding gas (Cseh et al. 2015) in a similar manner to SS433 (W50), the inflated bubble nebula in M83 S2 (Soria et al. 2020), M82 Q1 (Soria et al. 2014) and the collimated jet source in NGC 7793 (S26: Soria et al. 2010).

2.6.2. ULX host environment

There is a trend favouring increased numbers of ULXs with lower host metallicity (e.g. Mapelli et al. 2010) and higher host star formation rate (see Section 2.1). This makes it important to explore the sub-galactic environment where ULXs are located, as this can provide powerful constraints on formation channels.

Besides the ionised environment (which can be extremely large, e.g. the 800 pc region around NGC 1313 X-1: Pakull and Mirioni 2002), it has been widely observed that ULX counterparts tend to be coincident with young stellar clusters or OB associations (e.g. Zezas et al. 2002; Goad et al. 2002; Gao et al. 2003; Grisé et al. 2006, 2008, 2012; Swartz et al. 2009; Liu et al. 2007; Abolmasov et al. 2007b). Although ionizing, the stellar environment provides insufficient flux to explain the emission line luminosities seen from the bubble nebulae (and the expected kinetic input due to supernovae is also not enough to inflate them: Ramsey et al. 2006) – indeed, in the case of IC 342 X-1, there are no O stars within 300 pc of the ULX (Feng and Kaaret 2008).

ULXs are also found (albeit rarely) in globular clusters. Relatively few (17 in total) are known at the time of writing: three in NGC 1399 (Shih et al. 2010; Irwin et al. 2010; Dage et al. 2019), two in NGC 4649 (Roberts et al. 2012; Dage et al. 2019), five in NGC 4472 (Maccarone et al. 2007, 2011) and a further seven in M87 (Dage et al. 2020).

ULXs located in globular clusters are expected to differ markedly from those located in the wider population. Given the dense environment of a globular cluster, such ULXs likely have a dynamical origin (Ivanova et al. 2010) – distinctly *unlike* those ULXs located in star forming regions (e.g. Brightman et al. 2020b), and the companion stars are also considerably older (and therefore less massive, e.g. the ULX may be feeding from a white dwarf: Steele et al. 2014, potentially in a short period, ultracompact binary King 2011). In terms of brightness, the typical X-ray luminosity is $\sim 10^{39}$ erg s^{-1} with the only globular cluster ULX found to exceed 4×10^{39} erg s^{-1} being GCU8 in NGC 1399 (Dage et al. 2019).

2.7. 'Hyperluminous' X-ray sources?

The term 'hyperluminous' has sometimes been used to refer to sources with inferred (isotropic) luminosities in excess of 10^{41} erg s^{-1}. However there is little evidence to support the implicit suggestion that these bright ULXs form a physically distinct class. They certainly do not need to contain unusually high mass black holes or IMBH: the ULX

pulsar NGC 5907 ULX-1 reaches such luminosities (e.g. Israel et al. 2017a) and evidently contains a neutron star. The well known extreme source SS433 is probably a ULX viewed 'from the side' (i.e. from outside the X-ray beam: see Section (3.14.1) and inferred on evolutionary grounds (see King et al. 2000a) to be supplied with mass at a rate $\sim 10^{-5} \rightarrow 10^{-4}\,M_{\odot}\,yr^{-1}$. From the beaming formula (55), if viewed from within this beam, SS433 would have an inferred isotropic luminosity $L_{sph} \sim 10^{41}$erg s^{-1} if the accretor is a $10\,M_{\odot}$ black hole. We discuss the source HLX-1 in Section (3.16.2) below.

2.8. *Galactic ULXs*

A number of Galactic sources are known to reach or exceed their Eddington limit for extended periods of time (i.e. discounting type I bursts etc). Their proximity allows for more detailed tests of how super-Eddington mass supply operates. Here we report those sources which would qualify as ULXs if placed in another Galaxy, with observed (or inferred) X-ray luminosities $\gtrsim 10^{39}$ ergs^{-1}.

2.8.1. *Low mass X-ray binaries*

Several low mass X-ray binaries (LMXBs) containing black holes are known to exceed their Eddington limit during outbursts mediated by the classical disc instability (Lasota 2001), recently modified to account for large discs powering super-Eddington outbursts (Hameury and Lasota 2020). GRS 1915+105 reaches rates close to its Eddington limit (and has been in outburst for at least 30 years: Castro-Tirado et al. 1992), GRO J1655-40 may have entered a super-Eddington state in its 2005 outburst (Neilsen et al. 2016), V404 Cygni is thought to have exceeded its Eddington limit in its recent 2015 outburst (Motta et al. 2017; Miller-Jones et al. 2019, and potentially in the earlier outburst if not all of the radiation was visible to us) in a similar fashion to V4641 Sgr in 1999 (Revnivtsev et al. 2002). In addition to these confirmed black hole systems, neutron star LMXBs certainly exceed their own Eddington limit and may even approach the empirically defined ULX threshold of $\sim 10^{39}$ erg/s (for instance the bursting pulsar, GRO 1744-28: Sazonov et al. 1997). It is notable that all of these systems have fairly long orbital periods (2.6 - 31 d), which results in a large outer disc radius and the creation of a large reservoir of material for accretion (see Hameury and Lasota 2020 for details).

In addition to large X-ray and optical luminosities, and powerful mass-loaded outflows, optically thin, flaring jet emission is observed to coincide with outbursts of those sources approaching their Eddington limits (Fender et al. 1997). Such radio-bright, highly variable events provide another way of detecting extra-galactic systems entering a near-Eddington/super-Eddington state (and may favour the detection of black hole over neutron star systems: Middleton et al. 2013; van den Eijnden et al. 2018).

2.8.2. *High mass X-ray binaries*

A number of accretion powered pulsars fuelled by high mass donor stars (i.e. high mass X-ray binaries: HMXBs) are known to reach $\times 10^{39}$ ergs^{-1}, including the X-ray millisecond pulsar AO538-66 (Skinner et al. 1982), SMC X-1 (e.g. Bonnet-Bidaud and van der Klis 1981) and SMC X-3 (mentioned already in this review).

A recent important observation of Galactic HMXBs in the context of ULXs is that of Swift J0243.6+6124 (Kennea et al. 2017). This magnetised neutron star (with an inferred dipole field of $\geq 10^{12}$G: Doroshenko et al. 2018) accretes from the decretion disc of an O9.5Ve star (Reig et al. 2020), reaches a (0.5-10 keV) luminosity of 10^{39} ergs^{-1}, shows pulsations on a timescale of $\sim$ 10s (Jenke and Wilson-Hodge 2017), shows evidence for fast outflows (van den Eijnden et al. 2019; Tao et al. 2019), and produces radio jets (van den Eijnden et al. 2018). These jets are relatively weak radio emitters, with a maximum flux density of 100 μJy at 6 GHz (at an assumed distance of around 7 kpc: van den Eijnden et al. 2018), and are therefore unlikely to be detected in other galaxies in the absence of substantial Doppler boosting. However, detections of jet events from Galactic HMXBs may become more widespread with the advent of sensitive all sky radio monitoring (SKA) and will permit tests of neutron star jet models (e.g. Parfrey et al. 2016).

2.8.3. *SS433*

Discovered by Stephenson and Sanduleak (1977), the A type supergiant companion star in SS433 (Gies et al 2002) is transferring mass to the compact object at a rate $\sim 10^{-5} \rightarrow 10^{-4}\,M_{\odot}\,yr^{-1}$ (Shklovsky 1981; King et al. 2000a; Fuchs et al. 2006). This would imply $\dot{m} \sim 100$ and 1000 for a 10 $M_{\odot}$ black hole or 1.4 $M_{\odot}$ neutron star respectively. This strongly super-critical mass transfer rate suggests that SS433 is 'intrinsically' a Galactic ULX similar to those with

luminosities ≥ 10^{40}ergs^{-1} seen in other galaxies (Begelman et al. 2006). However it does not qualify as a ULX on the grounds of *observed* luminosity – see Section 3.14.1.

One of the most dramatic features of SS433 is the baryon-loaded jet (Fabian and Rees 1979; Margon et al. 1979; Kotani et al. 1994; Marshall et al. 2013) which is ejected at ~0.26c and is twisted into a helical shape by the 162 day precession of the surrounding disc and wind. The baryon-loading, low velocity ($v/c \simeq 0.25$), and 162.4 d precession period of the jet might result from a collision with the precessing outer disc (Begelman et al. 2006) or could simply be due to the jet being the highly collimated wind from the innermost regions (which matches simulations, e.g. Jiang et al. 2014, 2019b) tracing the precession.

We limit ourselves here to a discussion of the similarities and differences between SS433 and other ULXs, and direct the reader to (Fabrika, 2004) for a comprehensive review.

SS433 can be regarded as a key example of a ULX in our own Galaxy, merely inclined such that we do not see directly into the wind-cone (Begelman et al. 2006; Middleton et al. 2021b). As indicated in the previous sections, besides the similarities of the broad He II recombination lines (Fabrika et al. 2015) to those seen in other ULXs, there are a number of sources which look distinctly like SS433, viewed at similar edge-on inclinations. Notably the inflated nebula in M83 and collimated jet source in NGC 7793 (Pakull et al. 2010; Soria et al. 2010; Dopita et al. 2012). In both of these cases, the jet power appears to be greater than in SS433 for similar or slightly higher apparent X-ray luminosities. Indeed, very many ULXs must also be oriented in such a manner such that we only observe a relative proportion of the entire ULX population (see Middleton and King 2017; Wiktorowicz et al. 2019). Whilst it is rather hard to study the innermost regions of SS433 (although we can study the reflected emission and infer the intrinsic flux: Middleton et al. 2021b), it provides a unique opportunity to explore how such systems are fed, its feedback into the local ISM, the nature of the binary (e.g. probes of circumbinary structure: Waisberg et al. 2019), and the structure of the X-ray obscuring regions (Middleton et al. 2021b).

2.8.4. Future ULX observations

It is apparent that the study of ULXs has made dramatic progress as instrumentation has improved (e.g. the discovery of pulsations, winds and jets). In the near future, a number of developments will see the field evolve in new, exciting ways.

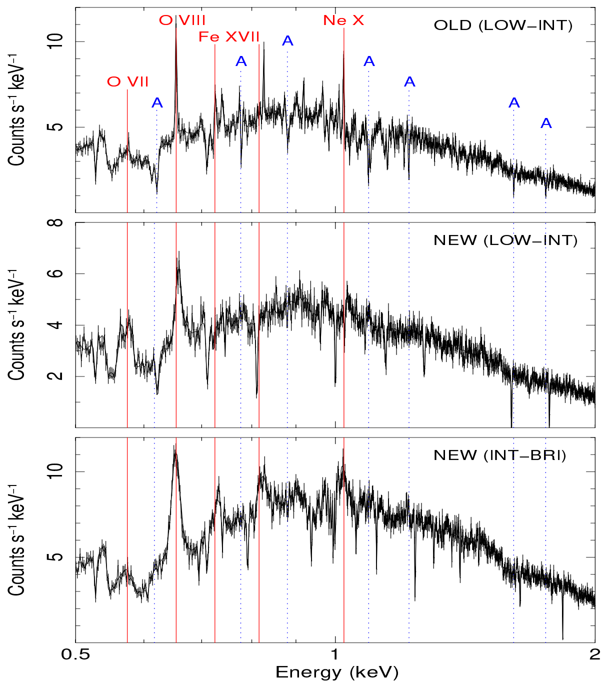


Figure 12 From Pinto et al. (2020b), showing simulations which highlight the spectral quality of observations of ULXs (in this case NGC 1313 X-1) which will be made possible by the launch of *Athena* with its X-ray integral field unit (X-IFU). The simulations utilise absorption and emission models derived from existing observations (see Pinto et al. 2020b for more details).

2.9. X-rays

Much of our understanding of ULXs derives from the X-ray band (even if this only actually grants us a restricted view of the full energetics of the system). Several new X-ray satellites are anticipated in the next two decades, including the *Astro-H* recovery mission, *XRISM* (dedicated to high energy-resolution X-ray imaging: XRISM Science Team 2020), and ESA's flagship *Athena* mission (scheduled to launch in the 2030s: Nandra et al. 2013), comprising a wide field imager (WFI) and X-ray

integral field unit (X-IFU). Both instruments onboard *Athena* represent a significant improvement in effective area for their respective specialisms: the WFI is around an order of magnitude more sensitive than *XMM-Newton*'s EPIC pn detector (from ~0.5-2 keV), and the X-IFU is between 45 (at 1 keV) and 6 (at 7 keV) times more sensitive even than *XRISM*. This improvement in sensitivity will allow considerably deeper searches for pulsations in known ULXs, placing important constraints on the underlying population demographic. The sensitivity will also allow new searches for QPOs and reveal new details in the lag spectra (Heil and Vaughan 2010; De Marco et al. 2013; Kara et al. 2020; Middleton et al. 2021b). Finally, the impact on studying ULX outflows and how they vary with spectral state will be dramatic, allowing results previously obtained in ~day exposures to be obtained in only a couple of hours (see Figure 12 which shows a simulation of the atomic lines detected in NGC 1313 X-1 as seen by *Athena*: Pinto et al. 2020b).

2.10. Multi-wavelength

As we have discussed in the preceding sections, multiwavelength observations of ULXs have been highly revealing, allowing the discovery of jets, studies of optical nebulae and likely donor stars, and have provided insights into the nature of the accretion flow (irradiation and emission from the outer photosphere).

The future of optical observing of ULXs – as with other variable astronomical objects of interest – is poised to change dramatically with the introduction of all–sky, high angular resolution, high–throughput observing via the Vera Rubin LSST, which is due to start operations in 2023. LSST will provide highly sensitive snapshots (e.g. a limiting r-band magnitude of 24.7 in a single 30s exposure at SNR = 5) of $\sim$18,000 deg^2 of the Southern sky (DEC = -65 $\rightarrow$ +5). Combined with a median seeing–limited angular resolution of 0.7", this will allow deeper probes of possible optical counterparts and explore optical variability for signs of irradiation or precession (e.g. Motch et al. 2014; Middleton et al. 2019b). LSST is not equipped with narrow filters (nor any spectroscopic instrumentation), precluding locating new bubble nebulae, but the MUSE IFU on the VLT is set to transform our understanding of ULX feedback by spatially resolving different regions of ULX bubble nebulae (e.g. Gúrpide et al. 2022). Finally, the introduction of the ELT (sometime after 2027), will also provide a step change in signal-to-noise, allowing deep spectroscopic studies of ULX counterparts. By identifying lines from the companion star, mass functions will no doubt follow.

At longer wavelengths, there will be a great deal of interest in the JWST view of ULXs, as this will provide opportunities to locate further red super-giant companions (e.g. Heida et al. 2016), study the surrounding nebulae (e.g. using the OIV line: Berghea et al. 2010b) at a resolution even higher than can be achieved by MUSE, search directly for IR bright ejecta or indirectly search for the presence of jets via IR variability (e.g. Dudik et al. 2016).

At the longest wavelengths, SKA will transform our view of the variable radio sky. In relation to ULXs, the enormous sensitivity of SKA will allow us to locate LMXB ULXs entering outburst in nearby galaxies (Middleton et al. 2013), search for variability in radio bubble nebulae, and potentially resolve jet structures (Cseh et al. 2014, 2015). In terms of the impact on studies of Galactic ULXs, SKA will allow the deepest searches for jet ejections associated with accreting pulsars (van den Eijnden et al. 2018) and allow models for their production to be tested (e.g. Parfrey et al. 2016).

3. Theory

3.1. Definitions and notation

The Eddington luminosity is

$$L_{\rm Edd} = \frac{4\pi G M m_p c}{\sigma_T} = 1.26 \times 10^{38} \left(\frac{M}{\rm M_\odot}\right) {\rm erg\,s^{-1}}, \tag{20}$$

where m_p is the proton mass, σ_T the Thomson scattering cross-section. In this review $L_{\rm Edd}$ defined by Eq. (20) is a unit of luminosity depending on accretor's mass only.

The Eddington accretion rate is defined as

$$\dot{M}_{\rm Edd} = 1.4 \times 10^{18} \eta_{0.1}^{-1} \left(\frac{M}{\rm M_\odot}\right) {\rm g\,s^{-1}} \tag{21}$$

$$= 2.2 \times 10^{-8}\, \eta_{0.1}^{-1} \left(\frac{M}{\rm M_\odot}\right) {\rm M_\odot\,yr^{-1}}, \tag{22}$$

ULX	P_{pulse} (s)	Spin up rate (ss^{-1}) (baseline)	Pulse fraction (E range)	P_{orb}	P_{s-orb} (d)	L_{max} ($\times 10^{39}$ erg s^{-1})	M_2 ($M_\odot$)
M82 X-2[a,b,c]	1.4	1×10^{-11} (2.5 years)	5-13% (3 - 30 keV) 8-23% (10 - 30 keV)	2.5	~60	20	≥ 5.2
NGC 5907 ULX-1[d,e]	1.1	-8×10^{-10} (11 years)	12% (0.2-2.5 keV) 20% (7-30 keV)	5.3	78	200	?
NGC 7793 P13[f,g,h]	0.4	4×10^{-11} (4 years)	18-22% (0.1-12 keV)	64	64	~ 10	18-23 (B9I)
NGC 300 ULX-1[i,j]	31.6	-6 ×10^{-7} (3.6 days)	~60% (0.2-10 keV) ~ 70% (3-20 keV)	> 290	?	5	8-10 (RSB?)
SMC X-3[k,l,m,n]	7.8	~-4×10^{-9} (110 days)	30-100 % (3-70 keV)	~45	?	~ 3	>3.7 (Be?)
M51 ULX-7[o,p]	2.8	-1×10^{-9} (13 years)	<5 - 20% (0.1-12 keV)	2	38	~ 10	> 8
NGC 1313 X-2[q]	1.5	1.2×10^{-12} (98 days)	~5% (0.3-10 keV)	< 4	?	20	?
NGC 2403 ULX[r]	18	3.4×10^{-10} (?)	?	60-100	?	1.2	Be?
Swift J0243.6+6124[s]	9.86	2.2×10^{-10} (?)	?	28.3	?	≥ 1.5	Be?
RXJ0209.6-7427[t]	9.3	1.165×10^{-10} (?)	?	>50	?	1-2	Be
M51 ULX-8[u]	?	?	?	8-400	?	2	40(?)
NGC 1313 PULX[v]	765.6	?	38% (0.3-7 keV)		?	1.6	Be?

Table 2 Key parameters of interest for the ULX pulsars with values taken from those papers indicated by the reference attached to the ULX name. The period over which the spin-up/down rate is calculated, is given in parentheses, as is the energy range for the measured pulse fraction. a: Bachetti et al. (2014), b: Bachetti et al. (2020). It is worth noting that in the case of M82 X-2, there are periods of both spin-up and spin-down – see Bachetti et al. (2020) for details. c: Brightman et al. (2019); d: Israel et al. (2017a); e: Walton et al. (2016a); f: Fürst et al. (2016); g: Israel et al. (2017b); h: Fuerst et al. (2021); i: Carpano et al. (2018); j: Heida et al. (2019b), k: Edge et al. (2004); l: Townsend et al. (2017); m: Tsygankov et al. (2017); n: Corbet et al. (2004); o: Rodríguez Castillo et al. (2020); p: Brightman et al. (2020a); q: Sathyaprakash et al. (2019b); r: Trudolyubov et al. (2007); s: Doroshenko et al. (2018); t: Vasilopoulos et al. (2020b); u:Brightman et al. (2018); v: Trudolyubov (2008).

where $\eta = 0.1\eta_{0.1}$ is the radiative efficiency of accretion, κ_{es} the electron scattering (Thomson) opacity. We will often use accretion rate measured in units of Eddington accretion rate and stellar mass in solar masses:

$$\dot{m} = \frac{\dot{M}}{\dot{M}_{\rm Edd}} \qquad \text{and} \qquad m = \frac{M}{{\rm M}_\odot}. \tag{23}$$

3.2. Discs with super-Eddington mass supply rates

At high local accretion rates $\dot{m} \gtrsim 1$, the radial structure of a stationary ($\dot{M} = const.$) disc around a compact object can be divided into three parts (Shakura and Sunyaev, 1973). In the outermost regions the pressure is dominated by gas and the electron scattering contribution to the opacity can be neglected. For radii

$$R_{\rm es} < 5 \times 10^3 \dot{m}^{2/3} R_g, \tag{24}$$

electron scattering is the main source of opacity, but gas pressure is still dominant. Finally, for radii

$$R_{\rm pr} < 1.9 \times 10^2 \dot{m}^{16/21} m^{-8/21} R_g, \tag{25}$$

the pressure is dominated by radiation, while the opacity is mainly due to electron scattering. $R_g \equiv GM/c^2$ is the gravitational radius.

The standard accretion disc model (Shakura and Sunyaev, 1973; Frank et al., 2002) applies only to geometrically thin discs, i.e., discs whose height satisfies the condition $H \ll R$. When the luminosity approaches the Eddington value this approximation breaks down.

The approximate vertical dynamical equilibrium equation

$$\frac{H}{R} \approx \frac{c_s}{v_{\rm K}}, \tag{26}$$

where $c_s = \sqrt{P/\rho}$, is the isothermal sound speed, P and ρ are the (total, gas + radiation) pressure and density respectively, and $v_{\rm K} = \sqrt{GM/R}$, can be written as

$$\frac{H}{R} \approx \frac{L(R)}{L_{\rm Edd}}. \tag{27}$$

To derive Eq. (27), we have used the expression for the radiative pressure $P_r = 4\sigma T_c^4/3c$ and the solution for the local vertical radiative transfer equation $T_c^4 = (3/8)\tau T_{\rm eff}^4$ (Lasota, 2016).

Therefore already at $L \sim 0.1\, L_{\rm Edd}$ the thin-disc approximation ceases to be valid and for $L \gtrsim L_{\rm Edd}$ one has $H \gtrsim R$ so that the accretion flow is more spherical than disc–like.

The point at which the local flux takes the Eddington value is called the spherization radius (Shakura and Sunyaev, 1973) and can be seen as the boundary separating the thin disc from a more spherical inner accretion flow.

3.2.1. Spherization radius

In a stationary disc ($\dot M = const$), the local radiative flux generated by the disc's (anomalous) viscosity becomes equal to the local Eddington flux at the *spherization radius* $R_{\rm sph}$.
The viscous flux (Frank et al., 2002) can be written as

$$F_{\rm visc} = \frac{3}{8\pi}\frac{R_g}{R^3}\dot M c^2 \left[1 - \left(\frac{R_{\rm in}}{R}\right)^{1/2}\right], \tag{28}$$

and the Eddington flux is

$$F_{\rm Edd} = \frac{L_{\rm Edd}}{4\pi R^2}. \tag{29}$$

From $F_{\rm visc} = F_{\rm Edd}$, one obtains

$$R_{\rm sph} = 15\dot m\, R_g, \tag{30}$$

We have neglected the boundary term in square brackets since $R_{\rm sph} \gg R_{\rm in}$ for $\dot m \gg 1$ and $R_{\rm in} \approx 6R_g$. The spherization radius defined in Eq. (30) is 1.1 times larger than the spherization radius in Shakura and Sunyaev (1973). Ohsuga and Mineshige (2014) assume $R_{\rm sph} \equiv \left(\dot M c^2/L_{\rm Edd}\right) R_{\rm S}$, where $R_{\rm S} = 2R_g$[6], which gives a value of $R_{\rm sph}$ 1.3 times larger than in Eq. (30).

The outer regions of accretion discs around compact objects can be strongly X–ray self–irradiated. Then the condition for $R_{\rm sph}$ is

$$F_{\rm Edd} = F_{\rm irr} + F_{\rm visc}, \tag{31}$$

where we put (see Dubus et al., 1999):

$$F_{\rm irr} = C\frac{\eta \dot M_{\rm in} c^2}{4\pi R^2}, \tag{32}$$

where C is a constant containing all the information about the disc irradiation process and $\dot M_{\rm in}$ is the accretion rate onto the accretor. The spherization radius becomes

$$R_{\rm sph} = 15\left(1 - C\frac{\dot m}{2}\right)^{-1} \dot m\, R_g. \tag{33}$$

For "standard" values of $C \sim 10^{-2}$ (Dubus et al., 2001) disc irradiation can be neglected in the definition of the spherization radius for $\dot m \ll 200\,(0.01/C)$. One should notice, however, that at very high accretion rates it is nor clear how self–irradiation can proceed. Even at sub–Eddington accretion rates when applying irradiation models to observed systems, one concludes that scattering in the wind is still not sufficient to produce the observed disc heating, even in combination with direct illumination (Tetarenko et al., 2020). On the other hand, until now, the disc considered in this context were rather smaller than those supposed to be present in many ULXs so it this latter case a component of order $L_{\rm Edd}$ emerging from the photosphere of the spherical wind, might irradiate the outer parts of the disc. Fortunately, as argued above, this effect is presumably not important at most luminosities of interest.

High accretion rates implying large optical depth and high radial velocities in the inner regions of the flow can result in photons being trapped in the accretion flow.

[6]In the literature both units of length, $R_{\rm S}$ and R_g are used.

3.2.2. Trapping radius

The *trapping radius* is defined as the place where the photon diffusion (escape) time $H\tau/c$ equals the viscous infall time R/v_r

$$R_{\rm trapp} = \frac{H\tau\, v_r}{c} = \frac{H\kappa\Sigma}{c}\frac{\dot M}{2\pi R\Sigma} = 20\frac{H}{R}\dot m R_g, \tag{34}$$

where $\Sigma = 2\int \rho dz$ is the disc surface density. For $R < R_{\rm trapp}$ photons trapped in the flow are entrained (advected) faster than they can escape, so that if the accreting body is a black hole, most of the accretion energy is accreted by the black hole and adds to its mass. In this state there is in principle no upper limit to the accretion *rate* $\dot M$ but the accretion *luminosity* grows only logarithmically with $\dot M$ (see Eq. 45). In other words, very super–Eddington mass supply rates do *not* imply (very) super–Eddington luminosities.

Eq. 34 assumes that the accretion flow moves only in the radial direction, and that there are no outflows. Shakura and Sunyaev (1973) proposed an alternative to such an advection–dominated solution (which they considered "improbable") where for $R \leq R_{\rm sph}$ the local flux is everywhere equal to its Eddington value.

3.3. Shakura-Sunyaev (1973) second (windy) solution

To keep $F_{\rm vis} = F_{\rm Edd}$, everywhere for $R \leq R_{\rm sph}$, one must arrange that $\dot M \sim R$ (see Eqs. 28 and 29). Hence

$$\dot m(R) \simeq \dot m_0 \frac{R}{R_{\rm sph}} \tag{35}$$

Using $\sigma T_{\rm eff}^4 \equiv F_{\rm visc} = F_{\rm Edd}$ one can calculate the luminosity of disc described by the windy SS73 solution

$$L_{\rm thick} = 2\int_{R_{\rm in}}^{R_{\rm sph}} \sigma T_{\rm eff}^4 2\pi R dR \approx L_{\rm Edd} \ln \dot m. \tag{36}$$

The total disc luminosity is then

$$\begin{aligned} L_{\rm total} =& L_{\rm thin} + L_{\rm thick} = \\ & 4\pi\left(\int_{R_{\rm in}}^{R_{\rm sph}} \sigma T_{\rm eff}^4\, RdR + \int_{R_{\rm sph}}^{R_\infty} \sigma T_{\rm eff}^4\, RdR\right) \approx L_{\rm Edd}\,(1 + \ln \dot m). \end{aligned} \tag{37}$$

In this SS73 'windy' solution, maintaining the radiation flux at the local Eddington value requires the accretion rate to decrease with radius as $\dot M \sim R$. This requires that matter is expelled from the disc flow as a wind. But the trapping radius is close to the spherization radius, so one can also legitimately consider discs in which the "excess" radiation is trapped in the inflow and advected on to the accretor, while the accretion rate remains constant. We examine these advective solutions in the next two subsections. They have played a very important role in the understanding of high–rate accretion onto compact bodies but, as we will see, they do not give suitable models for ULX accretion.

3.4. Slim discs

For a black hole accretor, the advected energy disappears behind the event horizon (growing its mass) and we can regard advection as an additional cooling mechanism. In contrast, for a neutron star accretor, the advected energy must be radiated from the stellar surface or the magnetosphere. Then the accretion luminosity violates the Eddington limit and the assumption of steady radial infall.

The energy conservation equation in a stationary disc is

$$F_{\rm visc} = F_r + F_{\rm adv}, \tag{38}$$

where F_r is the radiative flux and $F_{\rm adv}$ is the advective term (Lasota, 2016)

$$F^{\rm adv} = \frac{\Sigma T v_r}{R}\frac{ds}{d\ln R} = \frac{\dot M}{2\pi R^2} c_{\rm s}^2 \xi_a. \tag{39}$$

Here Σ is the surface density, T is the midplane temperature, v_r the radial velocity, $c_s = \sqrt{P/\rho}$ the speed of sound, s the specific entropy and $\xi_a \sim 1$ is a slowly varying function related to the entropy gradient. From Eqs. 28, 26 and 39 one obtains

$$\frac{F_{\rm adv}}{F_{\rm visc}} \sim \frac{c_s^2}{\Omega_K^2 R^2} \approx \left(\frac{H}{R}\right)^2, \tag{40}$$

so that for thin ($H/R \ll 1$) discs the advective term can be neglected. But at luminosities approaching $L_{\rm Edd}$ this term become dominant, leading to

$$F_{\rm visc} \approx F_{\rm adv}. \tag{41}$$

Solutions of this equation represent advection dominated accretion flows (ADAFs), which for high accretion rates are called "slim discs" (Abramowicz et al., 1988; Sądowski, 2009; Sadowski, 2011; Sądowski et al., 2011).

Solutions representing vertically–integrated slim-disc structure have the form

$$\dot m \sim \kappa_{\rm es} r^{1/2} \alpha\Sigma \tag{42}$$

on the $\dot M(\Sigma)$ plane. $\kappa_{\rm es}$ is the electron-scattering opacity and α the disc viscosity coefficient.

For these pure advection solutions, one has $H/R \approx 1$, *independent of accretion rate and radius* (see Eqs. 40, 41 and Lasota, 2016). But since $F_{\rm adv} \sim \dot m^2$ while $F_r \sim \dot m^{1/2}$ (Lasota et al., 2016), below $\dot m \lesssim 1$, radiative cooling overtakes advection and the disc structure switches to the standard radiation-pressure–dominated SS73 disc:

$$\dot m \sim \kappa_{\rm es}^{-1} r^{3/2} (\alpha\Sigma)^{-1}. \tag{43}$$

Using Eq. (27) the radiative flux of the advection-dominated flow becomes

$$F_r = \sigma T_{\rm eff}^4 \approx \frac{L_{\rm Edd}}{4\pi R^2}, \tag{44}$$

so that the luminosity of this part of the accretion flow is

$$L_{\rm slim} = 2\int_{R_{\rm in}}^{R_{\rm trans}} \sigma T_{\rm eff}^4\, 2\pi R dR \approx L_{\rm Edd} \cdot \ln\frac{R_{\rm trans}}{R_{\rm in}} \approx L_{\rm Edd}\, \ln \dot m. \tag{45}$$

Equations (36) and (45) both result from the mechanical equilibrium equation of a radiation-pressure dominated disc

$$F_r = \frac{c}{\kappa_{es}} g_z \approx \frac{c}{\kappa_{es}} \frac{GM}{R^2}, \tag{46}$$

for $H/R \approx 1$, and $g_z \approx (GM/R^2) H/R$ (Paczyński, 1982; Poutanen et al., 2007). But although the luminosities are similar, in the first case only $\dot m \approx 1$ is accreted on to the compact object while in an advection dominated flow the whole of $\dot m \gg 1$ arrives at the accretor's surface.

Since H/R in slim discs is independent of the accretion rate, one cannot get so–called "thick discs" or "Polish doughnuts" by increasing the rate at which matter is supplied to the compact object. Contrary to assertions found in the literature (e.g., Poutanen et al., 2007) slim discs are not the same objects as Polish doughnuts. As we have seen, they do not significantly increase the true emitted luminosity above $L_{\rm Edd}$, and do not collimate or beam it such that the apparent luminosity may be super–Eddington in a restricted solid angle. Accordingly they do not offer an explanation for the defining feature of ULXs. However for a black hole ULX they may describe the fate of some of the super–Eddington mass supply.

3.5. Polish doughnuts

Unlike slim discs, for which $H/R \lesssim 1$, Polish doughnuts (Kozlowski et al., 1978; Abramowicz et al., 1978; Jaroszynski et al., 1980; Paczynsky and Wiita, 1980) have by construction $H/R \gg 1$, with long central funnels along which most of the radiation is emitted. They were devised in the late 1970s and early 1980s to try to explain the high luminosities and jets of QSOs by assuming that these objects are fed at highly super-Eddington rates (see, e.g., Sikora, 1981). They are often confused with slim discs and incorrectly assumed to be advection dominated accretion flows. They have been invoked as solutions to the ULX problem, but we will see that this is not correct.

Polish doughnuts are models of stationary and axially symmetric accretion structures around black holes. All their properties are obtained from a single function $\ell(R)$ describing the specific (per unit mass) angular momentum distribution at the doughnut's photosphere. There is no explicit assumption about the doughnut's interior. One assumes only that a.) the photosphere coincides with an equipressure surface. b.) the specific angular momentum at the photosphere is assumed to be given by some function $\ell(R)$ (one often assumes $\ell(R) = const.$), c.) radiation is emitted at the photosphere at the local Eddington flux, that is, the local flux $\mathbf{F}_r$ is given by

$$\mathbf{F}_r = \frac{c}{\kappa}\,\mathbf{g}_{\rm eff}, \tag{47}$$

(Paczyński, 1982),where boldface symbols denote vectors. The specific angular momentum is assumed to be Keplerian at the inner and outer boundaries: $\ell\,(R_{\rm in}) = \ell_{\rm K}\,(R_{\rm in})$ and $\ell\,(R_{\rm out}) = \ell_{\rm K}\,(R_{\rm out})$, and the inner radius lies between the innermost stable circular orbit (ISCO) and the innermost bound orbit (IBCO), and $R_{\rm IBCO} < R_{\rm in} < R_{\rm ISCO}$. Because of the strong radial pressure gradients (negligible for thin discs) needed to have $H/R \gg 1$, the inner flow edge is pushed inside the ISCO.

The doughnut shape is obtained from

$$\frac{{\rm d}H}{{\rm d}R} = -\left(\frac{g^R_{\rm eff}}{g^z_{\rm eff}}\right)_{z=H} \equiv f(R,H), \tag{48}$$

where R, z are the cylindrical coordinates, and the radial component of the effective gravitational acceleration $g^R_{\rm eff}$is a function of $\ell(R)$.

The inner part of the doughnut forms a funnel with an opening angle obeying $\tan\alpha = 1/\chi \sim \sqrt{8\rho}$, where $\rho = (R_{\rm in} - R_{\rm IBCO})/R_{\rm S}$ $(0 \leq \rho \leq 1)$ and $\chi = (H/R)_{max}$ (Wielgus et al., 2016).

The luminosity is mainly emitted from the funnel, i.e.,

$$L_{\rm apparent} \approx \frac{L_{\rm funnel}}{1-\cos\alpha} \equiv \frac{1}{b}L_{\rm funnel}. \tag{49}$$

With $b = (1-\cos\alpha) \sim \rho$, the funnel can be very narrow, but this does not lead to an increase of the apparent luminosity. Indeed,

$$L_{\rm apparent} \approx \frac{1}{b}L_{\rm funnel} = \frac{\epsilon_{\rm rad}}{b}\dot{M}c^2 \approx const.\,\dot{M}c^2, \tag{50}$$

because the accretion radiation efficiency $\epsilon_{\rm rad} \sim \rho$, since by definition the binding energy at $R_{\rm IBCO}$ is equal to zero.

So although Eq. (49) at first sight resembles Eq. (3), in Polish doughnuts one does not have $L_{\rm apparent} \gg L_{\rm true}$. This means that, contrary to initial appearances, Polish doughnuts are not relevant to BH ULXs (Wielgus et al., 2016), and we already know that they are not applicable to NS ULXs. Together with the similar conclusions we arrived at in Subsection (3.4) for slim discs, this severely narrows the range of potential explanations for ULXs.

We are left with only one possibility for making an accretion flow *appear* super–Eddington while simultaneously ensuring that the mass supply rate very close to the accretor is *not* significantly super–Eddington. In the next Subsection we ask if the disc winds required by the Shakura–Sunyaev 'windy' solution can collimate the modestly super–Eddington intrinsic luminosity $L_{\rm Edd}(1 + \ln\dot{m})$ (cf 37) given by a super–Eddington mass supply. We note that Eq. (37) is an approximation since the spherization radius is not a uniquely defined quantity, which we should not see as a rigid limit defining the boundary of the wind. Eq. (37) is valid in both the SS73 and advection–dominated cases, but when these effects are simultaneously present one gets a slightly different formula (see e.g., Poutanen et al. 2007). In the following we therefore use $L = L_{\rm Edd}(1 + \ln\dot{m})$ as a "universal" reference value for unbeamed luminosity.

3.6. Beaming by accretion disc winds

We have seen that in the SS73 'windy' solution, the accretion flow carries only the local Eddington mass rate at each accretion disc radius, while the excess is blown away in winds at each radius near the disc centre. These winds must be quasispherical, but leave open funnels around the central disc axis (since they cannot achieve zero angular momentum). The funnels offer a suitable way of collimating the accretion luminosity, as all other photon escape routes have high optical depth. We will see in Section (3.8) that numerical solutions of such flows are still some way from providing a picture which is easy to apply to observed ULXs.

Fortunately, soft X–ray observations of ULXs provide a remarkable insight into the beaming by disc winds. The soft components of ULXs can be fitted with blackbody spectra, giving the temperature T and apparent (assumed isotropic) luminosity $L_{\rm soft}$. Kajava and Poutanen (2009) show that the brightest soft X–ray components (above 3×10^{39} erg s^{-1}) in 9 ULXs cluster around the relation

$$L_{\rm soft} \simeq 7 \times 10^{40} T_{0.1\,{\rm keV}}^{-4}\,{\rm erg\,s^{-1}}, \tag{51}$$

where $T_{0.1\,{\rm keV}}$ is the blackbody temperature expressed in units of 0.1 keV/k, where k is Boltzmann's constant. However, not all ULXs show such a relationship (cf Walton et al. 2020; Gúrpide et al. 2021) and – even in the absence of additional spectral components in the presence of a neutron star accretor – the combination of anisotropy/beaming, precession and the lack of a suitable model for extracting $L_{\rm soft}$ unambiguously (see, e.g. Robba et al. 2021), must result in complexity and a range of observed slopes.

At first sight (51) seems paradoxical, as one would expect a blackbody source of fixed size to vary as $L \propto T^4$ instead[7]. But the relation (51) would instead imply that the radius of the blackbody source varies along with the luminosity and temperature. This is of course what we should expect for emission from the central part of accretion discs fed at super–Eddington rates, progressively ejecting the excess accreting matter from inside the spherization radius, as the latter varies $\propto \dot m$ (see Section 3.1). We can see this explicitly by parametrizing the true emitted luminosity (pre–collimation) as

$$L = 4\pi p R^2 \sigma T^4 \tag{52}$$

where $R = rR_g \propto M$ with $r \simeq 15\dot m$ (see Eq. 30), and σ is the Stefan–Boltzmann constant. Setting $L = lL_{\rm Edd} \propto M$, where $l \sim 1$, and p allows for geometrical projection, we can write

$$L \propto R^2 T^4 p \propto M^2 T^4 r^2 p \propto L^2 T^4 \frac{r^2 p}{l^2}, \tag{53}$$

where we use $R \propto rR_g$ at the first step and $M \propto L/l$ at the second. The final form implies $L \propto T^{-4}$. An observer assuming that the flux is isotropic with the observed value, rather than collimated, now infers a total blackbody luminosity $L_{\rm sph} = b^{-1}L$, so that, inserting the constants,

$$L_{\rm sph} = \frac{4\pi c^6}{\sigma\kappa^2}\frac{1}{T^4}\frac{l^2}{pbr^2} = \frac{2.8 \times 10^{44}}{T_{0.1\,{\rm keV}}^4}\left(\frac{l^2}{pbr^2}\right)\,{\rm erg\,s^{-1}}. \tag{54}$$

The fact that observation gives $L \propto T^{-4}$ (cf Eq. 51) means that the factor l^2/pbr^2 in this equation must be a constant. Since $r \simeq (15/2)\dot m$ (Eq. 30), consistency with Eq. (51) requires

$$b \simeq \frac{73}{\dot m^2}, \tag{55}$$

where we have assumed that the slowly–varying factors $l \sim p \sim 1$. (Tight beaming means that we observe the source along the disc axis, so we view the central disc plane orthogonally, making $p \simeq 1$.)

The physical origin of the simple form (55) is straightforward. The beaming factor is the total solid angle of the two open cones around the disc axis, i.e

$$b = (1 - \cos\theta) \tag{56}$$

where θ is the opening half–angle. Near the spherization radius, where the wind outflow is maximal (see Section 3.3), the flow geometry scales with $\dot m$. But all flows, regardless of $\dot m$, reduce locally to the same Eddington inflow near the accretor, so we expect $\theta \sim$ constant $\times\, \dot m^{-1}$. For sufficiently large $\dot m$ we have $\theta \ll 1$ and so $b \sim \theta^2/2 \propto \dot m^{-2}$.

We see that the simple form (55) formally applies only for $\dot m \gtrsim 8$, since, at such rates, $b < 1$. Evidently it is legitimate to adopt a form of b interpolating smoothly between $b = 1$ for $\dot m = 0$, and the form (55) for $\dot m \gtrsim \sqrt{73} \simeq 8$. For example, Hameury and Lasota (2020) use

$$b \simeq \frac{73}{73 + \dot m^2}. \tag{57}$$

[7] Indeed one does find $L \propto T^4$ for sources which are permanently *below* 3×10^{39} erg s^{-1} (Kajava and Poutanen 2009). It is likely that these sources are black holes with masses large enough that their luminosities are sub–Eddington.

Importantly, although we have derived this relation by considering only the soft X–ray emission of ULXs, the fact that it is purely geometrical and involves only electron scattering means that it must apply to all forms of radiation from ULXs.

The true emission from the central accretion disc is $L \sim L_{\rm Edd}(1 + \ln \dot{m})$, so the apparent luminosity is

$$L_{\rm sph} = \frac{L_{\rm Edd}}{b} \sim M\dot{m}^2 \sim \frac{\dot{M}^2}{M}, \tag{58}$$

where $\dot{M}$ is the mass supply rate, since $\dot{m} = \dot{M}/\dot{M}_{\rm Edd} \propto \dot{M}/M^2$. So for a given mass supply rate, accretors of lower mass have *higher* apparent luminosities, as they are more super–Eddington, and the consequent increase in beaming outweighs the lower Eddington luminosity. This means that neutron stars are favoured as ULXs over black hole accretors in binaries where the mass transfer rate is insensitive to the accretor mass. This condition holds for mass transfer driven by the evolutionary expansion of the donor star, (see Sections 3.11 and 3.13), and also for cases where the increased mass transfer is a transient effect caused by a disc instability, e.g. in Be–X–ray binaries, and in soft X–ray transients, where the disc is subject to the thermal–viscous instability (cf Hameury and Lasota 2020).

The beaming formula (55) gives a simple explanation of the observed soft X–ray correlation (51). We can easily see that other explanations are problematic.

If we assume there is no beaming, i.e. $b = 1$, then (54) requires

$$r = 62\left(\frac{l}{p^{1/2}}\right). \tag{59}$$

The true accretion luminosity is $L = l\,L_{\rm Edd}$, and so (54) would require an accreting mass

$$M_{\rm accretor} = \frac{500\,{\rm M}_\odot}{T^4_{0.1\,{\rm keV}}}\left(\frac{1}{l}\right) \tag{60}$$

for each object.

Without beaming, the typical size, r, of the soft X–ray emitting region cannot self–consistently be much larger than $O(1)$ for an accretion disc spectrum. Then since $p \sim 1$, (59) requires $l \sim 1/62$, we find $M_{\rm accretor} \gtrsim 3\times10^4\,{\rm M}_\odot$ from (60), i.e. a significantly massive IMBH.

A magnetar model would require a neutron star mass, so (60) requires $l \gtrsim 350$. But then from (59) there must be an implausibly large soft X–ray region $r \sim 1.6\times10^4$, which is ~ 500 neutron star radii[8]. In addition, the implied luminosity is $L \sim 5\times10^{40}\ {\rm erg\,s^{-1}}$, beyond the domain of validity for magnetar models for ULXs (Canuto et al., 1971).

In the context of the model described above, the observed correlation (51) provides strong evidence in favour of accretion–disc wind beaming (and indeed, yields sensible results: King and Lasota 2020). We also note that the innermost (hottest) regions will naturally be the most collimated and therefore beamed, whilst one would expect radiation produced from around $r_{\rm sph}$ to be more isotropic. The final luminosity we observe may therefore be a somewhat complicated function and will naturally be inclination dependent. However, regardless of the final functional form of the beaming, it is inevitable that where the wind is optically thick and subtends a large scale-height (as seen in every MHD simulation of super-critical accretion), collimation and beaming must result.

3.7. Models of pulsing ULXs (PULXs)

The discovery (beginning in 2014) of a small group of ULXs showing coherent pulsing has had a significant effect on the study of ULXs in general. First, it subjected existing models of ULXs to a stringent new test, as the mass of the accretor must be close to $1.4\,{\rm M}_\odot$. As remarked above, it removed the main motivation for the IMBH model, and we will see in Section 3.7.1 below, that it fitted naturally and self–consistently into the the disc–wind beaming picture, even though this was not developed with PULXs in mind.

But the removal of one candidate model (IMBH) did not simplify the discussion, as the discovery of PULXs naturally stimulated suggestions that magnetic effects on the accretion flow might be significant.

[8]We will see in Section (3.14) that a large photosphere is possible in ULXs producing strong outflows, i.e. if a strong accretion–disc wind produces beaming.

3.7.1. The KLK17 model of PULXs

The discovery of PULXs has shown that ULX apparent luminosities can be highly super-Eddington. The luminosities of the classic (non Be-X) PULXs range from ∼ 20 to ∼ 385 times the Eddington value for a neutron star (see Table 2). For normal (pulsar-like) magnetic fields $\sim 10^{11} - 10^{13}$G, such values exclude the possibility that they correspond to the actual luminosities since this would require implausibly high accretion rates (see Eqs. 36 and 45). We will show in Sect 3.9 that the hypothesis that PULXs contain magnetars is extremely unlikely. Then the only physically reasonable option left is that the luminosity of magnetic ULXs is beamed according to Eq.(58). Given this, King and Lasota (2016) proposed a beamed-emission model for the first detected PULX, M82 ULX-2. This model was successfully used by King et al. (2017) (hereafter KLK17) to explain the properties of the three first–discovered PULXs, and later King and Lasota (2019) applied this model to the growing number of observed PULXs, including the Be-PULXs. King and Lasota (2020) explained how one obtains significant pulsed X-ray luminosity fraction in beamed radiation (see Section 3.7.5). It is assumed throughout that for neutron star magnetic fields of the standard X-ray binary strength (i.e. $B \lesssim 10^{13}$ G) the surface emission is locally isotropic.

Kluźniak and Lasota (2015) noted that PULXs are sharply distinct from other X–ray pulsars, not simply in their luminosities (by definition $L > 10^{39}\mathrm{erg\,s^{-1}}$) but also in their very large spinup rates ($\dot{\nu} > 10^{-10}\mathrm{s^{-2}}$ – up to two orders of magnitude larger than normal XRPs). Between superoutbursts, transient Be-PULXs are normal *spinning-down* X-ray pulsars, but when their luminosity reaches $\sim 10^{39}$ erg s^{-1} they become rapidly *spinning-up* sources with $\dot{\nu} \gtrsim 10^{-10}\mathrm{s^{-2}}$ (see Table 2), demonstrating that such high spin-up rates are a generic property of PULXs[9].

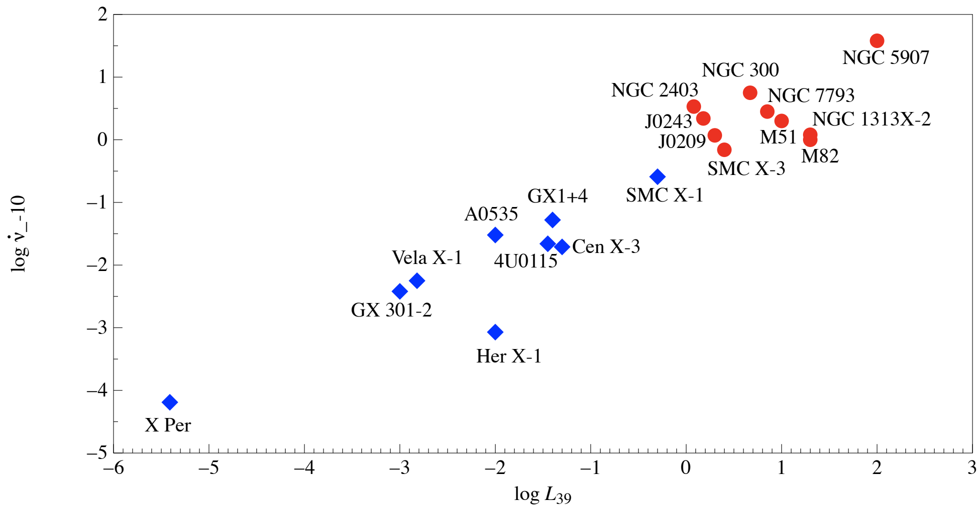


Figure 13 The $L_{39} - \dot{\nu}_{-10}$ diagram for XRPs and PULXs. Red dots: the ten PULXs with known spin-up rates (values from KLK17). Blue diamonds: selected (for comparison) X-ray pulsars (see Table Appendix A - in the Appendix)

The luminosities and spin-up rates of PULXs are tightly correlated (Fig. 13). This correlation strongly implies that the dominating torque in the system is provided by accretion, as assumed in KLK17 and Vasilopoulos et al. (2018), since

$$\dot{\nu} = \frac{\dot{J}(R_M)}{2\pi I} = \frac{\dot{M}(GMR_M)^{1/2}}{2\pi I} \propto \dot{M}^{6/7} \tag{61}$$

where $R_{\rm M} \propto \dot{M}^{-2/7}$ (e.g. Frank et al., 2002) is the magnetospheric radius and I the neutron star's moment of inertia.

If we define PULXs by the twin properties of luminosities larger than 10^{39} erg s^{-1} *and* spin-up rates larger than $\sim 10^{-10}\mathrm{s^{-2}}$, these two quantities should form the basis for models of these sources. At the very least, any cogent

[9]One might insist that it is a coincidence that Be-X systems show the same spin-up as other PULXs when they reach the same luminosities, but here one rather expects that “coincidences mean you’re on the right path”(Van Booy, 2009).

model must be able to reproduce these values. KLK17 chose the first option, using the observed quantities L_X, $\dot{\nu}$ as input for their PULX model. Although there are no direct mass measurements for neutron stars in PULXs, the likely mass range is limited. KLK17 make no assumptions about the magnetic field strengths, and these are outputs of the model. The resulting values lie in the typical range for standard pulsing X–ray binaries (see Table 3), and compare favourably with the dipole magnetic field strengths measured from CRSFs (one of them for a non-pulsing neutron star ULX - see also section 2.2.3).

For the mass inflow, KLK17 use the super–critical ('windy') solution of Shakura and Sunyaev (1973) described in Section 3.3. In this picture, the super–Eddington part of the mass supply below $R_{\rm sph}$ is eventually expelled as a wind. This simultaneously provides the beaming, making PULXs appear super–Eddington and explains the strong outflows observed from PULXs. The neutron star gains mass only at its effective Eddington rate (Eq. 36).

The spherization radius defined in Eq. (30) can be written as

$$R_{\rm sph} \simeq 2.3 \times 10^6 \dot{m}_0 m_1 \ {\rm cm}, \tag{62}$$

where $\dot{M}_0 = \dot{m}_0 \dot{M}_{\rm Edd}$ is the accretion rate at $R_{\rm sph}$, assumed equal to the mass transfer rate. For $R > R_{\rm sph}$ the disc is assumed to be a standard SS73 accretion disc. From Eq. (63) we have

$$\dot{M}(R) \simeq \dot{m}_0 \dot{M}_{\rm Edd} \frac{R}{R_{\rm sph}}. \tag{63}$$

for $R < R_{\rm sph}$.

KLK17 assume that the Shakura and Sunyaev (1973) 'windy' model describes the accretion flow between $R_{\rm sph}$ and the magnetospheric radius $R_{\rm M}$ defined by the equation (Frank et al., 2002)

$$R_{\rm M} = 1.2 \times 10^8 q \, \dot{m}^{-2/7} m_1^{-3/7} \mu_{30}^{4/7} \ {\rm cm}, \tag{64}$$

where $q \sim 1$ is a factor taking into account the geometry of the accretion flow at the magnetosphere. Then from Eq. (63)

$$\dot{M}(R_{\rm M}) \simeq \dot{M}_0 \frac{R_{\rm M}}{R_{\rm sph}}. \tag{65}$$

Applying the model to PULXs with measured spin-up gives $R_{\rm M} < R_{\rm sph}$ in all cases. This implies that in these objects the accretion flow inside the magnetosphere is highly super–Eddington. Since it is hypersonic but forced to follow the magnetic fieldlines it is highly dissipative, and one expects it to generate an outflow similar to that of Shakura and Sunyaev (1973), limiting the local luminosity to its Eddington value.

The total luminosity is then given by Eq. (36)

$$L \simeq L_{\rm Edd} \left[1 + \ln \dot{m}_0\right]. \tag{66}$$

The luminosity from both parts of the super–Eddington outflow is assumed to be beamed. Outside the magnetosphere the beaming factor is taken to be

$$b \simeq \frac{73}{\dot{m}^2}, \tag{67}$$

as in Eq. (55).

For accretion rates such that radiation is geometrically beamed as described by Eqs. (66) and (67), one can deduce $\dot{m}_0$ from the observed X-ray luminosity $L = L_X$ by combining these two equations into

$$L_X \simeq 2.0 \times 10^{36} \dot{m}_0^2 \left[1 + \ln \dot{m}_0\right] m_1 \ {\rm erg\,s^{-1}}. \tag{68}$$

Having $\dot{m}_0$ one obtains $R_{\rm sph}$ from Eq. (62).

The second observed quantity, the spinup, follows from Eqs. 61 and 64 as

$$\dot{\nu} = 3.3 \times 10^{-11} q^{1/2} \dot{m}^{6/7} m_1^{6/7} \mu_{30}^{2/7} I_{45}^{-1} \, {\rm s}^{-2}. \tag{69}$$

Table 3 KLK17 model: derived properties of neutron star ULXs.

Name	$\dot{m}_0$	b	$\boldsymbol{B}\, q^{7/4} m_1^{-1/2} I_{45}^{-3/2} R_6^3$ [G]	$\boldsymbol{R}_{\rm sph} m_1^{-1}$ [cm]	$\boldsymbol{R}_M m_1^{-1/3} I_{45}^{-2/3}$ [cm]	$\boldsymbol{P}_{\rm eq} q^{-7/6} m_1^{1/3}$ [s]	$\boldsymbol{t}_{\rm eq}$ [yr][1]
M82 ULX2	46	0.03	4.0×10^{10}	1.1×10^{8}	1.0×10^{7}	0.02	15600
NGC 7793 P13	25	0.12	1.1×10^{11}	5.8×10^{7}	1.6×10^{7}	0.09	1386
NGC5907 ULX1	95	0.01	9.4×10^{12}	2.2×10^{8}	1.1×10^{8}	1.86	0
NGC300 ULX1	24	0.13	$5.3 \times 10^{11\heartsuit}$	5.5×10^{7}	3.2×10^{7}	0.19	297
M51 ULX7[a]	28	0.09	1.9×10^{11}	6.4×10^{7}	2.0×10^{7}	0.08	1337
M51 ULX7[b]	28	0.09	6.9×10^{9}	6.4×10^{7}	4.6×10^{6}	0.01	$\sim 10^5$
NGC 1313 X-2	46	0.03	5.3×10^{10}	1.1×10^{8}	1.8×10^{6}	0.03	8641
SMC X-3[Be]	18	0.23	2.3×10^{10}	4.1×10^{7}	7.1×10^{6}	0.006	76621
NGC 2403 ULX[Be]	13	0.43	2.5×10^{11}	3.0×10^{7}	2.3×10^{7}	0.16	578
Swift J0243.6+6124[Be]	14	0.37	1.3×10^{11}	3.2×10^{7}	1.7×10^{7}	0.07	2047
RXJ0209.6-7427[Be]	17	0.25	5.3×10^{10}	3.2×10^{7}	1.8×10^{6}	0.03	8665
NGC 1313 ULX[Be;c]	15	0.32	?	3.5×10^{7}	?	?	?
M51 ULX8	17	0.25	$\sim 3 \times 10^{11\clubsuit}$	3.2×10^{7}	$2.7 \times 10^{7\spadesuit}$	non-pulsing	

– Systems with [Be] superscript have Be–star companions.
[1] - calculated using the value of $P_{\rm eq} q^{-7/6} m_1^{1/3}$ from the previous column.
$^\heartsuit$– consistent with observations Walton et al. (2018c).
$^\clubsuit$– from observations (Brightman et al., 2018; Middleton et al., 2021b).
$^\spadesuit$ – for a $\sim 10^{12}$ G magnetic field.
[a] – for $\dot{\nu} = 2.8 \times 10^{-10}$; [b] – for $\dot{\nu} = 3.1 \times 10^{-11}$ (Vasilopoulos et al., 2019).
[c] – unknown $\dot{\nu}$.

This gives the values of the magnetic moment $\mu = BR^3$ (where B is the field and R the neutron–star radius) which in turn allows one to calculate the values of R_M and $\dot{m}(R_M)$ from Eqs (64) and (65):

$$\mu_{30} = 0.04\, q^{-7/4} \dot{\nu}_{-10}^{3/2} m_1^{1/2} I_{45}^{3/2}\, \mathrm{G\,cm^3} \tag{70}$$

$$R_{\rm M} = 1.0 \times 10^{7} \dot{\nu}_{-10}^{2/3} m_1^{1/3} I_{45}^{2/3}\, \mathrm{cm} \tag{71}$$

$$\dot{m}(R_{\rm M}) = 9.9\, \dot{\nu}_{-10}^{2/3} m_1^{-2/3} I_{45}^{2/3}, \tag{72}$$

where $10^{-10}\dot{\nu}_{-10} = \dot{\nu}$.

The results are presented in Table 3, with the values of the equilibrium period $P_{\rm eq} = 0.23 q^{7/6} m_1^{-1/3} \mu_{30}^{2/3}$ s, and the lower limit on the time to reach equilibrium at the present spin-up rate

$$t_{\rm eq} \equiv \frac{1}{\dot{\nu}} \left(\frac{1}{P_{\rm eq}} - \frac{1}{P} \right). \tag{73}$$

(The corotation radius $R_{\rm co} \equiv \left(GMP_s^2/4\pi^2 \right)^{1/3}$ is always larger than the magnetospheric and spherization radii. Thus only possibly NGC 5907 ULX1 is close to its equilibrium spin, and none of the observed PULXs is a propeller.)

For NGC300 ULX-1, the KLK17 model predicts a neutron–star magnetic field of $B > 5 \times 10^{12}$G (since $q < 1$ and $m_1 > 1$, the entries provided in the 4th column of Table 3 are a factor of few lower than the predicted magnetic field values). A magnetic field of very similar strength is deduced by Walton et al. (2018a) from the CRSF inferred to be present in the X-ray spectrum of this PULX. According to the KLK17 model, all seven PULXs have magnetic fields in the range $10^{11} - 10^{13}$G, i.e. always in the standard pulsing X–ray binary range and below the value defining magnetars.

The predicted values of the beaming factor b are in the range $\sim 0.03 - 0.5$, except for the very luminous source in NGC 5709, for which $b \approx 0.01$. For NGC 300 ULX-1, the model gives $b \approx 0.13$: Binder et al. (2018) use the KLK17 model and obtain $b \approx 0.25$, because they deduce $\dot{m}_0$ from the average rather than the maximum luminosity. The beaming factor $b \approx 0.12$ for P13 in NGC7793 is consistent with observations of the X-ray irradiation of the

neutron-star companion (Motch, 2018). According to the KLK17 model, the luminosity of most of the known PULXs is only mildly beamed. This is worth stressing since critics of the KLK17 model often claim that there are problems with 'strong beaming'.

We see that for all seven PULXs with known spin-up rates $\dot{\nu}$, one has $R_{\rm M} \lesssim R_{\rm sph}$, which is probably the condition for observing pulses at all if the mass transfer is super–Eddington. The small difference between $R_{\rm sph}$ and $R_{\rm M}$ means that the flow is strongly super–Eddington on reaching $R_{\rm M}$. Most of this cannot land on the neutron star (let alone its polecaps only) and so must be ejected.

It is worth stressing that nothing in the assumptions of the model guarantees its self–consistency, i.e. that $R_{\rm sph} > R_{\rm M}$. But in every case this is satisfied by the deduced values. Further, exactly the same equations describe both the Be–star magnetic accretors and those PULXs which do not have Be–star companions: the first group cannot of course be modelled at all by assuming very strong dipole magnetic fields.

The spin-up time-scales $t_{\rm eq}$ are probably much shorter than the lifetimes of the individual PULXs (see Table for NGC 1313 X-2) so it seems very unlikely that we observe these systems during their only approach to spin equilibrium. Instead, although most of them are probably rather far from their $P_{\rm eq}$ they have nevertheless the time to alternate spin-up and spin-down phases. Evidently, we can only see these systems during spin-up phases (so that $\dot{\nu}$ has its maximum value) because centrifugal repulsion during spin-down presumably reduces the accretion rate and so the luminosity. In addition the magnetic fields of the PULXs appear to be significantly lower than is usual for a new-born neutron star ($10^{12} - 10^{13}$G) which is consistent with hypothesis that accretion of even a relatively small mass severely reduces the surface fields of neutron stars – this is central to the concept of pulsar recycling, which is implicated in the production of millisecond pulsars (see Bhattacharya and van den Heuvel, 1991, and references therein). Things are even more complicated by the fact that the vast majority of ULXs do not pulse, despite containing (magnetized) neutron stars, which suggests that alignment of spin and central disc axes is rapidly suppressing (perhaps temporarily?) the pulsations, which are observed to be transient anyway. As expected from the KLK17 model, Be-star systems are prominent among the PULXs, since accretion is relatively weak and transient.

Parametrizing $R_{\rm M} = fR_{\rm sph}$, with $f \approx 0.3 - 0.9$, then from Eq. (65), $\dot{m}(R_{\rm M}) = f\dot{m}_0$ (KLK17) and from Eqs (69) and (72) we find

$$\dot{\nu} = 7.8 \times 10^{-10} f^{7/6} q^{7/6} \mu_{30}^{2/3} m_1^{-1/7} I_{45}^{-1}, \tag{74}$$

in agreement with the observed spin-up values of PULXs (cf Fig 13).

It has been claimed (e.g. Mushtukov et al., 2020) that the KLK17 picture suffers from fundamental weaknesses since 'strong beaming' would be incompatible with the high observed pulsed fraction of the ULX radiation. As we noted (two paragraphs above), the beaming is not 'strong'. Further, in Sect. (3.7.5) using the results of King and Lasota (2020), we will show that the KLK17 model is fully compatible with the observed X–ray pulse fraction (which varies in time and frequency), and also explains the very small number of observed PULX.

3.7.2. The Gúrpide et al. PULX models

Gúrpide et al. (2021) suggest an alternative scenario in which the hardest ULXs are powered by strongly magnetised neutron stars, so that the high-energy emission is dominated by the hard direct emission from the accretion column. It is assumed that one can explain softer sources as weakly magnetised neutron stars or black holes, in which the presence of outflows naturally explains their softer spectra through Compton down-scattering and their spectral transitions. Outflows are also invoked to explain the dilution of the pulsed emission in sources containing neutron stars. According to these authors NGC 7793 P13 and NGC 1313 X-2 would be strongly magnetized with $R_M > R_{\rm sph}$ in contradiction with the prediction of the KLK17 model. However, they find that NGC 5907 ULX-1 appears harder when dimmer. This is difficult to reconcile with their scenario and they have to conclude that for this source $R_M \approx R_{\rm sph}$, in agreement with the KLK17 model prediction. However, Gúrpide et al. (2021) do not take into account the possibility that the flow geometry is as described in Sect. 3.7.4. In this case, under appropriate conditions one sees the "magnetic column" directly when $R_M > R_{\rm sph}$. In any case, one would expect that the flux–hardness relation would also depend on the intrinsic properties of the emitter and not on the source geometry only. The model geometry of King and Lasota (2020) is used by Pintore et al. (2021) with additional ingredients to interpret the spectral variation during the flares of NGC 4559 X7.

Although M51 ULX-8 is not a PULX, we know that it is a magnetic system. Assuming that its X-ray radiation is beamed, one can obtain its $\dot{m}_0$ and so both $R_{\rm M}$ and $R_{\rm sph}$. As in PULXs this gives $R_{\rm M} \lesssim R_{\rm sph}$ (see Table 3). King and

Lasota (2019) (see also Sect. 3.7.5) speculate that M51 ULX-8 might be a PULX, and suggest that pulsations may be seen in future observations of this system. Brightman et al. (2018) point out that rather long XMM-Newton observations would be needed to detect $\sim$ 1s pulsations if the pulsed fraction is $\lesssim 45\%$, as in most PULXs. (Interestingly the exception is NGC 300 ULX1, in which Walton et al., 2018a, inferred the presence of a cyclotron feature).

Although simple, the KLK17 model correctly reproduces the main observed properties of PULXs and has passed this test with each newly discovered PULX, in particular with the Be-PULX systems (see Table 3). In the KLK17 picture, PULXs are "normal" (non-magnetar) X-ray pulsars caught in a high accretion–rate episode of their binary evolution (non–Be systems: see Sections 3.11, 3.12) or orbital history (Be systems: see Section 3.15).

3.7.3. The Erkut et al. (2020) PULX models

Erkut et al. (2020) (hereafter ETEA20) base their models of PULX on the well–known approach to the disc–magnetosphere interaction best known from the paper of Ghosh and Lamb (1979). They assume that the luminosity in the magnetosphere is at most critical, using, as the relation between the observed X-ray luminosity and the accretion rate:

$$L_X = \frac{\eta}{b}\dot{M}_\star c^2, \tag{75}$$

where $\dot{M}_\star$ is the accretion rate at the neutron-star surface and b is a beaming factor, and assumes $\dot{M}_\star = \dot{M}_{\rm in}$, where $\dot{M}_{\rm in}$ is the accretion rate at the innermost disc radius $R_{\rm in}$. (This is separated from the magnetosphere by a boundary region of width $\Delta R \equiv \delta R \cdot b$.)

In other words

$$L_{\rm X} \leqslant L_{\rm c} \simeq \left[1 + 311\left(\frac{B}{B_{\rm c}}\right)^{4/3}\right] L_{\rm E}, \tag{76}$$

where $B_{\rm c} \equiv m_{\rm e}^2 c^3/\hbar e = 4.4 \times 10^{13}$G (see Eq. 94).

The beaming considered by ETEA20 is assumed *magnetic* (i.e. not due to an outflow in origin, with beaming factor

$$b_{\rm M} = \frac{A_{\rm c}}{\gamma A}, \tag{77}$$

where $A_{\rm c}$ is the polar cap area, $A = 4\pi R_\star^2$ is the total surface area of the neutron star, and $\gamma < 1$ "is a normalization constant corresponding to the maximum fractional area of the polar cap" (Erkut et al., 2020). Since they are physically different, and act in different parts of the accretion flow in PULXs, direct comparison of the values of ETEA20's $b_{\rm M}$ with those of KLK17's outflow–generated b is not of much interest.

The accretion flow between $R_{\rm in}$ and $R_{\rm sph}$ (defined as in Eq. (30), with a factor with 27/2, instead of 15) is allowed to be super–Eddington and is assumed to be described by the 'windy' Shakura and Sunyaev (1973) solution (Eq. 63).

The inner radius of the disk is determined by the balance between magnetic and material stresses

$$\frac{d}{dR}\left(\dot{M}R^2\Omega\right) = -R^2 B_\phi^+ B_z, \tag{78}$$

where Ω is the angular velocity of the innermost disc matter within the boundary region, B_z is the poloidal magnetic field, $B_\phi^+ = \gamma_\phi B_z$ is the toroidal magnetic field at the surface of the disc, and γ_ϕ is the azimuthal pitch that can be expressed as $\gamma_\phi \simeq \omega_\star - 1$, where $\omega_\star$ is the so-called "fastness parameter"

$$\omega_* \equiv \frac{\Omega_*}{\Omega_{\rm K}\left(R_{\rm in}\right)} = \left(\frac{R_{\rm in}}{R_{\rm co}}\right)^{3/2}. \tag{79}$$

At spin equilibrium, the fastness parameter is assumed to be equal to a (model-dependent) critical value $\omega_\star = \omega_c$. ETEA20 use $\omega_c = 0.75$.

Integrating Eq. (78), using Eq.(75) and defining poloidal field $B_z \simeq -\mu/R^3$ one obtains an expression for the inner disc radius

$$R_{\rm in} = \left(\frac{\mu^2\sqrt{GM_\star}\delta}{b_{\rm M} R_\star L_X}\right)^{2/7}. \tag{80}$$

Since one can write for a strong enough magnetic field

$$\frac{A_c}{A} \simeq \frac{R_\star}{4R_{\rm in}} \cos^2 \alpha, \tag{81}$$

where α is the angle between the rotation and magnetic axes (Frank et al., 2002, the star's spin and the disc rotation axes are assumed to be aligned), one gets $b = \left(\cos^2 \alpha/4\gamma\right) R_\star/R_{\rm in}$.

Using $\mu = B_z R_\star^3$ one can then write

$$b_{\rm M} = \left(\frac{\cos^7 \alpha L_X}{32\gamma^{7/2} \sqrt{GM_\star} B^2 R_\star^{3/2} \delta}\right)^{2/5}, \tag{82}$$

for the beaming factor and express the fastness parameter as

$$\omega_\star = \left(\frac{\gamma \sqrt{GM_\star} B^2 R_\star^4 \delta}{\cos^2 \alpha L_X}\right)^{3/5} \frac{2\pi}{P \sqrt{GM_\star}}, \tag{83}$$

where $P = 2\pi/\Omega_\star$. In addition to observed quantities, L_X (ETEA20 use the observed flux F_X, but since, with one exception, PULXs are extragalactic, this precaution does not seem to be necessary), and P, Eqs/ 82 and 83 contain unobservable (at least in PULXs) quantities α and γ. They can be eliminated by the use of the torque equation that ETEA20 write under the form

$$2\pi I \dot{\nu} = \omega_\star^{1/3} n_0 \sqrt{GM_\star R_{\rm co}} \dot{M}_\star, \tag{84}$$

where n_0 is a constant of order unity corresponding to a dimensionless torque. Given the neutron–star mass (ETEA20 try $M_\star = 2\,{\rm M}_\odot$ for M51 ULX-7), moment of inertia and radius, one then obtains two equations for the four quantities defining the physics of the system: B, $b_{\rm M}$, $\omega_\star$ and δ as a function of the observables L_X, P and $\dot{P}$ (or $\dot{\nu}$):

$$B = \frac{\omega_\star}{R_\star^3} \sqrt{\frac{2GM_\star I|\dot{P}|}{\pi n_0 \delta}}, \tag{85}$$

and

$$\omega_\star = 16\pi^4 GM_\star \left(\frac{I|\dot{P}|}{n_0 L_X P^{7/3} R_* b_{\rm M}}\right)^3. \tag{86}$$

These two equations allow us only for delimiting the range of magnetic-field strength and fastness-parameter values compatible with observation. The boundary region parameter is assumed to lie in the range $0.01 \leq \delta \leq 0.3$. The determined range of physical parameters can be made narrow by assuming that $L_X = L_c$, or $L_X < L_c$ and the fastness parameter can be set equal to the equilibrium value $\omega_\star = \omega_c = 0.75$.

In their paper, ETEA20 consider several alternative scenarios: (i) the PULXs are away from spin equilibrium; an efficient standard spin-up torque is used to account for the observed spin-up rates, (ii) the PULXs are so close to spin equilibrium that the fastness parameter is given by its critical value, (iii) the X-ray luminosities of the PULXs can be well represented by the maximum critical luminosity, (iv) the conditions described in (i) and (iii) both apply, (v) the conditions described in (ii) and (iii) both apply, and (vi) the X-ray luminosities of the PULXs are subcritical and either the condition described in (i) or the condition described in (ii) applies. They found that the narrowest ranges for B, $b_{\rm M}$, and $\omega_\star$ are found when they use the critical luminosity condition along with either the observed spin-up rates or the spin-equilibrium condition. Scenario (iv), based on the observed spin-up rates at critical luminosity, is the only one that works well for all the PULXs, implying B in the $10^{11} - 10^{13}$ G range. The results for scenario (iv) are presented in Table 4 (Table 5 in Erkut et al., 2020). The ETEA20 models do not allow for a prediction of the pulsed fraction of the emitted radiation, nor the pulse shapes, and the authors refer to the "accretion curtain" of Mushtukov et al. (2017) as a possible source of the pulsed luminosity.

The conclusions of the Erkut et al. (2020) paper: PULXs have sub–critical magnetic fields and their luminosity is subject to medium beaming are the same as those obtained by King and Lasota (2016); King et al. (2017); King and Lasota (2019, 2020) but they differ in their physical motivations. First, the beaming mechanisms are different in the two approaches to the problem. Second, while ETEA20 require the accretion flow to be always at most critical and assume that the accretion rate is constant inside the magnetosphere, KLK17 allow the accretion flow to be super-Eddington and losing mass also when following the magnetic field-lines. It is perhaps worth noting that these two very different models both exclude magnetar–strength fields.

Table 4 ETEA20 models of PULXs [scenario (iv)]

Source	$L_X\left(\mathrm{erg\,s^{-1}}\right)$	$\dot{\nu}\left(\mathrm{s^{-2}}\right)$	b_{M}	ω_*	$B\,(\mathrm{G})$
M82 X-2	6.5×10^{39}	1.1×10^{-10}	0.16–0.25	0.060–0.22	2.0–2.9 $\times10^{12}$
ULX NGC 7793 P13	9.4×10^{39}	1.2×10^{-11}	0.021–0.027	0.065–0.14	1.2–3.2 $\times10^{11}$
ULX NGC 5907	1.5×10^{41}	3.9×10^{-9}	0.19–0.30	0.16–0.61	2.7–3.8 $\times10^{13}$
NGC 300 ULX1	4.3×10^{39}	5.6×10^{-10}	~1	0.015	6.8 $\times10^{12}$
M51 ULX-7	7.0×10^{39}	3.1×10^{-11}	0.052–0.0	0.019–0.063	6.2–10 $\times10^{12}$
Swift J0243.6+6124	1.7×10^{39}	2.4×10^{-10}	~1	0.041	3.5$\times10^{12}$

Note. In this scenario the magnetic field, beaming fraction, and fastness parameter for Swift J0243.6+6124 are only marginally obtained at $b_{\mathrm{M}}\sim1$ for $M_\star=1.2\,\mathrm{M_\odot}$ and $R_\star=10$ km, and no common solution is found for NGC 1313 X-2 (even a mass as low as $0.9\,\mathrm{M_\odot}$ does not help). For all other sources $M_\star=1.4\,\mathrm{M_\odot}$ and $R_\star=10$ km are used.

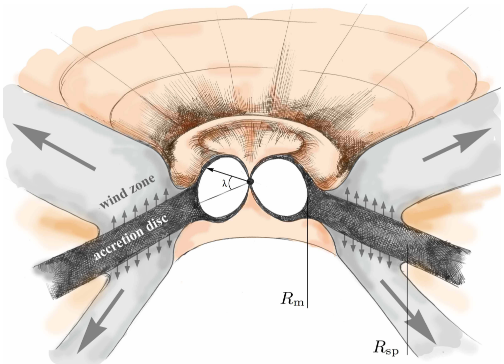


Figure 14 Schematic picture of a PULX according to Mushtukov et al. (2017, 2019). R_{m} and R_{sp} are respectively the magnetospheric and spherization radius. λ is the angle between the disc plane and the magnetic axis. Accreting matter not lost in the wind is accreted onto the central object forming an envelope which is optically thick at accretion rates typical of PULXs. In the KLK17 model, the configuration is similar, but $R_{\mathrm{m}}\lesssim R_{\mathrm{sp}}$ and the wind does not end up at the magnetospheric radius. (see Fig. 15). Note that the Figure of Mushtukov et al., (2017, 2019) shown here assumes that the neutron star spin is aligned with the disc axis, although this is not explicitly stated. We argue in subsection 3.7.4 that this assumption is in general not justified. In addition the configuration shown appears to be axisymmetric, i.e. has the magnetic axis parallel to the spin (and disc) axes. This would of course preclude pulsing, so there must in reality be some deviation from axisymmetry.

3.7.4. The origin of "sinusoidal" pulses in PULXs

X–ray pulse light curves for PULXs are generally described as being 'sinusoidal', i.e. without obvious eclipses, and continuously modulated (see Sect. 2.3.2). In other words, the X-ray light curves of PULXs are never flat and never zero.

Mushtukov et al. (2017, 2019) argued that this was understandable if, perhaps because of the large optical depth, the photospheric surface emitting the X-rays occupied a large fraction of the magnetosphere. Then this region would neither be permanently in view, nor periodically occulted. Accordingly, Mushtukov et al. (2017, 2019) proposed that the X–rays are emitted by an optically thick envelope defined by the accretion flow over the neutron–star magnetosphere. This is consistent with the accretion along fieldlines being a bending hypersonic flow, which must therefore shock as suggested by King and Lasota (2019) (see also Sect.3.7.1). The spin modulation occurs because the magnetic axis is inclined to the spin axis.

Mushtukov et al. (2017, 2019) do not attempt to reproduce the observed PULX lightcurves and do not explain why magnetized systems such as ULX-8 in M51 do not pulse. The simplest explanation would be that the spin and

magnetic axes are aligned, but then one would have to explain why the few pulsing systems are different in this respect from the probable majority of NULXs.

3.7.5. Beamed pulsed X-ray radiation

An argument often made against the beaming model of PULXs is the belief that the observed high ($\lesssim 45\%$) pulsed fraction of the X-ray emission cannot appear in radiation passing through a funnel because reflections from the funnel walls would destroy the signal coherence.

We note first that although many (if not most) ULXs probably contain magnetised neutron stars, only a small fraction show pulses. Second, King and Lasota (2020) point out that the argument above assumes (without any explicit statement) that the spin axis of the neutron star is aligned with the accretion disc axis, and so with the beam axis[10]. In fact observations of high–mass X–ray binaries show that the neutron star spin is generally not aligned with the disc axis, probably because of the asymmetric nature of the supernova giving birth to the neutron star.
The beamed emission will appear sinusoidal, (i.e. the light curve has no constant intervals) if three conditions hold simultaneously:
(a) there is significant misalignment of spin and beam (disc) axes (cf Figure 15), and
(b) the emitting region is not essentially symmetrical around the spin axis, and
(c) its linear scale is comparable to the neutron star radius, so that a significant fraction of its area, but not the whole of it, is occluded by this star as it spins

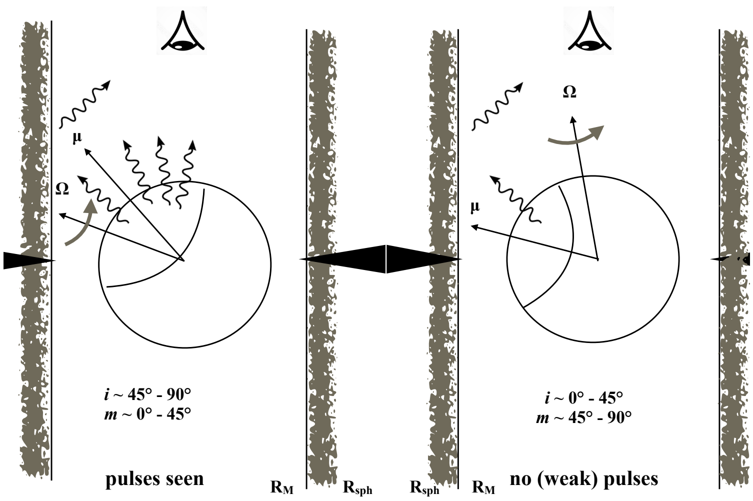


Figure 15 Effect of spin orientation on pulsing. Left: the neutron–star spin and the accretion disc beaming axes are strongly misaligned, so that a significant part of the pulsed emission is periodically occulted by the neutron–star body at certain spin phases. This gives a large pulse fraction. Right: the neutron–star spin and central disc axes are assumed to be substantially aligned (this special condition is assumed without any explicit statement in papers asserting that beaming cannot produce pulsed emission). Much of the primary X–ray emission is scattered by the walls of the beaming 'funnel' before escaping. In this kind of configuration the pulse fraction is reduced or suppressed. (King and Lasota, 2020).

[10]This unstated assumption has a similar status to the implicit belief that ULX nebulae must be Strömgren spheres powered by the direct radiation of the ULX, rather than wind bubbles made by its powerful near–spherical wind – see Sections 2.6.1 and 3.14. In both cases the effect is to 'rule out' beaming.

Two processes can align the spin and disc (beam) axes. One is warping of the central disc into the neutron–star spin plane through differential torques (both magnetic and precessional), and the other is direct accretion of angular momentum (characterized by R_M) from an unwarped disc lying in the binary orbital plane. The latter seems more likely, as any interruption in the accretion flow means that disc warping has to 'start again'. Neither process will be be very efficient in the Be–star PULXs, where accretion rate is less than $\lesssim 10\dot{M}_{\rm Edd}$ and confined to short transient episodes.

The outcomes of the two spin orientations are very different.

- If there is strong misalignment of the spin and beaming axes, a significant part of the pulsed emission can escape without scattering, giving a large pulse fraction (Fig. 15, left). This must be maximal at the highest X–ray energies, as scattering makes the X–rays both softer and less pulsed. This correlation of pulse fraction and X–ray energy is well known for observed PULXs (Kaaret et al., 2017).
- If instead there is substantial alignment of the spin and central disc axes, much of the primary X–ray emission is scattered by the walls of the beaming 'funnel' before escaping (Fig. 15, right). Since the light–travel time across the funnel is usually comparable with the pulse duration, the pulse amplitude can be severely reduced. This would result in an inability to detect many highly collimated PULXs through pulse searches (Mushtukov et al. 2019); as accumulate and improve in quality, this picture will be tested more thoroughly. The pulse fraction can of course also be reduced or entirely removed if enough matter accretes to weaken the neutron–star magnetic field. This presumably happened in the case of Cyg X–2, which is a survivor of a phase of strongly super–Eddington accretion (King and Ritter, 1999). Here the neutron star is not noticeably magnetic, and has probably gained a few tenths of $M_\odot$ during the super–Eddington phase.

These outcomes appear to be consistent with observations of ULXs. Very few ULXs show pulsing. But if most ULXs are the direct descendants of high–mass X–ray binaries (HMXBs, once the companion star fills its Roche lobe), or Be–star HMXBs, the vast (unpulsed) majority must contain neutron stars. First, almost all HMXBs contain neutron stars rather than black holes (King and Lasota, 2016; King et al., 2017). Second, neutron–star systems are more super–Eddington and more beamed than black–hole systems with the same mass transfer rate, and therefore have *higher* apparent ULX luminosities (see Section 3.6). In addition, there is at least one ULX whose spectrum shows a CRSF corresponding to a pulsar–strength magnetic field (Middleton et al., 2021b), but which does not show pulsing, strongly suggesting that is it an aligned accretor.

The vast majority of ULXs do not have detected pulses, despite containing neutron stars. Unless this is caused by a lack of data for ULX pulse searches it implies that alignment of spin and central disc axes is rapid, and possibly that field suppression through accretion occurs also. As expected in this picture, Be–star systems are prominent among the PULXs since accretion rates are relatively low and the episodes of increased luminosity are transient.

3.8. Numerical simulation of super-Eddington accretion flows

Most of the numerical simulations of super-Eddington accretion on to compact bodies concern black holes. The purely absorbing inner boundary conditions make the problem simpler than for neutron stars, which have hard surfaces and, in the most interesting case, strong and rotating magnetic fields. We first review the simulations of black–hole super-Eddington accretion.

3.8.1. Numerical simulations of black-hole accretion

Analytical or quasi-analytical solutions of super–Eddington accretion on to black holes represent two extreme possibilities: either the local emission is kept close to the Eddington value by blowing out the "excess" matter (Shakura and Sunyaev, 1973), or by advecting the "excess" energy towards the black hole, where it disappears from the Universe (Abramowicz et al., 1988). In both cases the total luminosity radiated by the accretion flow is $1 + \ln \dot{m}_0$ times the Eddington luminosity, where $\dot{m}_0$ corresponds either to a constant accretion rate (slim disc) or is equal to the rate at which matter is brought to the accretion flow, the accretion rate decreasing to keep the local flux at the Eddington value (wind/outflow solution). Although the accretion rate reaching the black hole can differ between the two cases

by several orders of magnitude, in neither case can the emitted luminosity be larger than $\sim 10\, L_{\rm Edd}$[11]. Then for a ULX with $L_X > 10\ L_{\rm Edd}$, this apparent luminosity cannot be equal to the physical luminosity, whatever the accretion flow model: the observed super-Eddington luminosity must be beamed. Both extreme models imply beaming depending on the accretion rate.

For slim discs, (Wiktorowicz et al., 2017) fitted the relative semi-height of the scattering photosphere calculated analytically and numerically by Lasota et al. (2016) by the formula:

$$\frac{H_{\rm phot}}{R} \approx \frac{1.6}{1 + \frac{4}{\dot{m}}}, \tag{87}$$

and from

$$\left(\frac{H_{\rm phot}}{R}\right)^{-1} = \tan\frac{\theta}{2}, \tag{88}$$

obtained the beaming factor

$$b = 1 - \cos\frac{\theta}{2}. \tag{89}$$

This beaming becomes nearly constant for $\dot{m} \gtrsim 100$ which gives the maximum beaming for $b \approx 0.15$. For the windy Shakura and Sunyaev (1973) model with beaming given by Eq. (55), $b = 0.15$ corresponds to $\dot{m} = 22$. One can expect that in reality the solution describing super-Eddington accretion on to a black hole may have both outflows and advection, but the relative proportions can only emerge from numerical calculations and comparison with observations. Unfortunately both these methods encounter serious difficulties.

Before we discuss numerical solutions describing super-Eddington mass supply to black holes, we should note that, without estimates of the black-hole masses in ULXs, these models remain untested, since we do not know the true Eddington luminosities. We now know that the masses of black holes descending from stellar evolution can differ by an order of magnitude (Abbott et al., 2020), so this is a real handicap. Currently there is only one upper limit on the compact-object mass in a ULX (Motch et al., 2014), and here the accretor was later found to be a neutron star (Fürst et al., 2016).

In discussing numerical simulations of super-Eddington accretion flows, we emphasize that these cannot so far represent the conditions expected in ULXs, i.e. a disc of at least $\gtrsim 10^5\, R_g$ in size, geometrically thin for $R \gtrsim 15\dot{m}R_g$. This is not a surprising result: MHD codes attempting to model the disc viscosity from a first–principles treatment of the magnetorotational instability currently find values of the dimensionless viscosity parameter α significantly smaller ($\lesssim 0.01$) than observational estimates from time variations, which strongly suggest $\alpha \gtrsim 0.3$ (Tetarenko et al., 2018). The reason for this discrepancy is likely to be numerical diffusivity, as already recognized in the solar and MHD–fluids literature. One should add, however, that the viscosity parameter can be reliably determined in the outer disc's regions only (see, e.g., Kotko and Lasota 2012).

Most, if not all, numerical simulations of such flows start with a torus, with an assumed distribution of angular momentum that after relaxation forms an accretion flow. In most cases the "circularization radius" of a torus–generated flow (the Keplerian orbit corresponding to the torus angular momentum) is kept rather small ($\sim 30 - 50\, R_g$). This is because the simulations aim to get quasi-stationary solutions, but this requires run times significantly longer than the viscous time of the accretion flow.

Since the viscous time at radius R is

$$t_{\rm vis} \sim \alpha^{-1}\left(\frac{H}{R}\right)^{-2}\left(\frac{R^3}{GM}\right)^{1/2}, \tag{90}$$

one can write

$$t_{\rm vis} \sim 1.1 \times 10^5 \left(\frac{R}{100R_g}\right)^{3/2}\left(\frac{\alpha}{0.1}\right)^{-1}\left(\frac{H/R}{0.5}\right)^{-2} t_g, \tag{91}$$

where the dynamical time $t_g \equiv R_g/c$, is often used to express the duration of numerical calculations ($t_g = 5 \times 10^{-5}$ s, for a $10\, {\rm M}_\odot$ black hole). Typical 3D GRRMHD (general-relativistic radiation magneto-hydrodynamic) calculations

[11] For "hyper-Eddington" accretion on to an intermediate-mass or super-massive black hole with $\dot{m} = 5000$, the luminosity is still $\sim 30\ L_{\rm Edd}$ (Sakurai et al., 2016).

by Sądowski and Narayan (2016) require runs of 20000 t_g, so it is not surprising that their quasi-stationary solutions require rather small discs, with $R \lesssim 40R_g$.

The pioneering simulations of super-Eddington accretion by Eggum et al. (1988) were able to represent only 0.6 seconds of physical evolution of the system, while the improved scheme of Okuda (2002) increased this duration to 1.6 seconds, both shorter than the corresponding viscous time. Ohsuga et al. (2005), using 2D radiation hydrodynamic (RHD) simulations were the first to obtain a quasi-steady structure of a supercritical accretion flow onto a black hole. It took another 10 years for other groups to join the Japanese team of Ken Ohsuga in trying to model supercritical accretion onto compact bodies. Sądowski and Narayan (2015); Sądowski and Narayan (2016) used a general-relativistic RMHD code first in two, then in three dimensions, while Jiang et al. (2014) performed 3D simulations in the framework of the so–called pseudo–Newtonian potential of Paczynsky and Wiita (1980)[12]. Except for Takahashi et al. (2016), who used the general-relativistic description of the black-hole accretor, other simulations of the Ohsuga group (Ohsuga et al., 2005; Ohsuga and Mineshige, 2011; Hashizume et al., 2015; Kitaki et al., 2018, 2021) used the pseudo-Newtonian description of particle motion in the gravitational field of the accreting body. All

Table 5 Numerical Models of super-Eddington black hole accretion (Adapted from Kitaki et al., 2021)

Paper	Method	Compton [Yes/No]	$R_{\rm out}$ $[R_g]$	$R_{\rm K}$ $[R_g]$	$R_{\rm qss}$ $[R_g]$	$R_{\rm trap}$ $[R_g]$	$\dot{M}_{\rm BH}$ $[\dot{m}]$	$\dot{M}_{\rm outflow}$ $[\dot{m}]$
Kitaki+21	2D-RHD	Yes	6000	4860	~ 1200	~ 540	~ 18	~ 2.4
Ohsuga+05	2D-RHD	No	1000	200	~ 60	~ 400	~ 260	
Ohsuga+11	2D-RMHD	No	105	40	~ 10	~ 150	~ 100	
Jiang+14	3D-RMHD	No	100	50	~ 40	~ 660	~ 22	~ 40
Sądowski+15	2D-GR-RMHD	Yes	5000	42	~ 70	~ 1280	~ 42	~ 700
Sądowski+16	3D-GR-RMHD	Yes	1000	40	~ 20	~ 520	~ 18	~ 52
Hashizume+15	2D-RHD	No	10000	200	~ 200	~ 460	~ 15	~ 50
Takahashi+16	3D-GR-RMHD	No	250	34	~ 20	~ 600	~ 20	
Kitaki+18	2D-RHD	Yes	6000	600	~ 400	~ 840	~ 28	~ 30
Jiang+19*	3D-RMHD	Yes	1600	80	~ 30	~ 760	~ 25	

$R_{\rm out}$ – radius at the outer boundary, $R_{\rm K}$ – initial Keplerian radius ("circularization radius"), $R_{\rm qss}$ – radius, inside which a quasi–steady state is established, $R_{\rm trap}$ – photon-trapping radius derived based on equation 34 (with right hand side multiplied by ~1.5), $\dot{M}_{\rm BH}$ is the accretion rate onto the black hole, $\dot{M}_{\rm outflow}$ is the outflow rate at around $R_{\rm out}$. It is indicated whether the Compton scattering effect is taken into account or not.

* In these simulations the black-hole mass is $5 \times 10^8\,{\rm M}_\odot$

these simulations produce rather similar results: strong outflows and regions of the inflow dominated by advection. They differ mostly in details, except for Jiang et al. (2014) who observe an effect not seen by the other teams: vertical advection of radiation caused by magnetic buoyancy that transports energy faster than photon diffusion. This allows a significant fraction of the photons to escape from the surface of the disk before being advected into the black hole; vertical "advection" reduces horizontal advection. The reason for this discrepancy between simulation results is not understood. The main suspect is the treatment of radiation in the code. While Jiang et al. (2014) solve the full radiative diffusion equations, other authors use approximations, such as flux limited diffusion (FLD) method or the M1 closure. This might explain differences between the radiative energy distribution and radiation collimation observed between the two sets of simulations. On the other hand, in Jiang et al. (2014) the inner edge of the simulation box is located outside the horizon which, as showed by McKinney and Gammie (2002) can lead to reflection of energy that would have normally been advected into the black hole.

However, as pointed out and discussed in some detail by Kitaki et al. (2021), all the simulations above suffer from one serious drawback that puts into question their relevance to direct modelling of ULXs: their circularization

[12]Since the Paczyński-Wiita "potential" mimics the general–relativistic description of massive particle orbits in the black–hole's equatorial plane, it should actually be called "pseudo–relativistic", but it is too late to change the widely accepted nomenclature. (The name "Paczyński" was misspelled in the original publication, hence the spelling used in the reference list.)

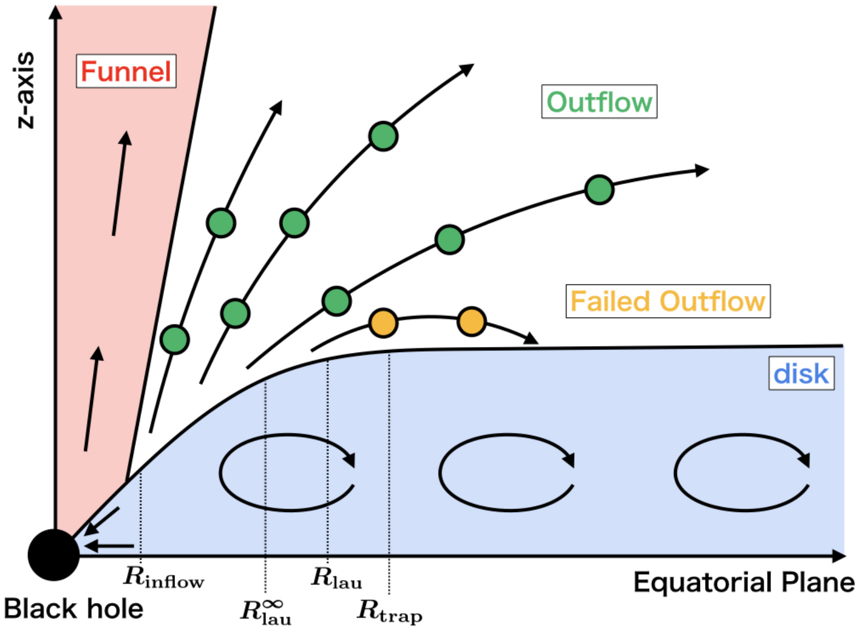


Figure 16 Schematic view of the structure of the super-Eddington accretion flow and associated outflow based on our numerical results. The black arrows indicate the gas motion. (Kitaki et al., 2021)

radii, as well as the outer radii of the quasi-steady disc region are always *inside* the trapping and spherization radii (see Table 5). Therefore although all numerical models predict wind plus advection dominated flow configurations it remains to be seen where such features occur, and what their properties are in real systems with, say, $R_{\rm out} > 10^4 R_g$ and $R_{\rm sph} > 750 R_g$ (corresponding to $R_{\rm out} > 3 \times 10^{10}$ cm for a $10\,{\rm M}_\odot$ black hole and $\dot{m} > 10$, respectively).

Kitaki et al. (2021) have made a substantial contribution towards reaching this objective (see first line of Table 5). They performed simulations with an outer radius of $6000 R_g$ and circularization radius $4860 R_g$. Their calculations achieved a quasi-stationary state inside $R_{\rm qqs} \approx 1200 R_g$, a radius 3 to 120 times larger than in previous simulations of super-Eddington accretion flows. Kitaki et al. (2021) used a 2D R-RH code, with a viscosity parameter $\alpha = 0.1$. The black hole mass is $10\,{\rm M}_\odot$ and a Paczyński-Wiita "potential" is used to describe massive–particle motions. Matter is continuously added at $R_{\rm out}$ at a rate $\dot{m} = 70$, with specific angular momentum $3.12 \times 10^{18} {\rm cm}^2 {\rm s}^{-1}$. All matter arriving at $R_{\rm in} = 4 R_g$ is absorbed.

The structure obtained by Kitaki et al. (2021) is schematically shown in Figure 16. The accretion rate onto the black hole is $\dot{m}_{\rm BH} = 18$. The flow forms a well–delimited disc structure with a surface defined as the loci at which the radiation force balances the gravity in the radial direction. Near the black hole and up to $R \sim R_{\rm trap}$ the disc height H is proportional to H ($H/R \sim 1$), above this radius it is constant $H \sim 22-34 \dot{m}_{\rm BH} R_g$. The trapping radius $R_{\rm trap} \sim 50 \dot{m}_{\rm BH} R_g$. This means, as expected from simple models (Section 3.2), that for $R \lesssim R_{\rm trap}$ the flow is advection dominated, while at larger radii it behaves like a radiation–pressure dominated, Shakura-Sunyaev–type accretion disc. Such discs should be thermally unstable, but this does not seem to occur in Kitaki et al. (2021) simulations despite the calculation time amply allowing the instability to develop. The reasons for this remain unclear (see, however, Jiang et al., 2013) but are worth investigating.

Closer to the black hole, at $R_{\rm lau} \sim 26 \dot{m}_{\rm BH} R_g$, an outflow is produced, but the expelled gas is not able to reach infinity and falls back on to the disc. Only at $R^{\infty}_{\rm lau} \sim 15 \dot{m}_{\rm BH} R_g$ is a real outflow (wind) blown out. The formula for $R^{\infty}_{\rm lau}$ has the same form as that for $R_{\rm sph}$ (Eq. 30) but with $\dot{m}_{\rm BH}$ instead of $\dot{m}$ which in Eq. (30) corresponds to the rate at which matter is fed to the outer radius (in the simulations under discussion, $\dot{m} = 70$, while $\dot{m}_{\rm BH} = 18$). We discuss this difference later in this section. Finally, in the regions closest to the black hole, below $R_{\rm inflow} \sim 4.4 \dot{m}_{\rm BH} R_g$, most of the gas flows in at a rate $\dot{m} = 18$, with some weak outflow $\dot{m}^{\rm out}_{\rm outfl} \sim 1.3$.

The Kitaki et al. (2021) solution is fully consistent with what one expects from an accretion–launched wind. The wind speed is $v \sim 0.1c$, and $L_{\rm mech} \approx 0.05 - 0.08 L_{\rm rad}$, with $L_{\rm rad} = L_X \approx 2 - 3 L_{\rm Edd}$, so $L_{\rm mech} \approx 0.1 - 0.24 L_{\rm Edd}$. The launch radius of the wind is $R_{\rm lau} \sim$ few $100 R_g$, in agreement with the wind speed $v \sim (2GM/R_{\rm lau})^{1/2}$. This gives a wind momentum rate $\dot{M}_{\rm out} v = (2/v)\, L_{\rm mech} \sim 20 L_{\rm mech}/c \sim L_{\rm rad}/c$ as one would expect when the mass supply is not hyper-Eddington (here it is $\sim \dot{m} = 18$). These values are similar to analytic estimates (King and Pounds, 2003) for momentum–driven winds.

This solution suggests that for black-hole accretors, below $R \sim 1000 R_g$, most of the mildly ($\dot{m} \sim$ few $\times$ 10) super-Eddington mass accretion is simply swallowed, as predicted by slim-disc models. The outflow to accretion ratio $\dot{m}_{\rm outflow}/\dot{m}_{\rm BH} - 0.14$ is much lower than in previous simulations which Kitaki et al. (2021) attribute to the sizes of the simulated flows, theirs being much larger than in the preceding calculations, thus avoiding having the whole simulated domain in the region where the flow is puffed–up from the start. But we note that although $R_{\rm qss} \sim 1200 R_g$ is 20 to 30 times larger than the corresponding radius in R-GR-MHD calculations, it is still "only" 1.8×10^9cm, well inside the circularization radius. The net accretion flow for $R \lesssim R_{\rm qss}$ is roughly constant ($\dot{m} \sim 18$) while the mass inflow rate decreases from $\dot{m} \sim 30$ at $R \approx R_{\rm qss}$ to $\dot{m} = 18$ for $R \sim 40 R_g$ ($\dot{m} \sim R^{-0.2}$), but it is not clear what happens above $1200 R_g$, where the simulated configuration is not relaxed.

For example, for $R > 2012 R_g$, the gas pressure dominates over radiation pressure and the disc should be geometrically thin (see Eq. (25) with $\dot{m} = 70$). This should reduce the outflows, thus making the whole configuration potentially inconsistent. It seems that we are still some distance from having a complete description of the whole picture of super-Eddington accretion onto black holes.

Indeed, recently, Hu et al. (2022) simulated super-Eddington accretion onto a $10^3\,{\rm M}_\odot$ black hole. The physical outer radius of their simulation domain is $R = 1500 R_g$, four times shorter then in Kitaki et al. (2021). In their case, however, the steady-state radius $R_{\rm qss} = 1500 R_g$, slightly longer than in Kitaki et al. (2018). The flows they study settle down to a quasi-steady state in millions of the orbital timescale, which in their case corresponds to the viscous time at $\sim 1000 R_g$ (they take $\alpha = 0.01$). In their case $\dot{M}_{\rm in} \propto r^p$ with $p \sim 0.5 - 0.7$ and contrary to the Kitaki et al. (2021) only a small fraction of the inflowing matter feeds the central black hole. Indeed, their solutions can be represented as

$$
\begin{aligned}
\dot{M}_{\rm BH} &= 17.1 \dot{M}_{\rm Edd} \left(\frac{\dot{m}_0}{300}\right)^{0.5} \\
\dot{P}_{\rm out} &= 0.51 c \dot{M}_{\rm Edd} \left(\frac{\dot{m}_0}{300}\right)^{0.5} \\
\beta &= 17.5 \left(\frac{\dot{m}_0}{300}\right)^{0.5} - 1
\end{aligned}
\tag{92}
$$

and the wind velocity is

$$
\langle v_{\rm wind} \rangle = 1.7 \times 10^{-3} c \left(\frac{\dot{m}_0}{300}\right)^{-0.5}, \tag{93}
$$

where $\beta = \dot{M}_{\rm out}/\dot{M}_{\rm in}$ is the wind loading fraction. It is only ~ 0.13 in Kitaki et al. (2021) but ~ 20 in the model of Hu et al. (2022), so that even in the case of a black hole, advection does not play a significant role when accretion rate are very strongly super-Eddington. Therefore the main difference between the two numerical models is that in Kitaki et al. (2021) most of the outflowing gas fails to escape from the outer boundary and falls back onto the disc, while in Hu et al. (2022) most matter is lost in the wind. Hu et al. (2022) attribute the large differences between the two approaches to several factors, numerical and physical. First, Kitaki et al. (2021) impose in their computational domain equatorial mirror-symmetry of the accretion flow across the equatorial plane. It seems that this imposed symmetry tends to suppress global convective motion that crosses the equator and is known to produce outflows coherently through the equator rather than the polar regions (see Li et al., 2013). The second reason would be that Kitaki et al. (2021) assume a viscous parameter of $\alpha = 0.1$ (Hu et al., 2022, assume $\alpha = 0.01$) which is apparently known to cease convective/turbulent motion of advection dominated flows and thus to reduce the outflow rate (see, e.g. Inayoshi et al., 2018). These differences do not necessarily favour the model with stronger outflows. For example, it seems that high values of the viscosity parameter $\alpha > 0.1$ are appropriate to the description of high–accretion rate flows (Tetarenko et al., 2018). Only a self-consistent calculation with a MRI–determined (anomal) viscosity could decide if numerical models can reproduce the mechanical power observed in some ULXs. In the most recent paper of the Ohsuga group (Yoshioka et al., 2022) it is concluded that the fraction of the failed outflow decreases with the decrease of

$\dot{M}_{\rm in}$. They leave the comparison with the Hu et al. (2022) simulation for a future paper. What's more important, their simulations confirm the effect of radiation beaming at high accretion rates since they found that "the higher $\dot{M}_{\rm in}$ is, the more vertically inflated becomes the disk surface, which makes radiation fields more confined in the region around the rotation axis".

An interesting result of most numerical simulations is that they do not see any evidence of the photon bubbles proposed as a solution of the super-Eddington luminosity problem by Begelman (2002). When such bubbles do appear, they play no significant role in super-Eddington accretion flows (see, e.g., Jiang et al., 2014).

We are even further away from understanding super-critical accretion through numerical simulation when the accretor is a rotating, magnetized neutron star, as discussed in the next section.

3.8.2. Numerical simulations relevant to PULXs

The difficulty of simulating super–Eddington accretion on to rotating, magnetized neutron stars is probably best illustrated by the fact that until now only four papers have dealt with the problem: Takahashi and Ohsuga (2017); Takahashi et al. (2018); Abarca et al. (2018, 2021). The maximum dipole field strength considered is $\sim 10^{10}$G (in two cases $B = 0$ G), and none of the simulations describes a rotating accretor with a hard surface.

All attempts to describe super–Eddington accretion on to neutron stars use GRRMHD codes, similar to, or inspired by, the codes used in the description of black–hole accretion, described above. There are, however, two further difficulties that must be overcome when such codes are applied to magnetized neutron stars. First, it is not easy to describe in the same code both magnetically–dominated flows with a force–free character and the "normal" properties expected from the (GRR)MHD equations. This difficulty has been partially removed by Parfrey and Tchekhovskoy (2017).

The second difficulty is in fixing the inner boundary conditions, i.e. the physical properties of the accreting matter at the the neutron star surface. In contrast to black–holes, whose surface is always fully absorbing independent of what – and how much – is falling onto it, the properties of matter arriving at the neutron–star surface depend on the magnetic field strength and the accretion rate (see Abarca et al., 2021, and references therein). As in most black–hole simulations, limits on the available computational time restrict the range of radii for which the solutions relax to quasi–stationarity; in all simulations $R_{\rm QSS} \lesssim 50R_g$, while the spherization radius is $R_{\rm sph} \lesssim 500R_g$ and the computational domain extends up to $1000R_g$.

Takahashi et al. (2018) and Abarca et al. (2018) consider the case of super–Eddington ($\dot{m} \sim 10$) accretion onto a non-magnetic and non-rotating neutron star with a reflective surface, and compare it with the case of accretion onto a black hole. They both observe more powerful outflows in the neutron–star case and Takahashi et al. (2018) find that for a neutron–star accretor, the accretion flow inside $R \lesssim 10R_g$ (in their case $R_{\rm QSS} \sim 10R_g$) corresponds to the SS73 windy solution (Sect. 3.3), whereas in the black-hole case, the flow is advection dominated[13]. The strong wind blown out from the vicinity of a super–Eddington accreting neutron star is very optically thick to electron scattering "which would lead to the obscuring of any NS pulsations observed in corresponding ultraluminous X-ray sources" (Abarca et al., 2018). Since the model of a non–rotating and unmagnetized neutron star would produce no pulses in any case, this is not a big drawback but stresses that the presence of optically–thick outflows from super–Eddington accreting neutron stars cannot be neglected when describing their X–ray emission.

Abarca et al. (2021) performed a 2D axisymmetric radiative GRMHD simulation of accretion onto a neutron star with a 2×10^{10} G dipolar magnetic field. The combination of the hard surface and confinement of the gas into an accretion column near the star, allows the flow to release radiative energy at a rate of several times the Eddington limit. They compared their results to the KLK17 model and found a larger beaming intensity, but they believe that post-processing would show a less intensely beamed distribution of radiation at infinity. They also note that they do not model the same system as considered in KLK17 (e.g. they have super-Eddinton accretion rates in the accretion column). In their case the distance between the Alfvén radius and spherization radius is large, and their star is non-rotating. This paper reveals the difficulties current numerical simulations still face in modelling real PULXs.

In all simulations, the estimated minimum values of the inverse of the beaming parameter b (maximum beaming) obtained from various models range from $1/b = 1/30 - 1/20 \approx 0.033 - 0.05$, which compares quite well with the range of values $b = 0.009 - 0.6$ from Table 3 in Section 3.7.1. i.e. with the results of the KLK17 model.

[13]This clear physical difference between accretion flows onto compact objects which have, or do not have, surfaces, makes the advection-dominated solutions of Chashkina et al. (2019) rather unrealistic.

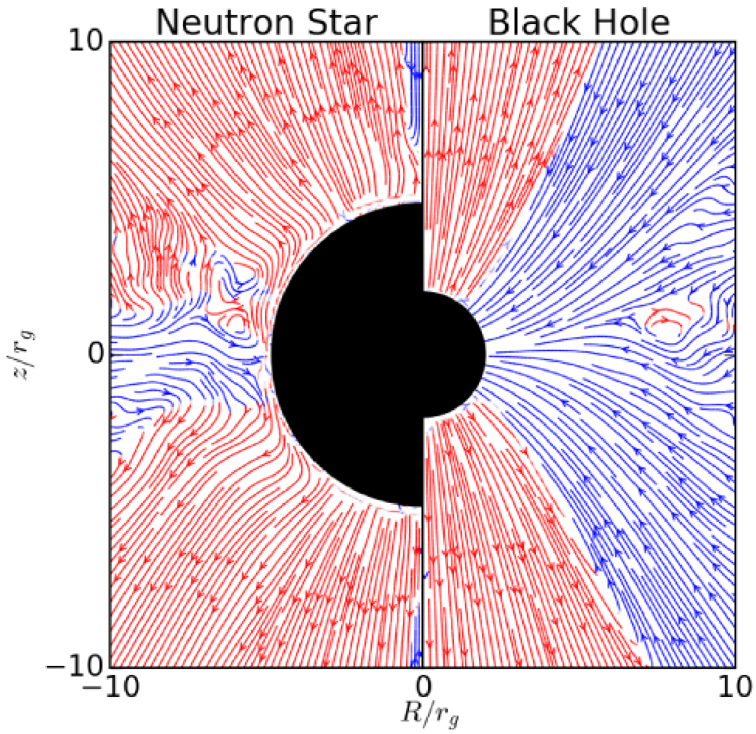


Figure 17 Stream lines around a (1.4 $M_\odot$) neutron star (left) and a (10 $M_\odot$) black hole (right). Red (blue) lines indicate that the radial velocity is in the positive (negative) direction. (From Takahashi et al., 2018).

The simulations of super–Eddington accretion onto neutron stars thus provide strong support for the assumptions of the KLK17 PULX model, i.e. that the accretion flow inside the spherization radius is well described by the SS73 windy model, and that the X-ray luminosity is beamed. Although these simulations assume weakly magnetized and non–rotating neutron stars, their basic results: weak advection, unlike in the black–hole case, and therefore strong optically thick outflows, probably hold for stronger fields and faster rotation of the accretor.

3.8.3. Numerical simulations of PULX accretion columns

Numerical models of super-Eddington accretion onto a strongly magnetized neutron star are given by Kawashima et al. (2016, hereafter K16) and Kawashima and Ohsuga (2020, hereafter K20). The simulations describe the last part of the accretion flow when the infalling plasma forms a column above the neutron star surface. In both papers, the accretion column is represented by a truncated cone with a base ("polecap") occupying a fraction 0.07 of the stellar surface. Since the method used is radiation hydrodynamics, the value of the magnetic field does not appear explicitly, but in K16 it is estimated to be $\sim 10^{10}$G, while in K20 the magnetic field strength is $\gtrsim 10^{12}$G. In the first case, the plasma is allowed to move transversely, in the second, the motion of matter is restricted to the radial directions. In K16 the initial uniform density in the column gives a time-averaged accretion rate of $\dot{m} = 50$; K20 uses the same initial set-up but also a lower-density model, giving $\dot{m} = 3$. In both types of model, a radiative shock forms above the neutron-star surface (fixed at 10 km) at a height $\sim$ 3 km for the "weak magnetic field" and at $\sim$ 10km in the case where the accreting matter motion is restricted to the radial direction. In the "weak-field" simulations, practically all the radiation is released below the shock and radiated sideways. The apparent luminosity is highly anisotropic; it can reach $\sim 50\, L_{\rm Edd}$ sideways, but is close to Eddington vertically along the accretion column. In contrast to the "weak-field" case, where the radiation field below the shock is homogenized by circular motions of radiation bubbles, the "strong-field" simulations show that matter is accreted along the side walls of "hollow cones" while matter inside the cones is blown away by radiation. For $\dot{m} = 3$, only one hollow cone forms, while for very high accretion rates ($\dot{m} = 50$), the column contains three such structures. Also in this case the apparent luminosity is highly anisotropic,

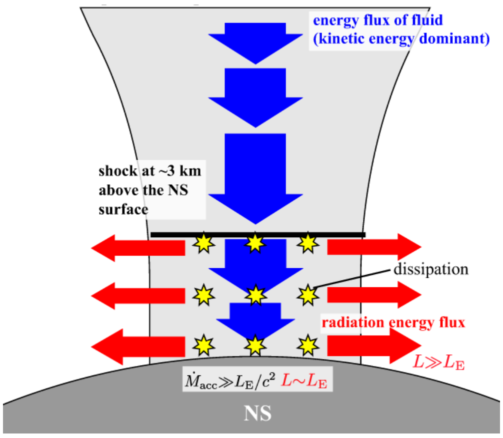


Figure 18 Schematic picture explaining energy flow from gas (potential energy) to outgoing radiation within a super-critical accretion column. The blue arrows represent the energy flow carried by gas: their length and width are drawn in proportion to the kinetic energy flux and the mass accretion rates, respectively, whereas the red arrows represent energy flow carried by radiation and their widths are drawn in proportion to the radiation energy flux (Kawashima et al., 2016)

.

radiation still managing to get out mainly sideways, but radiated from a larger surface than in the "weak-field" case. The sideways luminosity can reach $30\,L_{\rm Edd}$.

Using the K16 model, Inoue et al. (2020) calculated the light-curves produced by such an accretion column, taking into account general-relativistic effects on light propagation near the neutron-star surface. The pulses they obtain are quasi-sinusoidal. They obtain a high pulsed fraction of the emitted light, from 5% up to 50%, depending on the magnetic and observational inclination angles. However, a narrow magnetic column for a highly super-Eddington accretion rate, and field of $\sim 10^{10}$G does not seem to give the best representation of a real PULX since high accretion rates and low magnetic fields should instead favour wide accretion columns.

The papers K16 and K20 are important contributions to the understanding of supercritical accretion in strong magnetic fields, but it is unlikely that they correspond to the accretion structure of real PULXs. The accretion flow in these systems probably does not form a column extending to 2×10^8 cm ($\sim$ 200 neutron–star radii) above the neutron star surface. Since PULXs are binary systems, matter transferred from the neutron-star's companion forms a disc extending down to a magnetosphere where the pressure of the accreting matter is comparable to the magnetic pressure. The size of the magnetosphere will determine the angular size of the column, which will vary with magnetic–field intensity, differing by two orders of magnitude. For the parameters of K16, the magnetospheric radius is close to the neutron star surface at $\sim 3 \times 10^6$ cm (see Eq. 64) and for the K20 set-up $R_{\rm M} < 10^8$cm. What is most important, however, is that accretion within the magnetosphere is most likely highly dissipative, since the flow along field-lines requires a highly supersonic flow to bend and shock, while in K16 and K20, the first shock occurs very near the neutron-star surface, because in the simulations (different from the schematic view of Fig. 18) the field-lines are straight. By necessity, the K16 and K20 simulate only the last part of the PULX accretion flow and they assume that it arrives at the magnetosphere at a super-Eddington rate, which is rather unlikely in reality (Takahashi et al., 2018).

3.9. PULXs as magnetars in binary systems

The discovery that ULX M82 X–2, with an apparent luminosity $L \simeq 1.8 \times 10^{40}$ erg s^{-1}, is a pulsar with a coherent periodicity P = 1.37 s (Bachetti et al., 2014), raised the possibility that its apparent super–Eddington luminosity might be intrinsic (cf Tong, 2015; Ekşi et al., 2015; Dall'Osso et al., 2015; Mushtukov et al., 2015a). If the strength of its magnetic field is magnetar-like ($B \sim 10^{14}$G), the reduction in electron scattering opacity for some directions and polarizations can be quite substantial.

At first sight, this idea is similar to the one motivating Paczynski (1992) to explain the luminosity $L \sim 10^4\,L_{\rm Edd}$ observed in the soft-gamma repeater (SGR), GB 790305 ("the 5 March event"), by the presence of a magnetic field $B \approx$

3×10^{14}G. In a very strong magnetic field, the Thomson and Compton scattering cross-sections are strongly reduced for photons with energies E_γ much lower than the energy corresponding to cyclotron frequency $E_{\rm cyc} = 11.6 B_{12}$ keV, where $B_{12} 10^{12}$ G = B (Canuto et al., 1971). From Herold (1979) one has

$$\frac{\sigma_1}{\sigma_T} \approx \sin^2\theta + \left(\frac{E_\gamma}{E_{\rm cyc}}\right)^2 \cos^2\theta \tag{94}$$

$$\frac{\sigma_2}{\sigma_T} \approx \left(\frac{E_\gamma}{E_{\rm cyc}}\right)^2, \text{ for } \frac{\rm E_\gamma}{\rm E_{cyc}} \ll 1, \tag{95}$$

where indices 1 and 2 correspond to the two linear photon polarisations, and θ is the angle between the directions of the magnetic field and light propagation. Paczynski (1992) gives an approximate relation between the "new" critical luminosity and the Eddington luminosity, defined through the Rosseland mean opacity:

$$\frac{L_{\rm crit}}{L_{\rm Edd}} \approx 2 B_{12}^{4/3} \left(\frac{g}{2\times 10^{14} {\rm cm\, s^{-2}}}\right)^{-1/3}, \tag{96}$$

where $g = GM/R^2$, when $L_{\rm crit} \gg L_{\rm Edd}$. This critical luminosity is of course only approximate because it is not properly integrated over angles, but estimates of the Rosseland mean opacities vary with angle only by a factor two (Paczynski, 1992).

From Eq. (96), for a 1.4 $\mathrm{M}_\odot$ neutron star, a sub-critical luminosity $L \lesssim 0.1 L_{\rm crit}$ implies

$$L \lesssim 2 \times 10^{40} \left(\frac{B}{10^{14}\,{\rm G}}\right)^{4/3} \ {\rm erg\, s^{-1}}, \tag{97}$$

so that explaining PULXs with $L > 10^{40}$ erg s^{-1} assuming isotropic radiation, requires magnetic field strengths that would be considered extreme, even among magnetars.

In PULX models by Tong (2015); Dall'Osso et al. (2015); Ekşi et al. (2015); Chashkina et al. (2017), the fields are in the range $\sim 3\times 10^{13} - 6\times 10^{16}$ G (the last value considered by the authors to be "rather unphysical"), so that the critical luminosities corresponding to the first three PULXs discovered put them safely into the sub-critical luminosity regime, even with a magnetic moment derived by magnetic torque considerations.

But there is a fundamental difference between SGRs and PULXs: SGRs are powered by magnetic energy (Duncan and Thompson, 1992), while the luminosity of PULXs comes from accretion. For SGRs the magnetic field allowing $L \approx 10^4\ L_{\rm Edd}$ is consistent with pulsar slowdown and the required magnetic energy. There is no known alternative to magnetar-strength fields in SGRs and anomalous X-ray pulsars, and there is so far no observational evidence against the presence of fields with these strengths.

This is not true of the magnetar hypothesis for PULXs. First, no magnetar is observed to be a member of a binary system. *All* $\sim$ 30 known magnetars (or "candidate" magnetars) are isolated neutron stars (Olausen and Kaspi, 2014). Conversely, all neutron stars in X–ray binaries are observed to have magnetic field strengths $< 10^{13}$G, below the magnetar range (see, e.g., Revnivtsev and Mereghetti, 2016).

The super-strong magnetic field in magnetars is thought to be formed in a process which destroys (or merges) the binary, of which its progenitor was a member (Popov, 2016). This would explain their absence in binary systems. Magnetars are supposed to form through neutron-star mergers (e.g., Giacomazzo and Perna, 2013; Piro et al., 2017) or in type Ibc supernova outbursts in massive binaries. The first mechanism obviously produces a single object. In the second, the superluminous supernovae disrupt the binary and produce an isolated magnetar, as demonstrated by the magnetar CXOU J1647-45 in the young massive cluster, Westerlund 1 (Clark et al., 2014).

We note that "most of theoretical considerations do not favour even existence, not speaking about active decay, of magnetar-scale fields in neutron stars older than 10^6 yrs" (Popov, 2022).

These considerations make the presence of rapidly rotating, strongly accreting magnetars in binary systems highly unlikely. Their presence in ULXs would evidently require a cosmic conspiracy.

3.10. ULX populations

The beaming formula (55) allows one to study the populations of disc–wind beamed ULXs in galaxies. If the host galaxies have space density n_g Mpc^{-3}, and each host contains N ULXs with randomly oriented beams, one would

need to search through $\sim 1/Nb$ galaxies, occupying a space volume $\sim 1/n_g Nb$, to be sure of being in the beam of one ULX. Then the nearest ULX must be at a distance

$$D_{\rm min} \sim \left(\frac{3}{4\pi n_g Nb}\right)^{1/3} \sim 0.7(n_g N)^{-1/3}\dot{m}_1^{2/3}\,{\rm Mpc} \tag{98}$$

ń where $\dot{m}_1 = \dot{m}/10$, and has apparent (isotropic) luminosity

$$L = 2.2 \times 10^{39} m_* \dot{m}_1^2 \ {\rm erg\,s^{-1}} \tag{99}$$

where $m_* = m/(10\,{\rm M_\odot})$. The scalings $m_*, \dot{m}_1$ are appropriate for black holes or mass $\sim 10\,{\rm M_\odot}$, so by the argument following Eq. (58) the luminosity normalization here would be 2.2×10^{40} erg s^{-1} for neutron star ULXs. These relations can be used to show that the ULX luminosity function of the Local Group is consistent with the idea that beamed ULXs are the evolutionary stage following the standard high–mass X–ray binary phase (cf Mainieri et al., 2010).

3.10.1. Pseudoblazars?

The beaming described by (55) potentially allows one to see suitably–oriented ULXs out to very large distances. The extreme object SS433 has $\dot{m} \sim 300 - 10^4$ (King et al., 2000b; Begelman et al., 2006, see Section 3.14.1). With $\dot{m} = 10^4\dot{m}_4$ the nearest object of this kind which we would observe within the beam is at a distance

$$D_{\rm min} \sim \left(\frac{3}{4\pi n_g Nb}\right)^{1/3} \sim 660 N^{-1/3}\dot{m}_4^{2/3}\,{\rm Mpc} \tag{100}$$

where we have taken $n_g \sim 0.02\,{\rm Mpc^{-3}}$ as appropriate for L^* galaxies. The apparent isotropic luminosity of such an object would be

$$L_{\rm sph} = 2.2 \times 10^{45} m_* \dot{m}_4^2 \ {\rm erg\,s^{-1}}. \tag{101}$$

This distance and apparent luminosity are typical for active galactic nuclei (AGN), so without further information one could not easily pick out a bright ULX like this from a sample of observed AGN. But unlike a genuine AGN, there is no reason to suppose that a given ULX lies in the nucleus of the host galaxy. There are possible candidates for such systems: the BL Lac system PKS 1413+135 (Perlman et al., 2002) has distance $D \simeq 1$ Gpc and isotropic luminosity $\sim 10^{44}$ erg s^{-1} , but lies at 13 ± 4 mas from the centre of the host galaxy, and HLX-1 could be a system of this type (cf Section 2.7). Of course it is difficult to exclude the possibility that this system may lie at the nucleus of a fainter line–of–sight galaxy.

3.11. ULXs and binary stellar evolution

Sections 3.6, 3.7 and 3.8 above have shown how the phenomena characterizing ULXs arise, in many cases, from strongly super–Eddington mass transfer in binaries containing compact objects (white dwarfs, neutron stars or black holes) which have reached the end of their stellar evolution. We should now ask what causes these very high mass transfer rates. To do this we need to consider the evolution of binary systems where one of the stars is compact (a black hole, neutron star, or white dwarf) and the companion star transfers mass to it, powering accretion. The rate of mass transfer is determined by the evolution, both of the companion star, and of the binary orbit, as mass transfer in general changes this. Dissipation in the mass transfer process generally makes the binary orbit circularize.

Kepler's laws give the orbital angular momentum of a circular binary system consisting of stars of mass M_1, M_2 as

$$J = M_1 M_2 \left(\frac{Ga}{M}\right)^{1/2}, \tag{102}$$

where $M = M_1 + M_2$ is the total binary mass, and a is the orbital separation. We take star 1 as the compact object, and star 2 as an extended star. In a high–mass X–ray binary (HMXB), star 2 is hot, and loses mass in a wind. The X–rays result when some of this wind is captured by the compact star (a neutron star or black hole). But as the extended star 2 approaches the end of core hydrogen–burning it begins to expand. Eventually its radius R_2 fills its Roche lobe

$$R_L = f(q)a \tag{103}$$

(where $q = M_2/M_1$ is the binary mass ratio, and $f(q) < 1$ is a slowly–varying function of q). The star begins to transfer mass through the inner Lagrange point, the saddle point of the combined gravitational–centrifugal, Roche pseudopotential between the two stars. It is generally a good approximation to assume that all the mass lost by star 2 is accreted by the compact star 1, and that the orbital angular momentum J is conserved in this process. Then $\dot{J} = \dot{M} = 0, \dot{M}_1 + \dot{M}_2 = \dot{M} = 0$, and logarithmic differentiation of Eq. (102) gives

$$\frac{\dot{a}}{a} = 2\frac{(-\dot{M}_2)}{M_2}\left(1 - \frac{M_2}{M_1}\right) \tag{104}$$

Since $-\dot{M}_2 > 0$, we see that if the extended, mass–losing star is more massive than the compact star, the effect of mass transfer is to shrink the binary separation ($\dot{a} < 0$). As $f(q)$ varies only weakly with mass ratio q, R_L also shrinks, tending to increase the rate of mass transfer. The result is that mass transfer from the more massive to the less massive star is self–sustaining, at least for a time.

But there is a limit to this process. The outermost stellar gas – above the saddle point of the Roche potential – is lost on a dynamical timescale, and gas from below flows towards the saddle point on the same timescale, trying to refill the Roche lobe. But this gas is not now in thermal equilbrium because its rapid rise means that it retains the same specific entropy it had when deeper in the star. But in stars with a radiative envelope (typically, blue stars with effective temperatures $T_{\rm eff} \gtrsim 10^4$ K), the equilibrium entropy increases outwards, so the new gas has too little entropy for its new position. This means that it is denser and cooler than the gas it replaces, making the radius of this part of the star smaller, and reducing the mass transfer rate. To reach thermal equilibrium, this gas must absorb some heat from the stellar radiation field, on a thermal timescale. In doing so it expands, returning this part of the star to the equilibrium radius for its new (slightly smaller) mass[14].

The argument above shows that mass transfer from a more massive radiative companion cannot happen on a timescale shorter than the star's thermal timescale, $t_{\rm th} \sim GM_2^2/R_2L_2$ (where R_2, L_2 are the star's radius and luminosity respectively). But this is usually much shorter than the nuclear timescale in stars of mass a few $M_\odot$, and we find values $-\dot{M}_2 \sim M_2/t_{\rm th}$ as large as $\sim 10^{-7} - 10^{-4}\,M_\odot\,{\rm yr}^{-1}$, depending on the stellar mass M_2.

Rates like this are far higher than the value $\dot{M}_{\rm Edd}$ defined above, which would give the Eddington luminosity if it could be accreted and so it is very likely that the super–Eddington excess is likely to be expelled.

As we mentioned in the Introduction and Section 3.6, the neutron star in the long–period ($P = 9.84$ d) low–mass X–ray binary Cyg X-2, appears to have expelled most of the mass transferred to it in this way. The distinctive feature of this system is the unusual state of the companion star. Combining spectroscopic information, photometry of the ellipsoidal variation of the companion, and the geometry of the Roche potential, King and Ritter (1999) showed that this star had a low mass $M_2 \simeq 0.5 - 0.7\,M_\odot$, and yet a large radius ($R_2 \simeq 7\,R_\odot$) and very high luminosity ($L_2 \simeq 150\,L_\odot$). This is just what one expects at the end of an episode of thermal–timescale mass loss: the hot central region of what was initially a much more massive star has been exposed, and has had no time to cool. The evolution followed by Cyg X-2 is called early massive Case B, in the terminology of Kippenhahn and Weigert (1967).

The most important feature of this evolution is that the neutron star accretor has evidently gained almost none of the $\sim 3\,M_\odot$ transferred to it by the companion: its current mass is only $1.78 \pm 0.3\,M_\odot$. This expulsion cannot have come from common–envelope evolution – the orbital binding energy released in shrinking the binary to the separation given by the current period of almost 10 days is far too small to expel any matter. This leaves only accretion energy – the accretion disc around the neutron star must have expelled most of the transferred mass. This is just the process discussed by Shakura and Sunyaev (1973), and summarized in Section 3.3. As we discuss in Sections 3.8 and 3.14, it leads to the production of a quasi–spherical wind with typical outflow velocity $v \sim 0.1c$, with open funnels along the disc axes which collimate a large fraction of the accretion energy released as radiation. In this picture, ULXs are the evolutionary stage following the wind–fed HMXB phase, once the massive companion star fills its Roche lobe. This seems particularly likely for the pulsing PULXs, which contain neutron stars very similar to those in HMXBs.

Although thermal–timescale mass transfer is very probably the cause of ULX behaviour in many cases, it is not the only way to make a ULX. Evidently any process that produces a significantly super–Eddington mass transfer rate can

[14]If the star instead has a convective envelope, and so constant specific entropy, mass transfer can reach very high (near–dynamical) values, and the system develops a deep common envelope. This may lead to a merger of the two stars. King and Begelman (1999) show that this is very unlikely to happen with a radiative envelope, even for transfer rates as high as $\sim 10^{-4}\,M_\odot\,{\rm yr}^{-1}$.

do this. We have already mentioned that some Be – X–ray binary systems become ULXs from time to time, because of dynamical effects on the Be–star disc. Three other possible ways involve mass transfer on the nuclear timescale of a massive donor (Rappaport et al., 2005), transient outbursts involving the thermal–viscous disc instability (King, 2002; Hameury and Lasota, 2020, see Sect. 3.16), and gravitational–wave driven mass transfer from a white dwarf onto a neutron star (King, 2011) – a so–called ultracompact binary (UCB). UCBs are often found in globular clusters (see Dage et al., 2021, and references therein), where they are formed by dynamical capture, so these sources offer a possible explanation for ULXs sometimes claimed in elliptical galaxies. We will discuss other evolutionary paths, especially for weak ($L_X \simeq 3 \times 10^{39}\,\mathrm{erg\,s^{-1}}$) ULXs in Section 3.13.

3.12. 'Super–Eddington Accretion'

These possibilities illustrate that ULXs are likely to be binaries containing a compact accretor in an epoch of strongly super–Eddington mass transfer. It is worth emphasizing that the commonly used phrase 'super–Eddington accretion' is highly ambiguous, and a frequent cause of confusion. As the example of Cyg X–2 shows, the accretors in ULXs do not gain mass at significantly super–Eddington rates: it is the mass *supply rate* which is super–Eddington, not the accretion. Accordingly, the phrase *'super–Eddington mass supply'* is strongly preferable.

3.13. Population syntheses

Population synthesis of ULXs was first performed by Rappaport et al. (2005) who showed that the population of ULXs in spiral galaxies can be explained by short phases of high mass–transfer (with nuclear or thermal timescales) in black–hole plus evolved–star binaries. However, they neglected the pre–supernova evolution phase in their calculations and did not take into account other types of binaries, such as systems containing neutron–star accretors, or evolved donors. Their study was expanded by Madhusudhan et al. (2008) who completed it by predicting the observational properties of the ULX population. Linden et al. (2010) used the StarTrack population synthesis code (Belczynski et al., 2002, 2008) to show that the bulk of ULXs can be interpreted as the high-luminosity tail of high-mass X-ray binaries. Neutron–star accretors were included in population studies of ULXs only after the discovery of PULXs.

Wiktorowicz et al. (2015) performed a proof–of–concept study where they showed that any ULX, including the most luminous ones, and neutron–star systems, can be a short-lived phase in the life of a binary star. The detection of double compact object mergers (Abbott et al., 2016) triggered investigations of the connection between binary compact objects and ULXs (e.g., Finke and Razzaque, 2017; Marchant et al., 2017; Klencki et al., 2018).

A problem encountered when performing ULX population synthesis is the unfortunate choice of the threshold ULX luminosity at $10^{39}\,\mathrm{erg\,s^{-1}}$, because it fails to separate "standard" X-ray binaries (XRBs) from "generic" ULXs. At least five transient Galactic XRBs reach luminosities $> 10^{39}\,\mathrm{erg\,s^{-1}}$ (Tetarenko et al., 2016). Middleton et al. (2015a) suggested that one should take $3 \times 10^{39}\,\mathrm{erg\,s^{-1}}$ as the minimum luminosity defining ULXs whose nature is "contentious". The idea was to ensure that if the accretor was a black hole (BH), the apparent luminosity would be super-Eddington. But we now know that stellar evolution can produce black holes with masses $\gtrsim 30\,\mathrm{M_\odot}$ (Belczynski et al., 2010; Abbott et al., 2016), up to $50\,\mathrm{M_\odot}$ under favorable conditions (see, e.g., Belczynski 2020; the fact that the maximum value of black–hole masses observed in X-ray binaries is $\sim 20\,\mathrm{M_\odot}$ follows from the limited range of metallicities scanned by X-ray observations Olejak et al. 2020). So only sources with luminosities $\gtrsim 6 \times 10^{39}\,\mathrm{erg\,s^{-1}}$ qualify as (apparently) super-Eddington for a BH resulting from stellar evolution. BH[15]. The current outdated but default definition of ULXs as $L \gtrsim 10^{39}\,\mathrm{erg\,s^{-1}}$ tends to coerce population syntheses to use it, at the cost of producing "excesses" of sources with luminosities which in most cases are actually *sub*–Eddington.

Existing population syntheses do not include Be-X systems, and until recently they considered only Roche–lobe overflowing (RLOF) companions of the compact accretor, so excluding wind–fed systems. The second omission was corrected by Wiktorowicz et al. (2021), and wind–accreting ULXs will be discussed below, but there is not much hope that the difficulties inherent in the first (Be-X) will be overcome any time soon. Although current models of Be stars allow simple modelling of their discs at radii far from the stellar surface, they also contain hidden assumptions that are not physically plausible (Nixon and Pringle, 2020). If the model for Be–star discs proposed by the latter

[15]The limit can be even higher for He-rich accretion, and for the most massive BHs (e.g. Belczynski, 2020)

authors (the disc material originating from small-scale magnetic flaring events on the stellar surface) is correct, it will be problematic to incorporate it in a population–synthesis code.

Wiktorowicz et al. (2017, 2019) performed comprehensive simulations of ULX populations by using the `StarTrack` population synthesis code (Belczynski et al., 2002, 2008) with significant updates described in Dominik et al. (2012); Wiktorowicz et al. (2014). They simulated the evolution of 2×10^7 binary systems for every model and scaled the results to a Milky-Way equivalent galaxy ($M_{\rm MWEG} = 6 \times 10^{10}\,{\rm M}_\odot$; Licquia and Newman, 2015). Two star formation cases are considered: at a constant rate of $6.0\,{\rm M}_\odot\ {\rm yr}^{-1}$ for 10Gyr, and $600\,{\rm M}_\odot\ {\rm yr}^{-1}$ in bursts of star–formation lasting 100 Myr). They consider three metallicity prescriptions: solar ($Z_\odot$), 10% of solar ($Z_\odot/10$), and 1% of solar ($Z_\odot/100$). The fiducial accretion model for ULX evolution in this study assumes the SS73 windy solution and beaming described by Eq. (55), with a saturation limit at $\dot{m} = 150$. For higher mass accretion rates, the beaming is assumed to be constant and equal to $b \approx 3.2 \times 10^{-3}$ ($\theta \approx 9°$). For comparison, seven other models with different accretion and/or beaming configurations are considered. In general, the results do not depend strongly on the assumptions about the accretion mode or the beaning model, except for the case where beaming is assumed to be constant ($b = 0.1$) which, by lowering the ULX luminosity threshold, results in neutron–star ULX always dominating the population at late times.

It is known from observations, that ULXs are often associated with low metallicity environments (e.g. Pakull and Mirioni, 2002; Soria et al., 2005; Luangtip et al., 2015; Mapelli et al., 2010) Massive black holes apparently form more easily in low–metallicity environments (e.g., Zampieri and Roberts, 2009; Mapelli et al., 2009; Belczynski et al., 2010), and RLOF onto a compact object is therefore more frequent than in high metallicity cases (Linden et al., 2010).

Wiktorowicz et al. (2017) found that metallicity has a strong impact on the number of ULXs, but only in star–forming regions. They show that the number of black–hole ULXs increases significantly for $Z_\odot/10$ in comparison with $Z_\odot$. But the number of neutron–star ULXs is virtually unaffected by metallicity. Interestingly, for models with the lowest investigated metallicity ($Z_\odot/100$) they find fewer ULXs than for $Z = Z_\odot/10$. This suggests that the relation between the number of ULXs and metallicity is not monotonic (see Prestwich et al., 2013). The reasons for this inversion are currently not understood.

The general conclusions of the ULX population synthesis by Wiktorowicz et al. (2017) are:

- ULX with NS accretors dominate the post-burst ULX populations, and those with constant stellar formation (duration > 1 Gyr) in high-Z environments, consistent with current understanding of binary evolution. Neutron–star ULXs are present in significant numbers ($\gtrsim 10\%$) also during the star–formation bursts and in lower-Z ULX populations.
- ULXs appear in a very specific sequence after the start of the star formation (t denotes the time since the beginning of star formation):
  1. $t \approx 4 - 40$ Myr BH – MS ($5.6 - 11\,{\rm M}_\odot$),
  2. $t \approx 6 - 800$ Myr NS – MS ($0.9 - 1.5\,{\rm M}_\odot$),
  3. $t \approx 430 - 1100$ Myr NS – HG ($0.6 - 1.0\,{\rm M}_\odot$),
  4. $t \approx 540 - 4400$ Myr NS – RG ($\sim 1.0\,{\rm M}_\odot$);

  (BH–black hole, NS – neutron star, MS – main sequence, HG – H–rich Hertzsprung gap, RG – red giant.)
- Neutron–star ULXs may reach luminosities as high as those of black–hole ULXs ($L_{\rm X,max} > 10^{41}\,{\rm erg\,s^{-1}}$).
- The most luminous ULXs ($L_{\rm X} \gtrsim 10^{41}\,{\rm erg\,s^{-1}}$) contain HG donors (black–hole ULXs; $M_2 \approx 1.2 - 3.7\,{\rm M}_\odot$) or evolved helium stars (neutron–star ULXs; $M_2 \approx 1.7 - 2.6\,{\rm M}_\odot$), which overfill their Roche lobe and transfer mass on a thermal timescale. They form typically within 15 – 75 Myr after the ZAMS.

Finally, as seen in Table 6, the ULX population is in all cases strongly dominated by sources with $L_X < 3 \times 10^{39}\,{\rm erg\,s^{-1}}$.

The results of Wiktorowicz et al. (2017) describe the evolution of the *intrinsic* ULX population, but since at least these sources are supposed to be beamed, the observed ULX population is different. Wiktorowicz et al. (2019) use the results of the population synthesis described above to derive the properties of the observed ULX population. They use the fiducial model defined in Wiktorowicz et al. (2017) but remove the beaming saturation–condition because

Table 6 Number of ULXs per MWEG 100 Myr after the start of stellar formation

Metallicity		$> 10^{39}$ erg s^{-1}	$> 3 \times 10^{39}$ erg s^{-1}	$> 10^{40}$ erg s^{-1}	$> 10^{41}$ erg s^{-1}
	#ULX	407	65	14	0.5
$Z_\odot$	#BHULX	372	40	4.7	0.38
	#NSULX	35	25	9.4	0.13
	#ULX	7281	1940	200	12
$Z_\odot/10$	#BHULX	7200	1900	180	11
	#NSULX	81	40	12	0.43
	#ULX	5000	2400	390	15
$Z_\odot/100$	#BHULX	4900	2400	380	15
	#NSULX	16	12	9.0	0.075

(Adapted from Wiktorowicz et al., 2017). 'MWEG' = 'Milky Way Equivalent Galaxy'.

extremely beamed sources are not only hard to observe, but also extremely rare and short-lived so have no influence on the final results.

Mondal et al. (2020) discuss the full range of possible ways of making a ULX. This paper also estimates that at low redshift, about 50 per cent of merging BH–BH progenitor binaries evolved through a ULX phase. They find that observed ULXs with black–hole accretors typically emit isotropically ($b = 1$) and undergo nuclear–timescale mass transfer, whereas those with neutron–star accretors are predominantly beamed (typically $b = 0.7 - 0.2$) and in most cases the mass transfer occurs on a thermal timescale. They also show that beaming depends on the stellar environment; very young (burst) populations (age < 10 Myr), dominated by black-hole ULXs, are significantly beamed, while black–hole ULXs in older stellar populations are usually isotropic emitters. In contrast, the majority of neutron-star ULXs are always beamed, irrespective of the stellar environment. The ratio of neutron–star ULXs to black–hole ULXs is higher in the total sample than in the observed sample. For continuous star formation, black–hole ULXs typically outnumber the NS ULXs in the observed sample. Black–hole ULXs also outnumber neutron–star ULXs in the observed sample for burst stellar formation at early times, but after the star formation burst, neutron star ULXs tend to dominate the observed population. Here the observed neutron–star ULXs represent only 20% of the total neutron–star ULX population, and many are expected to be obscured (in the absence of precession, which may act to bring some into view, see, Dauser et al., 2017; Middleton et al., 2018).

Heida et al. (2019b) pointed out that the growing number of ULXs with (tentatively identified) red–supergiant donors (for which RLOF is dynamically unstable) motivates the study of wind-driven mass–transfer, previously neglected in the context of ULXs. Including wind accreting X-ray binary models into `StarTrack`, Wiktorowicz et al. (2021) showed that wind-fed ULXs can constitute a significant fraction of all ULXs, and in some environments may even be the majority. Bondi-Hoyle-Lyttleton accretion is a standard form of accretion in `StarTrack` (Belczynski et al., 2008, 2020) and they additionally adapt a wind RLOF (WRLOF) scheme from Mohamed and Podsiadlowski (2007), already used by Iłkiewicz et al. (2019), to analyse the relation between SNIa and wide symbiotic binaries. With somewhat optimistic assumptions for wind–accretion efficiency, they suggest that wind-fed ULXs should not be neglected. The wind–fed ULX sample they found contains a significant fraction of RSG companions, supporting the suggestion that the apparent superposition of some ULXs and RSGs results from coexistence as a binary. Although some of these systems will evolve into double compact objects, none of the ULX systems with a RSG donor is a viable progenitor of double compact object mergers with $t_{\rm merge} < 10$Gyr, because they have large orbital separations.

It is important to note that models of wind accretion and emission suffer from serious uncertainties. This problem cannot be solved only by extensive numerical simulations, but also requires systematic quantitative observational data. Wiktorowicz et al. (2017, 2019) and Wiktorowicz et al. (2021) do not consider the origin or evolution of neutron–star magnetic fields, considering that this problem contains too many unknowns to be worth including in population synthesis.

Kuranov et al. (2020) do not share this view, and perform population synthesis of binaries containing magnetized neutron stars only. They assume solar abundances and neglect magnetic–field evolution. They consider two accretion–flow models: the standard Shakura and Sunyaev (1973) model adapted to magnetized accretors by Chashkina et al. (2017) and for the supercritical accretion they use the Chashkina et al. (2019) "advective" model (for the suitability of

advection models to describe accretion onto neutron stars see Sect. 3.8.2). The results are presented as a $P_s - L_x$ figure on which the observed values of 10 PULXs are superposed. Although Be/X stars are not present in the modelled population, the authors use also four Be/ULX data points. When the data points fall into the regions where the calculations predict the existence of PULXs, they consider this as a success of their model. Which is the case for all accretion modes, only NGC 5097 ULX-1 shows, as usual, some resistance. They conclude that that standard evolution of close–binary systems and accretion onto magnetised neutron–stars can quantitatively explain the observed properties of PULX i.e. their X-ray luminosities, spin periods, orbital periods and masses of visual components, without assuming beamed X-ray emission. In a model galaxy with star formation rate 3–5 $M_\odot\,yr^{-1}$ "there can exist" several PULXs. If PULXs are not beamed, it is not clear why they are invisible in the Milky Way. (The single PULX observed in the Galaxy is in a Be-X binary – because of their uncertain evolutionary status, such systems are not taken into account in population syntheses.) Kuranov et al. (2020) assert that discovery of powerful winds from PULXs with $L_X \sim 10^{41}\,\mathrm{erg\,s^{-1}}$ may be a signature of super-Eddington accretion onto magnetised neutron stars. If so, this raises two questions. First, in the absence of beaming why would such sources not be observable as bright X-ray sources? Second, with such powerful outflows, how one can avoid beaming? Finally, although these authors say that, in their models, the PULXs represent "a subset of neutron stars at the stage of disc accretion in close binary systems with luminosity $L_X > 10^{39}\,\mathrm{erg\,s^{-1}}$", they take no account of the other distinctive parameter that singles out the PULXs: their extremely high spin frequency derivatives $\dot{\nu}$ (see Fig. 13).

3.14. Winds and Feedback from ULXs

We have seen (in Section 3.6) that the characteristic feature of the disc–wind beaming picture of ULXs is that their accretion discs eject the super–Eddington part of the mass transferred to them. If $-\dot{M} \gg \dot{M}_{\rm Edd}$ this is of course most of the transferred mass. In all cases we expect a quasispherical accretion disc wind, with most of the emitted radiation escaping through open funnels along the disc axis. The dynamics of the wind are controlled by radiation pressure, and therefore by the electron–scattering optical depth distribution of the outflow. For modest Eddington factors $\dot{m} = \dot{M}/\dot{M}_{\rm Edd} \gtrsim 1$ we expect that the photons produced by the conversion of accretion energy will find the open funnels around the rotational axis of the disc and so escape after only a small number of scatterings. The front–back symmetry of non–relativistic electron scattering means that, on average, a photon gives up all of its momentum (but not energy) in each scattering event. Then we expect that the accretion disc wind should have an outgoing momentum of order that in the original radiation field, i.e. just the Eddington momentum

$$\dot{M}v \simeq \frac{L_{\rm Edd}}{c}, \tag{105}$$

so that the outflow velocity is

$$v \simeq \frac{\eta}{\dot{m}}c \sim 0.1c, \tag{106}$$

where $\eta = L_{\rm Edd}/\dot{M}_{\rm Edd}c^2 \simeq 0.1$ is the radiative efficiency of accretion (King and Pounds, 2003). Winds with the properties (105, 106) are seen in many AGN (see King and Pounds, 2015, for a review), where the Eddington factor is unlikely to be large.

But in ULXs, the condition $\dot{m} \gg 1$ is a distinct possibility, and here we expect considerably more scatterings before a photon finds the open funnels around the disc axis and escapes. Instead we expect that the radiation field may put a significant fraction of its energy into the wind, i.e.

$$\frac{1}{2}\dot{M}v'^2 \simeq l' L_{\rm Edd}, \tag{107}$$

with $l' \sim 1$. This now leads to an outflow velocity

$$v' \simeq \left(\frac{2l'\eta}{\dot{m}}\right)^{1/2} c, \tag{108}$$

(King and Muldrew, 2016). Despite the different physics involved, the two types of winds have surprisingly similar velocities, i.e.

$$v,\ v' \simeq 0.05c - 0.2c \tag{109}$$

for values $10 < \dot{m} < 100$. Observations show the presence of winds with velocities of this order in most ($\sim 70\%$) ULXs (Sect. 2.2.1).

An observer not located very close to the central accretion disc axis (i.e. not in the narrow beam defining the ULX) would observe the photosphere of the quasi-spherical wind. King and Muldrew (2016) show that this has radius

$$R_{\rm ph} \simeq 10^4 \times l'^{-1/2} \dot{M}_{w10}^{3/2} {\eta_{0.1}}^{-3/2} M_{10}\,{\rm km} \tag{110}$$

and effective temperature

$$T_{\rm eff} = 1 \times 10^6 l'^{1/4} \dot{M}_{w10}^{-3/4} \eta_{0.1}^{3/4} M_{10}^{-1/4}\,{\rm K} \tag{111}$$

where $\dot{M}_{w10}$ is the wind mass outflow rate in units of $10\dot{m}$, $\eta_{0.1}$ is the accretor efficiency in units of 0.1, and M_{10} is the accretor mass in units of $10\,{\rm M}_\odot$.

Objects almost precisely like this – blackbody emission at temperature $\sim$ 100 eV from photospheres of order (110) are observed, in the form of the ultraluminous supersoft sources (ULSS, Kong and Di Stefano, 2003). Evidently these are ULXs viewed 'from the side'. The well–know extreme Galactic source SS433 is probably a member of this class, as we discuss below.

ULX/ULS winds are quasispherical, and hypersonic with respect to the interstellar medium (ISM) surrounding the ULX, and so must be slowed in a strong reverse shock against it. A weaker forward shock propagates into the surrounding ISM ahead of the contact discontinuity between the ULX wind and the ISM, sweeping this gas outwards in a shell. As in the similar problem for supermassive black holes (see King and Pounds, 2015, for a review) the nature of ULX feedback on the interstellar gas depends on whether the shock slowing the ULX wind is cooled by radiation losses within a flow timescale or not. In the first case, where the shock is efficiently cooled, most of the energy of the wind is lost to radiation, and the wind transmits only its momentum to the ISM. If instead shock cooling is inefficient, the outflow gives all of its energy adiabatically to this gas. These two cases are often called momentum–driven and energy–driven respectively[16].

For ULXs, we will see that feedback is in practice always energy–driven, which in turn means that ULXs generally have a significant effect on their surroundings. The temperature of the reverse shock slowing the ULX wind is $T_s \sim m_{\rm H}u^2/k \sim 10^{10} - 10^{11}$ K, where $u \sim v, v'$, and k is Boltzmann's constant. Since this is far higher than the $T \lesssim 10^8$ K radiation field of the ULX, inverse Compton scattering off the ULX radiation field is the main cooling mechanism, as in the SMBH case. (The thermal bremsstrahlung timescale is far longer.) King (2003) shows that the ratio of Compton cooling time and flow timescale R/v is

$$\frac{t_c}{t_{\rm flow}} \simeq \frac{2}{3}\left(\frac{m_e}{m_p}\right)^2 \frac{R}{R_g}\frac{c}{v} \tag{112}$$

at distance R from the ULX. From (109) this defines a cooling radius

$$R_c = 5 \times 10^5 R_g \sim 5 \times 10^{10}\,{\rm cm}, \tag{113}$$

which is generally smaller than the ULX binary's orbit. Shock cooling is never important for ULX outflows, and all ULX feedback is energy–driven.

We can easily see the effect of this feedback. If the interstellar gas has uniform density ρ and the shock exerts pressure P on it, momentum conservation at the radius R of the interface between the ULX wind and the ISM gives

$$4\pi R^2 P = \frac{{\rm d}}{{\rm d}t}\left(\frac{4\pi}{3}R^3\rho\dot{R}\right) \tag{114}$$

so that

$$\frac{P}{\rho} = \frac{1}{3}R\ddot{R} + \dot{R}^2. \tag{115}$$

[16]In SMBH accretion, feedback switches from momentum– to energy–driven once the SMBH mass reaches the $M - \sigma$ value $M \propto \sigma^4$. This fixes the limit to SMBH mass growth, since the ISM gas ultimately fuelling its growth is expelled at this point, in a galaxy–wide high–speed outflow. See King & Pounds (2015)

Since energy is transmitted adiabatically from the wind we have

$$\frac{\mathrm{d}}{\mathrm{d}t}\left[2\pi R^3 P\right] = L_{\rm Edd} - P\frac{\mathrm{d}}{\mathrm{d}t}\left(\frac{4\pi R^3}{3}\right)$$

Eliminating P gives the equation of motion for the shock as

$$\frac{L_{\rm Edd}}{2\pi\rho} = \frac{1}{3}R^4\dddot{R} + \frac{8}{3}R^3\dot{R}\ddot{R} + 5R^2\dot{R}^3 \tag{116}$$

All solutions of this equation tend to the attractor

$$R = \left(\frac{125\,L_{\rm Edd}}{101\pi\rho}\right)^{1/5} t^{3/5}, \tag{117}$$

(cf Eq. 18) or numerically

$$R \simeq 50\left(\frac{L_{39}}{\rho_{-25}}\right)^{1/5} t_5^{3/5}\ {\rm pc}, \tag{118}$$

where $L_{39} = L_{\rm Edd}/10^{39}\,{\rm erg\,s^{-1}}$, $t_5 = t/10^5$ yr, and $\rho_{-25} = \rho/10^{-25}\,{\rm g\,cm^{-3}}$. The conditions correspond to a ULX with a lifetime of order the thermal timescale of a massive companion star, driving a wind into an ISM of number density $\sim 0.1\,{\rm cm^{-3}}$ H atoms per $\rm cm^3$. The shell of swept–up ISM gas expands at a speed

$$\dot{R} = 300\left(\frac{L_{39}}{\rho_{-25}}\right)^{1/5} t_5^{-2/5}\ {\rm km\,s^{-1}}, \tag{119}$$

so the forward shock into the ISM is much weaker than the reverse shock slowing the ULX wind (cf Eq. 109). For longer thermal timescales or more powerful wind mechanical luminosities, $L_{39} \sim 10$, and the predicted nebulae can have sizes ∼ 500 pc. Observations (Sec. 2.6) show that many ULXs are associated with wind–blown nebulae of order 50 - 500 pc in size. These are significantly larger than supernova remnants (∼ 3 pc).

3.14.1. SS433

The well–known extreme Galactic binary system SS433 fits closely into this picture. King et al. (2000b) show that it probably has a mass transfer rate implying $\dot{m}_{w10} \sim 10^3$, and $t_5 \sim 1$. The mechanical luminosity is then. $\sim 10^{39}\,{\rm erg\,s^{-1}}$. For a $10\,{\rm M_\odot}$ black hole accretor, Eq. (119) implies a spherical nebula (excluding the 'ears' formed by the precessing jets) comparable with the observed ∼ 30 pc size. King and Muldrew (2016) note that this implies a quasispherical wind speed close to the observed velocity width $\sim 1500\,{\rm km\,s^{-1}}$ of the so-called stationary H alpha line. Despite its very high mass transfer rate, SS433 is a remarkably weak X–ray source – Watson et al. (1986) estimate $L_X \simeq 10^{36}\,{\rm erg\,s^{-1}}$ and a mechanical luminosity $\simeq 10^{39}\,{\rm erg\,s^{-1}}$, and it is likely that the softer (< 10 keV) X–rays come only from the prominent jets the system produces (whilst the harder X-ray emission may originate from scattering inside the wind-cone, Middleton et al. 2021b). In a detailed study, Begelman et al. (2006) show that SS433 has a viewing angle appropriate to a ULS, but is not observable as one: from (111) we have $kT_{\rm eff} \sim 10 \approx$, eV, which is too soft to be detectable as this system is heavily reddened ($A_V \simeq 7$). SS433 is distinctive because of the huge periodic redshift and blueshifts of the H–alpha lines emitted by its precessing jets. These evidently result from its extreme Eddington factor, and precess (and are baryon–loaded and slowed to $0.26c$) probably because they are deflected by a thick precessing central disc. As a mark of this, the precession rate of the jets does show power at the binary orbital period (Begelman et al., 2006).

3.15. Be–star ULXs

The luminosity of ULXs is generally variable, but two classes of ultraluminous X-ray sources are transient. One of these consists of systems appearing in the transient X-ray sky only as ultraluminous sources. We discuss these in the next section.

The other class is a small set of systems which normally appear as high–mass X–ray binaries, but occasionally become ULXs. This class has only recently been recognised, but actually includes A0538-66, the first system observed

to have an apparently super–Eddington X–ray luminosity (White and Carpenter, 1978), and also the Milky Way's only known ULX, Swift J0243.6+6124, first detected on 3 October 2017 during a giant X-ray outburst (Kennea et al., 2017, see Table 2). In all these systems, a neutron star, often with a noticeable magnetic field, accretes from a much more massive Be (or Oe) star in a wide eccentric orbit.

Be stars are unusual in having a large disc of material surrounding their rotational equator. The origin of the disc is unclear, but is evidently related to the star's rotation, and possibly mediated by small–scale surface magnetic fields (Nixon and Pringle, 2020, for a recent discussion). Be X–ray binaries generally produce most of their X–ray emission when the neutron star is near pericentre and interacts with the circumstellar disc. The X–rays therefore generally indicate the orbital period.

But it is now known that, on a much longer timescale, this interaction is much stronger, and the system becomes a ULX. The origin of this behaviour is probably von Zeipel–Lidov–Kozai (ZLK) oscillations of the Be star disc (Martin et al., 2014). Highly misaligned test particle orbits around one component of a binary cyclically exchange inclination for eccentricity (von Zeipel, 1910; Kozai, 1962; Lidov, 1962). This process conserves the component of the angular momentum orthogonal to the binary orbital plane, i.e.

$$(1 - e_p^2)^{1/2} \cos i_p = \text{constant}. \tag{120}$$

Here i_p is the inclination of the particle orbit to the binary orbit and e_p is the test–particle eccentricity. A test particle initially on a circular strongly misaligned orbit oscillates to closer alignment. Then $|\cos i_p|$ increases, requiring larger e_p. The oscillations occur only if the initial inclination i_{p0} inclination satisfies

$$\cos^2 i_{p0} < \frac{3}{5}, \tag{121}$$

so $39^{\rm o} < i_{p0} < 141^{\rm o}$, and the maximum eccentricity that an initially circular test orbit can reach is

$$e_{\rm max} = \left(1 - \frac{5}{3}\cos^2 i_{p0}\right)^{1/2}. \tag{122}$$

Martin et al. (2014) show that this test–particle behaviour extends to full hydrodynamical discs, which undergo global KL cycles of the disc inclination and eccentricity. The spins of Be stars are known in general to be strongly misaligned from the orbits of their neutron star companions in Be – X–ray binaries, probably as a result of the asymmetric supernova explosion producing the neutron star. At maximum disc eccentricity, it is likely that the neutron star accretes much more gas from the Be–star disc, and this may turn it into a ULX. Global KL cycles typically have periods an order of magnitude longer than the binary orbit, so the transition to the ULX state is relatively infrequent.

3.16. Modelling transient ULXs

Accretion discs in low-mass X-ray binaries are subject to a thermal–viscous instability when the mass transfer rate from the companion falls below a critical value depending mainly on the size of the disc (orbital period; Coriat et al., 2009). The instability is similar to that in cataclysmic variables leading to dwarf nova outbursts (Lasota, 2001; Hameury, 2020), but X-ray self–irradiation of the disc plays a crucial role both in the instability criterion (van Paradijs, 1996) and the outburst development (King and Ritter, 1998; Dubus et al., 1999, 2001).

The thermal–viscous disc instability is naturally associated with low mass transfer rates, but since the critical accretion rate increases strongly with the disc size, for large enough binary systems, even super–Eddington mass transfer can correspond to an unstable disc (Lasota et al., 2015; Hameury and Lasota, 2020). So for sufficiently large orbital periods, accreting systems have large unstable discs and can produce outbursts bright enough to explain some ULXs (King et al., 2000b). Although as discussed in Section 2.5.2 it is very difficult to determine the binary parameters of these distant systems, it is clear that many of them have giant or supergiant companion stars (Section 2.5.1) and have orbital periods longer than 2 days. Several ULXs are classified as transient (see e.g. Brightman et al. 2020a). Usually their light curves are only sparsely covered, but the recent well sampled observations of a transient ULX source in the galaxy M 51 by Brightman et al. (2020a) provides a light curve that can be compared with model predictions. Some long–period, sub-Eddington X-ray transients show long-lasting outbursts (tens of years), so some apparently steady ULXs could actually be transients observed during long outbursts.

The critical rate below which a disc is unstable is well approximated by:

$$\dot{M}^{+}_{\rm crit} \approx 2.4 \times 10^{19} M_1^{-0.4} f_{\rm irr}^{-0.5} \left(\frac{R_{\rm out}}{10^{12}\ \rm cm}\right)^{2.1}\ \ {\rm g\,s^{-1}}, \tag{123}$$

where $R_{\rm out}$ is the outer disc radius and $f_{\rm irr} = \eta_{\rm t} C/(5 \times 10^{-4})$ and C is defined through

$$\sigma T_{\rm irr}^4 = C \frac{\eta_{\rm t} \dot{M} c^2}{4\pi r^2}. \tag{124}$$

C contains all the physics of the irradiation process, and $\eta_{\rm t}$. Dubus et al. (2001) found that the light curves of low-mass X-ray transients are reasonably well reproduced, and Coriat et al. (2012) found that the corresponding stability criterion provides the observed division of sources into steady and outbursting, if one uses a constant $\eta_{\rm t} C$ of order 10^{-3}. The radiative accretion efficiency η_t is defined as the ratio of the true luminosity (without the beaming factor) to c^2, and is therefore:

$$\begin{aligned} \eta_{\rm t} &= 0.1 && \text{if } \dot{m} < 1, \\ &= 0.1(1 + \ln \dot{m})/\dot{m} && \text{if } \dot{m} \geq 1. \end{aligned} \tag{125}$$

From Eq. (123) it follows that neutron-star ULXs may be unstable for super–Eddington mass transfer rates at orbital periods $\gtrsim$ 10 days (slightly shorter for black-hole ULXs). But if the front fails to reach the outer disc edge, the peak outburst luminosity is given by Eq. (123) with $R_{\rm out}$ replaced by $R_{\rm tr,max} \leq R_{\rm out}$, where $R_{\rm tr,max}$ is the maximum radius reached by the instability–triggering heating front. In this case, the peak luminosity can be up to 50 times larger (Hameury and Lasota, 2020). This means that wide binaries in which the mass transfer is sub-Eddington might become transient ULXs at, and close to, the maximum outburst luminosity if their discs are unstable.

Hameury and Lasota (2020) derived analytical formulae describing typical X-ray transient light curves with great accuracy. They apply also to transient ULXs. When the heating front brings the whole disc to a hot state ($R_{\rm tr,max} \approx R_{\rm out}$), the $\dot{M}(t)$ relation during the decay from outburst maximum is very well described by (Ritter and King, 2001)[17]

$$\dot{M} = \dot{M}_{\rm max} \left[1 + \frac{t}{t_0}\right]^{-10/3}, \tag{126}$$

where the integration constant t_0 is given by:

$$t_0 = 3.19 \alpha_{0.2}^{-4/5} M_1^{1/4} R_{12}^{5/4} \dot{M}_{\rm max,19}^{-3/10}\ \rm yr, \tag{127}$$

with $\dot{M}_{\rm max,19} = \dot{M}_{\rm max}/10^{19}\ {\rm g\,s^{-1}}$. Here t_0 is *not* the characteristic timescale of disc evolution, which is instead

$$\tau = \frac{M_d}{\dot{M}} = 0.81 \psi f^{-0.3} M_1^{0.37} f_{\rm irr}^{0.15} R_{12}^{0.62} \alpha_{0.2}^{-0.8}\ \rm yr, \tag{128}$$

where M_d is the disc mass and $f = \dot{M}_{\rm max}/\dot{M}^{+}_{\rm crit}(r_{\rm out}) > 1$ (for the derivation see Hameury and Lasota, 2020). One can then relate the maximum outburst accretion rate to the characteristic decay time.

$$\dot{M}_{\rm max} = 2.0 \times 10^{19} \alpha_{0.2}^{2.71} f^{2.02} M_1^{-1.65} \left(\frac{\tau}{1\ \rm yr}\right)^{3.39} f_{\rm irr}^{-1.01}\ \ {\rm g\,s^{-1}}, \tag{129}$$

Then when both $\dot{M}_{\rm max}$ and τ are known from observations, this relation determines f, and hence $\dot{M}^{+}_{\rm crit}$ and the size of the accretion disc.

This phase of the outburst corresponds to a viscous decay, during which X–ray irradiation prevents the formation and propagation of a cooling front. This ends when the decreasing accretion rate falls to the critical value $\dot{M}^{+}_{\rm crit}$ and the front starts propagating into the disc.

---

[17]The corresponding formula in the original publication contains a misprint.

If the heating front is unable to reach the outer regions – which happens quite often in huge discs – the viscous decay phase is missing and, from the start, the decay-from-maximum $\dot{M}(t)$ relation corresponds to the cooling–front propagation, and has the form

$$\dot{M} = 1.31 \times 10^{17} \alpha_{0.2}^{2.71} M_1^{-1.65} f_{\rm irr}^{-1} \left[\xi \frac{(t_0' - t)}{1\ \rm yr} \right]^{3.39} \ {\rm g\,s^{-1}}, \tag{130}$$

where t_0' is a constant that is determined by the condition that, when the cooling front starts, $\dot{M}$ is equal to $\dot{M}^+_{\rm crit}$ at the maximum transition radius. Then t_0' can be written as:

$$t_0' = 4.64\, \xi^{-1} M_1^{0.37} f_{\rm irr}^{0.15} \alpha_{0.2}^{-0.8} r_{12}^{0.62}\ {\rm yr}, \tag{131}$$

and ξ is a constant to be calibrated by numerical simulations; it is found to be in the range $2.47 < \xi \lesssim 8.0$. Here t_0' is equal to the *duration* of this phase of the outburst, and can be directly compared to observations. As before, there exists a relation between $\dot{M}_{\rm max}$ and t_0':

$$\dot{M}_{\rm max} = 3.1 \times 10^{19} \alpha_{0.2}^{2.71} M_1^{-1.65} \left(\frac{\xi}{5} \frac{t_0'}{1\ \rm yr} \right)^{3.39} f_{\rm irr}^{-1.01} \ {\rm g\,s^{-1}}, \tag{132}$$

which is essentially the same as in Eq. (129), with $f = 1$.

It is important to realise that, for super-Eddington accretion rates, $\dot{M}(t)$ does not directly represent the observed $L_X(t)$ light curve, as the relation between the luminosity and accretion rate is no longer linear. Then when considering an outburst whose apparent luminosity is larger than $L_{\rm Edd}$ Hameury and Lasota (2020) use the following relations

$$\begin{aligned} L_{\rm x} &= (1 + \ln \dot{m}) \left[1 + \frac{\dot{m}^2}{\tilde{b}} \right] L_{\rm Edd} \qquad && \text{if } \dot{m} \geq 1 \\ &= \dot{m}\, L_{\rm Edd} && \text{if } \dot{m} < 1, \end{aligned} \tag{133}$$

where $b = (1 + \dot{m}^2/\tilde{b})^{-1}$ is a beaming term; the larger the beaming parameter $\tilde{b}$, the larger b and hence the smaller the beaming effect. Eq. (55) corresponds to $b = \tilde{b}/\dot{m}^2$ with $\tilde{b} = 73$. Since the beaming factor $\tilde{b}/\dot{m}^2$ applies only for $\dot{m} > \sqrt{\tilde{b}}$, in time-dependent calculations, one replaces it by $(1 + \dot{m}^2/\tilde{b})^{-1}$ in order to get a smooth transition with the case where beaming is negligible.

Further, when $\dot{m} \gg 1$ so that the apparent luminosity scales approximately as $\dot{m}^2$, the decay time of the luminosity $\tau_{\rm L}$ is one half of the decay time of the accretion rate, and Eq. (129) has to be written as:

$$\dot{m}_{\rm max} = 132\, \alpha_{0.2}^{2.71} f^{2.02} M_1^{-2.65} \left(\frac{\tau_{\rm L}}{1\ \rm yr} \right)^{3.39} f_{\rm irr}^{-1.01}. \tag{134}$$

If not all of the disc reaches the hot state, the total outburst duration is related to the maximum mass accretion rate via Eq. (132), and we must have:

$$\dot{m}_{\rm max} = 24.0\, \alpha_{0.2}^{2.71} M_1^{-2.65} \left(\frac{\xi}{5} \frac{t_0'}{1\ \rm yr} \right)^{3.39} f_{\rm irr}^{-1.01}, \tag{135}$$

where t_0' now refers to the outburst duration.

3.16.1. M51 XT-1

M51 XT-1 is currently the only ULX transient source whose light curve is suitable for comparison with the prediction of the disc–instability model. Figure 19 shows how observational data of M51 XT-1 (Brightman et al., 2020a) compare with the predictions of the disc–instability model when the light curve comes from Eqs. 126 and 130, combined with Eq. (133) with the beaming parameter $\tilde{b} = 73$. Two cases are shown. A 1.4 $M_\odot$ accreting neutron star with a disc size 4.8×10^{11} cm; and a 10 $M_\odot$ accreting black hole, with a disc extending to 4.9×10^{11} cm. As can be seen, the agreement is reasonably good, and as acceptable as the original fit with a power law with index $-5/3$

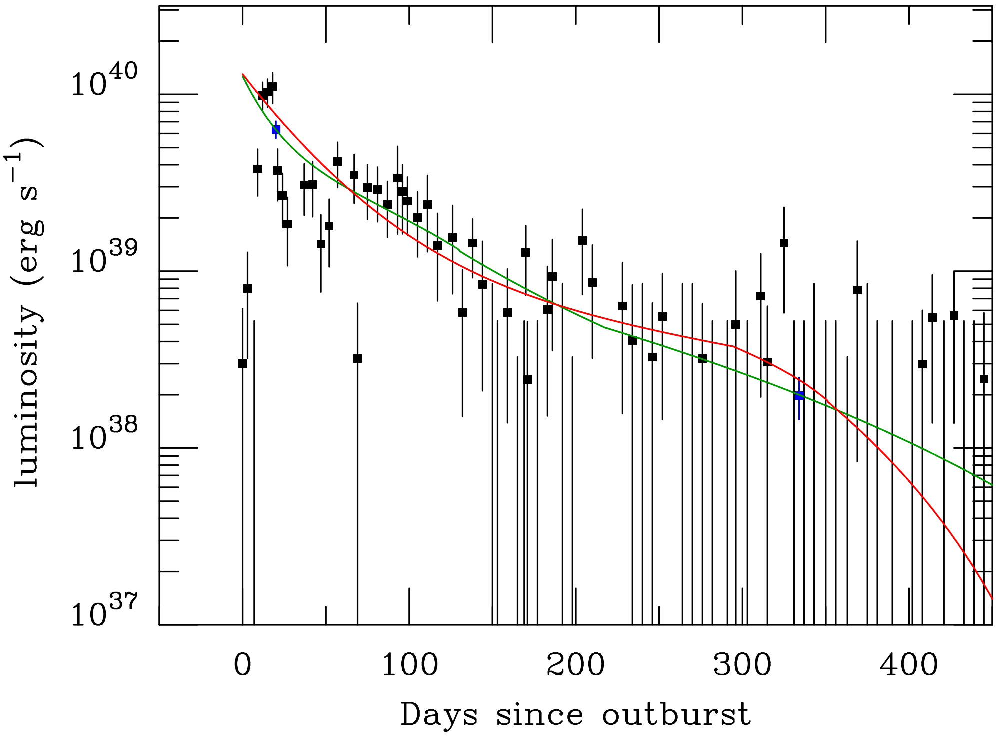


Figure 19 Observed flux from M51 XT-1 as compared with model predictions for a 1.4 $M_{\odot}$ neutron star (red curve) and a 10 $M_{\odot}$ black hole (green curve). Black points correspond to *SWIFT* data and blue points to *Chandra* or *XMM-Newton* observations (courtesy M. Brightman, see also Brightman et al., 2020a).

(Brightman et al., 2020a). These data can also be fitted with a 10 $M_{\odot}$ accreting black hole, with a disc extending to 4.9×10^{11} cm.

In the neutron star case, the maximum accretion rate is 6×10^{19} g s^{-1}, while in the black hole case it is 1.5×10^{20} g s^{-1}. Hence the emission from a black-hole system would not be beamed, but for a neutron-star accretor the beaming factor would be $b = 0.06$, as expected for $\dot{m} = 33$. The mass transfer rate can be very roughly estimated to be of order 1 – 2% of the maximum accretion rate, i.e. $1 - 3 \times 10^{18}$ g s^{-1}.

Hameury and Lasota (2020) showed that taking $\tilde{b} = 200$ instead of $\tilde{b} = 73$ in Eq. (133) also provides an acceptable fit, but $\tilde{b} = 20$ is excluded by the *Chandra* and *XMM-Newton* points, thus suggesting only moderate beaming.

3.16.2. HLX-1 in ESO 243-49

HLX-1 in the galaxy ESO 243-49 (Farrell et al., 2009) attracted a lot of attention as the best IMBH candidate among ULXs. It is the brightest ULX candidate known; its luminosity is variable and can exceed 10^{42} erg s^{-1} at maximum. Its association with the galaxy ESO 243-49 at a distance of 95 Mpc is fairly well established (Wiersema et al., 2010; Soria, 2013) so there is little doubt about its luminosity (see, however, Lasota et al., 2015). Greene et al. (2020) conclude that a self-consistent scenario is that HLX-1 is a central massive black hole on the low–mass end of the mass distribution of nucleated $10^9 - 10^{10}$ $M_{\odot}$ galaxies. Its small host galaxy was accreted and tidally stripped by ESO 243-49, leaving only the bare nuclear star cluster near the black hole (e.g., Mapelli et al. 2013). Star formation, perhaps encouraged by the merger, could have increased the capture rate for the hole to acquire a companion star on which it is currently feeding. Then by the definition adopted in this review HLX-1 is not an IMBH candidate, but was the central MBH of a small galaxy, which (unusually) has been accreted and disrupted by a larger one.

In line with this picture, HLX-1's historical light curve (see e.g. Godet et al. 2014) initially showed a promising series of almost annual outbursts, only to lose this quasi–periodicity later on. Subsequent to its discovery, a number of so–called QPE ('quasiperiodic eruption') sources have recently been found from the centres of small galaxies (e.g.

Miniutti et al. 2019, 2020; Arcodia et al. 2021). These can be modelled as tidal disruption near–misses (King 2020): instead of being fully disrupted by filling its tidal radius near the MBH (a tidal disruption event or TDE) an infalling star fills its tidal lobe only at the pericentre of a very eccentric orbit about the MBH. In the small galaxy GSN 069 the star is probably a low–mass white dwarf (King 2020), and the predicted CNO anomaly was later found (Sheng et al. 2021). It appears that this model works well for all the currently recognised QPE systems (King, 2022). These systems all have very short lifetimes as the orbits shrink under gravitational radiation, which is what drives the mass transfer.

Modelling HLX-1 instead as a transient IMBH source undergoing disc outbursts shows that the outburst timescales are incompatible with a central mass of $\gtrsim 10^4$ M$_\odot$, as would be required to explain the peak luminosity of 10^{41} erg s^{-1} (Hameury and Lasota 2020 and references therein).

3.17. Beaming or not?

The arguments in favour of luminosity beaming in PULXs presented above are simple and fundamental. The main one is that the observed X-ray luminosities of magnetic ULXs lie between 6 and 500 $L_{\rm Edd}$, with the classic (non BeX) systems having $L_X > 20 L_{\rm Edd}$. Even if mass is supplied at a super–Eddington rate, the luminosity is only $L \approx L_{\rm Edd}(1 + \ln \dot m)$, so even $\dot m \approx 1000\,(> 10^{-5}\,{\rm M_\odot yr^{-1}})$ produces only $\sim 8\,L_{\rm Edd}$.

Explaining these huge excess luminosities by appealing to super–strong magnetic fields appears unpromising. We have argued above that the presence of magnetars in PULXs is extremely unlikely. Among other problems, it requires a cosmic conspiracy confining magnetars to just these binary systems. Be–PULXs spend most of the time as standard pulsed X–ray sources, and clearly do not have magnetar–strength fields. Assertions that the "apparent luminosity [of PULXs] is close to the actual one" (Mushtukov et al., 2020) are rather surprising, especially when it is not explained how this is supposed to be achieved.

Mushtukov et al. (2020) refer to a table in King and Lasota (2020) to claim that these authors require $a = 1/b \sim 20$ for M82 ULX-2, NGC 7793 P13 and NGC 300 ULX1 and ~ 100 for NGC 5. But Table 3 shows that the values of $1/b$ for the first three sources are respectively 17, 6, 6, to which one can add 10 for ULX-7 in M51.

3.18. Measuring mass transfer via the orbital period derivative?

The most important parameter in understanding ULXs, as in any accreting system, is the instantaneous mass transfer rate $-\dot M_2$ in the host binary system. Unfortunately, precisely because we do not yet have a clear picture of how exactly the mass transfer rate specifies the luminosity of ULXs, it is difficult to measure $-\dot M_2$ directly from observation. But if we assume conservative mass transfer (i.e. conserving both total mass and angular momentum) we see from Section (3.11) that all quantities such as the companion mass M_2, the binary separation a, and by Kepler's law, the binary period $P \propto a^{3/2}$, evolve on the mass transfer timescale $M_2/(-\dot M_2)$ – see Eq. (104). This makes it tempting to use the much more easily measured orbital period derivative $\dot P$ to estimate $-\dot M_2$. The recent papers by Bachetti et al. (2021a,b) try to use this method for the ULX M82 X-2.

As we noted above, the problem of measuring $-\dot M_2$ is common to all interacting binary systems, not simply ULXs. There is a long history of efforts to find $-\dot M_2$ by using $\dot P$ and assuming conservative evolution, going back at least to early studies of cataclysmic variables (where a low–mass main–sequence star transfers mass to a white dwarf in a very circular orbit). But all these attempts give uniformly disappointing results – not least because even the *sign* of $\dot P$ often flatly contradicts that expected from conservative evolution. The underlying reason for these difficulties is that relations like (104) hold *only* if the quantities $\dot P, -\dot M_2$ are *averages over a timescale long compared with the time t_H for the Roche lobe to move one scaleheight within the donor star*. This requirement arises because stars have smooth density distributions rather than sharp edges. On timescales shorter than t_H the instantaneous value of $\dot P$ is always in practice dominated by large but short–term effects, with varying signs often in conflict with the long–term rate. This point has been made repeatedly in the literature, going back at least to Pringle (1975); see also e.g. Ritter (1988) and Frank et al. 2002 (Section 4.4). Pringle (1975) concluded that "... an accurate estimate of the rate of mass transfer cannot be deduced from a change of binary period".

In response to Bachetti et al. (2021a), King and Lasota (2021) estimated $t_H \sim 1000$ yr for M82 X-2. Then observations of $\dot P$ over humanly accessible timescales cannot give information about $-\dot M_2$. King and Lasota (2021) further pointed out that direct application of the method of Bachetti et al. (2021a) to three well–studied X–ray transients with known values of $\dot P$ (Nova Muscae 1991, XTE J1118+480, A0620–00, see González Hernández et al. 2017 and

references therein) was possible, but not encouraging. These Roche–lobe filling systems are all currently in the faint quiescent state. Under the assumption of conservative evolution, their values of $\dot{P}$ would instead predict that all three of them should currently have high mass transfer rates. Their accretion discs should therefore be steady rather than transient, putting them stably in bright states – indeed Nova Muscae 1991 would actually be a ULX. The subsequent publication (Bachetti et al., 2021b) does not answer these points.

4. Conclusions

Table 7 summarises how various models of ULX behaviour compare with observations. The case for disc–wind beaming appears fairly strong, and is so far compatible with a large body of data. Given that the photon–bubble model does not appear promising, this is the only model which can straightforwardly apply to both black–hole and neutron–star accretors.

Other models come into consideration if we allow for the idea that ULXs might not be a single homogenous population, but instead consist of various different types of systems (as in the example of long and short gamma–ray bursts). IMBH clearly cannot account for PULXs or Be–star ULXs, and have not been widely tested in other aspects. Unless their masses are $> 3 \times 10^4\,M_\odot$ they cannot account for the striking universal $L_{\rm soft} \propto T^{-4}$ behaviour of ULX soft X–ray components with luminosities $> 3 \times 10^{39}\,{\rm erg\,s^{-1}}$.

Table 7 Models of ULXs

model	blackbody $L \propto T^{-4}$	winds & nebulae	evolution	luminosity fn	$L > 3 \times 10^{40}\,{\rm erg\,s^{-1}}$	pulsing	BeX	BH & NS
disc-wind beaming	yes	yes	yes	yes	yes	yes	yes	yes
magnetic beaming	no	?	yes	?	yes	yes	no	no
IMBH	needs $M > 3 \times 10^4\,M_\odot$	?	?	?	yes	no	no	no
magnetars	no	no	fieldstrength?	no	no	yes	no	no
photon bubble	no	no	?	?	no	no	no	yes
oriented jets	?	?	?	?	no	?	no	?

Observations of Be – X–ray binaries pose a particular problem for models invoking magnetic beaming, as they make regular transitions between normal Be X–ray binary states to PULXs, and back again, when their mass supply rates are increased or decreased by Kozai–Lidov cycles. None of the Be–star ULXs is observationally distinct from other Be X–ray systems when it is in its usual Be X–ray binary state, and in the ULX state these systems have all the same properties as other PULXs, including a markedly more rapid spin up rate (cf Fig 13. None of the Be X–ray binaries appears to have a very strong magnetic field. This makes it inescapable that very strong dipole magnetic fields are not *required* for making a PULX. Highly–magnetic PULXs might then at most constitute some fraction of the PULX population, but there is so far no clinching demonstration that *any* PULX contains a neutron star with this kind of field. Even then there remains the difficulty that this model requires us to believe that strong–field neutron stars in binaries are unobservable unless the companion star supplies them with mass at a super–Eddington rate.

Acknowledgments

JPL was supported by a grant from the French Space Agency CNES. MM thanks G. Israel, S. Carpano, M. Bachetti, F. Fuerst, S. Tsygankov, R. Sathyaprakash and G. Rodriguez for providing the data for Figure 7.

Appendix A. "Standard" X-ray pulsars

To illustrate the fact that PULXs differ from standard X-ray pulsars not only in luminosity $> 10^{39}\,{\rm erg\,s^{-1}}$, but also in their very large spin-up rates $\dot{\nu} > 10^{-10}\,{\rm s^{-2}}$, we used the XRP sample with known luminosities and spin-up rates (Table Appendix A) as compiled by Ziolkowski (1985).

Table A.8 Observed properties of 'classical' X-ray pulsars

Name	L_X(max) [erg s^{-1}]	P_s [s]	$\dot{\nu}$ [s^{-2}]
SMC X-1	5.0×10^{38}	0.71	2.6×10^{-11}
Cen X-3	5.0×10^{37}	4.84	1.9×10^{-12}
GX 1+4	4.0×10^{37}	122	5.2×10^{-12}
4U 0115+63	3.4×10^{37}	3.61	2.2×10^{-12}
A 0535+26	1.0×10^{37}	104	3.0×10^{-12}
Her X-1	1.0×10^{37}	1.24	8.5×10^{-14}
Vela X-1	1.5×10^{36}	283	5.6×10^{-13}
GX 301-2	1.0×10^{36}	696	3.8×10^{-13}
X-Per	3.9×10^{33}	835	6.4×10^{-15}

References

Abarca, D., Kluźniak, W., Sądowski, A., Sep. 2018. Radiative GRMHD simulations of accretion and outflow in non-magnetized neutron stars and ultraluminous X-ray sources. MNRAS 479, 3936–3951.

Abarca, D., Parfrey, K., Kluźniak, W., Jul. 2021. Beamed emission from a neutron-star ULX in a GRRMHD simulation. arXiv e-prints, arXiv:2107.01149.

Abbott, B. P., Abbott, R., Abbott, T. D., Abernathy, M. R., Acernese, F., Ackley, K., Adams, C., Adams, T., Addesso, P., Adhikari, R. X., et al., Feb. 2016. Astrophysical Implications of the Binary Black-hole Merger GW150914. ApJL 818, L22.

Abbott, R., Abbott, T. D., Abraham, S., Acernese, F., Ackley, K., Adams, e., Oct. 2020. GWTC-2: Compact Binary Coalescences Observed by LIGO and Virgo During the First Half of the Third Observing Run. arXiv e-prints, arXiv:2010.14527.

Abolmasov, P., Fabrika, S., Sholukhova, O., Afanasiev, V., Mar. 2007a. Spectroscopy of optical counterparts of ultraluminous X-ray sources. Astrophysical Bulletin 62 (1), 36–51.

Abolmasov, P., Fabrika, S., Sholukhova, O., Kotani, T., Sep. 2008. Optical Spectroscopy of the ULX-Associated Nebula MF16. arXiv e-prints, arXiv:0809.0409.

Abolmasov, P. K., Swartz, D. A., Fabrika, S., Ghosh, K. K., Sholukhova, O., Tennant, A. F., Oct. 2007b. Optical Spectroscopy of the Environment of a ULX in NGC 7331. ApJ 668 (1), 124–129.

Abramowicz, M., Jaroszynski, M., Sikora, M., Feb. 1978. Relativistic, accreting disks. A&A 63, 221–224.

Abramowicz, M. A., Czerny, B., Lasota, J. P., Szuszkiewicz, E., Sep. 1988. Slim accretion disks. ApJ 332, 646–658.

Agrawal, V. K., Nandi, A., Feb. 2015. Discovery of a quasi-periodic oscillation in the ultraluminous X-ray source IC 342 X-1: XMM-Newton results. MNRAS 446 (4), 3926–3931.

Alston, W. N., Pinto, C., Barret, D., D'Aì, A., Del Santo, M., Earnshaw, H., Fabian, A. C., Fuerst, F., Kara, E., Kosec, P., Middleton, M. J., Parker, M. L., Pintore, F., Robba, A., Roberts, T. P., Sathyaprakash, R., Walton, D., Ambrosi, E., Aug. 2021. Quasi-periodic dipping in the ultraluminous X-ray source, NGC 247 ULX-1. MNRAS 505 (3), 3722–3729.

Andersen, B. C., Ransom, S. M., Aug. 2018. A Fourier Domain "Jerk" Search for Binary Pulsars. ApJL 863 (1), L13.

Anderson, P. W., Itoh, N., Jul. 1975. Pulsar glitches and restlessness as a hard superfluidity phenomenon. Nature 256 (5512), 25–27.

Archibald, R. F., Kaspi, V. M., Tendulkar, S. P., Scholz, P., Sep. 2016. A Magnetar-like Outburst from a High-B Radio Pulsar. ApJL 829 (1), L21.

Arcodia, R., Merloni, A., Nandra, K., Buchner, J., Salvato, M., Pasham, D., Remillard, R., Comparat, J., Lamer, G., Ponti, G., Malyali, A., Wolf, J., Arzoumanian, Z., Bogensberger, D., Buckley, D. A. H., Gendreau, K., Gromadzki, M., Kara, E., Krumpe, M., Markwardt, C., Ramos-Ceja, M. E., Rau, A., Schramm, M., Schwope, A., Apr. 2021. X-ray quasi-periodic eruptions from two previously quiescent galaxies. Nature 592 (7856), 704–707.

Arévalo, P., Uttley, P., Apr. 2006. Investigating a fluctuating-accretion model for the spectral-timing properties of accreting black hole systems. MNRAS 367 (2), 801–814.

Arnaud, K., Dorman, B., Gordon, C., Oct. 1999. XSPEC: An X-ray spectral fitting package.

Asvarov, A. I., Jan. 2014. Size distribution of supernova remnants and the interstellar medium: the case of M 33. A&A 561, A70.

Atapin, K., Fabrika, S., Caballero-García, M. D., Jun. 2019. Ultraluminous X-ray sources with flat-topped noise and QPO. MNRAS 486 (2), 2766–2779.

Bachetti, M., Harrison, F. A., Walton, D. J., Grefenstette, B. W., Chakrabarty, D., Fürst, F., Barret, D., Beloborodov, A., Boggs, S. E., Christensen, F. E., Craig, W. W., Fabian, A. C., Hailey, C. J., Hornschemeier, A., Kaspi, V., Kulkarni, S. R., Maccarone, T., Miller, J. M., Rana, V., Stern, D., Tendulkar, S. P., Tomsick, J., Webb, N. A., Zhang, W. W., Oct. 2014. An ultraluminous X-ray source powered by an accreting neutron star. Nature 514, 202–204.

Bachetti, M., Heida, M., Maccarone, T., Huppenkothen, D., Israel, G. L., Barret, D., Brightman, M., Brumback, M., Earnshaw, H. P., Forster, K., Fürst, F., Grefenstette, B. W., Harrison, F. A., Jaodand, A. D., Madsen, K. K., Middleton, M., Pike, S. N., Pilia, M., Poutanen, J., Stern, D., Tomsick, J. A., Walton, D. J., Webb, N., Wilms, J., Dec. 2021a. Orbital decay in M82 X-2. arXiv e-prints, arXiv:2112.00339.

Bachetti, M., Heida, M., Maccarone, T., Huppenkothen, D., Israel, G. L., Barret, D., Brightman, M., Brumback, M., Earnshaw, H. P., Forster, K., Fürst, F., Grefenstette, B. W., Harrison, F. A., Jaodand, A. D., Madsen, K. K., Middleton, M., Pike, S. N., Pilia, M., Poutanen, J., Stern, D., Tomsick, J. A., Walton, D. J., Webb, N., Wilms, J., Dec. 2021b. Orbital decay in M82 X-2. arXiv e-prints, arXiv:2112.00339v2.

Bachetti, M., Maccarone, T. J., Brightman, M., Brumback, M. C., Fürst, F., Harrison, F. A., Heida, M., Israel, G. L., Middleton, M. J., Tomsick, J. A., Webb, N. A., Walton, D. J., Mar. 2020. All at Once: Transient Pulsations, Spin-down, and a Glitch from the Pulsating Ultraluminous X-Ray Source M82 X-2. ApJ 891 (1), 44.

Bachetti, M., Rana, V., Walton, D. J., Barret, D., Harrison, F. A., Boggs, S. E., Christensen, F. E., Craig, W. W., Fabian, A. C., Fürst, F., Grefenstette, B. W., Hailey, C. J., Hornschemeier, A., Madsen, K. K., Miller, J. M., Ptak, A. F., Stern, D., Webb, N. A., Zhang, W. W., Dec. 2013. The Ultraluminous X-Ray Sources NGC 1313 X-1 and X-2: A Broadband Study with NuSTAR and XMM-Newton. ApJ 778 (2), 163.

Baldassare, V. F., Dickey, C., Geha, M., Reines, A. E., Jul. 2020. Populating the Low-mass End of the M_{BH}-σ Relation. ApJL 898 (1), L3.

Basko, M. M., Sunyaev, R. A., May 1976. The limiting luminosity of accreting neutron stars with magnetic fields. MNRAS 175, 395–417.

Begelman, M. C., Apr. 2002. Super-Eddington Fluxes from Thin Accretion Disks? ApJL 568, L97–L100.

Begelman, M. C., King, A. R., Pringle, J. E., Jul. 2006. The nature of SS433 and the ultraluminous X-ray sources. MNRAS 370, 399–404.

Belczynski, K., Dec. 2020. The Most Ordinary Formation of the Most Unusual Double Black Hole Merger. ApJL 905 (2), L15.

Belczynski, K., Bulik, T., Fryer, C. L., Ruiter, A., Valsecchi, F., Vink, J. S., Hurley, J. R., May 2010. On the Maximum Mass of Stellar Black Holes. ApJ 714, 1217–1226.

Belczynski, K., Kalogera, V., Bulik, T., Jun. 2002. A Comprehensive Study of Binary Compact Objects as Gravitational Wave Sources: Evolutionary Channels, Rates, and Physical Properties. ApJ 572, 407–431.

Belczynski, K., Kalogera, V., Rasio, F. A., Taam, R. E., Zezas, A., Bulik, T., Maccarone, T. J., Ivanova, N., Jan. 2008. Compact Object Modeling with the StarTrack Population Synthesis Code. ApJs 174, 223–260.

Belczynski, K., Klencki, J., Fields, C. E., Olejak, A., Berti, E., Meynet, G., Fryer, C. L., Holz, D. E., O'Shaughnessy, R., Brown, D. A., Bulik, T., Leung, S. C., Nomoto, K., Madau, P., Hirschi, R., Kaiser, E., Jones, S., Mondal, S., Chruslinska, M., Drozda, P., Gerosa, D., Doctor, Z., Giersz, M., Ekstrom, S., Georgy, C., Askar, A., Baibhav, V., Wysocki, D., Natan, T., Farr, W. M., Wiktorowicz, G., Coleman Miller, M., Farr, B., Lasota, J. P., Apr. 2020. Evolutionary roads leading to low effective spins, high black hole masses, and O1/O2 rates for LIGO/Virgo binary black holes. A&A 636, A104.

Belloni, T. M., Altamirano, D., Jun. 2013. High-frequency quasi-periodic oscillations from GRS 1915+105. MNRAS 432 (1), 10–18.

Berghea, C. T., Dudik, R. P., Jun. 2012. Spitzer Observations of MF 16 Nebula and the Associated Ultraluminous X-Ray Source. ApJ 751 (2), 104.

Berghea, C. T., Dudik, R. P., Weaver, K. A., Kallman, T. R., Jan. 2010a. The First Detection of [O IV] from an Ultraluminous X-Ray Source with Spitzer. I. Observational Results for Holmberg II ULX. ApJ 708 (1), 354–363.

Berghea, C. T., Dudik, R. P., Weaver, K. A., Kallman, T. R., Jan. 2010b. The First Detection of [O IV] from an Ultraluminous X-ray Source with Spitzer. II. Evidence for High Luminosity in Holmberg II ULX. ApJ 708 (1), 364–374.

Bhattacharya, D., van den Heuvel, E. P. J., Jan. 1991. Formation and evolution of binary and millisecond radio pulsars. Physical Reports 203 (1-2), 1–124.

Binder, B., Levesque, E. M., Dorn-Wallenstein, T., Aug. 2018. No Strong Geometric Beaming in the Ultraluminous Neutron Star Binary NGC 300 ULX-1 (SN 2010da) from Swift and Gemini. ApJ 863 (2), 141.

Bonnet-Bidaud, J. M., van der Klis, M., Apr. 1981. Long term X-ray observations of SMC X-1 including a turn-on. A&A 97, 134–138.

Brice, N., Zane, S., Turolla, R., Wu, K., Jun. 2021. Super-eddington emission from accreting, highly magnetized neutron stars with a multipolar magnetic field. MNRAS 504 (1), 701–715.

Brightman, M., Earnshaw, H., Fürst, F., Harrison, F. A., Heida, M., Israel, G., Pike, S., Stern, D., Walton, D. J., Jun. 2020a. Swift Monitoring of M51: A 38 day Superorbital Period for the Pulsar ULX7 and a New Transient Ultraluminous X-Ray Source. ApJ 895 (2), 127.

Brightman, M., Harrison, F., Walton, D. J., Fuerst, F., Hornschemeier, A., Zezas, A., Bachetti, M., Grefenstette, B., Ptak, A., Tendulkar, S., Yukita, M., Jan. 2016. Spectral and Temporal Properties of the Ultraluminous X-Ray Pulsar in M82 from 15 years of Chandra Observations and Analysis of the Pulsed Emission Using NuSTAR. ApJ 816 (2), 60.

Brightman, M., Harrison, F. A., Bachetti, M., Xu, Y., Fürst, F., Walton, D. J., Ptak, A., Yukita, M., Zezas, A., Mar. 2019. A ~60 day Super-orbital Period Originating from the Ultraluminous X-Ray Pulsar in M82. ApJ 873 (2), 115.

Brightman, M., Harrison, F. A., Fürst, F., Middleton, M. J., Walton, D. J., Stern, D., Fabian, A. C., Heida, M., Barret, D., Bachetti, M., Apr. 2018. Magnetic field strength of a neutron-star-powered ultraluminous X-ray source. Nature Astronomy 2, 312–316.

Brightman, M., Walton, D. J., Xu, Y., Earnshaw, H. P., Harrison, F. A., Stern, D., Barret, D., Jan. 2020b. Spectral Evolution of the Ultraluminous X-Ray Sources M82 X-1 and X-2. ApJ 889 (1), 71.

Brorby, M., Kaaret, P., Prestwich, A., Jul. 2014. X-ray binary formation in low-metallicity blue compact dwarf galaxies. MNRAS 441 (3), 2346–2353.

Bykov, S. D., Gilfanov, M. R., Tsygankov, S. S., Filippova, E. V., Oct. 2022. ULX pulsar Swift J0243.6+6124 observations with NuSTAR: dominance of reflected emission in the super-Eddington state. MNRAS 516 (2), 1601–1611.

Campana, S., Stella, L., Kennea, J. A., Sep. 2008. Swift Observations of SAX J1808.4-3658: Monitoring the Return to Quiescence. ApJL 684 (2), L99.

Canuto, V., Lodenquai, J., Ruderman, M., May 1971. Thomson Scattering in a Strong Magnetic Field. Phys. Rev. D 3 (10), 2303–2308.

Cappelluti, N., Predehl, P., Böhringer, H., Brunner, H., Brusa, M., Burwitz, V., Churazov, E., Dennerl, K., Finoguenov, A., Freyberg, M., Friedrich, P., Hasinger, G., Kenziorra, E., Kreykenbohm, I., Lamer, G., Meidinger, N., Mühlegger, M., Pavlinsky, M., Robrade, J., Santangelo, A., Schmitt, J., Schwope, A., Steinmitz, M., Strüder, L., Sunyaev, R., Tenzer, C., Jan 2011. eROSITA on SRG. A X-ray all-sky survey mission. Memorie della Societa Astronomica Italiana Supplementi 17, 159.

Carpano, S., Haberl, F., Maitra, C., Vasilopoulos, G., May 2018. Discovery of pulsations from NGC 300 ULX1 and its fast period evolution. MNRAS 476, L45–L49.

Castro-Tirado, A. J., Brandt, S., Lund, N., Aug. 1992. GRS 1915+105. IAU Circ 5590, 2.

Chandra, A. D., Roy, J., Agrawal, P. C., Choudhury, M., Jul. 2020. Study of recent outburst in the Be/X-ray binary RX J0209.6-7427 with AstroSat: a new ultraluminous X-ray pulsar in the Magellanic Bridge? MNRAS 495 (3), 2664–2672.

Chashkina, A., Abolmasov, P., Poutanen, J., Sep. 2017. Super-Eddington accretion on to a magnetized neutron star. MNRAS 470 (3), 2799–2813.

Chashkina, A., Lipunova, G., Abolmasov, P., Poutanen, J., Jun. 2019. Super-Eddington accretion discs with advection and outflows around magnetized neutron stars. A&A 626, A18.

Christodoulou, D. M., Laycock, S. G. T., Kazanas, D., Oct. 2019. Meta-analysis of electron cyclotron resonance absorption features detected in high-mass X-ray binaries. Research in Astronomy and Astrophysics 19 (10), 146.

Churazov, E., Gilfanov, M., Revnivtsev, M., Mar. 2001. Soft state of Cygnus X-1: stable disc and unstable corona. MNRAS 321 (4), 759–766.

Clark, J. S., Ritchie, B. W., Najarro, F., Langer, N., Negueruela, I., May 2014. A VLT/FLAMES survey for massive binaries in Westerlund 1. IV. Wd1-5 - binary product and a pre-supernova companion for the magnetar CXOU J1647-45? A&A 565, A90.

Colbert, E. J. M., Mushotzky, R. F., Jul. 1999. The Nature of Accreting Black Holes in Nearby Galaxy Nuclei. ApJ 519, 89–107.

Copperwheat, C., Cropper, M., Soria, R., Wu, K., Apr. 2007. Irradiation models for ULXs and fits to optical data. MNRAS 376 (3), 1407–1423.

Corbet, R. H. D., Laycock, S., Coe, M. J., Marshall, F. E., Markwardt, C. B., Jul. 2004. Monitoring and Discovering X-ray Pulsars in the Small Magellanic Cloud. In: Kaaret, P., Lamb, F. K., Swank, J. H. (Eds.), X-ray Timing 2003: Rossi and Beyond. Vol. 714 of American Institute of Physics Conference Series. pp. 337–341.

Coriat, M., Corbel, S., Buxton, M. M., Bailyn, C. D., Tomsick, J. A., Körding, E., Kalemci, E., Nov. 2009. The infrared/X-ray correlation of GX 339-4: probing hard X-ray emission in accreting black holes. MNRAS 400, 123–133.

Coriat, M., Fender, R. P., Dubus, G., Aug. 2012. Revisiting a fundamental test of the disc instability model for X-ray binaries. MNRAS 424, 1991–2001.

Cseh, D., Corbel, S., Kaaret, P., Lang, C., Grisé, F., Paragi, Z., Tzioumis, A., Tudose, V., Feng, H., Apr. 2012. Black Hole Powered Nebulae and a Case Study of the Ultraluminous X-Ray Source IC 342 X-1. ApJ 749 (1), 17.

Cseh, D., Grisé, F., Kaaret, P., Corbel, S., Scaringi, S., Groot, P., Falcke, H., Körding, E., Nov. 2013. Towards a dynamical mass of the ultraluminous X-ray source NGC 5408 X-1. MNRAS 435 (4), 2896–2902.

Cseh, D., Kaaret, P., Corbel, S., Grise, F., Lang, C., Kording, E., Falcke, H., Jonker, P. G., Miller-Jones, J. C. A., Farrell, S., Yang, Y. J., Paragi, Z., Frey, S., Mar. 2014. Unveiling recurrent jets of the ULX Holmberg II X-1: evidence for a massive stellar-mass black hole? MNRAS 439, L1–L5.

Cseh, D., Miller-Jones, J. C. A., Jonker, P. G., Grisé, F., Paragi, Z., Corbel, S., Falcke, H., Frey, S., Kaaret, P., Körding, E., Sep. 2015. The evolution of a jet ejection of the ultraluminous X-ray source Holmberg II X-1. MNRAS 452 (1), 24–31.

Cui, W., Jun. 1997. Evidence for "Propeller" Effects in X-Ray Pulsars GX 1+4 and GRO J1744-28. ApJL 482 (2), L163–L166.

Dage, K. C., Kundu, A., Thygesen, E., Bahramian, A., Haggard, D., Irwin, J. A., Maccarone, T. J., Nair, S., Peacock, M. B., Strader, J., Zepf, S. E., Mar. 2021. Three Ultraluminous X-ray Sources Hosted by Globular Clusters in NGC 1316. arXiv e-prints, arXiv:2103.16576.

Dage, K. C., Zepf, S. E., Peacock, M. B., Bahramian, A., Noroozi, O., Kundu, A., Maccarone, T. J., May 2019. X-ray spectral variability of ultraluminous X-ray sources in extragalactic globular clusters. MNRAS 485 (2), 1694–1707.

Dage, K. C., Zepf, S. E., Thygesen, E., Bahramian, A., Kundu, A., Maccarone, T. J., Peacock, M. B., Strader, J., Sep. 2020. X-ray spectroscopy of newly identified ULXs associated with M87's globular cluster population. MNRAS 497 (1), 596–608.

Dai, H. L., Li, X. D., May 2006. Accretion torque on magnetized neutron stars. A&A 451 (2), 581–585.

Dall'Osso, S., Perna, R., Papitto, A., Bozzo, E., Stella, L., Dec. 2015. The accretion regimes of a highly magnetised NS: the unique case of NuSTAR J095551+6940.8. ArXiv e-prints.

Dauser, T., Middleton, M., Wilms, J., Apr. 2017. Modelling the light curves of ultraluminous X-ray sources as precession. MNRAS 466, 2236–2241.

Davis, S. W., Narayan, R., Zhu, Y., Barret, D., Farrell, S. A., Godet, O., Servillat, M., Webb, N. A., Jun. 2011. The Cool Accretion Disk in ESO 243-49 HLX-1: Further Evidence of an Intermediate-mass Black Hole. ApJ 734 (2), 111.

De Marco, B., Ponti, G., Miniutti, G., Belloni, T., Cappi, M., Dadina, M., Muñoz-Darias, T., Dec. 2013. Time lags in the ultraluminous X-ray source NGC 5408 X-1: implications for the black hole mass. MNRAS 436 (4), 3782–3791.

Dewangan, G. C., Griffiths, R. E., Rao, A. R., Apr. 2006. Quasi-periodic Oscillations and Strongly Comptonized X-Ray Emission from Holmberg IX X-1. ApJL 641 (2), L125–L128.

Dib, R., Kaspi, V. M., Mar. 2014. 16 yr of RXTE Monitoring of Five Anomalous X-Ray Pulsars. ApJ 784 (1), 37.

Dib, R., Kaspi, V. M., Gavriil, F. P., Sep. 2009. Rossi X-Ray Timing Explorer Monitoring of the Anomalous X-ray Pulsar 1E 1048.1 - 5937: Long-term Variability and the 2007 March Event. ApJ 702 (1), 614–630.

Dolan, J. F., Boyd, P. T., Fabrika, S., Tapia, S., Bychkov, V., Panferov, A. A., Nelson, M. J., Percival, J. W., van Citters, G. W., Taylor, D. C., Taylor, M. J., Nov. 1997. SS 433 in the ultraviolet. A&A 327, 648–655.

Dominik, M., Belczynski, K., Fryer, C., Holz, D. E., Berti, E., Bulik, T., Mandel, I., O'Shaughnessy, R., Nov. 2012. Double Compact Objects. I. The Significance of the Common Envelope on Merger Rates. ApJ 759, 52.

Done, C., Gierliński, M., Kubota, A., Dec. 2007. Modelling the behaviour of accretion flows in X-ray binaries. Everything you always wanted to know about accretion but were afraid to ask. A&Ar 15 (1), 1–66.

Dopita, M. A., Payne, J. L., Filipović, M. D., Pannuti, T. G., Dec. 2012. The physical parameters of the microquasar S26 in the Sculptor Group galaxy NGC 7793. MNRAS 427 (2), 956–967.

Doroshenko, V., Santangelo, A., Ducci, L., Jul. 2015. Searching for coherent pulsations in ultraluminous X-ray sources. A&A 579, A22.

Doroshenko, V., Tsygankov, S., Santangelo, A., May 2018. Orbit and intrinsic spin-up of the newly discovered transient X-ray pulsar Swift J0243.6+6124. A&A 613, A19.

Dubus, G., Hameury, J.-M., Lasota, J.-P., Jul. 2001. The disc instability model for X-ray transients: Evidence for truncation and irradiation. A&A 373, 251–271.

Dubus, G., Lasota, J.-P., Hameury, J.-M., Charles, P., Feb. 1999. X-ray irradiation in low-mass binary systems. MNRAS 303, 139–147.

Dudik, R. P., Berghea, C. T., Roberts, T. P., Grisé, F., Singh, A., Pagano, R., Winter, L. M., Nov. 2016. Spitzer IRAC Observations of IR Excess in Holmberg IX X-1: A Circumbinary Disk or a Variable Jet? ApJ 831 (1), 88.

Duncan, R. C., Thompson, C., Jun. 1992. Formation of Very Strongly Magnetized Neutron Stars: Implications for Gamma-Ray Bursts. ApJL 392, L9.

Earnshaw, H. P., Heida, M., Brightman, M., Fürst, F., Harrison, F. A., Jaodand, A., Middleton, M. J., Roberts, T. P., Sathyaprakash, R., Stern, D., Walton, D. J., Mar. 2020. The (Re)appearance of NGC 925 ULX-3, a New Transient ULX. ApJ 891 (2), 153.

Earnshaw, H. P., Roberts, T. P., Middleton, M. J., Walton, D. J., Mateos, S., Mar 2019. A new, clean catalogue of extragalactic non-nuclear X-ray

sources in nearby galaxies. MNRAS 483 (4), 5554–5573.
Earnshaw, H. P., Roberts, T. P., Sathyaprakash, R., May 2018. Searching for propeller-phase ULXs in the XMM-Newton Serendipitous Source Catalogue. MNRAS 476 (3), 4272–4277.
Edge, W. R. T., Coe, M. J., Galache, J. L., McBride, V. A., Corbet, R. H. D., Markwardt, C. B., Laycock, S., Oct. 2004. Three new X-ray pulsars detected in the Small Magellanic Cloud and the positions of two other known pulsars determined. MNRAS 353 (4), 1286–1292.
Eggum, G. E., Coroniti, F. V., Katz, J. I., Jul. 1988. Radiation Hydrodynamic Calculation of Super-Eddington Accretion Disks. ApJ 330, 142.
Ekşi, K. Y., Andaç, İ. C., Çıkıntoğlu, S., Gençali, A. A., Güngör, C., Öztekin, F., Mar. 2015. The ultraluminous X-ray source NuSTAR J095551+6940.8: a magnetar in a high-mass X-ray binary. MNRAS 448, L40–L42.
El Mellah, I., Sundqvist, J. O., Keppens, R., Feb. 2019. Wind Roche lobe overflow in high-mass X-ray binaries. A possible mass-transfer mechanism for ultraluminous X-ray sources. A&A 622, L3.
Erkut, M. H., Türkoğlu, M. M., Ekși, K. Y., Alpar, M. A., Aug. 2020. On the Magnetic Fields, Beaming Fractions, and Fastness Parameters of Pulsating Ultraluminous X-Ray Sources. ApJ 899 (2), 97.
Evans, I. N., Primini, F. A., Glotfelty, K. J., Anderson, C. S., Bonaventura, N. R., Chen, J. C., Davis, J. E., Doe, S. M., Evans, J. D., Fabbiano, G., Galle, E. C., Gibbs, Danny G., I., Grier, J. D., Hain, R. M., Hall, D. M., Harbo, P. N., He, X. H., Houck, J. C., Karovska, M., Kashyap, V. L., Lauer, J., McCollough, M. L., McDowell, J. C., Miller, J. B., Mitschang, A. W., Morgan, D. L., Mossman, A. E., Nichols, J. S., Nowak, M. A., Plummer, D. A., Refsdal, B. L., Rots, A. H., Siemiginowska, A., Sundheim, B. A., Tibbetts, M. S., Van Stone, D. W., Winkelman, S. L., Zografou, P., Jul. 2010. The Chandra Source Catalog. ApJs 189 (1), 37–82.
Fabbiano, G., Jan. 1989. X-rays from normal galaxies. ARAA 27, 87–138.
Fabbiano, G., Zezas, A., Murray, S. S., Jun. 2001. Chandra Observations of "The Antennae" Galaxies (NGC 4038/9). ApJ 554, 1035–1043.
Fabian, A. C., Rees, M. J., Apr. 1979. SS 433: a double jet in action? MNRAS 187, 13P–16.
Fabrika, S., Jan. 2004. The jets and supercritical accretion disk in SS433. ASPRv 12, 1–152.
Fabrika, S., Ueda, Y., Vinokurov, A., Sholukhova, O., Shidatsu, M., Jul. 2015. Supercritical accretion disks in ultraluminous X-ray sources and SS 433. Nature Physics 11 (7), 551–553.
Fabrika, S. N., Atapin, K. E., Vinokurov, A. S., Sholukhova, O. N., Jan. 2021. Ultraluminous X-Ray Sources. Astrophysical Bulletin 76 (1), 6–38.
Falanga, M., Bozzo, E., Lutovinov, A., Bonnet-Bidaud, J. M., Fetisova, Y., Puls, J., May 2015. Ephemeris, orbital decay, and masses of ten eclipsing high-mass X-ray binaries. A&A 577, A130.
Falcke, H., Körding, E., Markoff, S., Feb. 2004. A scheme to unify low-power accreting black holes. Jet-dominated accretion flows and the radio/X-ray correlation. A&A 414, 895–903.
Farrell, S. A., Webb, N. A., Barret, D., Godet, O., Rodrigues, J. M., Jul. 2009. An intermediate-mass black hole of over 500 solar masses in the galaxy ESO243-49. Nature 460, 73–75.
Fender, R. P., Homan, J., Belloni, T. M., Jul. 2009. Jets from black hole X-ray binaries: testing, refining and extending empirical models for the coupling to X-rays. MNRAS 396 (3), 1370–1382.
Fender, R. P., Pooley, G. G., Brocksopp, C., Newell, S. J., Oct. 1997. Rapid infrared flares in GRS 1915+105: evidence for infrared synchrotron emission. MNRAS 290 (4), L65–L69.
Feng, H., Kaaret, P., Mar. 2008. Optical Counterpart of the Ultraluminous X-Ray Source IC 342 X-1. ApJ 675 (2), 1067–1075.
Feng, H., Tao, L., Kaaret, P., Grisé, F., nov 2016. Nature of the soft ulx in ngc 247: Super-eddington outflow and transition between the supersoft and soft ultraluminous regimes. The Astrophysical Journal 831 (2), 117.
URL `https://dx.doi.org/10.3847/0004-637X/831/2/117`
Ferland, G. J., Korista, K. T., Verner, D. A., Ferguson, J. W., Kingdon, J. B., Verner, E. M., Jul. 1998. CLOUDY 90: Numerical Simulation of Plasmas and Their Spectra. PASP 110 (749), 761–778.
Finke, J. D., Razzaque, S., Dec. 2017. The binary black hole merger rate from ultraluminous X-ray source progenitors. MNRAS 472, 3683–3691.
Fragile, P. C., Blaes, O. M., Anninos, P., Salmonson, J. D., Oct 2007. Global General Relativistic Magnetohydrodynamic Simulation of a Tilted Black Hole Accretion Disk. ApJ 668 (1), 417–429.
Fragos, T., Lehmer, B. D., Naoz, S., Zezas, A., Basu-Zych, A., Oct. 2013. Energy Feedback from X-Ray Binaries in the Early Universe. ApJL 776 (2), L31.
Frank, J., King, A., Raine, D. J., Jan. 2002. Accretion Power in Astrophysics: Third Edition.
Fuchs, Y., Koch Miramond, L., Ábrahám, P., Jan. 2006. SS 433: a phenomenon imitating a Wolf-Rayet star. A&A 445 (3), 1041–1052.
Fuerst, F., Walton, D. J., Heida, M., Bachetti, M., Pinto, C., Middleton, M. J., Brightman, M., Earnshaw, H. P., Barret, D., Fabian, A. C., Kretschmar, P., Pottschmidt, K., Ptak, A., Roberts, T., Stern, D., Webb, N., Wilms, J., May 2021. Long-term pulse period evolution of the ultra-luminous X-ray pulsar NGC 7793 P13. arXiv e-prints, arXiv:2105.04229.
Fürst, F., Walton, D. J., Harrison, F. A., Stern, D., Barret, D., Brightman, M., Fabian, A. C., Grefenstette, B., Madsen, K. K., Middleton, M. J., Miller, J. M., Pottschmidt, K., Ptak, A., Rana, V., Webb, N., Nov. 2016. Discovery of Coherent Pulsations from the Ultraluminous X-Ray Source NGC 7793 P13. ApJL 831, L14.
Fürst, F., Walton, D. J., Stern, D., Bachetti, M., Barret, D., Brightman, M., Harrison, F. A., Rana, V., Jan. 2017. Spectral Changes in the Hyperluminous Pulsar in NGC 5907 as a Function of Super-orbital Phase. ApJ 834 (1), 77.
Galloway, D. K., Morgan, E. H., Levine, A. M., Oct. 2004. A Frequency Glitch in an Accreting Pulsar. ApJ 613 (2), 1164–1172.
Gandhi, P., Dhillon, V. S., Durant, M., Fabian, A. C., Kubota, A., Makishima, K., Malzac, J., Marsh, T. R., Miller, J. M., Shahbaz, T., Spruit, H. C., Casella, P., Oct. 2010. Rapid optical and X-ray timing observations of GX339-4: multicomponent optical variability in the low/hard state. MNRAS 407 (4), 2166–2192.
Gao, Y., Wang, Q. D., Appleton, P. N., Lucas, R. A., Oct. 2003. Nonnuclear Hyper/Ultraluminous X-Ray Sources in the Starbursting Cartwheel Ring Galaxy. ApJL 596, L171–L174.
Ghosh, P., Lamb, F. K., Aug. 1979. Accretion by rotating magnetic neutron stars. II. Radial and vertical structure of the transition zone in disk accretion. ApJ 232, 259–276.
Giacomazzo, B., Perna, R., Jul. 2013. Formation of Stable Magnetars from Binary Neutron Star Mergers. ApJL 771 (2), L26.
Gilfanov, M., Churazov, E., Revnivtsev, M., Aug. 2000. Frequency-resolved spectroscopy of Cyg X-1: fast variability of the reflected emission in

the soft state. MNRAS 316 (4), 923–928.
Gladstone, J. C., Copperwheat, C., Heinke, C. O., Roberts, T. P., Cartwright, T. F., Levan, A. J., Goad, M. R., Jun. 2013. Optical Counterparts of the Nearest Ultraluminous X-Ray Sources. ApJs 206 (2), 14.
Gladstone, J. C., Roberts, T. P., Done, C., Aug. 2009. The ultraluminous state. MNRAS 397 (4), 1836–1851.
Goad, M. R., Roberts, T. P., Knigge, C., Lira, P., Sep. 2002. The optical counterpart of the ultraluminous X-ray source NGC 5204 X-1. MNRAS 335 (3), L67–L70.
Godet, O., Lombardi, J. C., Antonini, F., Barret, D., Webb, N. A., Vingless, J., Thomas, M., Oct. 2014. Implications of the Delayed 2013 Outburst of ESO 243-49 HLX-1. ApJ 793, 105.
González Hernández, J. I., Suárez-Andrés, L., Rebolo, R., Casares, J., Feb. 2017. Extremely fast orbital decay of the black hole X-ray binary Nova Muscae 1991. MNRAS 465 (1), L15–L19.
Greene, J. E., Strader, J., Ho, L. C., Aug. 2020. Intermediate-Mass Black Holes. ARAA 58, 257–312.
Grisé, F., Kaaret, P., Corbel, S., Cseh, D., Feng, H., Aug. 2013. A long-term X-ray monitoring of the ultraluminous X-ray source NGC 5408 X-1 with Swift reveals the presence of dips but no orbital period. MNRAS 433 (2), 1023–1038.
Grisé, F., Kaaret, P., Corbel, S., Feng, H., Cseh, D., Tao, L., Feb. 2012. Optical Emission of the Ultraluminous X-Ray Source NGC 5408 X-1: Donor Star or Irradiated Accretion Disk? ApJ 745 (2), 123.
Grisé, F., Pakull, M. W., Motch, C., Jan. 2006. The Ultraluminous X-ray Source in Holmberg IX and its Environment. In: Meurs, E. J. A., Fabbiano, G. (Eds.), Populations of High Energy Sources in Galaxies. Vol. 230. pp. 302–303.
Grisé, F., Pakull, M. W., Soria, R., Motch, C., Smith, I. A., Ryder, S. D., Böttcher, M., Jul. 2008. The ultraluminous X-ray source NGC 1313 X-2. Its optical counterpart and environment. A&A 486 (1), 151–163.
Gültekin, K., Cackett, E. M., Miller, J. M., Di Matteo, T., Markoff, S., Richstone, D. O., Nov. 2009. The Fundamental Plane of Accretion onto Black Holes with Dynamical Masses. ApJ 706 (1), 404–416.
Gúrpide, A., Godet, O., Koliopanos, F., Webb, N., Olive, J.-F., Feb. 2021. Long-term X-ray spectral evolution of Ultraluminous X-ray sources: implications on the accretion flow geometry and the nature of the accretor. arXiv e-prints, arXiv:2102.11159.
Gúrpide, A., Parra, M., Godet, O., Contini, T., Olive, J. F., Oct. 2022. MUSE spectroscopy of the ULX NGC 1313 X-1: A shock-ionised bubble, an X-ray photoionised nebula, and two supernova remnants. A&A 666, A100.
Hameury, J. M., Sep. 2020. A review of the disc instability model for dwarf novae, soft X-ray transients and related objects. Advances in Space Research 66 (5), 1004–1024.
Hameury, J. M., Lasota, J. P., Nov. 2020. Models of ultraluminous X-ray transient sources. A&A 643, A171.
Harrison, F. A., Craig, W. W., Christensen, F. E., Hailey, C. J., Zhang, W. W., Boggs, S. E., Stern, D., Cook, W. R., Forster, K., Giommi, P., Grefenstette, B. W., Kim, Y., Kitaguchi, T., Koglin, J. E., Madsen, K. K., Mao, P. H., Miyasaka, H., Mori, K., Perri, M., Pivovaroff, M. J., Puccetti, S., Rana, V. R., Westergaard, N. J., Willis, J., Zoglauer, A., An, H., Bachetti, M., Barrière, N. M., Bellm, E. C., Bhalerao, V., Brejnholt, N. F., Fuerst, F., Liebe, C. C., Markwardt, C. B., Nynka, M., Vogel, J. K., Walton, D. J., Wik, D. R., Alexander, D. M., Cominsky, L. R., Hornschemeier, A. E., Hornstrup, A., Kaspi, V. M., Madejski, G. M., Matt, G., Molendi, S., Smith, D. M., Tomsick, J. A., Ajello, M., Ballantyne, D. R., Baloković, M., Barret, D., Bauer, F. E., Blandford, R. D., Brandt, W. N., Brenneman, L. W., Chiang, J., Chakrabarty, D., Chenevez, J., Comastri, A., Dufour, F., Elvis, M., Fabian, A. C., Farrah, D., Fryer, C. L., Gotthelf, E. V., Grindlay, J. E., Helfand, D. J., Krivonos, R., Meier, D. L., Miller, J. M., Natalucci, L., Ogle, P., Ofek, E. O., Ptak, A., Reynolds, S. P., Rigby, J. R., Tagliaferri, G., Thorsett, S. E., Treister, E., Urry, C. M., Jun. 2013. The Nuclear Spectroscopic Telescope Array (NuSTAR) High-energy X-Ray Mission. ApJ 770 (2), 103.
Hashizume, K., Ohsuga, K., Kawashima, T., Tanaka, M., Aug. 2015. Radiation hydrodynamics simulations of wide-angle outflows from super-critical accretion disks around black holes. PASJ 67 (4), 58.
Heida, M., Harrison, F. A., Brightman, M., Fürst, F., Stern, D., Walton, D. J., Feb. 2019a. Searching for the Donor Stars of ULX Pulsars. ApJ 871 (2), 231.
Heida, M., Jonker, P. G., Torres, M. A. P., Kool, E., Servillat, M., Roberts, T. P., Groot, P. J., Walton, D. J., Moon, D. S., Harrison, F. A., Aug. 2014. Near-infrared counterparts of ultraluminous X-ray sources. MNRAS 442 (2), 1054–1067.
Heida, M., Jonker, P. G., Torres, M. A. P., Roberts, T. P., Walton, D. J., Moon, D. S., Stern, D., Harrison, F. A., Jun. 2016. Keck/MOSFIRE spectroscopy of five ULX counterparts. MNRAS 459 (1), 771–778.
Heida, M., Lau, R. M., Davies, B., Brightman, M., Fürst, F., Grefenstette, B. W., Kennea, J. A., Tramper, F., Walton, D. J., Harrison, F. A., Oct 2019b. Discovery of a Red Supergiant Donor Star in SN2010da/NGC 300 ULX-1. ApJL 883 (2), L34.
Heil, L. M., Vaughan, S., Jun. 2010. The linear rms-flux relation in an ultraluminous X-ray source. MNRAS 405 (1), L86–L89.
Heil, L. M., Vaughan, S., Roberts, T. P., Aug. 2009. A systematic study of variability in a sample of ultraluminous X-ray sources. MNRAS 397 (2), 1061–1072.
Hernández-García, L., Vaughan, S., Roberts, T. P., Middleton, M., Nov. 2015. X-ray time lags and non-linear variability in the ultraluminous X-ray sources NGC 5408 X-1 and NGC 6946 X-1. MNRAS 453 (3), 2877–2884.
Herold, H., May 1979. Compton and Thomson scattering in strong magnetic fields. Phys. Rev. D 19 (10), 2868–2875.
Hu, C.-P., Li, K. L., Kong, A. K. H., Ng, C. Y., Lin, L. C.-C., Jan. 2017. Swift Detection of a 65 Day X-Ray Period from the Ultraluminous Pulsar NGC 7793 P13. ApJL 835 (1), L9.
Hu, H., Inayoshi, K., Haiman, Z., Quataert, E., Kuiper, R., Mar. 2022. Long-term evolution of supercritical black hole accretion with outflows: a subgrid feedback model for cosmological simulations. arXiv e-prints, arXiv:2203.14994.
Iłkiewicz, K., Mikołajewska, J., Belczyński, K., Wiktorowicz, G., Karczmarek, P., Jun. 2019. Wind Roche lobe overflow as a way to make Type Ia supernovae from the widest symbiotic systems. MNRAS 485 (4), 5468–5473.
Inayoshi, K., Ostriker, J. P., Haiman, Z., Kuiper, R., May 2018. Low-density, radiatively inefficient rotating-accretion flow on to a black hole. MNRAS 476 (1), 1412–1426.
Inoue, A., Ohsuga, K., Kawashima, T., Apr. 2020. Pulsed fraction of super-critical column accretion flows on to neutron stars: Modeling of ultraluminous X-ray pulsars. PASJ 72 (2), 34.
Irwin, J. A., Brink, T. G., Bregman, J. N., Roberts, T. P., Mar. 2010. Evidence for a Stellar Disruption by an Intermediate-mass Black Hole in an

Extragalactic Globular Cluster. ApJL 712 (1), L1–L4.
Israel, G. L., Belfiore, A., Stella, L., Esposito, P., Casella, P., De Luca, A., Marelli, M., Papitto, A., Perri, M., Puccetti, S., Castillo, G. A. R., Salvetti, D., Tiengo, A., Zampieri, L., D'Agostino, D., Greiner, J., Haberl, F., Novara, G., Salvaterra, R., Turolla, R., Watson, M., Wilms, J., Wolter, A., Feb. 2017a. An accreting pulsar with extreme properties drives an ultraluminous x-ray source in NGC 5907. Science 355 (6327), 817–819.
Israel, G. L., Papitto, A., Esposito, P., Stella, L., Zampieri, L., Belfiore, A., Rodríguez Castillo, G. A., De Luca, A., Tiengo, A., Haberl, F., Greiner, J., Salvaterra, R., Sandrelli, S., Lisini, G., Mar. 2017b. Discovery of a 0.42-s pulsar in the ultraluminous X-ray source NGC 7793 P13. MNRAS 466, L48–L52.
Ivanova, N., Chaichenets, S., Fregeau, J., Heinke, C. O., Lombardi, J. C., J., Woods, T. E., Jul. 2010. Formation of Black Hole X-ray Binaries in Globular Clusters. ApJ 717 (2), 948–957.
Jaisawal, G. K., Naik, S., Sep. 2016. Detection of cyclotron resonance scattering feature in high-mass X-ray binary pulsar SMC X-2. MNRAS 461 (1), L97–L101.
Jansen, F., Lumb, D., Altieri, B., Clavel, J., Ehle, M., Erd, C., Gabriel, C., Guainazzi, M., Gondoin, P., Much, R., Munoz, R., Santos, M., Schartel, N., Texier, D., Vacanti, G., Jan. 2001. XMM-Newton observatory. I. The spacecraft and operations. A&A 365, L1–L6.
Jaroszynski, M., Abramowicz, M. A., Paczynski, B., Jan. 1980. Supercritical accretion disks around black holes. AcA 30 (1), 1–34.
Jenke, P., Wilson-Hodge, C. A., Oct. 2017. Fermi GBM detects pulsations from Swift J0243.6+6124. The Astronomer's Telegram 10812, 1.
Jiang, Y.-F., Stone, J. M., Davis, S. W., Nov. 2013. On the Thermal Stability of Radiation-dominated Accretion Disks. ApJ 778 (1), 65.
Jiang, Y.-F., Stone, J. M., Davis, S. W., Dec. 2014. A Global Three-dimensional Radiation Magneto-hydrodynamic Simulation of Super-Eddington Accretion Disks. ApJ 796, 106.
Jiang, Y.-F., Stone, J. M., Davis, S. W., Aug. 2019a. Super-Eddington Accretion Disks around Supermassive Black Holes. ApJ 880 (2), 67.
Jiang, Y.-F., Stone, J. M., Davis, S. W., Aug. 2019b. Super-Eddington Accretion Disks around Supermassive Black Holes. ApJ 880 (2), 67.
Jones, D. I., Andersson, N., Jul. 2001. Freely precessing neutron stars: model and observations. MNRAS 324 (4), 811–824.
Kaaret, P., Corbel, S., May 2009. A Photoionized Nebula Surrounding and Variable Optical Continuum Emission from the Ultraluminous X-Ray Source in NGC 5408. ApJ 697 (1), 950–956.
Kaaret, P., Corbel, S., Prestwich, A. H., Zezas, A., Jan. 2003. Radio Emission from an Ultraluminous X-ray Source. Science 299 (5605), 365–368.
Kaaret, P., Feng, H., Nov. 2007. Confirmation of the 62 Day X-Ray Periodicity from M82. ApJ 669 (1), 106–108.
Kaaret, P., Feng, H., Roberts, T. P., Aug. 2017. Ultraluminous X-Ray Sources. ARAA 55, 303–341.
Kaaret, P., Feng, H., Wong, D. S., Tao, L., May 2010. Direct Detection of an Ultraluminous Ultraviolet Source. ApJL 714 (1), L167–L170.
Kaaret, P., Simet, M. G., Lang, C. C., Jan 2006. The orbital period of the ultraluminous X-ray source in M 82. Science 311, 491–491.
Kaaret, P., Ward, M. J., Zezas, A., Jul. 2004. High-resolution imaging of the HeII λ4686 emission line nebula associated with the ultraluminous X-ray source in Holmberg II. MNRAS 351 (3), L83–L88.
Kajava, J. J. E., Poutanen, J., Sep 2008. Spectral variability of ultraluminous X-ray sources. In: Axelsson, M. (Ed.), American Institute of Physics Conference Series. Vol. 1054 of American Institute of Physics Conference Series. pp. 39–47.
Kajava, J. J. E., Poutanen, J., Sep. 2009. Spectral variability of ultraluminous X-ray sources. MNRAS 398, 1450–1460.
Kara, E., Pinto, C., Walton, D. J., Alston, W. N., Bachetti, M., Barret, D., Brightman, M., Canizares, C. R., Earnshaw, H. P., Fabian, A. C., Fürst, F., Kosec, P., Middleton, M. J., Roberts, T. P., Soria, R., Tao, L., Webb, N. A., Feb. 2020. Discovery of a soft X-ray lag in the ultraluminous X-ray source NGC 1313 X-1. MNRAS 491 (4), 5172–5178.
Kawashima, T., Mineshige, S., Ohsuga, K., Ogawa, T., Oct. 2016. A radiation-hydrodynamics model of accretion columns for ultra-luminous X-ray pulsars. PASJ 68 (5), 83.
Kawashima, T., Ohsuga, K., Feb. 2020. Super-critical column accretion on to strongly magnetized neutron stars in ULX pulsars. PASJ 72 (1), 15.
Kennea, J. A., Lien, A. Y., Krimm, H. A., Cenko, S. B., Siegel, M. H., Oct. 2017. Swift J0243.6+6124: Swift discovery of an accreting NS transient. The Astronomer's Telegram 10809, 1.
Khan, N., Middleton, M. J., Wiktorowicz, G., Dauser, T., Roberts, T. P., Wilms, J., Oct. 2021. The impact of precession on the observed population of ULXs. MNRAS.
King, A., May 2011. The Brightest Cluster X-ray Sources. ApJL 732, L28.
King, A., Mar. 2020. GSN 069 - A tidal disruption near miss. MNRAS 493 (1), L120–L123.
King, A., Jun. 2022. Quasi-Periodic Eruptions from Galaxy Nuclei. MNRAS.
King, A., Lasota, J.-P., May 2016. ULXs: Neutron stars versus black holes. MNRAS 458, L10–L13.
King, A., Lasota, J.-P., May 2019. No magnetars in ULXs. MNRAS 485, 3588–3594.
King, A., Lasota, J.-P., Mar. 2020. Pulsing and Non-Pulsing ULXs: the Iceberg Emerges. arXiv e-prints, arXiv:2003.14019.
King, A., Lasota, J.-P., Dec. 2021. One for the Future: measuring the mass transfer rate in the ULX M82 X-2 by using orbital period changes will take millenia. arXiv e-prints, arXiv:2112.03779.
King, A., Lasota, J.-P., Kluźniak, W., Jun. 2017. Pulsing ULXs: tip of the iceberg? MNRAS 468, L59–L62.
King, A., Muldrew, S. I., Jan. 2016. Black hole winds II: Hyper-Eddington winds and feedback. MNRAS 455 (2), 1211–1217.
King, A., Nealon, R., Aug. 2019. Supermassive black hole demographics: evading M - σ. MNRAS 487 (4), 4827–4831.
King, A., Pounds, K., Aug. 2015. Powerful Outflows and Feedback from Active Galactic Nuclei. ARAA 53, 115–154.
King, A. R., Sep. 2002. The brightest black holes. MNRAS 335, L13–L16.
King, A. R., Jan. 2004. Ultraluminous X-ray sources and star formation. MNRAS 347, L18–L20.
King, A. R., Feb 2009. Masses, beaming and Eddington ratios in ultraluminous X-ray sources. Monthly Notices of the Royal Astronomical Society 393 (1), L41–L44.
King, A. R., Begelman, M. C., Jul. 1999. Radiatively Driven Outflows and Avoidance of Common-Envelope Evolution in Close Binaries. ApJL 519 (2), L169–L171.
King, A. R., Davies, M. B., Ward, M. J., Fabbiano, G., Elvis, M., May 2001. Ultraluminous X-Ray Sources in External Galaxies. ApJL 552, L109–L112.
King, A. R., Pounds, K. A., Oct. 2003. Black hole winds. MNRAS 345 (2), 657–659.

King, A. R., Ritter, H., Jan. 1998. The light curves of soft X-ray transients. MNRAS 293 (1), L42–L48.
King, A. R., Ritter, H., Oct. 1999. Cygnus X-2, super-Eddington mass transfer, and pulsar binaries. MNRAS 309, 253–260.
King, A. R., Taam, R. E., Begelman, M. C., Feb. 2000a. The Evolutionary Status of SS 433. ApJL 530 (1), L25–L28.
King, A. R., Taam, R. E., Begelman, M. C., Feb. 2000b. The Evolutionary Status of SS 433. ApJL 530 (1), L25–L28.
Kippenhahn, R., Weigert, A., Jan. 1967. Entwicklung in engen Doppelsternsystemen I. Massenaustausch vor und nach Beendigung des zentralen Wasserstoff-Brennens. Z. Astrophys. 65, 251.
Kitaki, T., Mineshige, S., Ohsuga, K., Kawashima, T., Dec. 2018. Systematic two-dimensional radiation-hydrodynamic simulations of super-Eddington accretion flow and outflow: Comparison with the slim disk model. PASJ 70 (6), 108.
Kitaki, T., Mineshige, S., Ohsuga, K., Kawashima, T., Apr. 2021. The origins and impact of outflow from super-Eddington flow. PASJ 73 (2), 450–466.
Klencki, J., Moe, M., Gladysz, W., Chruslinska, M., Holz, D. E., Belczynski, K., Nov. 2018. Impact of inter-correlated initial binary parameters on double black hole and neutron star mergers. A&A 619, A77.
Klochkov, D., Staubert, R., Postnov, K., Shakura, N., Santangelo, A., Nov. 2009. Continuous monitoring of pulse period variations in Hercules X-1 using Swift/BAT. A&A 506 (3), 1261–1267.
Kluźniak, W., Lasota, J.-P., Mar. 2015. An ultraluminous nascent millisecond pulsar. MNRAS 448, L43–L47.
Koliopanos, F., Vasilopoulos, G., Buchner, J., Maitra, C., Haberl, F., Jan. 2019. Investigating ULX accretion flows and cyclotron resonance in NGC 300 ULX1. A&A 621, A118.
Koliopanos, F., Vasilopoulos, G., Godet, O., Bachetti, M., Webb, N. A., Barret, D., Dec. 2017. ULX spectra revisited: Accreting, highly magnetized neutron stars as the engines of ultraluminous X-ray sources. A&A 608, A47.
Kong, A. K. H., Di Stefano, R., Jun. 2003. A Luminous Recurrent Supersoft X-Ray Source in NGC 300. ApJL 590 (1), L13–L16.
Kong, A. K. H., Hu, C.-P., Lin, L. C.-C., Li, K. L., Jin, R., Liu, C. Y., Yen, D. C.-C., Oct. 2016. A possible 55-d X-ray period of the ultraluminous accreting pulsar M82 X-2. MNRAS 461, 4395–4399.
Kong, L.-D., Zhang, S., Zhang, S.-N., Ji, L., Doroshenko, V., Santangelo, A., Chen, Y.-P., Lu, F.-J., Ge, M.-Y., Wang, P.-J., Tao, L., Qu, J.-L., Li, T.-P., Liu, C.-Z., Liao, J.-Y., Chang, Z., Peng, J.-Q., Shui, Q.-C., Jul. 2022. Insight-HXMT Discovery of the Highest-energy CRSF from the First Galactic Ultraluminous X-Ray Pulsar Swift J0243.6+6124. ApjL 933 (1), L3.
Körding, E., Colbert, E., Falcke, H., Jun. 2005. A radio monitoring survey of ultra-luminous X-ray sources. A&A 436 (2), 427–436.
Körding, E., Falcke, H., Markoff, S., Jan. 2002. Population X: Are the super-Eddington X-ray sources beamed jets in microblazars or intermediate mass black holes? A&A 382, L13–L16.
Kosec, P., Pinto, C., Fabian, A. C., Walton, D. J., Feb. 2018a. Searching for outflows in ultraluminous X-ray sources through high-resolution X-ray spectroscopy. MNRAS 473 (4), 5680–5697.
Kosec, P., Pinto, C., Reynolds, C. S., Guainazzi, M., Kara, E., Walton, D. J., Fabian, A. C., Parker, M. L., Valtchanov, I., Dec. 2021. Ionized emission and absorption in a large sample of ultraluminous X-ray sources. MNRAS 508 (3), 3569–3588.
Kosec, P., Pinto, C., Walton, D. J., Fabian, A. C., Bachetti, M., Brightman, M., Fürst, F., Grefenstette, B. W., Sep. 2018b. Evidence for a variable Ultrafast Outflow in the newly discovered Ultraluminous Pulsar NGC 300 ULX-1. MNRAS 479 (3), 3978–3986.
Kotani, T., Kawai, N., Aoki, T., Doty, J., Matsuoka, M., Mitsuda, K., Nagase, F., Ricker, G., White, N. E., Aug. 1994. Discovery of the Double Doppler-Shifted Emission-Line Systems in the X-Ray Spectrum of SS 433. PASJ 46, L147–L150.
Kotko, I., Lasota, J. P., Sep. 2012. The viscosity parameter α and the properties of accretion disc outbursts in close binaries. A&A 545, A115.
Kotze, M. M., Charles, P. A., Feb. 2012. Characterizing X-ray binary long-term variability. MNRAS 420 (2), 1575–1589.
Kovlakas, K., Fragos, T., Schaerer, D., Mesinger, A., Jul. 2022. The ionizing and heating power of ultraluminous X-ray sources under the geometrical beaming model. arXiv e-prints, arXiv:2207.09331.
Kovlakas, K., Zezas, A., Andrews, J. J., Basu-Zych, A., Fragos, T., Hornschemeier, A., Kouroumpatzakis, K., Lehmer, B., Ptak, A., Sep. 2021. The Heraklion Extragalactic Catalogue (HECATE): a value-added galaxy catalogue for multimessenger astrophysics. MNRAS 506 (2), 1896–1915.
Kovlakas, K., Zezas, A., Andrews, J. J., Basu-Zych, A., Fragos, T., Hornschemeier, A., Lehmer, B., Ptak, A., Nov. 2020. A census of ultraluminous X-ray sources in the local Universe. MNRAS 498 (4), 4790–4810.
Kozai, Y., Nov. 1962. Secular perturbations of asteroids with high inclination and eccentricity. AJ 67, 591–598.
Kozlowski, M., Jaroszynski, M., Abramowicz, M. A., Feb. 1978. The analytic theory of fluid disks orbiting the Kerr black hole. A&A 63 (1-2), 209–220.
Kretschmar, P., Kreykenbohm, I., Wilms, J., Staubert, R., Heindl, W. A., Gruber, D. E., Rothschild, R. E., Apr. 2000. Disappearing pulses in Vela X-1. In: McConnell, M. L., Ryan, J. M. (Eds.), The Fifth Compton Symposium. Vol. 510 of American Institute of Physics Conference Series. pp. 163–167.
Kuranov, A. G., Postnov, K. A., Yungelson, L. R., Oct. 2020. Population Synthesis of Ultraluminous X-ray Sources with Magnetized Neutron Stars. Astronomy Letters 46 (10), 658–676.
Lai, D., Jul. 2003. Warping of Accretion Disks with Magnetically Driven Outflows: A Possible Origin for Jet Precession. ApJL 591 (2), L119–L122.
Lander, S. K., Jones, D. I., Jun. 2009. Magnetic fields in axisymmetric neutron stars. MNRAS 395 (4), 2162–2176.
Lang, C. C., Kaaret, P., Corbel, S., Mercer, A., Sep. 2007. A Radio Nebula Surrounding the Ultraluminous X-Ray Source in NGC 5408. ApJ 666 (1), 79–85.
Lasota, J.-P., Jun. 2001. The disc instability model of dwarf novae and low-mass X-ray binary transients. New Astronomy Reviews 45, 449–508.
Lasota, J.-P., 2016. Black Hole Accretion Discs. In: Bambi, C. (Ed.), Astrophysics of Black Holes: From Fundamental Aspects to Latest Developments. Vol. 440 of Astrophysics and Space Science Library. p. 1.
Lasota, J.-P., King, A. R., Dubus, G., Mar. 2015. X-ray Transients: Hyper- or Hypo-Luminous? ApJL 801, L4.
Lasota, J.-P., Vieira, R. S. S., Sądowski, A., Narayan, R., Abramowicz, M. A., Mar. 2016. The slimming effect of advection on black-hole accretion flows. A&A 587, A13.
Lau, R. M., Heida, M., Walton, D. J., Kasliwal, M. M., Adams, S. M., Cody, A. M., De, K., Gehrz, R. D., Fürst, F., Jencson, J. E., Kennea, J. A., Masci, F., Jun. 2019. Uncovering Red and Dusty Ultraluminous X-Ray Sources with Spitzer. ApJ 878 (1), 71.
Lehmer, B. D., Eufrasio, R. T., Basu-Zych, A., Doore, K., Fragos, T., Garofali, K., Kovlakas, K., Williams, B. F., Zezas, A., Santana-Silva, L., Jan.

2021. The Metallicity Dependence of the High-mass X-Ray Binary Luminosity Function. ApJ 907 (1), 17.
Lewin, W. H. G., van Paradijs, J., van den Heuvel, E. P. J., 1997. X-ray Binaries.
Li, J., Ostriker, J., Sunyaev, R., Apr. 2013. Rotating Accretion Flows: From Infinity to the Black Hole. ApJ 767 (2), 105.
Licquia, T. C., Newman, J. A., Jun. 2015. Improved Estimates of the Milky Way's Stellar Mass and Star Formation Rate from Hierarchical Bayesian Meta-Analysis. ApJ 806, 96.
Lidov, M. L., Oct. 1962. The evolution of orbits of artificial satellites of planets under the action of gravitational perturbations of external bodies. PLANSS 9 (10), 719–759.
Lin, D., Irwin, J. A., Webb, N. A., Barret, D., Remillard, R. A., Dec. 2013. Discovery of a Highly Variable Dipping Ultraluminous X-Ray Source in M94. ApJ 779 (2), 149.
Linden, T., Kalogera, V., Sepinsky, J. F., Prestwich, A., Zezas, A., Gallagher, J. S., Dec. 2010. The Effect of Starburst Metallicity on Bright X-ray Binary Formation Pathways. ApJ 725, 1984–1994.
Lipunov, V. M., Shakura, N. I., Feb. 1980. Interaction of the accretion disk with the magnetic field of a neutron star. Soviet Astronomy Letters 6, 14–17.
Liu, J.-F., Bregman, J., Miller, J., Kaaret, P., May 2007. Optical Studies of the Ultraluminous X-Ray Source NGC 1313 X-2. ApJ 661 (1), 165–172.
Liu, J.-F., Bregman, J. N., Bai, Y., Justham, S., Crowther, P., Nov. 2013. Puzzling accretion onto a black hole in the ultraluminous X-ray source M 101 ULX-1. Nature 503 (7477), 500–503.
López, K. M., Heida, M., Jonker, P. G., Torres, M. A. P., Roberts, T. P., Walton, D. J., Moon, D. S., Harrison, F. A., Jul. 2017. A systematic search for near-infrared counterparts of nearby ultraluminous X-ray sources (II). MNRAS 469 (1), 671–682.
López, K. M., Heida, M., Jonker, P. G., Torres, M. A. P., Roberts, T. P., Walton, D. J., Moon, D. S., Harrison, F. A., Sep. 2020. NIR counterparts to ULXs (III): completing the photometric survey and selected spectroscopic results. MNRAS 497 (1), 917–932.
Luangtip, W., Roberts, T. P., Done, C., Aug. 2016. The X-ray spectral evolution of the ultraluminous X-ray source Holmberg IX X-1. MNRAS 460 (4), 4417–4432.
Luangtip, W., Roberts, T. P., Mineo, S., Lehmer, B. D., Alexander, D. M., Jackson, F. E., Goulding, A. D., Fischer, J. L., Jan. 2015. A deficit of ultraluminous X-ray sources in luminous infrared galaxies. MNRAS 446, 470–492.
Lutovinov, A. A., Tsygankov, S. S., Jul. 2009. Timing characteristics of the hard X-ray emission from bright X-ray pulsars based on INTEGRAL data. Astronomy Letters 35 (7), 433–456.
Lyubarskii, Y. E., Dec. 1997. Flicker noise in accretion discs. MNRAS 292 (3), 679–685.
Maccarone, T. J., Kundu, A., Zepf, S. E., Rhode, K. L., Jan. 2007. A black hole in a globular cluster. Nature 445 (7124), 183–185.
Maccarone, T. J., Kundu, A., Zepf, S. E., Rhode, K. L., Jan. 2011. A new globular cluster black hole in NGC 4472. MNRAS 410 (3), 1655–1659.
Madhusudhan, N., Rappaport, S., Podsiadlowski, P., Nelson, L., Dec. 2008. Models for the Observable System Parameters of Ultraluminous X-Ray Sources. ApJ 688, 1235–1249.
Mainieri, V., Vignali, C., Merloni, A., Civano, F., Puccetti, S., Brusa, M., Gilli, R., Bolzonella, M., Comastri, A., Zamorani, G., Aller, M., Carollo, M., Scarlata, C., Elvis, M., Aldcroft, T. L., Cappelluti, N., Fabbiano, G., Finoguenov, A., Fiore, F., Fruscione, A., Koekemoer, A. M., Contini, T., Kneib, J.-P., Le Fèvre, O., Lilly, S., Renzini, A., Scodeggio, M., Bardelli, S., Bongiorno, A., Caputi, K., Coppa, G., Cucciati, O., de la Torre, S., de Ravel, L., Franzetti, P., Garilli, B., Iovino, A., Kampczyk, P., Knobel, C., Kovač, K., Lamareille, F., Le Borgne, J.-F., Le Brun, V., Maier, C., Mignoli, M., Pello, R., Peng, Y., Perez Montero, E., Ricciardelli, E., Silverman, J. D., Tanaka, M., Tasca, L., Tresse, L., Vergani, D., Zucca, E., Capak, P., Ilbert, O., Impey, C., Salvato, M., Scoville, N., Taniguchi, Y., Trump, J., May 2010. Ultraluminous X-ray sources out to z ˜ 0.3 in the COSMOS field. A&A 514, A85.
Mapelli, M., Annibali, F., Zampieri, L., Soria, R., Nov. 2013. A disrupted bulgeless satellite galaxy as counterpart of the ultraluminous X-ray source ESO 243-49 HLX-1. A&A 559, A124.
Mapelli, M., Colpi, M., Zampieri, L., May 2009. Low metallicity and ultra-luminous X-ray sources in the Cartwheel galaxy. MNRAS 395, L71–L75.
Mapelli, M., Ripamonti, E., Zampieri, L., Colpi, M., Bressan, A., Oct. 2010. Ultra-luminous X-ray sources and remnants of massive metal-poor stars. MNRAS 408, 234–253.
Marchant, P., Langer, N., Podsiadlowski, P., Tauris, T. M., de Mink, S., Mandel, I., Moriya, T. J., Aug. 2017. Ultra-luminous X-ray sources and neutron-star-black-hole mergers from very massive close binaries at low metallicity. A&A 604, A55.
Margon, B., Ford, H. C., Grandi, S. A., Stone, R. P. S., Oct. 1979. Enormous periodic Doppler shifts in SS433. ApJL 233, L63–L68.
Marshall, H. L., Canizares, C. R., Hillwig, T., Mioduszewski, A., Rupen, M., Schulz, N. S., Nowak, M., Heinz, S., Sep. 2013. Multiwavelength Observations of the SS 433 Jets. ApJ 775 (1), 75.
Martin, R. G., Nixon, C., Lubow, S. H., Armitage, P. J., Price, D. J., Doğan, S., King, A., Sep. 2014. The Kozai-Lidov Mechanism in Hydrodynamical Disks. ApJL 792 (2), L33.
Mauerhan, J. C., Muno, M. P., Morris, M. R., Stolovy, S. R., Cotera, A., Feb. 2010. Near-infrared Counterparts to Chandra X-ray Sources Toward the Galactic Center. II. Discovery of Wolf-Rayet Stars and O Supergiants. ApJ 710 (1), 706–728.
McClintock, J. E., Shafee, R., Narayan, R., Remillard, R. A., Davis, S. W., Li, L.-X., Nov. 2006. The Spin of the Near-Extreme Kerr Black Hole GRS 1915+105. ApJ 652 (1), 518–539.
McKinney, J. C., Gammie, C. F., Jul. 2002. Numerical Models of Viscous Accretion Flows near Black Holes. ApJ 573 (2), 728–737.
Medvedev, A., Fabrika, S., Feb. 2010. Evidence of supercritical disc funnel radiation in X-ray spectra of SS 433. MNRAS 402 (1), 479–491.
Merloni, A., Heinz, S., di Matteo, T., Nov. 2003. A Fundamental Plane of black hole activity. MNRAS 345 (4), 1057–1076.
Mezcua, M., Farrell, S. A., Gladstone, J. C., Lobanov, A. P., Dec. 2013a. Milliarcsec-scale radio emission of ultraluminous X-ray sources: steady jet emission from an intermediate-mass black hole? MNRAS 436 (2), 1546–1554.
Mezcua, M., Lobanov, A. P., May 2011. Compact radio emission in Ultraluminous X-ray sources. Astronomische Nachrichten 332 (4), 379.
Mezcua, M., Roberts, T. P., Lobanov, A. P., Sutton, A. D., Apr. 2015. The powerful jet of an off-nuclear intermediate-mass black hole in the spiral galaxy NGC 2276. MNRAS 448 (2), 1893–1899.
Mezcua, M., Roberts, T. P., Sutton, A. D., Lobanov, A. P., Dec. 2013b. Radio observations of extreme ULXs: revealing the most powerful ULX radio nebula ever or the jet of an intermediate-mass black hole? MNRAS 436 (4), 3128–3134.

Middleton, M. J., Brightman, M., Pintore, F., Bachetti, M., Fabian, A. C., Fürst, F., Walton, D. J., Jun. 2019a. On the magnetic field in M51 ULX-8. MNRAS 486 (1), 2–9.
Middleton, M. J., Fragile, P. C., Bachetti, M., Brightman, M., Jiang, Y. F., Ho, W. C. G., Roberts, T. P., Ingram, A. R., Dauser, T., Pinto, C., Walton, D. J., Fuerst, F., Fabian, A. C., Gehrels, N., Mar 2018. Lense-Thirring precession in ULXs as a possible means to constrain the neutron star equation of state. MNRAS 475 (1), 154–166.
Middleton, M. J., Fragile, P. C., Ingram, A., Roberts, T. P., Oct 2019b. The Lense-Thirring timing-accretion plane for ULXs. MNRAS 489 (1), 282–296.
Middleton, M. J., Heil, L., Pintore, F., Walton, D. J., Roberts, T. P., Mar. 2015a. A spectral-timing model for ULXs in the supercritical regime. MNRAS 447, 3243–3263.
Middleton, M. J., Heil, L., Pintore, F., Walton, D. J., Roberts, T. P., Mar. 2015b. A spectral-timing model for ULXs in the supercritical regime. MNRAS 447 (4), 3243–3263.
Middleton, M. J., Higginbottom, N., Knigge, C., Khan, N., Wiktorowicz, G., Oct. 2021a. Thermally driven winds in ULXs. MNRAS.
Middleton, M. J., King, A., Oct. 2016. Geometrical beaming of stellar mass ULXs. MNRAS 462 (1), L71–L74.
Middleton, M. J., King, A., Sep. 2017. Predicting ultraluminous X-ray source demographics from geometrical beaming. MNRAS 470 (1), L69–L71.
Middleton, M. J., Miller-Jones, J. C. A., Markoff, S., Fender, R., Henze, M., Hurley-Walker, N., Scaife, A. M. M., Roberts, T. P., Walton, D., Carpenter, J., Macquart, J.-P., Bower, G. C., Gurwell, M., Pietsch, W., Haberl, F., Harris, J., Daniel, M., Miah, J., Done, C., Morgan, J. S., Dickinson, H., Charles, P., Burwitz, V., Della Valle, M., Freyberg, M., Greiner, J., Hernanz, M., Hartmann, D. H., Hatzidimitriou, D., Riffeser, A., Sala, G., Seitz, S., Reig, P., Rau, A., Orio, M., Titterington, D., Grainge, K., Jan. 2013. Bright radio emission from an ultraluminous stellar-mass microquasar in M 31. Nature 493 (7431), 187–190.
Middleton, M. J., Roberts, T. P., Done, C., Jackson, F. E., Feb. 2011. Challenging times: a re-analysis of NGC 5408 X-1. MNRAS 411 (1), 644–652.
Middleton, M. J., Walton, D. J., Alston, W., Dauser, T., Eikenberry, S., Jiang, Y. F., Fabian, A. C., Fuerst, F., Brightman, M., Marshall, H., Parker, M., Pinto, C., Harrison, F. A., Bachetti, M., Altamirano, D., Bird, A. J., Perez, G., Miller-Jones, J., Charles, P., Boggs, S., Christensen, F., Craig, W., Forster, K., Grefenstette, B., Hailey, C., Madsen, K., Stern, D., Zhang, W., Sep. 2021b. NuSTAR reveals the hidden nature of SS433. MNRAS 506 (1), 1045–1058.
Middleton, M. J., Walton, D. J., Fabian, A., Roberts, T. P., Heil, L., Pinto, C., Anderson, G., Sutton, A., Dec. 2015c. Diagnosing the accretion flow in ultraluminous X-ray sources using soft X-ray atomic features. MNRAS 454 (3), 3134–3142.
Middleton, M. J., Walton, D. J., Fabian, A., Roberts, T. P., Heil, L., Pinto, C., Anderson, G., Sutton, A., Dec. 2015d. Diagnosing the accretion flow in ultraluminous X-ray sources using soft X-ray atomic features. MNRAS 454, 3134–3142.
Middleton, M. J., Walton, D. J., Roberts, T. P., Heil, L., Feb. 2014. Broad absorption features in wind-dominated ultraluminous X-ray sources? MNRAS 438 (1), L51–L55.
Miller, B. W., Jun. 1995. The Optical Counterpart to the Extremely Luminous X-Ray Source near Holmberg IX: A Possible Supershell in a Tidal Tail. ApJL 446, L75.
Miller, J. M., Fabian, A. C., Miller, M. C., Oct. 2004a. A Comparison of Intermediate-Mass Black Hole Candidate Ultraluminous X-Ray Sources and Stellar-Mass Black Holes. ApJL 614 (2), L117–L120.
Miller, J. M., Fabian, A. C., Miller, M. C., Jun. 2004b. Revealing a Cool Accretion Disk in the Ultraluminous X-Ray Source M81 X-9 (Holmberg IX X-1): Evidence for an Intermediate-Mass Black Hole. ApJ 607 (2), 931–938.
Miller, J. M., Fabian, A. C., Miller, M. C., Jun. 2004c. Revealing a Cool Accretion Disk in the Ultraluminous X-Ray Source M81 X-9 (Holmberg IX X-1): Evidence for an Intermediate-Mass Black Hole. ApJ 607 (2), 931–938.
Miller, J. M., Walton, D. J., King, A. L., Reynolds, M. T., Fabian, A. C., Miller, M. C., Reis, R. C., Oct. 2013. Revisiting Putative Cool Accretion Disks in Ultraluminous X-Ray Sources. ApJL 776 (2), L36.
Miller, M. C., Hamilton, D. P., Feb. 2002. Production of intermediate-mass black holes in globular clusters. MNRAS 330, 232–240.
Miller-Jones, J. C. A., Tetarenko, A. J., Sivakoff, G. R., Middleton, M. J., Altamirano, D., Anderson, G. E., Belloni, T. M., Fender, R. P., Jonker, P. G., Körding, E. G., Krimm, H. A., Maitra, D., Markoff, S., Migliari, S., Mooley, K. P., Rupen, M. P., Russell, D. M., Russell, T. D., Sarazin, C. L., Soria, R., Tudose, V., Apr. 2019. A rapidly changing jet orientation in the stellar-mass black-hole system V404 Cygni. Nature 569 (7756), 374–377.
Mineo, S., Gilfanov, M., Sunyaev, R., Jan. 2012. X-ray emission from star-forming galaxies - I. High-mass X-ray binaries. MNRAS 419 (3), 2095–2115.
Mineshige, S., Hirano, A., Kitamoto, S., Yamada, T. T., Fukue, J., May 1994. Time-dependent Disk Accretion in X-Ray Nova MUSCAE 1991. ApJ 426, 308.
Miniutti, G., Alexander, K. D., Bianchi, S., Chiaberge, M., Giustini, M., Laor, A., Read, A., Saxton, R., Uttley, P., Jan. 2020. Quasi-Periodic Eruptions (QPEs) in GSN 069. HST Proposal.
Miniutti, G., Saxton, R. D., Giustini, M., Alexander, K. D., Fender, R. P., Heywood, I., Monageng, I., Coriat, M., Tzioumis, A. K., Read, A. M., Knigge, C., Gandhi, P., Pretorius, M. L., Agís-González, B., Sep. 2019. Nine-hour X-ray quasi-periodic eruptions from a low-mass black hole galactic nucleus. NATURE 573 (7774), 381–384.
Mitsuda, K., Inoue, H., Koyama, K., Makishima, K., Matsuoka, M., Ogawara, Y., Shibazaki, N., Suzuki, K., Tanaka, Y., Hirano, T., Jan. 1984. Energy spectra of low-mass binary X-ray sources observed from Tenma. PASJ 36, 741–759.
Mohamed, S., Podsiadlowski, P., Sep. 2007. Wind Roche-Lobe Overflow: a New Mass-Transfer Mode for Wide Binaries. In: Napiwotzki, R., Burleigh, M. R. (Eds.), 15th European Workshop on White Dwarfs. Vol. 372 of Astronomical Society of the Pacific Conference Series. p. 397.
Monard, L. A. G., May 2010. Supernova 2010da in NGC 300. Central Bureau Electronic Telegrams 2289, 1.
Mondal, S., Belczyński, K., Wiktorowicz, G., Lasota, J.-P., King, A. R., Jan. 2020. The connection between merging double compact objects and the ultraluminous X-ray sources. MNRAS 491 (2), 2747–2759.
Mondal, S., Różańska, A., De Marco, B., Markowitz, A., Jul. 2021. Evidence for Fe K_α line and soft X-ray lag in NGC 7456 ultraluminous X-ray source-1. MNRAS 505 (1), L106–L111.
Moon, D.-S., Harrison, F. A., Cenko, S. B., Shariff, J. A., Apr. 2011. Large Highly Ionized Nebulae Around Ultra-luminous X-ray Sources. ApJL 731 (2), L32.

Motch, C., 2018. Optical Observations of Ultra-luminous X-ray Pulsars, presentation at "Ultra-luminous X-ray Pulsars", 6 - 8 june 2018, European Space Astronomy Centre (ESAC), Villafranca del Castillo, Spain. Available at `https://www.cosmos.esa.int/documents/1518557/1518574/motch.pdf/a08257a9-9b9b-b56f-63d1-067cd7ae8f8f`.

Motch, C., Pakull, M. W., Soria, R., Grisé, F., Pietrzyński, G., Oct. 2014. A mass of less than 15 solar masses for the black hole in an ultraluminous X-ray source. Nature 514, 198–201.

Motta, S. E., Kajava, J. J. E., Sánchez-Fernández, C., Beardmore, A. P., Sanna, A., Page, K. L., Fender, R., Altamirano, D., Charles, P., Giustini, M., Knigge, C., Kuulkers, E., Oates, S., Osborne, J. P., Oct. 2017. Swift observations of V404 Cyg during the 2015 outburst: X-ray outflows from super-Eddington accretion. MNRAS 471 (2), 1797–1818.

Mukherjee, E. S., Walton, D. J., Bachetti, M., Harrison, F. A., Barret, D., Bellm, E., Boggs, S. E., Christensen, F. E., Craig, W. W., Fabian, A. C., Fuerst, F., Grefenstette, B. W., Hailey, C. J., Madsen, K. K., Middleton, M. J., Miller, J. M., Rana, V., Stern, D., Zhang, W., Jul. 2015. A Hard X-Ray Study of the Ultraluminous X-Ray Source NGC 5204 X-1 with NuSTAR and XMM-Newton. ApJ 808 (1), 64.

Mushtukov, A., Tsygankov, S., Apr. 2022. Accreting strongly magnetised neutron stars: X-ray Pulsars. arXiv e-prints, arXiv:2204.14185.

Mushtukov, A. A., Ingram, A., Middleton, M., Nagirner, D. I., van der Klis, M., Mar. 2019. Timing properties of ULX pulsars: optically thick envelopes and outflows. MNRAS 484 (1), 687–697.

Mushtukov, A. A., Portegies Zwart, S., Tsygankov, S. S., Nagirner, D. I., Poutanen, J., Nov. 2020. Pulsating ULXs: large pulsed fraction excludes strong beaming. arXiv e-prints, arXiv:2011.09710.

Mushtukov, A. A., Suleimanov, V. F., Tsygankov, S. S., Ingram, A., May 2017. Optically thick envelopes around ULXs powered by accreating neutron stars. MNRAS 467, 1202–1208.

Mushtukov, A. A., Suleimanov, V. F., Tsygankov, S. S., Poutanen, J., Dec. 2015a. On the maximum accretion luminosity of magnetized neutron stars: connecting X-ray pulsars and ultraluminous X-ray sources. MNRAS 454, 2539–2548.

Mushtukov, A. A., Suleimanov, V. F., Tsygankov, S. S., Poutanen, J., Feb. 2015b. The critical accretion luminosity for magnetized neutron stars. MNRAS 447, 1847–1856.

Nandra, K., Barret, D., Barcons, X., Fabian, A., den Herder, J.-W., Piro, L., Watson, M., Adami, C., Aird, J., Afonso, J. M., Alexander, D., Argiroffi, C., Amati, L., Arnaud, M., Atteia, J.-L., Audard, M., Badenes, C., Ballet, J., Ballo, L., Bamba, A., Bhardwaj, A., Stefano Battistelli, E., Becker, W., De Becker, M., Behar, E., Bianchi, S., Biffi, V., Bîrzan, L., Bocchino, F., Bogdanov, S., Boirin, L., Boller, T., Borgani, S., Borm, K., Bouché, N., Bourdin, H., Bower, R., Braito, V., Branchini, E., Branduardi-Raymont, G., Bregman, J., Brenneman, L., Brightman, M., Brüggen, M., Buchner, J., Bulbul, E., Brusa, M., Bursa, M., Caccianiga, A., Cackett, E., Campana, S., Cappelluti, N., Cappi, M., Carrera, F., Ceballos, M., Christensen, F., Chu, Y.-H., Churazov, E., Clerc, N., Corbel, S., Corral, A., Comastri, A., Costantini, E., Croston, J., Dadina, M., D'Ai, A., Decourchelle, A., Della Ceca, R., Dennerl, K., Dolag, K., Done, C., Dovciak, M., Drake, J., Eckert, D., Edge, A., Ettori, S., Ezoe, Y., Feigelson, E., Fender, R., Feruglio, C., Finoguenov, A., Fiore, F., Galeazzi, M., Gallagher, S., Gandhi, P., Gaspari, M., Gastaldello, F., Georgakakis, A., Georgantopoulos, I., Gilfanov, M., Gitti, M., Gladstone, R., Goosmann, R., Gosset, E., Grosso, N., Guedel, M., Guerrero, M., Haberl, F., Hardcastle, M., Heinz, S., Alonso Herrero, A., Hervé, A., Holmstrom, M., Iwasawa, K., Jonker, P., Kaastra, J., Kara, E., Karas, V., Kastner, J., King, A., Kosenko, D., Koutroumpa, D., Kraft, R., Kreykenbohm, I., Lallement, R., Lanzuisi, G., Lee, J., Lemoine-Goumard, M., Lobban, A., Lodato, G., Lovisari, L., Lotti, S., McCharthy, I., McNamara, B., Maggio, A., Maiolino, R., De Marco, B., de Martino, D., Mateos, S., Matt, G., Maughan, B., Mazzotta, P., Mendez, M., Merloni, A., Micela, G., Miceli, M., Mignani, R., Miller, J., Miniutti, G., Molendi, S., Montez, R., Moretti, A., Motch, C., Nazé, Y., Nevalainen, J., Nicastro, F., Nulsen, P., Ohashi, T., O'Brien, P., Osborne, J., Oskinova, L., Pacaud, F., Paerels, F., Page, M., Papadakis, I., Pareschi, G., Petre, R., Petrucci, P.-O., Piconcelli, E., Pillitteri, I., Pinto, C., de Plaa, J., Pointecouteau, E., Ponman, T., Ponti, G., Porquet, D., Pounds, K., Pratt, G., Predehl, P., Proga, D., Psaltis, D., Rafferty, D., Ramos-Ceja, M., Ranalli, P., Rasia, E., Rau, A., Rauw, G., Rea, N., Read, A., Reeves, J., Reiprich, T., Renaud, M., Reynolds, C., Risaliti, G., Rodriguez, J., Rodriguez Hidalgo, P., Roncarelli, M., Rosario, D., Rossetti, M., Rozanska, A., Rovilos, E., Salvaterra, R., Salvato, M., Di Salvo, T., Sanders, J., Sanz-Forcada, J., Schawinski, K., Schaye, J., Schwope, A., Sciortino, S., Severgnini, P., Shankar, F., Sijacki, D., Sim, S., Schmid, C., Smith, R., Steiner, A., Stelzer, B., Stewart, G., Strohmayer, T., Strüder, L., Sun, M., Takei, Y., Tatischeff, V., Tiengo, A., Tombesi, F., Trinchieri, G., Tsuru, T. G., Ud-Doula, A., Ursino, E., Valencic, L., Vanzella, E., Vaughan, S., Vignali, C., Vink, J., Vito, F., Volonteri, M., Wang, D., Webb, N., Willingale, R., Wilms, J., Wise, M., Worrall, D., Young, A., Zampieri, L., In't Zand, J., Zane, S., Zezas, A., Zhang, Y., Zhuravleva, I., Jun. 2013. The Hot and Energetic Universe: A White Paper presenting the science theme motivating the Athena+ mission. arXiv e-prints, arXiv:1306.2307.

Narayan, R., Sądowski, A., Soria, R., Aug. 2017. Spectra of black hole accretion models of ultraluminous X-ray sources. MNRAS 469 (3), 2997–3014.

Neilsen, J., Rahoui, F., Homan, J., Buxton, M., May 2016. A Super-Eddington, Compton-thick Wind in GRO J1655-40? ApJ 822 (1), 20.

Nixon, C. J., Pringle, J. E., Dec. 2020. Be Star Disks: Powered by a Nonzero Central Torque. ApJL 905 (2), L29.

Ohsuga, K., Mineshige, S., Jul. 2011. Global Structure of Three Distinct Accretion Flows and Outflows around Black Holes from Two-dimensional Radiation-magnetohydrodynamic Simulations. ApJ 736, 2.

Ohsuga, K., Mineshige, S., Sep. 2014. Outflow Launching Mechanisms. Space Science Reviews 183 (1-4), 353–369.

Ohsuga, K., Mori, M., Nakamoto, T., Mineshige, S., Jul. 2005. Supercritical Accretion Flows around Black Holes: Two-dimensional, Radiation Pressure-dominated Disks with Photon Trapping. ApJ 628, 368–381.

Okuda, T., Apr. 2002. Super-Eddington Black-Hole Models for SS 433. PASJ 54, 253–266.

Okuda, T., Lipunova, G. V., Molteni, D., Oct. 2009. The jets and disc of SS 433 at super-Eddington luminosities. MNRAS 398 (4), 1668–1677.

Olausen, S. A., Kaspi, V. M., May 2014. The McGill Magnetar Catalog. The Astrophysical Journal Supplement Series 212, 6.

Olejak, A., Belczynski, K., Bulik, T., Sobolewska, M., Jun. 2020. Synthetic catalog of black holes in the Milky Way. A&A 638, A94.

Oskinova, L. M., Aug. 2005. Evolution of X-ray emission from young massive star clusters. MNRAS 361 (2), 679–694.

Paczyński, B., Jan. 1982. Thick Accretion Disks around Black Holes (Karl-Schwarzschild-Vorlesung 1981). Mitteilungen der Astronomischen Gesellschaft Hamburg 57, 27.

Paczynski, B., Jul. 1992. GB 790305 as a Very Strongly Magnetized Neutron Star. AcA 42, 145–153.

Paczynsky, B., Wiita, P. J., Aug. 1980. Thick accretion disks and supercritical luminosities. A&A 500, 203–211.

Pakull, M. W., Grisé, F., May 2008. Ultraluminous X-ray Sources: Beambags and Optical Counterparts. In: Bandyopadhyay, R. M., Wachter, S., Gelino, D., Gelino, C. R. (Eds.), A Population Explosion: The Nature & Evolution of X-ray Binaries in Diverse Environments. Vol. 1010 of

American Institute of Physics Conference Series. pp. 303–307.
Pakull, M. W., Grisé, F., Motch, C., Jan 2006. Ultraluminous X-ray Sources: Bubbles and Optical Counterparts. In: Meurs, E. J. A., Fabbiano, G. (Eds.), Populations of High Energy Sources in Galaxies. Vol. 230 of IAU Symposium. pp. 293–297.
Pakull, M. W., Mirioni, L., Feb. 2002. Optical Counterparts of Ultraluminous X-Ray Sources. ArXiv Astrophysics e-prints.
Pakull, M. W., Soria, R., Motch, C., Jul. 2010. A 300-parsec-long jet-inflated bubble around a powerful microquasar in the galaxy NGC 7793. Nature 466 (7303), 209–212.
Parfrey, K., Spitkovsky, A., Beloborodov, A. M., May 2016. Torque Enhancement, Spin Equilibrium, and Jet Power from Disk-Induced Opening of Pulsar Magnetic Fields. ApJ 822 (1), 33.
Parfrey, K., Tchekhovskoy, A., Dec. 2017. General-relativistic Simulations of Four States of Accretion onto Millisecond Pulsars. ApJL 851, L34.
Pasham, D. R., Cenko, S. B., Zoghbi, A., Mushotzky, R. F., Miller, J., Tombesi, F., Sep. 2015. Evidence for High-frequency QPOs with a 3:2 Frequency Ratio from a 5000 Solar Mass Black Hole. ApJL 811 (1), L11.
Pasham, D. R., Remillard, R. A., Fragile, P. C., Franchini, A., Stone, N. C., Lodato, G., Homan, J., Chakrabarty, D., Baganoff, F. K., Steiner, J. F., Coughlin, E. R., Pasham, N. R., Feb. 2019. A loud quasi-periodic oscillation after a star is disrupted by a massive black hole. Science 363 (6426), 531–534.
Pasham, D. R., Strohmayer, T. E., Jul. 2012. A Multi-epoch Timing and Spectral Study of the Ultraluminous X-Ray NGC 5408 X-1 with XMM-Newton. ApJ 753 (2), 139.
Pasham, D. R., Strohmayer, T. E., Sep 2013. Can the 62 Day X-Ray Period of ULX M82 X-1 Be Due to a Precessing Accretion Disk? ApJL 774 (2), L16.
Pasham, D. R., Strohmayer, T. E., Mushotzky, R. F., Sep. 2014. A 400-solar-mass black hole in the galaxy M82. Nature 513 (7516), 74–76.
Pérez-Ramírez, D., Mezcua, M., Leon, S., Caballero-García, M. D., May 2011. A search for radio counterparts to Chandra ULX candidates. Astronomische Nachrichten 332 (4), 384.
Perlman, E. S., Stocke, J. T., Carilli, C. L., Sugiho, M., Tashiro, M., Madejski, G., Wang, Q. D., Conway, J., Nov. 2002. The Apparent Host Galaxy of PKS 1413+135: Hubble Space Telescope, ASCA, and Very Long Baseline Array Observations. Aj 124 (5), 2401–2412.
Petterson, J. A., Dec. 1977. The 35 day cycle of the X-ray binary Hercules X-1. ApJ 218, 783–791.
Pfeiffer, H. P., Lai, D., Apr. 2004. Warping and Precession of Accretion Disks around Magnetic Stars: Nonlinear Evolution. ApJ 604 (2), 766–774.
Pinto, C., Alston, W., Soria, R., Middleton, M. J., Walton, D. J., Sutton, A. D., Fabian, A. C., Earnshaw, H., Urquhart, R., Kara, E., Roberts, T. P., Jul. 2017. From ultraluminous X-ray sources to ultraluminous supersoft sources: NGC 55 ULX, the missing link. MNRAS 468 (3), 2865–2883.
Pinto, C., Mehdipour, M., Walton, D. J., Middleton, M. J., Roberts, T. P., Fabian, A. C., Guainazzi, M., Soria, R., Kosec, P., Ness, J. U., Feb. 2020a. Thermal stability of winds driven by radiation pressure in super-Eddington accretion discs. MNRAS 491 (4), 5702–5716.
Pinto, C., Middleton, M. J., Fabian, A. C., May 2016. Resolved atomic lines reveal outflows in two ultraluminous X-ray sources. Nature 533 (7601), 64–67.
Pinto, C., Soria, R., Walton, D. J., D'Aì, A., Pintore, F., Kosec, P., Alston, W. N., Fuerst, F., Middleton, M. J., Roberts, T. P., Del Santo, M., Barret, D., Ambrosi, E., Robba, A., Earnshaw, H., Fabian, A. C., Aug. 2021. XMM-Newton campaign on the ultraluminous X-ray source NGC 247 ULX-1: outflows. MNRAS 505 (4), 5058–5074.
Pinto, C., Walton, D. J., Kara, E., Parker, M. L., Soria, R., Kosec, P., Middleton, M. J., Alston, W. N., Fabian, A. C., Guainazzi, M., Roberts, T. P., Fuerst, F., Earnshaw, H. P., Sathyaprakash, R., Barret, D., Mar. 2020b. XMM-Newton campaign on ultraluminous X-ray source NGC 1313 X-1: wind versus state variability. MNRAS 492 (4), 4646–4665.
Pintore, F., Esposito, P., Zampieri, L., Motta, S., Wolter, A., Apr. 2015. Spectral variability in Swift and Chandra observations of the ultraluminous source NGC 55 ULX1. MNRAS 448 (2), 1153–1161.
Pintore, F., Motta, S., Pinto, C., Bernardini, M. G., Rodriguez-Castillo, G., Salvaterra, R., Israel, G. L., Esposito, P., Ambrosi, E., Salvaggio, C., Zampieri, L., Wolter, A., Mar. 2021. The rare X-ray flaring activity of the Ultraluminous X-ray source NGC 4559 X7. arXiv e-prints, arXiv:2103.14541.
Pintore, F., Zampieri, L., Stella, L., Wolter, A., Mereghetti, S., Israel, G. L., Feb. 2017. Pulsator-like Spectra from Ultraluminous X-Ray Sources and the Search for More Ultraluminous Pulsars. ApJ 836 (1), 113.
Piro, A. L., Giacomazzo, B., Perna, R., Aug. 2017. The Fate of Neutron Star Binary Mergers. ApJL 844 (2), L19.
Podsiadlowski, P., Rappaport, S., Feb. 2000. Cygnus X-2: The Descendant of an Intermediate-Mass X-Ray Binary. ApJ 529, 946–951.
Ponti, G., Fender, R. P., Begelman, M. C., Dunn, R. J. H., Neilsen, J., Coriat, M., May 2012. Ubiquitous equatorial accretion disc winds in black hole soft states. MNRAS 422 (1), L11–L15.
Popov, S. B., Jan 2016. Origins of magnetars in binary systems. Astronomical and Astrophysical Transactions 29, 183–192.
Popov, S. B., Jan. 2022. High magnetic field neutron stars and magnetars in binary systems. arXiv e-prints, arXiv:2201.07507.
Portegies Zwart, S. F., McMillan, S. L. W., Sep. 2002. The Runaway Growth of Intermediate-Mass Black Holes in Dense Star Clusters. ApJ 576 (2), 899–907.
Pottschmidt, K., Ballhausen, R., Wilms, J., Zezas, A., Fuerst, F., Nowak, M. A., Grinberg, V., Kuehnel, M., Kretschmar, P., Tomsick, J. A., Antoniou, V., Kennea, J., Hong, J., Haberl, F., Maccarone, T., Hornschemeier, A., Ptak, A., Yukita, M., Wik, D., Lehmer, B., Fornasini, F., Bodaghee, A., McBride, V., Aug. 2016. NuSTAR Observations of SMC X-3. The Astronomer's Telegram 9404, 1.
Poutanen, J., Lipunova, G., Fabrika, S., Butkevich, A. G., Abolmasov, P., May 2007. Supercritically accreting stellar mass black holes as ultraluminous X-ray sources. MNRAS 377, 1187–1194.
Prestwich, A. H., Tsantaki, M., Zezas, A., Jackson, F., Roberts, T. P., Foltz, R., Linden, T., Kalogera, V., Jun. 2013. Ultra-luminous X-Ray Sources in the Most Metal Poor Galaxies. ApJ 769, 92.
Pringle, J. E., Mar. 1975. Period changes in eruptive binaries. MNRAS 170, 633–642.
Pringle, J. E., Jul 1996. Self-induced warping of accretion discs. MNRAS 281 (1), 357–361.
Qiu, Y., Feng, H., Jan. 2021. Linking Soft Excess in Ultraluminous X-Ray Sources with Optically Thick Wind Driven by Supercritical Accretion. ApJ 906 (1), 36.
Ramsey, C. J., Williams, R. M., Gruendl, R. A., Chen, C. H. R., Chu, Y.-H., Wang, Q. D., Apr. 2006. An Optical Study of Stellar and Interstellar Environments of Seven Luminous and Ultraluminous X-Ray Sources. ApJ 641 (1), 241–251.

Ransom, S. M., Jan. 2001. New search techniques for binary pulsars. Ph.D. thesis, Harvard University.

Ransom, S. M., Eikenberry, S. S., Middleditch, J., Sep. 2002. Fourier Techniques for Very Long Astrophysical Time-Series Analysis. AJ 124 (3), 1788–1809.

Rao, F., Feng, H., Kaaret, P., Oct. 2010. Detection of Strong Short-term Variability in NGC 6946 X-1. ApJ 722 (1), 620–624.

Rappaport, S. A., Podsiadlowski, P., Pfahl, E., Jan. 2005. Stellar-mass black hole binaries as ultraluminous X-ray sources. MNRAS 356, 401–414.

Ray, P. S., Guillot, S., Ho, W. C. G., Kerr, M., Enoto, T., Gendreau, K. C., Arzoumanian, Z., Altamirano, D., Bogdanov, S., Campion, R., Chakrabarty, D., Deneva, J. S., Jaisawal, G. K., Kozon, R., Malacaria, C., Strohmayer, T. E., Wolff, M. T., Jul. 2019. Anti-glitches in the Ultraluminous Accreting Pulsar NGC 300 ULX-1 Observed with NICER. ApJ 879 (2), 130.

Reig, P., Fabregat, J., Alfonso-Garzón, J., Aug. 2020. Optical counterpart to Swift J0243.6+6124. A&A 640, A35.

Revnivtsev, M., Gilfanov, M., Churazov, E., Jul. 1999. The frequency resolved spectroscopy of CYG X-1: fast variability of the Fe K_α line. A&A 347, L23–L26.

Revnivtsev, M., Gilfanov, M., Churazov, E., Sunyaev, R., Sep. 2002. Super-Eddington outburst of V4641 Sgr. A&A 391, 1013–1022.

Revnivtsev, M., Mereghetti, S., 2016. Magnetic Fields of Neutron Stars in X-Ray Binaries. Vol. 54. p. 299.

Ritter, H., Aug. 1988. Turning on and off mass transfer in cataclysmic binaries. A&A 202, 93–100.

Ritter, H., King, A. R., Jan. 2001. On the Spin-Up of Neutron Stars to Millisecond Pulsars in Long-Period Binaries. In: Podsiadlowski, P., Rappaport, S., King, A. R., D'Antona, F., Burderi, L. (Eds.), Evolution of Binary and Multiple Star Systems. Vol. 229 of Astronomical Society of the Pacific Conference Series. p. 423.

Robba, A., Pinto, C., Walton, D. J., Soria, R., Kosec, P., Pintore, F., Roberts, T. P., Alston, W. N., Middleton, M., Cusumano, G., Earnshaw, H. P., Fuerst, F., Sathyaprakash, R., Kyritsis, E., Fabian, A. C., Jun. 2021. Broadband X-ray spectral variability of the pulsing ULX NGC 1313 X-2. arXiv e-prints, arXiv:2106.04501.

Roberts, T. P., Fabbiano, G., Luo, B., Kim, D. W., Strader, J., Middleton, M. J., Brodie, J. P., Fragos, T., Gallagher, J. S., Kalogera, V., King, A. R., Zezas, A., Dec. 2012. A Variable Ultraluminous X-Ray Source in a Globular Cluster in NGC 4649. ApJ 760 (2), 135.

Roberts, T. P., Gladstone, J. C., Goulding, A. D., Swinbank, A. M., Ward, M. J., Goad, M. R., Levan, A. J., May 2011. (No) dynamical constraints on the mass of the black hole in two ULXs. Astronomische Nachrichten 332 (4), 398.

Roberts, T. P., Goad, M. R., Ward, M. J., Warwick, R. S., Jul. 2003. The unusual supernova remnant surrounding the ultraluminous X-ray source IC 342 X-1. MNRAS 342 (3), 709–714.

Roberts, T. P., Goad, M. R., Ward, M. J., Warwick, R. S., O'Brien, P. T., Lira, P., Hands, A. D. P., Aug. 2001. The identification of an optical counterpart to the super-Eddington X-ray source NGC 5204 X-1. MNRAS 325 (2), L7–L11.

Roberts, T. P., Kilgard, R. E., Warwick, R. S., Goad, M. R., Ward, M. J., Oct. 2006. Chandra monitoring observations of the ultraluminous X-ray source NGC 5204 X-1. MNRAS 371 (4), 1877–1890.

Roberts, T. P., Levan, A. J., Goad, M. R., Jun. 2008. New Hubble Space Telescope imaging of the counterparts to six ultraluminous X-ray sources. MNRAS 387 (1), 73–78.

Roberts, T. P., Warwick, R. S., Ward, M. J., Goad, M. R., Jenkins, L. P., Mar. 2005. XMM-Newton EPIC observations of the ultraluminous X-ray source NGC 5204 X-1. MNRAS 357 (4), 1363–1369.

Rodríguez Castillo, G. A., Israel, G. L., Belfiore, A., Bernardini, F., Esposito, P., Pintore, F., De Luca, A., Papitto, A., Stella, L., Tiengo, A., Zampieri, L., Bachetti, M., Brightman, M., Casella, P., D'Agostino, D., Dall'Osso, S., Earnshaw, H. P., Fürst, F., Haberl, F., Harrison, F. A., Mapelli, M., Marelli, M., Middleton, M., Pinto, C., Roberts, T. P., Salvaterra, R., Turolla, R., Walton, D. J., Wolter, A., May 2020. Discovery of a 2.8 s Pulsar in a 2 Day Orbit High-mass X-Ray Binary Powering the Ultraluminous X-Ray Source ULX-7 in M51. ApJ 895 (1), 60.

Rosen, S. R., Webb, N. A., Watson, M. G., Ballet, J., Barret, D., Braito, V., Carrera, F. J., Ceballos, M. T., Coriat, M., Della Ceca, R., Denkinson, G., Esquej, P., Farrell, S. A., Freyberg, M., Grisé, F., Guillout, P., Heil, L., Koliopanos, F., Law-Green, D., Lamer, G., Lin, D., Martino, R., Michel, L., Motch, C., Nebot Gomez-Moran, A., Page, C. G., Page, K., Page, M., Pakull, M. W., Pye, J., Read, A., Rodriguez, P., Sakano, M., Saxton, R., Schwope, A., Scott, A. E., Sturm, R., Traulsen, I., Yershov, V., Zolotukhin, I., May 2016. The XMM-Newton serendipitous survey. VII. The third XMM-Newton serendipitous source catalogue. A&A 590, A1.

Russell, D. M., Yang, Y. J., Gladstone, J. C., Wiersema, K., Roberts, T. P., May 2011. New observations of ULX supershells, and their implications. Astronomische Nachrichten 332 (4), 371.

Sadowski, A., Aug. 2011. Slim accretion disks around black holes. arXiv e-prints, arXiv:1108.0396.

Sakurai, Y., Inayoshi, K., Haiman, Z., Oct. 2016. Hyper-Eddington mass accretion on to a black hole with super-Eddington luminosity. MNRAS 461 (4), 4496–4504.

Sathyaprakash, R., Roberts, T. P., Grisé, F., Kaaret, P., Ambrosi, E., Done, C., Gladstone, J. C., Kajava, J. J. E., Soria, R., Zampieri, L., Apr. 2022. A multi-wavelength view of distinct accretion regimes in the pulsating ultraluminous X-ray source NGC 1313 X-2. MNRAS 511 (4), 5346–5362.

Sathyaprakash, R., Roberts, T. P., Siwek, M. M., Oct. 2019a. Observational limits on the X-ray emission from the bubble nebula surrounding Ho IX X-1. MNRAS 488 (4), 4614–4622.

Sathyaprakash, R., Roberts, T. P., Walton, D. J., Fuerst, F., Bachetti, M., Pinto, C., Alston, W. N., Earnshaw, H. P., Fabian, A. C., Middleton, M. J., Soria, R., Sep 2019b. The discovery of weak coherent pulsations in the ultraluminous X-ray source NGC 1313 X-2. MNRAS 488 (1), L35–L40.

Sazonov, S. Y., Sunyaev, R. A., Lund, N., May 1997. Super-Eddington x-ray luminosity of the bursting pulsar GRO J1744-28: WATCH/Granat observations. Astronomy Letters 23 (3), 286–292.

Sądowski, A., Aug. 2009. Slim Disks Around Kerr Black Holes Revisited. ApJS 183 (2), 171–178.

Sądowski, A., Abramowicz, M., Bursa, M., Kluźniak, W., Lasota, J. P., Różańska, A., Mar. 2011. Relativistic slim disks with vertical structure. A&A 527, A17.

Sądowski, A., Narayan, R., Nov. 2015. Powerful radiative jets in supercritical accretion discs around non-spinning black holes. MNRAS 453, 3213–3221.

Sądowski, A., Narayan, R., Tchekhovskoy, A., Abarca, D., Zhu, Y., McKinney, J. C., Feb. 2015. Global simulations of axisymmetric radiative black hole accretion discs in general relativity with a mean-field magnetic dynamo. MNRAS 447, 49–71.

Sądowski, A., Narayan, R., Mar. 2016. Three-dimensional simulations of supercritical black hole accretion discs - luminosities, photon trapping and variability. MNRAS 456 (4), 3929–3947.

Schwarm, F. W., Schönherr, G., Falkner, S., Pottschmidt, K., Wolff, M. T., Becker, P. A., Sokolova-Lapa, E., Klochkov, D., Ferrigno, C., Fürst, F., Hemphill, P. B., Marcu-Cheatham, D. M., Dauser, T., Wilms, J., Jan. 2017. Cyclotron resonant scattering feature simulations. I. Thermally averaged cyclotron scattering cross sections, mean free photon-path tables, and electron momentum sampling. A&A 597, A3.

Serim, M. M., Şahiner, Ş., ćerri-Serim, D., Inam, S. ć., Baykal, A., Nov. 2017. Discovery of a glitch in the accretion-powered pulsar SXP 1062. MNRAS 471 (4), 4982–4989.

Shakura, N. I., Sunyaev, R. A., 1973. Black holes in binary systems. Observational appearance. A&A 24, 337–355.

Sheng, Z., Wang, T., Ferland, G., Shu, X., Yang, C., Jiang, N., Chen, Y., Oct. 2021. Evidence of a Tidal-disruption Event in GSN 069 from the Abnormal Carbon and Nitrogen Abundance Ratio. ApJL 920 (1), L25.

Shih, I. C., Kundu, A., Maccarone, T. J., Zepf, S. E., Joseph, T. D., Sep. 2010. A Variable Black Hole X-ray Source in an NGC 1399 Globular Cluster. ApJ 721 (1), 323–328.

Shklovsky, I. S., Jun. 1981. The mass loss of SS 433 and its effect on the X-ray and radio emission of this source. Astr. Zh. 58, 554–560.

Sikora, M., Jul. 1981. Superluminous Accretion Discs. MNRAS 196, 257.

Skinner, G. K., Bedford, D. K., Elsner, R. F., Leahy, D., Weisskopf, M. C., Grindlay, J., Jun. 1982. Discovery of 69 ms periodic X-ray pulsations in A0538 - 66. Nature 297 (5867), 568–570.

Song, X., Walton, D. J., Lansbury, G. B., Evans, P. A., Fabian, A. C., Earnshaw, H., Roberts, T. P., Jan. 2020. The hunt for pulsating ultraluminous X-ray sources. MNRAS 491 (1), 1260–1277.

Soria, R., Jan. 2013. Eccentricity of HLX-1. MNRAS 428, 1944–1949.

Soria, R., Blair, W. P., Long, K. S., Russell, T. D., Winkler, P. F., Jan. 2020. A New Microquasar Candidate in M83. ApJ 888 (2), 103.

Soria, R., Cropper, M., Pakull, M., Mushotzky, R., Wu, K., Jan. 2005. The star-forming environment of an ultraluminous X-ray source in NGC4559: an optical study. MNRAS 356, 12–28.

Soria, R., Fender, R. P., Hannikainen, D. C., Read, A. M., Stevens, I. R., Jun. 2006. An ultraluminous X-ray microquasar in NGC5408? MNRAS 368 (4), 1527–1539.

Soria, R., Kong, A., Feb. 2016. Revisiting the ultraluminous supersoft source in M 101: an optically thick outflow model. MNRAS 456 (2), 1837–1858.

Soria, R., Long, K. S., Blair, W. P., Godfrey, L., Kuntz, K. D., Lenc, E., Stockdale, C., Winkler, P. F., Mar. 2014. Super-Eddington Mechanical Power of an Accreting Black Hole in M83. Science 343 (6177), 1330–1333.

Soria, R., Pakull, M. W., Broderick, J. W., Corbel, S., Motch, C., Dec. 2010. Radio lobes and X-ray hotspots in the microquasar S26. MNRAS 409 (2), 541–551.

Soria, R., Pakull, M. W., Motch, C., Miller-Jones, J. C. A., Schwope, A. D., Urquhart, R. T., Ryan, M. S., Feb. 2021. The ultraluminous X-ray source bubble in NGC 5585. MNRAS 501 (2), 1644–1662.

Staubert, R., Trümper, J., Kendziorra, E., Klochkov, D., Postnov, K., Kretschmar, P., Pottschmidt, K., Haberl, F., Rothschild, R. E., Santangelo, A., Wilms, J., Kreykenbohm, I., Fürst, F., Feb. 2019. Cyclotron lines in highly magnetized neutron stars. A&A 622, A61.

Steele, M. M., Zepf, S. E., Maccarone, T. J., Kundu, A., Rhode, K. L., Salzer, J. J., Apr. 2014. Composition of an Emission Line System in Black Hole Host Globular Cluster RZ2109. ApJ 785 (2), 147.

Stephenson, C. B., Sanduleak, N., Apr. 1977. New H-alpha emission stars in the Milky Way. ApJs 33, 459–469.

Stobbart, A. M., Roberts, T. P., Warwick, R. S., Jul. 2004. A dipping black hole X-ray binary candidate in NGC 55. MNRAS 351 (3), 1063–1070.

Stobbart, A. M., Roberts, T. P., Wilms, J., May 2006. XMM-Newton observations of the brightest ultraluminous X-ray sources. MNRAS 368 (1), 397–413.

Straub, O., Done, C., Middleton, M., May 2013. The effect of advection at luminosities close to Eddington: The ULX in M 31. A&A 553, A61.

Strohmayer, T. E., Mushotzky, R. F., Mar. 2003. Discovery of X-Ray Quasi-periodic Oscillations from an Ultraluminous X-Ray Source in M82: Evidence against Beaming. ApJL 586 (1), L61–L64.

Strohmayer, T. E., Mushotzky, R. F., Oct. 2009. Evidence for an Intermediate-mass Black Hole in NGC 5408 X-1. ApJ 703 (2), 1386–1393.

Strohmayer, T. E., Mushotzky, R. F., Winter, L., Soria, R., Uttley, P., Cropper, M., May 2007. Quasi-periodic Variability in NGC 5408 X-1. ApJ 660 (1), 580–586.

Sutton, A. D., Done, C., Roberts, T. P., Nov. 2014. Irradiated, colour-temperature-corrected accretion discs in ultraluminous X-ray sources. MNRAS 444 (3), 2415–2427.

Sutton, A. D., Roberts, T. P., Middleton, M. J., Oct. 2013. The ultraluminous state revisited: fractional variability and spectral shape as diagnostics of super-Eddington accretion. MNRAS 435 (2), 1758–1775.

Sutton, A. D., Roberts, T. P., Middleton, M. J., Nov. 2015. X-Ray Spectral Residuals in NGC 5408 X-1: Diffuse Emission from Star Formation, or the Signature of a Super-Eddington Wind? ApJ 814 (1), 73.

Swartz, D. A., Ghosh, K. K., Tennant, A. F., Wu, K., Oct. 2004. The Ultraluminous X-Ray Source Population from the Chandra Archive of Galaxies. ApJs 154 (2), 519–539.

Swartz, D. A., Soria, R., Tennant, A. F., Yukita, M., Nov. 2011. A Complete Sample of Ultraluminous X-ray Source Host Galaxies. ApJ 741 (1), 49.

Swartz, D. A., Tennant, A. F., Soria, R., Sep. 2009. Ultraluminous X-Ray Source Correlations with Star-Forming Regions. ApJ 703 (1), 159–168.

Takahashi, H. R., Mineshige, S., Ohsuga, K., Jan. 2018. Supercritical Accretion onto a Non-magnetized Neutron Star: Why is it Feasible? apJ 853 (1), 45.

Takahashi, H. R., Ohsuga, K., Aug. 2017. General Relativistic Radiation MHD Simulations of Supercritical Accretion onto a Magnetized Neutron Star: Modeling of Ultraluminous X-Ray Pulsars. ApJL 845 (1), L9.

Takahashi, H. R., Ohsuga, K., Kawashima, T., Sekiguchi, Y., Jul. 2016. Formation of Overheated Regions and Truncated Disks around Black Holes: Three-dimensional General Relativistic Radiation-magnetohydrodynamics Simulations. ApJ 826 (1), 23.

Takeuchi, S., Ohsuga, K., Mineshige, S., Aug. 2013. Clumpy Outflows from Supercritical Accretion Flow. PASJ 65, 88.

Taniguchi, Y., Shioya, Y., Tsuru, T. G., Ikeuchi, S., Jun. 2000. Formation of Intermediate-Mass Black Holes in Circumnuclear Regions of Galaxies. PASJ 52, 533–537.

Tao, L., Feng, H., Grisé, F., Kaaret, P., Aug. 2011. Compact Optical Counterparts of Ultraluminous X-Ray Sources. ApJ 737 (2), 81.

Tao, L., Feng, H., Zhang, S., Bu, Q., Zhang, S., Qu, J., Zhang, Y., Mar. 2019. Super-Eddington Accretion onto the Galactic Ultraluminous X-Ray Pulsar Swift J0243.6+6124. ApJ 873 (1), 19.

Tetarenko, B. E., Dubus, G., Marcel, G., Done, C., Clavel, M., Jul. 2020. Thermally driven disc winds as a mechanism for X-ray irradiation heating in black hole X-ray binaries: the case study of GX339-4. MNRAS 495 (4), 3666–3682.

Tetarenko, B. E., Lasota, J. P., Heinke, C. O., Dubus, G., Sivakoff, G. R., Feb. 2018. Strong disk winds traced throughout outbursts in black-hole X-ray binaries. NATURE 554 (7690), 69–72.

Tetarenko, B. E., Sivakoff, G. R., Heinke, C. O., Gladstone, J. C., Feb. 2016. WATCHDOG: A Comprehensive All-sky Database of Galactic Black Hole X-ray Binaries. The Astrophysical Journal Supplement Series 222, 15.

Tong, H., Nov. 2015. Ultraluminous X-ray pulsar: Accreting magnetar? Astronomische Nachrichten 336, 835.

Townsend, L. J., Charles, P. A., May 2020. Orbital and superorbital periods in ULX pulsars, disc-fed HMXBs, Be/X-ray binaries, and double-periodic variables. MNRAS 495 (1), 139–143.

Townsend, L. J., Kennea, J. A., Coe, M. J., McBride, V. A., Buckley, D. A. H., Evans, P. A., Udalski, A., Nov. 2017. The 2016 super-Eddington outburst of SMC X-3: X-ray and optical properties and system parameters. MNRAS 471 (4), 3878–3887.

Trudolyubov, S. P., Jun. 2008. XMM-Newton discovery of transient X-ray pulsar in NGC 1313. MNRAS 387 (1), L36–L40.

Trudolyubov, S. P., Priedhorsky, W. C., Córdova, F. A., Jul. 2007. Chandra and XMM-Newton Discovery of Transient X-Ray Pulsar in the Nearby Spiral Galaxy NGC 2403. ApJ 663 (1), 487–496.

Tsygankov, S. S., Doroshenko, V., Lutovinov, A. A., Mushtukov, A. A., Poutanen, J., Sep. 2017. SMC X-3: the closest ultraluminous X-ray source powered by a neutron star with non-dipole magnetic field. A&A 605, A39.

Tsygankov, S. S., Lutovinov, A. A., Churazov, E. M., Sunyaev, R. A., Sep. 2006. V0332+53 in the outburst of 2004-2005: luminosity dependence of the cyclotron line and pulse profile. MNRAS 371 (1), 19–28.

Tsygankov, S. S., Lutovinov, A. A., Doroshenko, V., Mushtukov, A. A., Suleimanov, V., Poutanen, J., Aug. 2016a. Propeller effect in two brightest transient X-ray pulsars: 4U 0115+63 and V 0332+53. A&A 593, A16.

Tsygankov, S. S., Mushtukov, A. A., Suleimanov, V. F., Poutanen, J., Mar. 2016b. Propeller effect in action in the ultraluminous accreting magnetar M82 X-2. MNRAS 457 (1), 1101–1106.

Tzanavaris, P., Hornschemeier, A. E., Gallagher, S. C., Lenkić, L., Desjardins, T. D., Walker, L. M., Johnson, K. E., Mulchaey, J. S., Feb. 2016. Exploring X-Ray Binary Populations in Compact Group Galaxies with Chandra. ApJ 817 (2), 95.

Urpin, V., Geppert, U., Aug. 1995. Accretion and evolution of the neutron star magnetic field. MNRAS 275 (4), 1117–1124.

Urquhart, R., Soria, R., Feb. 2016a. Optically thick outflows in ultraluminous supersoft sources. MNRAS 456 (2), 1859–1880.

Urquhart, R., Soria, R., Nov. 2016b. Two Eclipsing Ultraluminous X-Ray Sources in M51. ApJ 831 (1), 56.

Uttley, P., Cackett, E. M., Fabian, A. C., Kara, E., Wilkins, D. R., Aug. 2014. X-ray reverberation around accreting black holes. A&Ar 22, 72.

Van Booy, S., May 2009. Love Begins in Winter: Five Stories.

van den Eijnden, J., Degenaar, N., Russell, T. D., Wijnands, R., Miller-Jones, J. C. A., Sivakoff, G. R., Hernández Santisteban, J. V., Sep. 2018. An evolving jet from a strongly magnetized accreting X-ray pulsar. Nature 562 (7726), 233–235.

van den Eijnden, J., Degenaar, N., Schulz, N. S., Nowak, M. A., Wijnands, R., Russell, T. D., Hernández Santisteban, J. V., Bahramian, A., Maccarone, T. J., Kennea, J. A., Heinke, C. O., Aug. 2019. Chandra reveals a possible ultrafast outflow in the super-Eddington Be/X-ray binary Swift J0243.6+6124. MNRAS 487 (3), 4355–4371.

van Paradijs, J., Jun. 1996. On the Accretion Instability in Soft X-Ray Transients. ApJL 464, L139.

Vasilopoulos, G., Haberl, F., Carpano, S., Maitra, C., Dec. 2018. NGC 300 ULX1: A test case for accretion torque theory. A&A 620, L12.

Vasilopoulos, G., Koliopanos, F., Haberl, F., Treiber, H., Brightman, M., Earnshaw, H. P., Gúrpide, A., Feb. 2021. Chandra probes the X-ray variability of M51 ULX-7: evidence of propeller transition and X-ray dips on orbital periods. arXiv e-prints, arXiv:2102.07996.

Vasilopoulos, G., Lander, S. K., Koliopanos, F., Bailyn, C. D., Feb. 2020a. M51 ULX-7: superorbital periodicity and constraints on the neutron star magnetic field. MNRAS 491 (4), 4949–4959.

Vasilopoulos, G., Petropoulou, M., Koliopanos, F., Ray, P. S., Bailyn, C. B., Haberl, F., Gendreau, K., Oct. 2019. NGC 300 ULX1: spin evolution, super-Eddington accretion, and outflows. MNRAS 488 (4), 5225–5231.

Vasilopoulos, G., Ray, P. S., Gendreau, K. C., Jenke, P. A., Jaisawal, G. K., Wilson-Hodge, C. A., Strohmayer, T. E., Altamirano, D., Iwakiri, W. B., Wolff, M. T., Guillot, S., Malacaria, C., Stevens, A. L., Jun. 2020b. The 2019 super-Eddington outburst of RX J0209.6-7427: detection of pulsations and constraints on the magnetic field strength. MNRAS 494 (4), 5350–5359.

Vaughan, B. A., Nowak, M. A., Jan. 1997. X-Ray Variability Coherence: How to Compute It, What It Means, and How It Constrains Models of GX 339-4 and Cygnus X-1. ApJL 474 (1), L43–L46.

Vinokurov, A., Fabrika, S., Atapin, K., Apr. 2013. Ultra-luminous X-ray sources as supercritical accretion disks: Spectral energy distributions. Astrophysical Bulletin 68 (2), 139–153.

Voges, W., Aschenbach, B., Boller, T., Bräuninger, H., Briel, U., Burkert, W., Dennerl, K., Englhauser, J., Gruber, R., Haberl, F., Hartner, G., Hasinger, G., Kürster, M., Pfeffermann, E., Pietsch, W., Predehl, P., Rosso, C., Schmitt, J. H. M. M., Trümper, J., Zimmermann, H. U., Sep. 1999. The ROSAT all-sky survey bright source catalogue. A&A 349, 389–405.

von Zeipel, H., Mar. 1910. Sur l'application des séries de M. Lindstedt à l'étude du mouvement des comètes périodiques. Astronomische Nachrichten 183 (22), 345.

Waisberg, I., Dexter, J., Olivier-Petrucci, P., Dubus, G., Perraut, K., Apr. 2019. Collimated radiation in SS 433. Constraints from spatially resolved optical jets and Cloudy modeling of the optical bullets. A&A 624, A127.

Walton, D. J., Bachetti, M., Fürst, F., Barret, D., Brightman, M., Fabian, A. C., Grefenstette, B. W., Harrison, F. A., Heida, M., Kennea, J., Kosec, P., Lau, R. M., Madsen, K. K., Middleton, M. J., Pinto, C., Steiner, J. F., Webb, N., Apr. 2018a. A Potential Cyclotron Resonant Scattering Feature in the Ultraluminous X-Ray Source Pulsar NGC 300 ULX1 Seen by NuSTAR and XMM-Newton. ApJL 857 (1), L3.

Walton, D. J., Fürst, F., Bachetti, M., Barret, D., Brightman, M., Fabian, A. C., Gehrels, N., Harrison, F. A., Heida, M., Middleton, M. J., Rana, V., Roberts, T. P., Stern, D., Tao, L., Webb, N., Aug 2016a. A 78 Day X-Ray Period Detected from NGC 5907 ULX1 by Swift. ApJL 827 (1), L13.

Walton, D. J., Fürst, F., Harrison, F. A., Middleton, M. J., Fabian, A. C., Bachetti, M., Barret, D., Miller, J. M., Ptak, A., Rana, V., Stern, D., Tao, L., Apr. 2017. The Broadband Spectral Variability of Holmberg IX X-1. ApJ 839 (2), 105.

Walton, D. J., Fürst, F., Harrison, F. A., Stern, D., Bachetti, M., Barret, D., Brightman, M., Fabian, A. C., Middleton, M. J., Ptak, A., Tao, L., Feb. 2018b. Super-Eddington accretion on to the neutron star NGC 7793 P13: Broad-band X-ray spectroscopy and ultraluminous X-ray sources. MNRAS 473 (4), 4360–4376.

Walton, D. J., Fürst, F., Heida, M., Harrison, F. A., Barret, D., Stern, D., Bachetti, M., Brightman, M., Fabian, A. C., Middleton, M. J., Apr. 2018c. Evidence for Pulsar-like Emission Components in the Broadband ULX Sample. ApJ 856, 128.

Walton, D. J., Mackenzie, A. D. A., Gully, H., Patel, N. R., Roberts, T. P., Earnshaw, H. P., Mateos, S., Jan. 2022. A multimission catalogue of ultraluminous X-ray source candidates. MNRAS 509 (2), 1587–1604.

Walton, D. J., Middleton, M. J., Pinto, C., Fabian, A. C., Bachetti, M., Barret, D., Brightman, M., Fuerst, F., Harrison, F. A., Miller, J. M., Stern, D., Aug. 2016b. An Iron K Component to the Ultrafast Outflow in NGC 1313 X-1. ApJL 826 (2), L26.

Walton, D. J., Middleton, M. J., Rana, V., Miller, J. M., Harrison, F. A., Fabian, A. C., Bachetti, M., Barret, D., Boggs, S. E., Christensen, F. E., Craig, W. W., Fuerst, F., Grefenstette, B. W., Hailey, C. J., Madsen, K. K., Stern, D., Zhang, W., Jun. 2015. NuSTAR, XMM-Newton, and Suzaku Observations of the Ultraluminous X-Ray Source Holmberg II X-1. ApJ 806 (1), 65.

Walton, D. J., Miller, J. M., Reis, R. C., Fabian, A. C., Oct. 2012. Searching for massive outflows in Holmberg IX X-1 and NGC 1313 X-1: the iron K band. MNRAS 426 (1), 473–483.

Walton, D. J., Pinto, C., Nowak, M., Bachetti, M., Sathyaprakash, R., Kara, E., Roberts, T. P., Soria, R., Brightman, M., Canizares, C. R., Earnshaw, H. P., Fürst, F., Heida, M., Middleton, M. J., Stern, D., Tao, L., Webb, N., Alston, W. N., Barret, D., Fabian, A. C., Harrison, F. A., Kosec, P., Jun. 2020. The unusual broad-band X-ray spectral variability of NGC 1313 X-1 seen with XMM-Newton, Chandra, and NuSTAR. MNRAS 494 (4), 6012–6029.

Walton, D. J., Roberts, T. P., Mateos, S., Heard, V., Sep. 2011. 2XMM ultraluminous X-ray source candidates in nearby galaxies. MNRAS 416 (3), 1844–1861.

Wang, S., Qiu, Y., Liu, J., Bregman, J. N., Sep. 2016. Chandra ACIS Survey of X-Ray Point Sources in Nearby Galaxies. II. X-Ray Luminosity Functions and Ultraluminous X-Ray Sources. ApJ 829 (1), 20.

Wang, S., Soria, R., Urquhart, R., Liu, J., Jul. 2018. Discovery of two eclipsing X-ray binaries in M 51. MNRAS 477 (3), 3623–3645.

Watson, M. G., Stewart, G. C., Brinkmann, W., King, A. R., Sep. 1986. Doppler-shifted X-ray line emission from SS 433. MNRAS 222, 261–271.

Weaver, R., McCray, R., Castor, J., Shapiro, P., Moore, R., Dec. 1977. Interstellar bubbles. II. Structure and evolution. ApJ 218, 377–395.

Webb, N., Cseh, D., Lenc, E., Godet, O., Barret, D., Corbel, S., Farrell, S., Fender, R., Gehrels, N., Heywood, I., Aug. 2012. Radio Detections During Two State Transitions of the Intermediate-Mass Black Hole HLX-1. Science 337 (6094), 554.

Webb, N. A., Coriat, M., Traulsen, I., Ballet, J., Motch, C., Carrera, F. J., Koliopanos, F., Authier, J., de la Calle, I., Ceballos, M. T., Colomo, E., Chuard, D., Freyberg, M., Garcia, T., Kolehmainen, M., Lamer, G., Lin, D., Maggi, P., Michel, L., Page, C. G., Page, M. J., Perea-Calderon, J. V., Pineau, F. X., Rodriguez, P., Rosen, S. R., Santos Lleo, M., Saxton, R. D., Schwope, A., Tomás, L., Watson, M. G., Zakardjian, A., Sep. 2020. The XMM-Newton serendipitous survey. IX. The fourth XMM-Newton serendipitous source catalogue. A&A 641, A136.

Weisskopf, M. C., Tananbaum, H. D., Van Speybroeck, L. P., O'Dell, S. L., Jul. 2000. Chandra X-ray Observatory (CXO): overview. In: Truemper, J. E., Aschenbach, B. (Eds.), X-Ray Optics, Instruments, and Missions III. Vol. 4012 of Society of Photo-Optical Instrumentation Engineers (SPIE) Conference Series. pp. 2–16.

Weng, S.-S., Feng, H., Feb. 2018. Evidence for Precession due to Supercritical Accretion in Ultraluminous X-Ray Sources. ApJ 853 (2), 115.

White, N. E., Carpenter, G. F., Apr. 1978. The recurrent X-ray transient A 0538-66. MNRAS 183, 11P–15.

Wielgus, M., Yan, W., Lasota, J. P., Abramowicz, M. A., Mar. 2016. Limits on thickness and efficiency of Polish doughnuts in application to the ULX sources. A&A 587, A38.

Wiersema, K., Farrell, S. A., Webb, N. A., Servillat, M., Maccarone, T. J., Barret, D., Godet, O., Oct. 2010. A Redshift for the Intermediate-mass Black Hole Candidate HLX-1: Confirmation of its Association with the Galaxy ESO 243-49. ApJL 721, L102–L106.

Wiktorowicz, G., Belczynski, K., Maccarone, T., Sep. 2014. Black hole X-ray transients: The formation puzzle. In: Binary Systems, their Evolution and Environments. p. 37.

Wiktorowicz, G., Lasota, J.-P., Belczynski, K., Lu, Y., Liu, J., Iłkiewicz, K., Mar. 2021. Wind-powered ultraluminous X-ray sources. arXiv e-prints, arXiv:2103.02026.

Wiktorowicz, G., Lasota, J.-P., Middleton, M., Belczynski, K., Apr 2019. The Observed versus Total Population of ULXs. ApJ 875 (1), 53.

Wiktorowicz, G., Sobolewska, M., Lasota, J.-P., Belczynski, K., Sep. 2017. The Origin of the Ultraluminous X-Ray Sources. ApJ 846, 17.

Wiktorowicz, G., Sobolewska, M., Sądowski, A., Belczynski, K., Sep. 2015. Nature of the Extreme Ultraluminous X-Ray Sources. ApJ 810, 20.

Wilkinson, T., Uttley, P., Aug. 2009. Accretion disc variability in the hard state of black hole X-ray binaries. MNRAS 397 (2), 666–676.

XRISM Science Team, Mar. 2020. Science with the X-ray Imaging and Spectroscopy Mission (XRISM). arXiv e-prints, arXiv:2003.04962.

Yao, Y., Feng, H., Oct. 2019. A Wind-disk Self-irradiation Model for Supercritical Accretion. ApJL 884 (1), L3.

Yoshioka, S., Mineshige, S., Ohsuga, K., Kawashima, T., Kitaki, T., Sep. 2022. Large-scale outflow structure and radiation properties of super-Eddington flow: Dependence on the accretion rates. arXiv e-prints, arXiv:2209.01427.

Zampieri, L., Roberts, T. P., Dec. 2009. Low-metallicity natal environments and black hole masses in ultraluminous X-ray sources. MNRAS 400, 677–686.

Zezas, A., Fabbiano, G., Rots, A. H., Murray, S. S., Oct. 2002. Chandra Observations of "The Antennae" Galaxies (NGC 4038/4039). III. X-Ray Properties and Multiwavelength Associations of the X-Ray Source Population. ApJ 577 (2), 710–725.

Zhou, Y., Feng, H., Ho, L. C., Yao, Y., Jan. 2019. Evidence for Optically Thick, Eddington-limited Winds Driven by Supercritical Accretion. ApJ 871 (1), 115.

Ziolkowski, J., Jan. 1985. Rotational status of X-ray pulsars. A&A 35, 185–198.